

PURDUE UNIVERSITY
GRADUATE SCHOOL
Thesis/Dissertation Acceptance

This is to certify that the thesis/dissertation prepared

By Sravan Kumar Dheeraj Kapilavai

Entitled Unsteady Computational Analysis of Shrouded Plug Nozzle Flows and Reacting Impinging Jets

For the degree of Doctor of Philosophy

Is approved by the final examining committee:

Charles L. Merkle

Chair

Steven H. Frankel

Gregory A. Blaisdell

Nicole L. Key

To the best of my knowledge and as understood by the student in the *Research Integrity and Copyright Disclaimer (Graduate School Form 20)*, this thesis/dissertation adheres to the provisions of Purdue University's "Policy on Integrity in Research" and the use of copyrighted material.

Approved by Major Professor(s): Charles L. Merkle

Approved by: Anil K. Bajaj

Head of the Graduate Program

06/15/2011

Date

**PURDUE UNIVERSITY
GRADUATE SCHOOL**

Research Integrity and Copyright Disclaimer

Title of Thesis/Dissertation:

Unsteady Computational Analysis of Shrouded Plug Nozzle Flows and Reacting Impinging Jets

For the degree of Doctor of Philosophy

I certify that in the preparation of this thesis, I have observed the provisions of *Purdue University Executive Memorandum No. C-22*, September 6, 1991, *Policy on Integrity in Research*.*

Further, I certify that this work is free of plagiarism and all materials appearing in this thesis/dissertation have been properly quoted and attributed.

I certify that all copyrighted material incorporated into this thesis/dissertation is in compliance with the United States' copyright law and that I have received written permission from the copyright owners for my use of their work, which is beyond the scope of the law. I agree to indemnify and save harmless Purdue University from any and all claims that may be asserted or that may arise from any copyright violation.

Sravan Kumar Dheeraj Kapilavai

Printed Name and Signature of Candidate

06/15/2011

Date (month/day/year)

*Located at http://www.purdue.edu/policies/pages/teach_res_outreach/c_22.html

UNSTEADY COMPUTATIONAL ANALYSIS OF SHROUDED PLUG NOZZLE
FLOWS AND REACTING IMPINGING JETS

A Dissertation

Submitted to the Faculty

of

Purdue University

by

Dheeraj S. K. Kapilavai

In Partial Fulfillment of the

Requirements for the Degree

of

Doctor of Philosophy

August 2011

Purdue University

West Lafayette, Indiana

UMI Number: 3481048

All rights reserved

INFORMATION TO ALL USERS

The quality of this reproduction is dependent on the quality of the copy submitted.

In the unlikely event that the author did not send a complete manuscript and there are missing pages, these will be noted. Also, if material had to be removed, a note will indicate the deletion.



UMI 3481048

Copyright 2011 by ProQuest LLC.

All rights reserved. This edition of the work is protected against unauthorized copying under Title 17, United States Code.



ProQuest LLC.
789 East Eisenhower Parkway
P.O. Box 1346
Ann Arbor, MI 48106 - 1346

To my parents and grandparents.

ACKNOWLEDGMENTS

I am thankful to my advisor Prof. Charles Merkle for allowing me to work at my own pace but at the same time for providing his valuable feedback which served as important course correction throughout my journey here at Purdue. Both his technical insight and patience will remain as inspirations with me.

The thesis benefited extensively from the comments I received from Prof. Steven Frankel, Prof. Gregory Blaisdell and Prof. Nicole Key who served on on my thesis committee and reviewed my work. I want to thank Prof. Steven Heister, Prof. John Sullivan and their graduate students who generously provided me with experimental data that I have used extensively throughout my work.

I gained tremendously from my association with all members in our group. I want to thank Dr. Guoping Xia for his extensive support with GEMS and in helping me understand its many details. The discussions on various topics with Dr. Dima Voytovich and Matthew Harvazinski were both technically beneficial as well as enjoyable.

My stay at Purdue proved lucky as Padmasini became a permanent member of my life. She has always stood by me, highs and lows alike of my graduate life.

Finally, this thesis would be incomplete without mentioning the role my parents and grandparents played throughout my academic career by extending their unconditional support which always propelled me to achieve higher goals.

The work done in this thesis was supported by the Rolls-Royce University Technology Center and the MURI project. Their help is gratefully acknowledged.

TABLE OF CONTENTS

	Page
LIST OF TABLES	vi
LIST OF FIGURES	vii
ABBREVIATIONS	xv
ABSTRACT	xvi
CHAPTER 1. INTRODUCTION	1
1.1 Shrouded Plug Nozzle	2
1.2 Reacting Impinging Jets of MMH/RFNA	16
1.3 Outline of Thesis	22
CHAPTER 2. NUMERICAL SCHEME	24
2.1 Governing Equations of Fluid Dynamics	24
2.1.1 Reynolds Averaged Navier Stokes Equations	27
2.2 Turbulence Modeling	31
2.3 Chemical Kinetics and Turbulence Chemistry Interaction	33
2.4 Thermo-Chemistry	37
2.4.1 Transport Properties	38
2.4.2 Thermodynamic Properties	42
2.5 Numerical Scheme	42
2.5.1 Spatial Discretization	45
2.5.2 Temporal Discretization	50
2.6 Boundary Conditions	52
2.6.1 Entropy, Total Enthalpy and Flow Angle at the Inlet	53
2.6.2 Outlet Boundary Condition	55
2.6.3 Inviscid Wall	55
2.6.4 Viscous Wall Boundary Condition	56
CHAPTER 3. NUMERICAL SIMULATION OF SHROUDED PLUG NOZZLE	58
3.1 Introduction	60
3.2 Experimental Configuration	63
3.3 Axisymmetric Computations	68
3.3.1 Computational Domain and Boundary Conditions	68
3.4 Axisymmetric Steady Analysis	73
3.4.1 Global Shock Structure	74
3.4.2 Computational Vs. Experimental Shock Pattern	82
3.4.3 Pressure Distribution	88

	Page
3.5 Unsteady Characteristics	101
3.5.1 Analysis of Experimental Data	102
3.5.2 Axisymmetric Unsteady Analysis	106
3.6 Three-Dimensional Computations	118
3.6.1 Computational Domain and Boundary Conditions	120
3.7 Three-Dimensional Steady Analysis	122
3.8 Three-Dimensional Unsteady Analysis	128
3.8.1 Unsteady Results at NPR = 1.59	130
3.8.2 Unsteady Results at NPR = 1.26	143
3.9 Performance Analysis	153
3.9.1 Nozzle Thrust Efficiencies	157
3.9.2 Nozzle Discharge Coefficient	160
CHAPTER 4. REACTING IMPINGING JETS OF MMH/RFNA	163
4.1 Constant Volume Combustion	166
4.2 Two-Dimensional Analysis	170
4.2.1 Introduction	170
4.3 Problem Definition	173
4.4 Combustion Behavior	178
4.4.1 Combustion in Helium Environment at 800K and 101325Pa	179
4.4.2 Combustion in Argon Environment at 800K and 101325Pa	188
4.4.3 Combustion at 800K and 10132500Pa	197
4.4.4 Comparison of Time-Averaged Results	203
4.5 Unsteady Three-Dimensional Analysis	209
4.5.1 Problem Definition	210
4.6 Three-Dimensional Combustion Behavior	222
4.6.1 Combustion at 800K and 101325Pa	222
4.6.2 Combustion at 800K and 10132500Pa	223
CHAPTER 5. SUMMARY AND CONCLUSIONS	228
LIST OF REFERENCES	234
APPENDIX: REDUCED MECHANISM FOR MMH/RFNA	240
VITA	248

LIST OF TABLES

Table	Page
3.1 Comparison of two 3-D grids.	121
4.1 Computations detail for $T=800K$, $p=101325Pa$	179
4.2 Helium ambient properties.	179
4.3 Argon ambient properties.	189
4.4 Computations detail for $T=800K$, $p=10132500Pa$	198
4.5 Computations detail for $T=800K$, $p=10132500Pa$	223
4.6 Computations detail for $T=800K$, $p=10132500Pa$	224

LIST OF FIGURES

Figure	Page
1.1 Sketch of a traditional plug nozzle(top). Flow structure for Nozzle Pressure Ratio (NPR, defined as the ratio of inlet total pressure to the ambient pressure) less than design (middle) and flow structure at design (bottom) [13].	6
1.2 Notional view of supersonic plug nozzle concept with key features highlighted. [4].	7
1.3 Schematic of various flow structures in a transonic diffuser based on incoming Mach number [25].	10
1.4 Shock oscillation, unchoking and upstream propagating disturbances in a transonic diffuser at NPR of 1.28(left) and 1.29 (right) [25].	11
1.5 Schematic of Free(top) and restricted(bottom) shock separation regimes for a thrust optimized parabolic nozzle [31].	12
1.6 Shadowgraph images for the annular plug nozzle shown in the figure for (a) NPR = 2.1, (b) = 2.57 and (c) NPR = 3.82 [35].	13
1.7 Schematic of mixing and separation combustion for hypergolic impinging jets from reference [50].	20
3.1 Low sonic boom propulsion system concept. Dashed ellipse shows the co-annular plug nozzle.	59
3.2 Cut-away view of the sub-scale model of the shrouded plug nozzle.	61
3.3 Schematic of nozzle used for computations along with detail of throat area showing sharp corner.	65
3.4 Schematic showing the instrumentation available on the plug as well as the shroud surface.	67
3.5 Computational domain and grid for axisymmetric computations. Boundary conditions are treated as shown. The plug nozzle walls are treated as no-slip wall.	69
3.6 Details of grid near the splitter tip and shroud tip.	70
3.7 Convergence of steady axisymmetric computations at low NPRs.	73

Figure	Page
3.8 Computational schlieren compared to experimental schlieren at NPR = 6.12.	76
3.9 Computational schlieren (top half) and Mach number (bottom half) for progressing NPRs depicting shock structure.	77
3.10 Near throat region computational schlieren (grayscale) and Mach number (rainbow) at NPR = 1.26.	78
3.11 Computational schlieren showing lambda shock and expansion fan impinging on plug at NPR = 1.59.	79
3.12 Computational schlieren showing lambda shock and shocklets in mean flow at NPR = 1.93.	80
3.13 Computational schlieren showing Mach reflection at NPR = 2.56 (left) and regular reflection at NPR = 3.06 (right).	81
3.14 Computational schlieren showing oblique shock from shroud tip impinging on plug surface at NPR = 5.01.	82
3.15 Computational schlieren compared to experimental Shadowgraph at NPR = 2.11.	84
3.16 Computational schlieren compared to experimental schlieren at NPR = 3.73.	87
3.17 Normalized Static Pressure from data showing axisymmetry.	93
3.18 FSS normalized Static Pressure distribution on plug and shroud superimposed on computational schlieren, line - computations, square - experiment data point.	94
3.19 RSS regime normalized Static Pressure distribution on plug and shroud superimposed on computational schlieren, line - computations, square symbol - data point.	95
3.20 Oblique shock regime normalized Static Pressure distribution on plug and shroud superimposed on computational schlieren, line - computations, square - experiment data point.	96
3.21 Static pressure on plug and shroud exhibits sudden jump at NPR of 2.04 due to transition from FSS to RSS.	97
3.22 Normalized Static Pressure distribution for hot core flow with varying NPR.	99
3.23 Mach number and pressure at constant radius location passing through the center of the throat.	100

Figure	Page
3.24 PSD measured from Kulite data and its variation with NPR.	103
3.25 Relative position of shock location on shroud with respect to Kulite location as a function of NPR.	104
3.26 Kulite frequency variation with NPR.	106
3.27 Schematic of locations at which space-time plots are shown, plug(PP'), shroud(SS') and mid-plane(MM').	109
3.28 Space time plot of pressure on the plug(left) and shroud(right) of the nozzle at NPR of 1.59.	110
3.29 Space time plot of pressure oscillation at mid-plane of the nozzle.	111
3.30 Pressure oscillations on the plug and shroud for NPR of 1.59 at locations indicated on the plot.	113
3.31 PSD estimate for location $x/L_{plug} = 0.18$ for the plug(left) and shroud(right) taken from the duration $22ms$ to $86ms$ showing a peak at $60 Hz$	114
3.32 Time averaged schlieren from unsteady computations (top half) compared to steady computations (bottom half).	114
3.33 Time averaged pressure from unsteady computations compared to steady computations and data for NPR of 1.59.	115
3.34 Space time plot of pressure on the plug(left) and shroud(right) of the nozzle at NPR of 1.26.	116
3.35 Pressure oscillations on the plug and shroud for NPR of 1.26 at different locations.	117
3.36 NPR=1.26, PSD estimate for location $x/L_{plug} = 0.18$ for the plug(left) and shroud(right) taken from the duration $11ms$ to $80ms$ showing a peak at $110 Hz$	118
3.37 Time averaged schlieren from unsteady computations (top half) compared to steady computations (bottom half).	119
3.38 Time averaged pressure from unsteady computations compared to steady computations and data for NPR of 1.26.	119
3.39 Quarter grid for three dimensional computations.	123
3.40 Quarter grid for three dimensional computations.	124
3.41 Grid in the axial direction in the diverging section compared for grid 1(top) and grid 2(bottom).	125
3.42 Convergence of steady 3D computations.	125

Figure	Page
3.43 Static pressure distribution from 3-D computations on grid 1 and 2 compared to axisymmetric computations and data at NPR of 1.76(FSS) and 3.73(RSS).	127
3.44 Static pressure distribution from 3-D computations on grid 1 and 2 compared to axisymmetric computations and data.	128
3.45 Instantaneous schlieren from unsteady computations in a tangential plane depicting the initial transient. Six instants starting at time - a) 1ms, b)2ms, c)3ms, d)5ms, e) 7.5ms and f)8.8ms into the unsteady computation are shown.	132
3.46 Location reference for plug (PP'), mid-plane (MM') and shroud (SS'). . .	133
3.47 Space time plot at MM' location in the plug depicting the transient process and the shock movement. The red lines indicate the time instants at which schlieren images in Fig. 3.45.	134
3.48 Space time plot of pressure on the shroud wall(left), mid-plane(center) and plug wall(right) of the nozzle at NPR of 1.59.	136
3.49 Pressure oscillations on the plug and shroud for NPR of 1.59 at the locations indicated on the plug.	138
3.50 Power Spectral density at two locations on plug and shroud for NPR of 1.59.	139
3.51 Instantaneous schlieren from unsteady computations in a plane. Four instants starting at time, τ are shown - a) τ , b) $\tau+2ms$, c) $\tau+4ms$, d) $t = \tau+6ms$	140
3.52 Instantaneous pressure distribution(solid) on the plug at four azimuthal locations compared to steady pressure(dotted). Four instants for a frequency of 150 Hz starting at time, τ are shown - a) τ , b) $\tau+2ms$, c) $\tau+4ms$, d) $t = \tau+6ms$	141
3.53 Instantaneous pressure distribution(solid) on the shroud at four azimuthal locations compared to steady pressure(dotted). Four instants for a frequency of 200Hz starting at time, τ are shown - a) τ , b) $\tau+2ms$, c) $\tau+4ms$, d) $t = \tau+6ms$	143
3.54 NPR=1.59. Time-averaged schlieren from 3-D and 2-D unsteady compared to 3-D steady. Time-averaged Solid lines - avg. unsteady, dotted line - steady computations, symbols - data.	145
3.55 Space time plot of pressure on the shroud(left), mid-plane(center) and plug (right) of the nozzle at NPR of 1.26. (Legend for all contours at the end.)	146

Figure	Page
3.56 Instantaneous schlieren images at a plane in the nozzle depicting shock motion starting from the farthest downstream shock location at time, τ - a) τ , b) $\tau+15ms$, c) $\tau+25ms$, d) $t = \tau+54ms$, e) $t = \tau+72ms$ and f) $t = \tau+86ms$	148
3.57 Instantaneous pressure distribution (solid) on the plug surface at four azimuthal locations compared to steady pressure (dotted) during a cycle of shock motion starting from the farthest downstream shock location at time, τ - a) τ , b) $\tau+15ms$, c) $\tau+25ms$, d) $t = \tau+54ms$, e) $t = \tau+72ms$ and f) $t = \tau+86ms$	150
3.58 Pressure oscillations on the plug and shroud for NPR of 1.26.	151
3.59 Power Spectral density at $x/L_{plug} = 0.18$ on plug(top) and shroud(bottom).	152
3.60 NPR=1.26. Time-averaged schlieren from 3-D and 2-D unsteady compared to 3-D steady. Time-averaged Solid lines - avg. unsteady, dotted line - steady computations, symbols - data.	154
3.61 Total temperature profile at the nozzle throat normalized by upstream core temperature.	157
3.62 Experiment vs. Predicted thrust efficiency: area and mass based.	159
3.63 Experiment vs. Predicted discharge coefficient: area and mass based.	162
4.1 Schematic sketch of constant volume combustion computation with no heat conduction at the inviscid walls. A homogeneous mixture of fuel and oxidizer at given temperature and pressure are used as initial condition.	166
4.2 Ignition time delay as function of pressure and temperature for various O/F ratios.	169
4.3 Reactant and intermediate species consumption (top) and product formation (bottom) at $T = 800K$ and $p=101325Pa$ for O/F = 2.0. Mass fraction axis on left and temperature axis on right.	171
4.4 Intermediate reaction species formation in the reaction zone, primarily HONO, NO ₂ and CH ₄ N ₂ . Mass fraction axis on left and temperature axis on right at $T = 800K$ and $p=101325Pa$ for O/F = 2.0.	172
4.5 Computational domain with grid and details on boundary conditions (RFNA - RFNA inlet, MMH - MMH Inlet, W - Wall, AI - Ambient Inlet, O - Outlet).	175
4.6 Computational domain near RFNA and MMH orifices along with the cavity. Also marked are the boundary conditions(RFNA - RFNA inlet, MMH - MMH Inlet, W - Wall, AI - Ambient Inlet).	176

Figure	Page
4.7 Grid details at RFNA orifice exit(left) and MMH orifice exit (right). . .	176
4.8 Density contours MMH/RFNA streams coming into a grazing contact at $T=800K$, $p=101325Pa$ in helium environment with HNO_3 on left and MMH on right at $t=1.4ms$	180
4.9 HONO mass fraction contours showing HONO formation in the reactive interface between the two streams and ignition at $T=800K$, $p=101325Pa$ in helium environment. The streamline from the RFNA orifice helps in demarcating the fuel and oxidizer streams.	182
4.10 Mass fraction of fuel, oxidizer, temperature and prominent products of combustion after ignition at $3.5ms$ at $T=800K$, $p=101325Pa$ in helium environment. The streamline from the RFNA and MMH orifice helps in demarcating the fuel and oxidizer streams.	184
4.11 Mass fraction of products and intermediate species of combustion after ignition at $3.5ms$ in helium environment. The streamline from the RFNA and MMH orifice helps in demarcating the fuel and oxidizer streams. . .	185
4.12 Mass fraction of fuel, oxidizer, temperature and HONO at $6.1ms$. The flame front is propagating downstream and considerable build-up of HONO in the cavity.	186
4.13 Temperature contours at $t = 6.4ms$ when ignition occurs in the cavity, $t=7.1ms$ when the flame is half way between cavity and downstream flame and at $t=7.6ms$ when the two flame fronts merge.	187
4.14 Mass fraction of HNO_3 , MMH and CH_4N_2 along with temperature at time $t=40ms$ after the flame is set up in the domain for helium background at $T=800K$ and $p=101325Pa$	190
4.15 Mass fraction of N_2 , O_2 , H_2O and CO_2 at time $t=40ms$ after the flame is set up in the domain for helium background at $T=800K$ and $p=101325Pa$	191
4.16 Mass fraction of NO and NO_2 at time $t=40ms$ after the flame is set up in the domain for helium background at $T=800K$ and $p=101325Pa$	192
4.17 argon, $T=800K$, $p=101325Pa$. Series of contour plots of temperature at $t=1.6ms$ (initial impingement), $3.0ms$ (mid-way of impingement and ignition), $4.5ms$ (before ignition) and $4.7ms$ (after ignition) showing the initial combustion process.	193
4.18 Mass fraction contours of HNO_3 , MMH, NO and H_2O after ignition in argon environment at $T = 800K$ and $p=101325Pa$ at $t=4.7ms$	194

Figure	Page
4.19 Mass fraction contours of HNO_3 , MMH and H_2O along with temperature when the flame front has reached the exit at $t = 24.6\text{ms}$ in argon environment at $T = 800\text{K}$ and $p=101325\text{Pa}$	195
4.20 Temperature contours at $t = 25.8\text{ms}$ when ignition occurs at the cavity, $t= 26.2\text{ms}$ when the flame is half way between cavity and downstream flame and at $t=26.5\text{ms}$ when the two flame fronts merge for argon at $T = 800\text{K}$ and $p=101325\text{Pa}$	196
4.21 Instantaneous contour plots of MMH, HNO_3 , NO and temperature for argon environment at 101325Pa for argon at $T = 800\text{K}$ and $p=101325\text{Pa}$	199
4.22 Instantaneous contour plots of density and temperature for helium at 10132500Pa showing flame propagation between the fuel and oxidizer interface for three instants of time $t = 2\text{ms}$, 2.3ms and 2.8ms for helium background gas at $p = 10132500\text{Pa}$	202
4.23 Mass fraction contours of MMH, HNO_3 and NO along with temperature for argon at $t=40\text{ms}$, 10132500Pa	204
4.24 Mass fraction contours of MMH, HNO_3 and NO along with temperature for helium at $t=40\text{ms}$, 10132500Pa	205
4.25 Time-averaged mass fraction contours of HNO_3 and MMH for argon (right) and helium (left) environment at $p=101325\text{Pa}$	207
4.26 Time-averaged contours of mass fraction of NO and temperature for argon (right) and helium (left) environment at $p=101325\text{Pa}$	212
4.27 Time averaged temperature at $y = -0.02\text{m}$ (left) and $y = -0.08\text{m}$ for argon (black) and helium (red) ambient environment at $p = 101325\text{Pa}$	213
4.28 Time averaged species mass fraction at $y = -0.02\text{m}$ for argon (black) and helium (red) ambient environment at $p = 101325\text{Pa}$	214
4.29 Time averaged species mass fraction at $y = -0.08\text{m}$ for argon (black) and helium (red) ambient environment at $p = 101325\text{Pa}$	215
4.30 Time-averaged mass fraction contours of HNO_3 and MMH for helium (left) and argon (right) environment at $p=10132500\text{Pa}$	216
4.31 Time-averaged mass fraction contour of NO along with temperature contour for helium (left) and argon (right) environment at $p=10132500\text{Pa}$	217
4.32 Time averaged temperature at $y = -0.02\text{m}$ (left) and $y = -0.08\text{m}$ for argon (black) and helium (red) ambient environment at $p = 10132500\text{Pa}$	218
4.33 Time averaged species mass fraction at $y = -0.02\text{m}$ for argon (black) and helium (red) ambient environment at $p = 10132500\text{Pa}$	219

Figure	Page
4.34 Time averaged species mass fraction at $y = -0.08m$ for argon (black) and helium (red) ambient environment at $p = 10132500Pa$	220
4.35 Isometric view of the computational domain with plane of symmetry marked along with grids at two planes perpendicular to each other. The boundary conditions are as marked.	221
4.36 View of the domain from the top (top) and in the upstream direction (bottom). Also shown is the detail of grid at the plane of symmetry (top) and at a location midway between orifices and outlet.	225
4.37 View of the domain seen perpendicular to flow direction along with the grid at a plane.	226
4.38 Detail of grid in the plane of symmetry close to the RFNA orifice (left) and MMH orifice (right)	226
4.39 Contour plot of HNO_3 (left), MMH (center) and temperature (right) at a pressure of 1 atm in argon environment.	227
4.40 Contour plot of HNO_3 (left), MMH (center) and temperature (right) at a pressure of 100 atm in helium environment.	227

ABBREVIATIONS

NPR Nozzle Pressure Ratio
BANR Bi-Annular Nozzle Rig
CFD Computational Fluid Dynamics
RSS Restricted Shock Separation
FSS Free Shock Separation
MMH Monomethylhydrazine
RFNA Red fuming nitric acid

ABSTRACT

Kapilavai, S. K. Dheeraj Ph.D., Purdue University, August 2011. Unsteady Computational Analysis of Shrouded Plug Nozzle Flows and Reacting Impinging Jets. Major Professor: Charles L. Merkle, School of Mechanical Engineering.

The computations of a non-reacting nozzle-flow problem and a reacting impinging jet problem using a unified numerical methodology is presented. The nozzle problem is a shrouded plug configuration that operates at nozzle pressure ratio (NPR, ratio of inlet pressure to ambient pressure) between one to a design NPR of 6.23 for supersonic applications. An sub-scale model with extensive instrumentation is the basis of axisymmetric and three-dimensional computations done as both steady and unsteady problems with an aim to understand nozzle flow physics. The pressure distribution and shock structure predicted by steady computations not only detailed the shock physics but were also in close agreement with measured pressure data and visualization. The nozzle is observed to transition from normal shock at NPR's just above one to a lambda shock below NPR of 2.0 and then from a Mach reflection to a regular reflection within NPR range 2.25 to 3.1. A barrel oblique shock is observed above NPR of 3.1 before achieving perfect expansion at design NPR. During the shock transition the separation region behind the shock is observed to be fully attached for NPR's below 2.0, a regime called free shock separation (FSS), followed by reattached flow on plug wall called restricted shock separation (RSS) at higher NPR's. The unsteady computational analysis explained the shifts in frequencies observed in measurements. The unsteady computations at NPR of 1.26 show that the measured frequency of 170Hz is because of periodic choking and unchoking driven by large scale shock motion. In the FSS regime identified by computations the measured frequency remains constant at 200Hz . Following this the frequency shifts to above 300Hz and increases monotonically as the nozzle transitions from FSS to RSS observed to occur

between NPR of 2.0 and approximately 2.25. Unsteady 3-D computations showed axisymmetric instantaneous flowfield at NPR of 1.26 while at NPR of 1.59 the dynamic flowfield was observed to be asymmetric. Time-averaged pressure distribution and oscillation frequency from three-dimensional unsteady computations were closer to the measurements than with axisymmetric assumption.

An experimental impinging jet configuration involving MMH as fuel stream and RFNA as oxidizer stream, impinging at an included angle is studied to analyze combustion initiation, flame propagation, holding and sustenance. A newly devised reduced chemical mechanism is evaluated in this context for two background gases of argon and helium which showed different combustion behavior in recent experiments. Also, combustion is studied at two pressures corresponding to experiments (1 atm) and applications (100 atm). Before the impinging jet configuration is studied, a simple homogeneous mixture constant volume combustion problem is formulated to understand chemical time scales. The chemical mechanism resulted in combustion in a millisecond time frame only for an initial mixture temperature of 800 K with initial pressure of 100 atm showing faster combustion than 1 atm . The impinging configuration is studied first with a planar assumption before three-dimensional analysis is taken up to understand effect of background gas. In agreement with experiments, the helium and argon gases showed considerable differences. At low pressure of 1 atm the combustion initiation, propagation and holding were analogous to experiments in both gases but the ignition event timings and flame sustenance were different in the two gases. Argon resulted in wider flame zone compared to helium. At high pressures the flame propagation behavior differed from low pressures with instantaneous combustion initiation but different flame behaviors in both gases. The flame propagation, holding and sustenance behavior has been explained in detail in the two background gases at both pressure extremes. The three-dimensional computations showed that the combustion behavior is different with predictions using planar assumption. The differences have been documented.

CHAPTER 1. INTRODUCTION

Computational Fluid Dynamics (CFD) deals with the computer solution of the Navier-Stokes equations describing fluid dynamics. The CFD solver of the present generation is no longer tailored to the problem of interest. The rapid progress in developing fluid flow models for varied situations coupled with improved algorithms have led to a single CFD solver being applied in different applications. The application can be as varied as reacting and non-reacting. CFD is now a mainstay in understanding flowfields at the industrial scale and also at a fundamental level. The domain of flow situations where CFD is growing is expanding rapidly.

The dissertation work concerns with two applications: one a non-reacting industrial scale problem and the other a reacting situation. The non-reacting flowfield is that of a unique exhaust nozzle concept called the shrouded plug nozzle that finds application in supersonic propulsion systems. The second application, a flowfield with reacting hypergolic MMH/RFNA propellants aims at understanding transient processes governing combustion initiation and sustenance. Both flows draw on a generic formulation of the Navier-Stokes equations that can be tailored to solve either one. The reacting and non-reacting case share common features in terms of flow physics and algorithm development which makes their solution using a single tool possible. The difficulties posed by both non-reacting and reacting flows to algorithm development are also shared. For example, both flowfield need sufficient resolution of wall boundaries which leads to difficulties with high aspect ratio cells [1]. The presence of source terms in turbulence models in non-reacting flows and both turbulence as well as species source terms in reacting flows pose a common challenge to CFD [2]. The present work makes use of a CFD solver which deals with both flowfields. The algorithm details are given later. In the next two sections we discuss the two applications where the CFD solver is applied.

1.1 Shrouded Plug Nozzle

The most persuasive arguments for a supersonic transport aircraft is the significant time savings and thereby increase in productivity for passengers, relative to a subsonic aircraft. Earlier development in commercial aircraft design concentrated in increasing the size till supersonic flight allowed higher passenger productivity as evident from programs like the Concorde supersonic transport. The Concorde program proved that commercially viable supersonic transport is possible but also directed the attention of the later generation of propulsion engineers to its drawbacks. The low passenger capacity, high fuel consumption and powerplants which were not designed to meet the noise regulations eventually led to the aircraft being grounded. The powerplant of a supersonic transport aircraft, thus, plays a major role in the success of any such developmental endeavor. In recent years buoyed by the tremendous market for subsonic business jet aircrafts focus has been directed for the development of a supersonic business jet [3]; [4]; [5]; [6]; [7]. In realizing this goal special focus is required for the development of an efficient propulsion system and its components.

The development of exhaust nozzles is one of the difficult tasks for a successful supersonic transport propulsion system. Exhaust system performance is extremely important at takeoff and supersonic cruise but may also be equally important in the subsonic and transonic flight conditions depending on the flight profile of the aircraft. The importance of the exhaust system can be gauged by the fact that Stitt [8], in his review on supersonic aircraft exhaust nozzles, pointed that a 1-percent increase in efficiency in exhaust system is at least three times as effective as a gain in performance of any other propulsion component. The exhaust systems optimum performance is, therefore, important at all operating expansion ratios combined with external freestream conditions. In supersonic flight the adoption to environmental pressure was achieved using nozzles which can vary their area ratio according to flight conditions. Mechanisms to vary area ratio are complicated and heavy, therefore, the final design is a trade-off between performance and weight.

Mechanical design simplicity will also prove to be a serious consideration for obtaining an efficient exhaust nozzle for supersonic aircraft. In order to achieve optimum thrust and drag characteristics the earlier designs relied on varying area ratios in line with the nozzle pressure ratios for the entire range of flight conditions. The problem then boils down to designing an exhaust system that can obtain optimum thrust minus drag characteristics, which is simple, lightweight, easy to fabricate and service during the life cycle of the propulsion system. This task is further complicated when the harsh environments at which nozzles operate are taken into consideration which relies on development in areas of materials.

Although not a focus in the present thesis, the noise characteristics are the most significant aspect of an exhaust system due to the ever increasing restrictions on noise requirements for civil transport. A propulsion system which will be able to meet the demands of environmental issues such as sensitivity to noise and sonic booms will see commercial success. In this context, the exhaust system performs the key role of noise suppression of the ensuing hot jet exhaust. This results in conflicting requirement of high aerodynamic performance and low noise levels particularly at take-off conditions. At supersonic cruise the aerodynamic performance becomes important as an efficient nozzle system directly translates into higher number of miles gained, an important metric for civilian transport.

In order to achieve such requirements a number of exhaust systems have been considered since the early 1960s. Stitt [8] provides an excellent review of supersonic exhaust systems for air-breathing propulsion. The early studies on various configurations were categorized into the first generation concepts and second generation concepts. The first generation concept (1963-1971) consisted of a variable-flap ejector nozzle, auxiliary-inlet ejector nozzle and the low angle plug nozzle. The second generation (1971-1985) consisted of the co-annular ejector nozzle and the co-annular plug nozzle concepts. Thus, the exhaust systems were envisaged were mainly based on the ejector and the plug nozzle concepts. In the present work the plug nozzle

concept is revisited, but with certain modifications, to see its efficacy for supersonic transport applications.

Plug nozzles have been studied [9]; [10]; [11] extensively since the 1950s because of the considerable advantages they provide in compensating for thrust at high altitudes. The basic concept of plug nozzle existed from the early 1950s [10]; air-breathing propulsion research establishments as well as research centers have studied them in various configurations and at different operating conditions based on the application.

In its simplest form a plug nozzle consists of an axisymmetric plug surrounded by a primary nozzle which contains the gases to be expanded to the ambient conditions. Depending on the length of the shroud in comparison to the plug, three classifications may be considered: a plug nozzle in which the entire expansion occurs externally i.e. a sonic throat exit nozzle, a plug nozzle with partial internal expansion i.e. the primary nozzle shroud extends beyond the sonic throat section and a third configuration in which none of the supersonic expansion occurs externally. The third configuration in which the primary nozzle shroud extends the entire length of the plug is equivalent to a divergent section and has not been studied extensively.

The earliest interest in plug nozzles arose because of their intended application to rocket engines. An intelligent combination of annular combustors with plug nozzle in solid or liquid rocket engines can provide considerable gains not just in aerodynamic performance but also a possible reduction in weight as well as additional complexity due to thrust vector control [12]. As a result of these envisaged advantages the early work was centered around design and understanding the flow physics of plug nozzles.

The generic character of an axisymmetric plug nozzle is shown in Fig. 1.1 [13] and is composed of a primary nozzle surrounding an internal plug. The primary nozzle, contains the gases upstream of the throat, can extend somewhat downstream of the throat (as shown in Fig. 1.1) to provide a combination of internal and external expansion or can end at the throat giving rise to completely external expansion. In either case, upon reaching the end of the shroud the gas on the outer periphery adjusts to the ambient pressure by means of a shock or expansion fan, while the fluid on

the inner periphery expands along the plug surface. When the nozzle is operating at off-design conditions, expansion/compression waves from the lip travel across the flow to the plug surface, impinge and reflect, eventually reaching the constant pressure interface separating the nozzle flow from the ambient fluid. Upon reaching the interface, they reflect with opposite sign and the process repeats until the plug tip is reached as suggested in middle schematic of Fig. 1.1(c). At design, the successive characteristics forming a centered expansion fan originating from the shroud lip are canceled as they reach the plug with the tail of the fan just impinging at the plug tip as shown in bottom of Fig. 1.1(b), to produce uniform exit flow. This expansion against ambient pressure enables a plug nozzle to adapt to a wide range of back pressures so that it can perform efficiently at low and high altitudes. A considerable body of theoretical and experimental data indicates that this altitude compensating characteristic enables a plug nozzle to provide a gain in performance relative to a conventional converging-diverging nozzle. An additional advantage of a plug nozzle is that it is less susceptible to separation at high back pressures than are conventional nozzles [14].

While engines on subsonic aircraft normally operate at nozzle pressure ratios (NPR, defined as the ratio of inlet total pressure to the ambient pressure) that are low enough that the complexities of a converging-diverging nozzle are not warranted, supersonic vehicles require a converging-diverging nozzle for efficient propulsive performance. The supersonic business jet application, however, is considerably different from the rocket/hypersonic applications because the supersonic speed dictates much lower NPR's. In the past analysis of plug nozzle flowfields, a variety of designs have been studied. In all the configurations a primary nozzle which surrounds the plug performs the function of internally expanding the gases and directing them onto the plug contoured surface at the correct angle. In most of the designs considered till date the primary nozzle extends to a very small portion or has an extensible shroud section aft of the throat. Also previous work focused primarily on NPR's of order 100 or larger, the present application deals with NPR's below 10. This work also tries

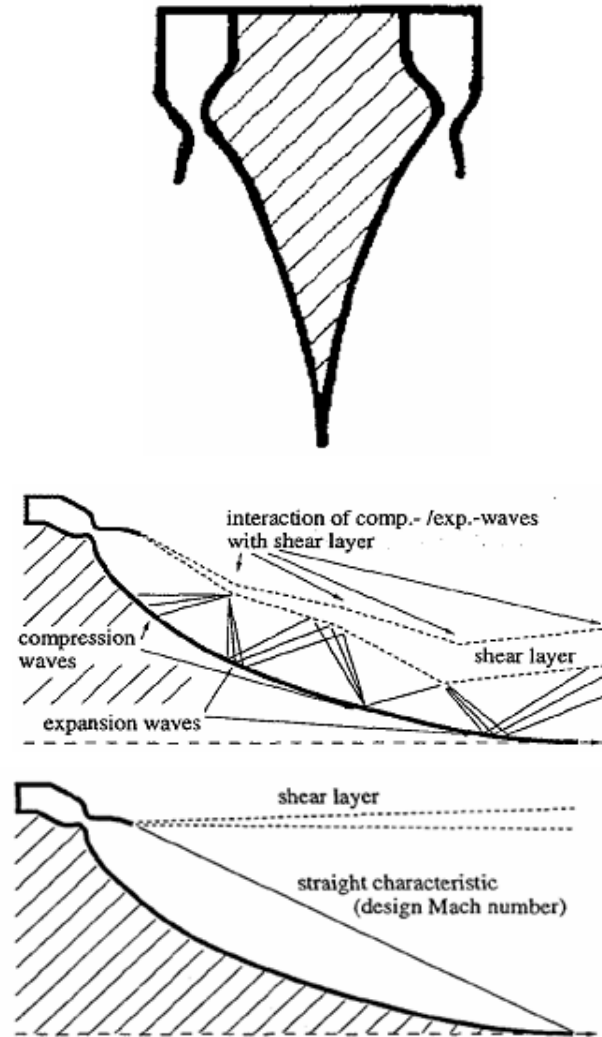


Figure 1.1. Sketch of a traditional plug nozzle(top). Flow structure for Nozzle Pressure Ratio (NPR, defined as the ratio of inlet total pressure to the ambient pressure) less than design (middle) and flow structure at design (bottom) [13].

to address the dearth of pertinent computational analysis for plug nozzles with an extended primary nozzle shroud that operates at NPR's below 10.

The nozzle system on a supersonic aircraft must not only provide attractive propulsive performance, but must also have favorable acoustic performance. The potential for routine supersonic flight in the civilian realm requires achieving an acceptable vehicle sonic boom and the plug configuration in conjunction with other technolo-

gies [15]; [3]; [4] may provide an advantage here. In supersonic flight the engine geometry itself is also of concern. The many subsystems such as fuel lines, gear boxes and pumps on the exterior of a gas turbine engine create a series of non-axisymmetric protuberances that result in increased pressure drag and a stronger inlet shock, thereby directly contributing to the sonic boom. To circularize the nacelle, a high bypass, co-annular, shrouded plug nozzle has been envisaged [4]. The notional view of the concept is shown in Fig. 1.2 highlighting the various components and the two flowpaths. In comparison to a conventional plug nozzle the shroud in the shrouded design extends to considerable portion of the plug length. Hence, called the shrouded plug nozzle.

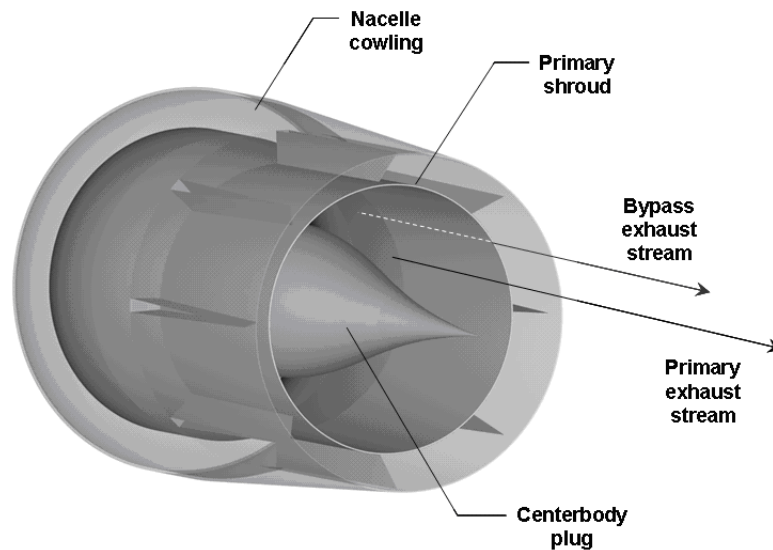


Figure 1.2. Notional view of supersonic plug nozzle concept with key features highlighted. [4].

In the case of conventional plug nozzles the operating pressure ratio range always results in expansion or compression waves occurring external to the shroud. The primary nozzle of the plug only serves to feed the contoured plug surface with supersonic flow. As mentioned earlier, the interaction of the exhausting gases with the external ambient results in self-adaption of the flow to the external ambient. The region

of interest in the case of plug nozzles for rocket applications always exists external to the primary nozzle exit. The external shroud in the current concept results in a traditional converging-diverging passage which leads to a return to shock/boundary layer separation characteristics at low operating NPR's within the exit plane. Thus, the flow structure within the shrouded part of the plug nozzle can no longer be ignored. The presence of an extended shroud in the present nozzle, therefore, results in a marked change in the behavior of the nozzle particularly at off-design conditions. The presence of flow phenomena associated with nozzle flow separation seen in supersonic nozzles can be expected in the present nozzle. The shock/boundary layer interaction also results in unsteady shock oscillation at the off-design nozzle pressure ratios. This oscillating shock may in turn lead to substantial unsteady loads on the nozzle structure and lead to performance which is completely different from a conventional plug nozzle.

Hagemann [13] considered an axisymmetric plug nozzle intended for rocket applications with NPR's above 100. In this work they describe the flow phenomenon observed at these operating conditions. The small shroud length, however, resulted in the flow field of interest to occur external to the shroud exit. Motivated by different applications variety of plug nozzle concepts were designed including linear aerospike nozzles, truncated plug nozzles during the recent past. The most recent research activity on plug nozzle flowfields concerned with computational fluid dynamic prediction, aerodynamic performance with freestream effects was done as part of a European RTO/AVT working group. The research activity [14] was concerned with plug nozzle applications for rocket applications and therefore only considered NPR's above 100. In all the computations they were able to predict steady pressure distribution in close agreement with experimental data. The configuration they considered had a long plug with considerably small shroud section.

To understand the multitude of shock physics that is likely to occur in the present shrouded plug configuration it is instructive to look at the analysis for converging-diverging nozzles. The early know work which combined both experimental and

computational analysis was that due to Coakley [16]; [17]; [18] and others [19]; [20]. In the case of experimental work the early work was due to Sajben [21]; [22]; [23]; [24]. In the work they considered a transonic diffuser channel intended to replicate the inlet of a supersonic aircraft. They note that the nozzle shock behavior varied with the nozzle operating conditions as shown in Fig. 1.3. In their work they divided the transonic flow into four groups according to the Mach number upstream of the shock. When $M_1 < 1.1$ the shock alternates between shock free and multiple shocklet patterns; for $1.1 < M_1 < 1.3$, the shocklets disappear and a single shock wave is generated downstream of the throat. The boundary layers in both flows are separated due to the adverse pressure gradient in the diverging section. For the flow with $M_1 > 1.3$, the boundary layer is separated by the shock wave. When $M_1 > 1.35$, the shock wave near the upper wall exhibits a lambda pattern. The vortex sheet is generated at the bifurcation point and the shocklets propagating upstream are clearly visible. In all these scenarios the flow is unsteady and associated with the motion of the shock.

Handa *et al.* [25] later were able to confirm the behavior through experimental study which involved high speed imaging of the shock motion. They observed that in the low upstream Mach number case ($M_1 < 1.1$) compression waves were generated in the nozzle section which steepen while propagating upstream and eventually become new shock waves. The ordinary shock thus is seen to move beyond the throat or to disappear while moving downstream depending on the pressure ratio across the nozzle. Fig. 1.4 shows the shock dynamics through a series of schlieren photographs at two operating pressure ratios of 1.28 and 1.29 where the shock moves upstream and unchoking the nozzle momentarily and then choking again at a downstream location. In the work they also indicate the presence of upstream propagating disturbances which are generated at a higher frequency than shock oscillation frequency.

The experimental work on planar supersonic nozzles and transonic diffusers [21]; [25]; [26]; [27]; [28]; [29] has shown that the unsteady self-sustained shock oscillations can have considerable effect on the nozzle behavior. The actual cause for these oscillations is still debatable but the analytical study of shock oscillation by Plotkin [30]

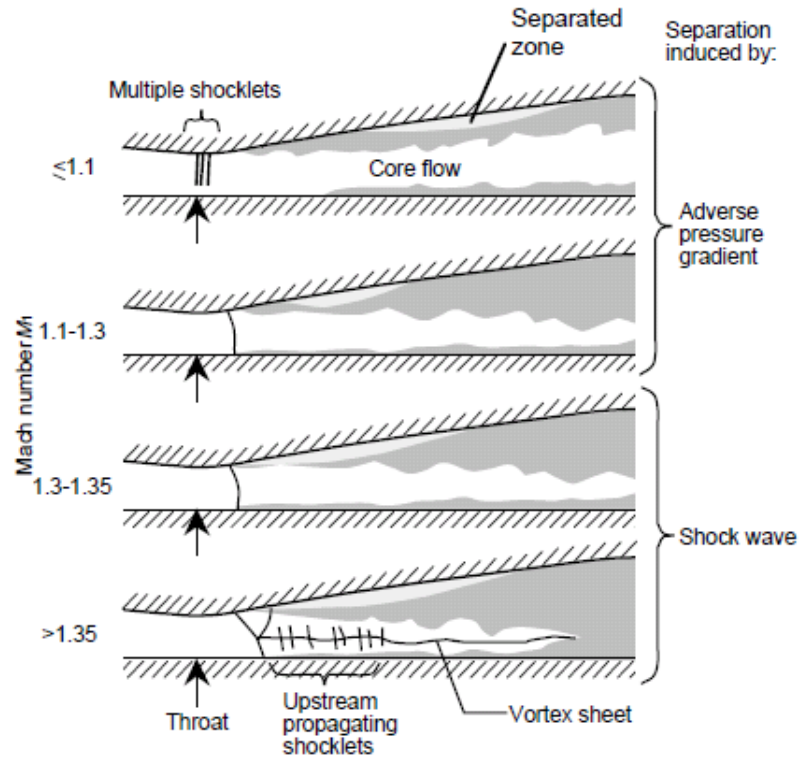


Figure 1.3. Schematic of various flow structures in a transonic diffuser based on incoming Mach number [25].

has suggested that this phenomenon is driven by velocity fluctuations in turbulent boundary layer. The analysis which proposed a simple model based on the convection of the shock wave by turbulent fluctuations and linear restoring mechanism due to the mean flow was able to predict peak *rms* pressure fluctuations in good agreement with the experiments. The low NPR result in considerable separation particularly on the plug surface aft of the shock region. A number of experimental work pertaining to the unsteady behavior of the shock system have been reported [21].

Earlier work on converging diverging supersonic nozzles, particularly thrust-optimized contour nozzles, for rocket applications with flow separation at low NPR's has associated them with the presence of two distinct flow separation regimes: Free Shock Separation (FSS) and Restricted Shock Separation (RSS) [31]; [32]. In the FSS regime the flow on the nozzle wall separates and never reattaches whereas in the RSS

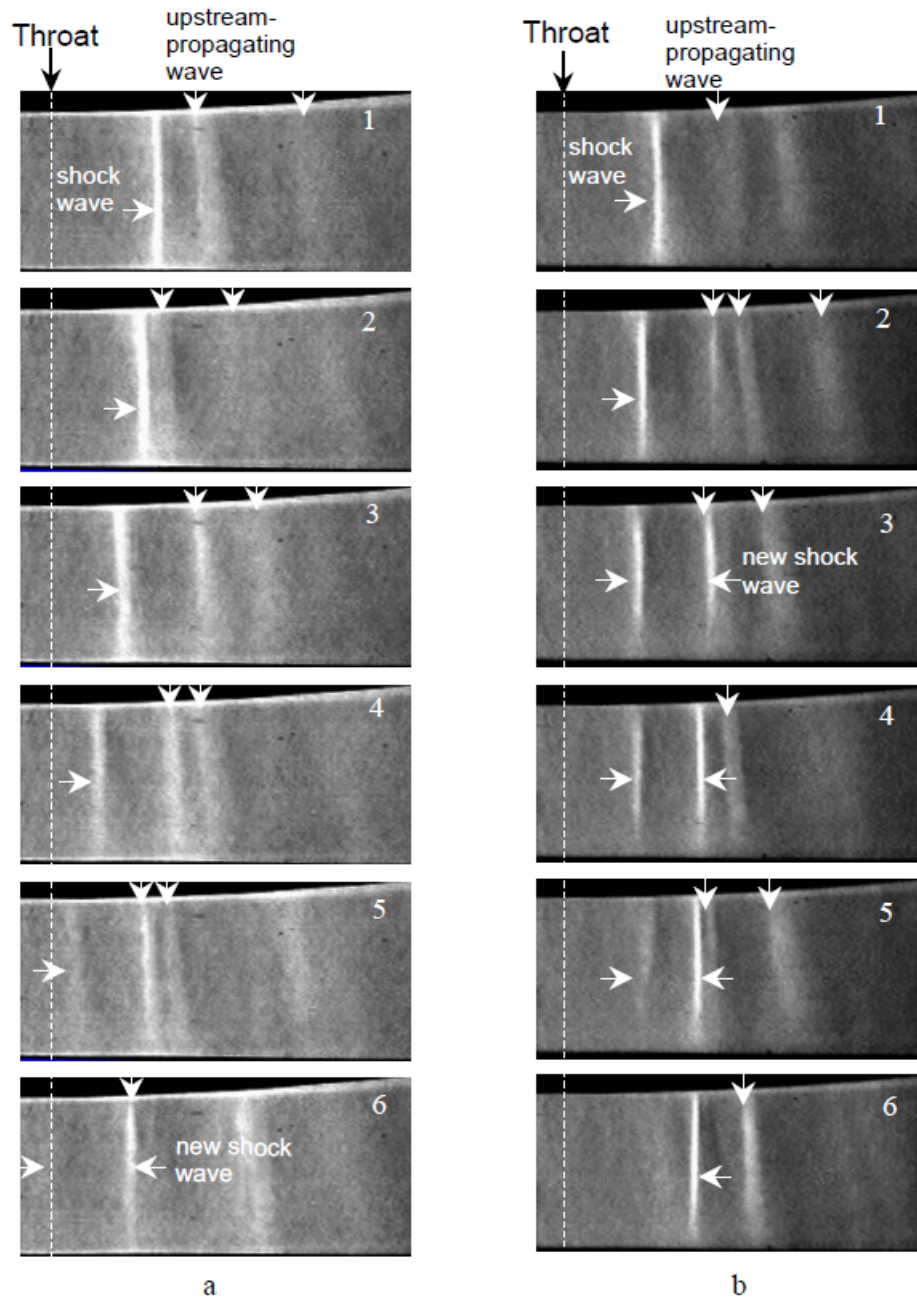


Figure 1.4. Shock oscillation, unchoking and upstream propagating disturbances in a transonic diffuser at NPR of 1.28(left) and 1.29 (right) [25].

regime the flow on the nozzle wall is characterized by a recirculation bubble. In the past many researchers have distinguished this behavior and identified the presence of

a hysteresis regime during the FSS/RSS transition. The identification of this transition is important for nozzles as it is directly attributed to the peak side-loads seen due to the three dimensionality that sets in at this transition [33]; [34]. Figure 1.5 shows a schematic of the FSS and RSS regime.

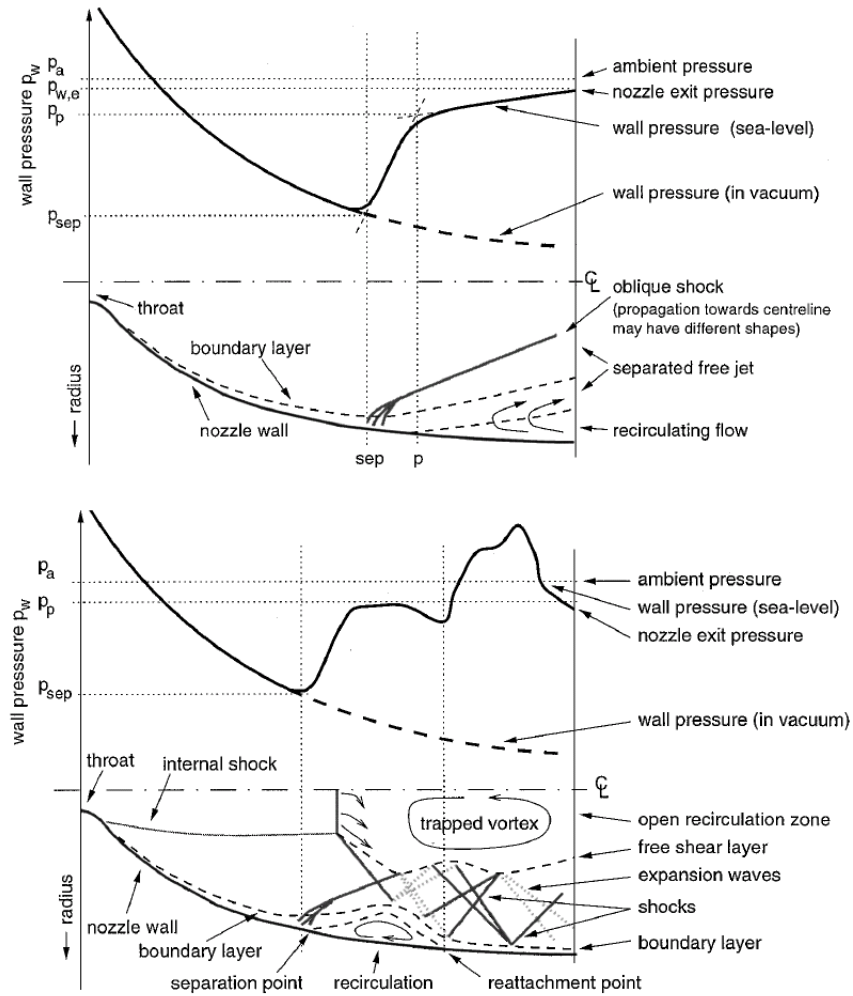


Figure 1.5. Schematic of Free(top) and restricted(bottom) shock separation regimes for a thrust optimized parabolic nozzle [31].

Verma [35] reports experimental data that describe shock physics for two configurations, truncated and full length low angle plug with an extended cowl, studied under freestream effects. The shock structure, steady pressure distribution and the thrust coefficients were obtained for the model. Although the work did not consider

expansion ratios when the shock structure will reside within the shroud it gives an idea of the flowfield once the shock moves out of the plug nozzle. Figure. 1.6 shows the complex shock structure that is associated with this plug nozzle (also shown in figure). The figures show the presence of an internal shock and reattached as well as separated depending on the operating condition. The shock appears to emanate from the cowl tip and impinge on the plug. The paper also provides details on the pressure distribution and unsteady pressure fluctuations on the plug.

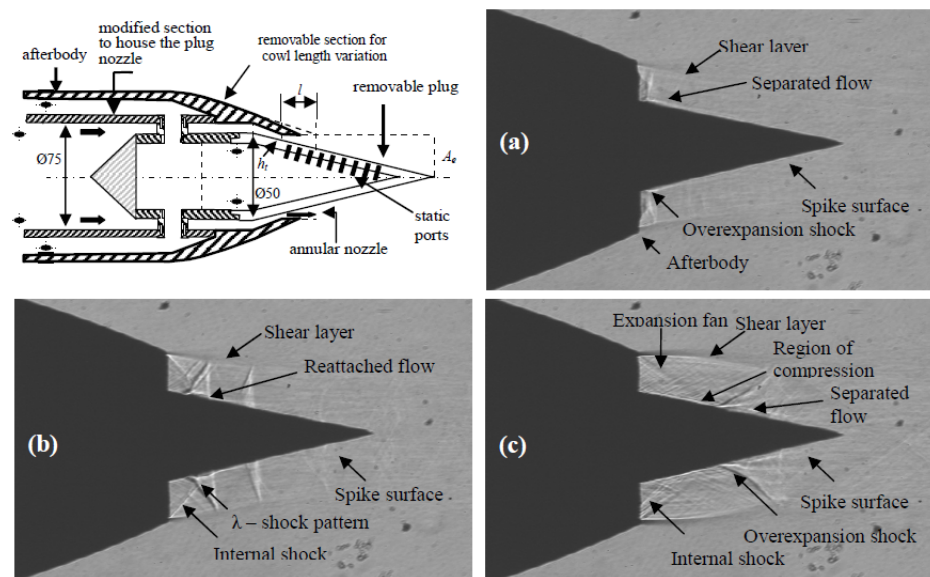


Figure 1.6. Shadowgraph images for the annular plug nozzle shown in the figure for (a) NPR = 2.1, (b) = 2.57 and (c) NPR = 3.82 [35].

In the present case the presence of an extended shroud section in the primary stream will result in shock turbulent boundary layer interaction with separated flow over the plug in a similar manner to what has been observed above. The plug nozzle will exhibit multitude of shock structures depending on the operating conditions and nozzle design.

For the computational prediction of such flowfields, the literature focused on studying nozzles at off-design conditions is a good indicator. Reynolds Averaged Navier Stokes(RANS) equation solutions are a wide spread tool for predicting shock

physics in nozzles [32]; [31]. The shock waves are automatically captured based on the formulation of the inviscid and viscous fluxes. The specification of the inviscid flux in combination with a turbulence model for turbulence closure have resulted in successful steady predictions that have helped in the design process of many exhaust nozzle configurations. Recent CFD results have also suggested that the flows which were considered to be steady are inherently unsteady in nature, thus requiring the need for resolution of the turbulence spectrum.

Although LES-like methods are available they are restricted to simple flow configurations like compression corners [36] and reflecting shocks on flat plates [37]. This is primarily due to the exorbitant grid resolution that is needed to obtain accurate results. The restriction proves particularly daunting when flows of industrial scale like the one considered here are attempted to model. This is in spite of the tremendous progress that has been achieved in computational power. In recent times hybrid RANS/LES models like Detached Eddy Simulation (DES) have shown promise with respect to resolving large scale turbulent structures in the flow particularly recirculation regions. In these models the RANS formulation is applied at the solid surface, while the LES methodology is applied to massively separated regions through a grid dependent switch. The hybrid methodology is considered to involve much less computational cost than LES as it alleviates the required mesh resolution near and along the walls and the resultant time step restriction. The limited understanding in terms of the interaction of boundary layer with the shock makes the modeling more difficult. Two scenarios are often interpreted of the self-sustained oscillations: a first scenario that seeks the driving mechanism of the oscillations to be the turbulent boundary layer, more precisely the interaction of upstream turbulence with the shock. The second scenario does not seek the origin of the low frequency shock oscillation in the turbulent boundary layer but rather in the intrinsic dynamics of the recirculation zone aft of the shock. The precise mechanism is, however, still unknown and the literature is strife with speculation.

With regard to predictive capability a number of survey papers have been published over the last decade [38]; [39]. Zheltovodov [38] is the most recent account of the prediction of shock wave turbulent boundary layer interaction. In recent past unsteady hybrid RANS/LES techniques have been applied to a number of high-speed flow configurations involving shocks. Deck and co-workers have looked at several configurations like controlled propulsive jet, thrust optimized contour nozzle and mixing in a supersonic round jet using hybrid RANS/LES models. In the thrust optimized contour nozzle they were able to predict the side-loads acting on the nozzle during various operating conditions along with obtaining a detailed understanding of nozzle flowfield.

The co-annular plug nozzle primary and secondary stream are separated from each other by a long barrel shroud (Fig. 1.2). This allows us, to a first approximation, study the primary stream consisting of the plug and the shroud alone and therefore, will be the focus in the thesis. The primary stream is referred as the shrouded plug nozzle. The shrouded plug nozzle when employed in supersonic propulsion systems will experience varying operating conditions during flight. The operating conditions are determined by the total pressure and the total temperature at the exit of the turbine core and fan streams which provide the working fluid for the nozzle. A sub-scale shrouded plug nozzle was designed at Purdue University [40] with an intention to obtain exhaust nozzle data and also serve as a means to validate computations. The data obtained from testing of the sub-scale model with extensive instrumentation will be used to validate the computations performed here. The test campaigns provided data in terms of flow structure, pressure distribution and pressure oscillation on the plug and shroud surface [40]; [41].

The computations will be performed using the finite volume based solver which accounts for larger than grid flow turbulence as described in the next chapter. The turbulence will be treated in a RANS mode in the boundary layer while away from the wall larger than grid size turbulence will be resolved. By exploiting the axisymmetric nature of the plug the study begins by performing steady and unsteady computa-

tions with an axisymmetric assumption. These computations serve as a quick step to understand the flow field in the shrouded plug nozzle and lay the basis for complete three-dimensional computations. In particular axisymmetric computations will result in an understanding of the flow regimes as a function of operating conditions. The comparison of the axisymmetric computations with the experimental data will help understand the validity of axisymmetric assumption. The three-dimensional computations, both steady and unsteady, are performed to explore asymmetry in the flowfield and simultaneously contrast with axisymmetric computations. The unsteady three-dimensional computations will relax the axisymmetric assumption and treat the turbulence in three-dimensional fashion. The unsteadiness within the nozzle will be studied in detail in view of the examples that have presented earlier in this section.

1.2 Reacting Impinging Jets of MMH/RFNA

Application of reactive flow simulations for combustion systems can yield fundamental insights into the transient combustion and the ensuing stationarity. Understanding of these phenomena can help in designing the combustion systems with desired and efficient performance. Combustion simulations remain challenging due to the large number of fundamental processes that govern combustion: turbulent mixing, multi-species chemical kinetics, multi-phase flow and varied time scales of physical processes. The combustion of bipropellant combinations like the one considered here is challenging because of the same reason. Monomethylhydrazine (CH_3NHNH_2), abbreviated as MMH, is used as a propellant in many space applications. It continues to be of great interest [42] as a fuel in propellant combinations involving RFNA or Red fuming nitric acid as an oxidizer. Hypergolicity refers to a spontaneous heat release that occurs when the two propellants come into contact with each other. The initiation of the process is determined by both chemical kinetics of the reacting species and the physical processes involved. By understanding the interplay of chemical kinetics

with convection and diffusion processes through simple configurations we may be able to understand the complexities of a real system.

Computational simulations of bipropellant mixtures is limited in literature from a stand point of understanding fundamental mechanisms. The mixture combination in real systems is used in condensed phase which makes the analysis difficult. Nevertheless attempts have been made by incorporating simple models that describe the process of going from condensed phase to gaseous reactions [43]. Unlike the approaches that have been adopted so far, a simple configuration with impinging fuel and oxidizer jets is used here to understand the mechanism at the gaseous reaction phase. For this simple configuration the geometry from the injector studies currently being performed at Purdue University are adopted. The papers Pourpoint *et al.* describes the injector configuration in detail.

Hypergolic propellants ignite after an induction phase where the fuel and oxidizer undergo mass and thermal diffusion to form a chemical mixture combination that is suitable for thermal runaway. Theory and experiments suggest that the time for this exponential heat release to take place depends on interaction of the chemical and physical processes. The chemical kinetics dictates a finite time to ignite based on the initial and final combination of the mixture. The mass and thermal diffusive properties of the mixture or the environment where combustion occurs add to the physical delay. Both these processes are further dependent on the temperature, pressure and gaseous environment where combustion occurs. The chemical reaction mechanism dictates the chemical delay time. The properties of the species depend on the thermal conductivity, specific heats, molecular viscosity and mass diffusion coefficients.

The chemical reaction between a hypergolic or storable fuel/oxidizer combinations proceeds through a large number of multiple intermediate species and elementary reactions. In 2009 the first ever detailed mechanism was published [44]. Since then reduced mechanism have been suggested by Westmoreland and Nicole [45] based upon asymptotic considerations or sensitivity analysis. This mechanism with 25 species and

98 reactions is used here close to the full mechanism in employed. The MMH/RFNA chemistry has been studied extensively in literature at different ambient conditions. Recently as part of the MURI initiative a reduced mechanism has been developed that has been used here.

Environment in which combustion occurs heavily influence the combustion process. Pourpoint *et al.* [46]; [47] in their work with rocket grade hydrogen peroxide along with a synthetic fuel combination have found contrasting combustion behavior in argon and helium ambient gas. The gas mass and thermal transfer properties of fuel and oxidizer in helium are different than that in argon. This results in disparity in the combustion behavior in either environment due to relative effect of these two physical processes. Lewis number was found to be one for propellant mixtures in argon while that of helium was above one. The thermal diffusivity dominated in the case of helium. The result was that the fuel/oxidizer flame which grew rapidly for the initial few milliseconds of combustion lost heat rapidly to the surroundings in the helium environment. The flame was then extinguished for a few milliseconds before a second ignition occurred. In combustion of hypergolic MMH/RFNA mixtures the gaseous environment where combustion occurs is composed of multiple species whose mass and thermal diffusivity vary. Hence, it will be of interest to study ambient gas effect on combustion by considering the environment to be made up of different gases.

The chemical kinetic mechanism itself is heavily dependent on the ambient temperature and pressure through the rate constants. According to chemical kinetics theory, the reaction rate of the overall global reaction mechanism is dependent on the species concentrations and the rate constant given by the Arrhenius relation. The combustion initiation occurs at critical values of temperature and pressure depending on these rate constants with the combustion initiation reactions having high activation energies becoming the rate determining reactions. The time to ignite improves as the temperature increases as a consequence of the exponential dependence on temperature in the Arrhenius relation. Thus, it seems necessary to understand the impact of ambient environment properties on combustion initiation and sustenance.

Impinging jet configurations in which metered doses of fuel and oxidizer are shot at each other at an included angle help in understanding global time scales of combustion processes. The impinging jet configuration described and studied later is the configuration used in the experimental work done at Purdue University as part of the Multiple University Research Initiative (MURI) [48]; [49]. In these configurations a fuel and oxidizer stream issue from two orifices with an included angle and impinge in a downstream ambient. Following which the two streams merge and undergo combustion. The fluid dynamics of the merging process in the impinging jet is similar to reacting shear layers. This kind of fuel/oxidizer impinging configurations also forms the basis for practical rocket combustors [42]. The early known work on providing a theoretical understanding of combustion in such configurations is due to Lawver and Breen [50]. They hypothesized that combustion in hypergolic impinging configurations occurred primarily in two means depending on the impingement velocity, impingement angle and the ambient conditions, one by mixing at the interface followed by combustion at downstream location and the other through separation of the jet streams of oxidizer and fuel by a reaction zone. In that they proposed that the diffusion time scale and the chemical kinetic time scale determine the combustion process. Under mixing conditions a mixing zone is exhibited similar to that of nonreactive streams. This zone extends from a point of contact to some distance downstream at the end of which hypergolic ignition occurs and flame is anchored. The condition of jet separation is characterized by a reaction interface from the initial point of contact downward and preventing mixing. The combustion zone exists all along the streams. In Fig. 1.7 taken from the same reference these two conditions are shown schematically. In the figure τ_{ign} is the chemical time scale for ignition and τ_{mix} is the diffusion time scale. For mixing τ_{ign} is greater than τ_{diff} and vice versa for separation.

In the context of understanding impinging jet configuration combustion of hypergolic propellants, hybrid RANS/LES methodologies adopted with a finite rate chemistry model to account for species mass fractions is the tool adopted here. These

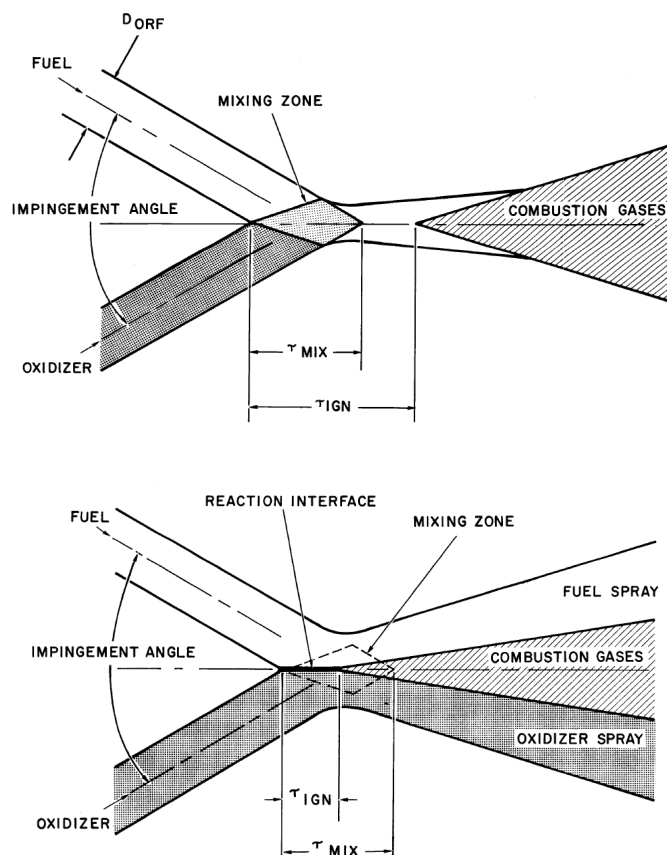


Figure 1.7. Schematic of mixing and separation combustion for hypergolic impinging jets from reference [50].

method of dealing with the fluid dynamic equations of have been used extensively in a wide variety of applications. Ohminami *et al.* [43] have used a finite rate chemistry model coupled with chemical kinetic mechanism for hydrogen fuel and di-nitrogen tetroxide to study combustion in bipropellant thrusters. In this work they have adopted the realizable $k - \epsilon$ model to account for the turbulence. They were able to predict the flame structure and understand the cooling mechanism within the combustor. In [42], Nusca has used a time-accurate CFD solver to simulate the unsteady, chemically reacting flow again in a rocket combustor. In the work the thrust from the rocket combustor was obtained compared against experimental measurements. Although both these computations make use of reactive flow equations to simulate

gas phase reactions they also consider the entire process of hypergolic combustion from condensed phase break-up to gas phase reactions. In the work presented here the emphasis has been laid on understanding the gas-phase reaction and the effect of various physical processes on combustion.

The primary focus of CHAPTER 3 of the thesis is to evaluate the newly devised reduced mechanism for MMH/RFNA chemistry in the context of impinging reacting jets. The reduced mechanism will be employed in the context of the finite volume based solver discussed in the next chapter which assumes a finite rate Arrhenius chemistry model for the chemical species source. The model assumes perfect mixing at the sub-grid scale level with the species source term evaluated based on filtered averaged quantities at the cell center. As with any real combustion system the reaction of MMH/RFNA is determined by both chemical kinetics as well as the convection and diffusion processes. To first understand the global chemical kinetic time scales a constant volume problem is formulated. A uniform grid wherein a homogeneous mixture of MMH/RFNA is allowed to react at a given initial temperature and pressure is used for the constant volume problem. The combustion time scales which correspond to the chemistry are studied using this problem formulation. Following the constant volume problem the effect of convection and diffusion is included along with chemistry in the impinging reacting jets configuration. As a first step towards complete three-dimensional computations the impinging jet problem is studied initially with a planar assumption. This will allow quick assessment of the chemistry with relatively fine grids. As mentioned earlier, the background gas can significantly effect the combustion process. The effect of background temperature and pressure as well as different background gases can be studied quickly with the planar problem. Two background gases of helium and argon are considered which provide for background gases with different mass and thermal diffusivities. The mass diffusivity of helium is higher than that of argon while the thermal diffusivity of argon is higher than that of helium. The relative effect of mass and thermal diffusivity in each background gas will effect combustion process. The three-dimensional computations are presented

next wherein the planar assumption is relaxed and the turbulence is treated as three-dimensional. For both the planar and three-dimensional computations the emphasis will be on understanding flame initiation, propagation, holding and sustenance. The turbulence closure employed using turbulent length scale switch based on grid size (DES) will account for mixing based on turbulent length scales larger than grid but will assume perfect mixing at the sub-grid level.

1.3 Outline of Thesis

In order to lay a foundation for the unsteady analysis of the two problems of interest, CHAPTER 2 discusses the computational treatment of the fluid dynamic equations of reactive flow. The non-reacting case for the analysis of shrouded plug nozzles follows as a subset of the reacting flow equations. The RANS equations which are solved are detailed followed by a discussion of the turbulence closure employed. The evaluation of source term term based on a finite rate Arrhenius model is presented which is employed in the reacting flow computations of impinging jets of MMH/RFNA. The definition of thermo-chemistry to include effects of temperature on flow properties along with definition of mixture properties for reacting flows is given. The numerical scheme for spatial and temporal discretization of the conservation equations based on a finite volume based preconditioned dual time stepping algorithm is presented followed by the boundary conditions for the equations.

The details of the computations performed in the context of the shrouded plug nozzle flowfield are presented in CHAPTER 2. Both steady and unsteady computations with axisymmetric assumption and complete three-dimensional geometry are presented. The relative merit of performing three-dimensional computations against axisymmetric computations is evaluated both in the steady and unsteady context. The discussion employs experimental data obtained from the sub-scale nozzle testing to validate the computations. In the process the flow physics in the nozzle is studied with the symbiosis of computational and experimental data.

The combustion of impinging jets of MMH as fuel and RFNA as oxidizer is studied in CHAPTER 3. The newly formulated chemical mechanism is evaluated for combustion initiation, flame propagation, holding and sustenance in the context of two problems. First, a simple constant volume problem is devised based on the present framework to evaluate global chemical kinetic time scales as a function of temperature and pressure. The impinging jet problem is studied in the planar context with an emphasis on understanding flame behavior as a function of background gas. The effect of pressure as well as effect of two different background gases that help evaluate flame behavior when mass and thermal diffusive properties are varied is presented. Following this foundation the impinging jets are studied for the complete three-dimensional geometry.

The last chapter summarizes the work and presents the future direction to be taken with regard to both the flows.

CHAPTER 2. NUMERICAL SCHEME

The numerical scheme for solving the Navier-Stokes equations of motion for both aerodynamic and reacting flows are described in this chapter. The chapter begins with a discussion of the governing equations and the turbulence closure used, followed by a discussion of the preconditioned dual-time step finite-volume based solver.

2.1 Governing Equations of Fluid Dynamics

The Navier-Stokes equations are generally accepted as the governing equations of fluid flow. The Navier-Stokes systems of equations for multi-species are given by,

$$\frac{\partial Q}{\partial t} + \nabla \cdot (\vec{F} - \vec{F}_v) = H \quad (2.1)$$

with $Q = (\rho, \rho u, \rho v, \rho w, E, Y_k)^T$ being the primitive variable vector.

The inviscid and viscous vectors appearing in the equations are as follows,

$$\begin{aligned} \vec{F} &= F_x \vec{i} + F_y \vec{j} + F_z \vec{k} \\ \vec{F}_v &= F_{vx} \vec{i} + F_{vy} \vec{j} + F_{vz} \vec{k} \end{aligned} \quad (2.2)$$

with \vec{i} , \vec{j} and \vec{k} denoting the unit vectors in the three co-ordinate directions while F_x , F_y and F_z denote inviscid vector components and F_{vx} , F_{vy} and F_{vz} denoting the components of the viscous vector.

The vector components of inviscid fluxes are given by,

$$F_x(Q) = \begin{pmatrix} \rho u \\ \rho u u + p \\ \rho u v \\ \rho u w \\ u(E + p) \\ \rho u Y_k \end{pmatrix} \quad F_y(Q) = \begin{pmatrix} \rho v \\ \rho v u \\ \rho v v + p \\ \rho v w \\ v(E + p) \\ \rho v Y_k \end{pmatrix} \quad F_z(Q) = \begin{pmatrix} \rho w \\ \rho w u \\ \rho w v \\ \rho w w + p \\ w(E + p) \\ \rho w Y_k \end{pmatrix} \quad (2.3)$$

and the vector components of viscous fluxes ($i = x, y, z$) are given by,

$$F_{vi}(Q) = \begin{pmatrix} 0 \\ \tau_{ix} \\ \tau_{iy} \\ \tau_{iz} \\ u_j \tau_{ij} - q_i \\ -\rho Y_k V_{i,k} \end{pmatrix} \quad (2.4)$$

with u, v, w denoting the three components of velocity, ρ the fluid density, Y_k the species mass fraction for each of the N species, p the fluid pressure and E the energy in the above equation. In the vector components of inviscid and viscous fluxes the first row is the global mass conservation, the next three rows are the momentum equations for each of the x, y and z co-ordinates followed by the energy and species mass conservation equations. The species mass conservation equations are N in number for each of the species involved in the chemical reaction giving a total of $N + 5$ system of equations.

The source term consists of the species chemical reaction rate, ω_k :

$$H = (0, 0, 0, 0, 0, \omega_k)^T \quad (2.5)$$

which will be determined in a later section in this CHAPTER.

The heat release due to combustion can be obtained as, $\omega_T = \sum_{k=1}^N \Delta h_{f,k}^0 \omega_k$ with $\Delta h_{f,k}^0$ denotes the enthalpy change for species k .

The viscous stress tensor components ($i = x, y, z$) are given by,

$$\tau_{ij} = 2\mu(T) \left(S_{ij} - \frac{1}{3} S_{kk} \delta_{ij} \right) \quad (2.6)$$

where μ is the dynamic viscosity while S_{ij} is the mean shear stress tensor given by $S_{ij} = 0.5 ((\partial u_i) / (\partial x_j) + (\partial u_j) / (\partial x_i))$.

The heat flux, q_i , appearing in the energy equation is given by,

$$q_i = -\kappa(T) \frac{\partial T}{\partial x_i} + \rho \sum_{k=1 \dots N} V_{k,i} Y_k h_k + Q \quad (2.7)$$

with $V_{k,i}$ denoting the diffusion velocity for the k th species in the i th direction. The definition of this term is given in a later section. The first term represents heat conduction with $\kappa(T)$ denoting thermal conductivity. The second term represents heat flux due to species diffusion which is important for multi-species reacting systems. The third term represents a heat source, for example, due to specified heat addition or ignition element. In general knowing the Prandtl number, Pr , of the flow, the thermal conductivity is obtained as: $\kappa = \mu C_p / Pr$ where C_p is the specific heat coefficient at constant pressure.

For a calorically perfect gas the following relation holds for the total energy E ,

$$E = \rho e = \frac{p}{\gamma - 1} + \frac{1}{2} \rho |\vec{u}|^2 \quad (2.8)$$

where γ is the ratio of specific heat at constant pressure, C_p to constant volume C_v . The internal energy is related to the total enthalpy, h , as, $\rho e = \rho h - p$.

The Navier-Stokes systems of equations can be written in integral form by integrating over a control volume, Ω . Then, by applying the divergence theorem,

$$\int_{\Omega} \frac{\partial Q}{\partial t} dV + \int_{\delta\Omega} F(Q, \vec{n}) dS = \int_{\delta\Omega} \vec{F}_v(Q) \cdot \vec{n} dS + \int_{\Omega} H dV \quad (2.9)$$

with $F(Q, \vec{n}) = \vec{F} \cdot \vec{n}$ being the inviscid flux vector. In the above equation, $\vec{n} = n_x \vec{i} + n_y \vec{j} + n_z \vec{k}$ is the normal vector pointing out of the control volume whose boundary is $\delta\Omega$. The inviscid flux vector can be written concisely for implementation in a numerical code as,

$$F(Q, \vec{n}) = \begin{pmatrix} \rho u_n \\ \rho u_n u_1 + p n_x \\ \rho u_n u_2 + p n_y \\ \rho u_n u_3 + p n_z \\ u_n (E + p) \\ \rho u_n Y_k \end{pmatrix} \quad (2.10)$$

with $u_n = \vec{u} \cdot \vec{n}$ being the normal velocity at the control surface.

The Navier-Stokes systems of equations for two dimensional or axisymmetric computations can be grouped by incorporating the following switch between the two

forms: $\omega_a = 1 - \omega + \omega y$ [51]. The logical switch, ω , takes the value of 0 for two-dimensional formulations and 1 for axisymmetric equations. By including this switch the Navier-Stokes equations are rewritten as,

$$\int \omega_a \frac{\partial Q}{\partial t} dV + \int \omega_a F(Q, \vec{n}) dS = \int \omega_a \vec{F}_v(Q) \cdot \vec{n} dS + \int \omega_a H dV + \int \omega (H_i - H_v) dV \quad (2.11)$$

for both axisymmetric and two-dimensional analysis. The primary variable, inviscid flux vector and viscous vector component reduce to,

$$Q = \begin{pmatrix} \rho \\ \rho u \\ \rho v \\ E \\ \rho Y_k \end{pmatrix} \quad F(Q, \vec{n}) = \begin{pmatrix} \rho \\ \rho u_n u + p n_x \\ \rho u_n v + p n_y \\ u_n (E + p) \\ \rho u_n Y_k \end{pmatrix} \quad F_{vi}(Q) = \begin{pmatrix} 0 \\ \tau_{i1} \\ \tau_{i2} \\ u_j \tau_{ij} - q_i \\ -\rho Y_k V_{i,k} \end{pmatrix} \quad (2.12)$$

and the source terms appearing in the axisymmetric form of the equations given by,

$$H_i = \begin{pmatrix} 0 \\ 0 \\ p \\ 0 \\ 0 \end{pmatrix} \quad H_v = \begin{pmatrix} 0 \\ 0 \\ \frac{2\mu}{3} \left(2\frac{v}{y} - \nabla \cdot \vec{u} \right) \\ 0 \\ 0 \end{pmatrix} \quad H = \begin{pmatrix} 0 \\ 0 \\ 0 \\ 0 \\ \dot{\omega}_k \end{pmatrix} \quad (2.13)$$

where the source term $H_i - H_v$ remains in the equations only if the solution is axisymmetric according to the switch ω .

2.1.1 Reynolds Averaged Navier Stokes Equations

The numerical simulation of the complete Navier-Stokes equations, which comes under the domain of Direct Numerical Simulations, requires fine grids to resolve the entire turbulence spectrum. Since computations of this scale are largely beyond the scope of present computational power, a part of the turbulence is modeled and the rest of the fluid flow is resolved by the algorithm. Thus, the instantaneous flow variable, q ,

is split into a time-dependent averaged part \bar{q} and a modeled turbulent perturbation, q' , for computational procedures which results in,

$$\begin{aligned} q &= \bar{q}(x, t) + q'(x, t) \\ \bar{q} &= \frac{1}{\Delta t} \int_t^{t+\Delta t} q(x, t) dt \end{aligned} \quad (2.14)$$

with Δt being the time period over which the flow quantity is averaged.

The complete turbulence picture of any unsteady flow field is composed of large length scale turbulence that derive energy from the mean flow to be dissipated as heat at the smallest scales. The time scale for these smallest high frequency eddies is much smaller than the largest turbulent structures in the flow. This is called scale separation. The aim of any turbulent compressible computation would be to resolve this entire spectrum of turbulence. As mentioned earlier, owing to constraints on computational power for large scale industrial problems only a part of the turbulence is resolved. The idea of unsteady computations is to choose the time scale of computations, Δt , to be larger than the time scale of the small scale turbulence but smaller than the turn over time of the larger eddies in the flow. Thus, the smaller scale eddies are modeled whereas the larger eddies are resolved. In the present analysis, the turbulence is incorporated by two different means. In the first, an averaging procedure is conducted over all the time scales to give the Reynolds Averaged Navier Stokes equations. In the second, the averaging procedure is conducted over only the "smaller" scales while the "larger" scales are computed directly. To preserve effective viscous effect at the wall a hybrid DES (Detached Eddy Simulation) method is used to separate scales. We begin by discussing RANS and then discuss DES. In this work most computations are performed using DES.

Applying an averaging procedure over all time scales in the laminar Navier-Stokes equations will lead to the Reynolds Averaged Navier-Stokes equations. The averaging procedure is combined with mass averaged (called Favre averaging) velocity components to avoid the appearance of additional correlations between the density and

velocity perturbations which need further modeling. The Favre averaged quantities are defined as,

$$\begin{aligned} u &= \tilde{u} + u'' \\ \tilde{u} &= \frac{\overline{\rho u}}{\bar{\rho}} \end{aligned} \quad (2.15)$$

where the tilde quantities refer to Favre-averages. The primary variable vector is then given by $\bar{Q} = (\bar{\rho}, \bar{\rho}\tilde{u}_1, \bar{\rho}\tilde{u}_2, \bar{\rho}\tilde{u}_3, \bar{\rho}\tilde{e}, \bar{\rho}\tilde{Y}_k)$ by employing the Favre-average definition. The Favre-averaged inviscid and viscous fluxes after some manipulation become,

$$F(\bar{Q}, \vec{n}) = \begin{pmatrix} \bar{\rho}\tilde{u}_n \\ \bar{\rho}\tilde{u}_n\tilde{u}_1 + \bar{p}n_x \\ \bar{\rho}\tilde{u}_n\tilde{u}_2 + \bar{p}n_y \\ \bar{\rho}\tilde{u}_n\tilde{u}_3 + \bar{p}n_z \\ \tilde{u}_n(\tilde{E} + \bar{p}) \\ \bar{\rho}\tilde{u}_n\tilde{Y}_k \end{pmatrix} F_{vi}(\bar{Q}) = \begin{pmatrix} 0 \\ \tilde{\tau}_{ix} - \overline{\bar{\rho}u_i''u_x''} \\ \tilde{\tau}_{iy} - \overline{\bar{\rho}u_i''u_y''} \\ \tilde{\tau}_{iz} - \overline{\bar{\rho}u_i''u_z''} \\ \tilde{u}_j(\tilde{\tau}_{ij} - \overline{\bar{\rho}u_i''u_j''}) - \tilde{q}_i - \overline{\bar{\rho}u_i''e''} \\ -(\bar{\rho}\tilde{Y}_k\tilde{V}_{i,k} + \overline{\bar{\rho}u_i''Y_k''}) \end{pmatrix} \quad (2.16)$$

and the source terms vector containing chemistry term determination the formation and destruction of each species is given by,

$$\bar{H} = (0, 0, 0, 0, 0, \overline{\omega_k})^T \quad (2.17)$$

with the definition of ω_k given in the following section.

The Favre-averaged stress tensor is given by,

$$\begin{aligned} \tilde{\tau}_{ij} &= 2\mu(\tilde{T})\left(\tilde{S}_{ij} - \frac{1}{3}\tilde{S}_{kk}\delta_{ij}\right) \\ \tilde{S}_{ij} &= \frac{1}{2}\left(\frac{\partial\tilde{u}_i}{\partial x_j} + \frac{\partial\tilde{u}_j}{\partial x_i}\right) \end{aligned} \quad (2.18)$$

and the heat flux is approximated as,

$$\tilde{q}_i = -\kappa(\tilde{T})\frac{\partial\tilde{T}}{\partial x_i} + \bar{\rho}\sum_{k=1..N}\overline{V_{k,i}\tilde{Y}_k h_k} \quad (2.19)$$

with all the quantities defined earlier but now interpreted as an average.

The objective of turbulent RANS computations is to provide closures for the correlations for turbulence perturbations which appear in the above equations. The

auto-correlation between the velocity fluctuations, called the Reynolds Stress tensor is closed by Boussinesq eddy viscosity approximation as,

$$\tau_{t,ij} = -\overline{\rho u_i'' u_j''} = \mu_t \left(\frac{\partial \tilde{u}_i}{\partial x_j} + \frac{\partial \tilde{u}_j}{\partial x_i} - \frac{2}{3} \delta_{ij} \frac{\partial \tilde{u}_k}{\partial x_k} \right) - \frac{2}{3} \overline{\rho} k \quad (2.20)$$

where μ_t is the turbulent dynamic viscosity and δ_{ij} is the Kronecker delta in the above equation. The trace of the shear stress tensor recovers the turbulent kinetic energy, $k = \frac{1}{2} \sum_{i=1}^3 \overline{u_i'' u_i''}$.

The species and energy fluxes appearing in the species equation and the energy equation respectively are closed using a gradient assumption. The two terms are then defined as,

$$\begin{aligned} \overline{\rho u_i'' Y_k''} &= -\frac{\mu_t}{Sc_{kt}} \frac{\partial \tilde{Y}_k}{\partial x_i} \\ \overline{\rho u_i'' e''} &= -\frac{\mu_t C_p}{Pr_t} \frac{\partial \tilde{T}}{\partial x_i} \end{aligned} \quad (2.21)$$

based on the gradient assumption. In the above equations Sc_{kt} is the turbulent Schmidt number for the k th species and Pr_t is the turbulent Prandtl number. There are additional correlations between turbulent perturbations in the energy equation which are usually ignored and considered only in the hypersonic regime. The viscous fluxes reduce to,

$$F_{vi}(\bar{Q}) = \begin{pmatrix} 0 \\ \tilde{\tau}_{ix} + \tau_{t,ix} \\ \tilde{\tau}_{iy} + \tau_{t,iy} \\ \tilde{\tau}_{iz} + \tau_{t,iz} \\ \tilde{u}_j (\tilde{\tau}_{ij} + \tau_{t,ij}) - \tilde{q}_i + \left(\frac{\mu_t C_p}{Pr_t} \right) \frac{\partial \tilde{T}}{\partial x_i} \\ - \left(\overline{\rho} \tilde{Y}_k \tilde{V}_{i,k} - \frac{\mu_t}{Sc_{kt}} \frac{\partial \tilde{Y}_k}{\partial x_i} \right) \end{pmatrix} \quad (2.22)$$

on substituting the approximations in Eq. 2.16.

The sum of the average shear stress tensor and Reynolds stress ($i = x, y, z$) can be reduced to

$$\overline{\tau}_{ij} = \tilde{\tau}_{ij} + \tau_{t,ij} = (\mu + \mu_t) \left(\tilde{S}_{ij} - \frac{2}{3} \delta_{ij} \tilde{S}_{kk} \right) - \frac{2}{3} \overline{\rho} k \quad (2.23)$$

where the term $-2/3\rho k$ appearing in the sum of laminar and Reynolds shear stresses is combined with the pressure in the inviscid flux terms.

The total energy equation becomes,

$$\bar{E} = \bar{\rho} \bar{e} = \frac{\bar{p}}{\gamma - 1} + \frac{1}{2} \bar{\rho} |\mathbf{u}|^2 \quad (2.24)$$

with all the terms defined as earlier.

2.2 Turbulence Modeling

The equations presented in the previous section need turbulence closure. In the present work the two equation k - ω model of Wilcox [52] has been used which does not allow for the hybrid DES method without modifications. The model makes use of the Boussinesq approximation to compute the Reynolds stresses. The two differential equations of turbulent kinetic energy, (k) and turbulent dissipation (ω) are used to form the velocity scale and the length scale to compute the eddy viscosity. The velocity scale here is the turbulent kinetic energy (k) and the length scale as $k^{1/2}/\omega$. Wilcox [52] in his recent formulation has included a stress-limiter modification to the turbulent eddy viscosity. The model gives the eddy viscosity as:

$$\begin{aligned} \mu_t &= \frac{\rho k}{\tilde{\omega}} \\ \tilde{\omega} &= \max \left[\omega, C_{lim} \sqrt{\frac{2S_{ij}S_{ij}}{\beta^*}} \right] \\ C_{lim} &= \frac{7}{8} \end{aligned} \quad (2.25)$$

in which Wilcox suggests that a value of 0.95 for C_{lim} yields better prediction for shock-separated flows up to Mach 3, which is used in the present work for nozzle flow. The turbulence kinetic energy, k , and dissipation, ω , appearing in the eddy viscosity definition are obtained by solving the following equations,

$$\frac{\partial(\bar{\rho}k)}{\partial t} + \frac{\partial(\bar{\rho}\tilde{u}_j k)}{\partial x_j} = \bar{\rho}\tau_{ij} \frac{\partial\tilde{u}_i}{\partial x_j} - \beta^* k \omega + \frac{\partial}{\partial x_j} \left[\left(\mu + \sigma^* \frac{\bar{\rho}k}{\omega} \right) \frac{\partial k}{\partial x_j} \right] \quad (2.26)$$

$$\frac{\partial(\bar{\rho}\omega)}{\partial t} + \frac{\partial(\bar{\rho}\tilde{u}_j \omega)}{\partial x_j} = \alpha \frac{\omega}{k} \bar{\rho}\tau_{ij} \frac{\partial\tilde{u}_i}{\partial x_j} - \beta \bar{\rho}\omega^2 + \sigma_d \frac{\bar{\rho}}{\omega} \frac{\partial k}{\partial x_j} \frac{\partial \omega}{\partial x_j} + \frac{\partial}{\partial x_j} \left[\left(\mu + \sigma \frac{\bar{\rho}k}{\omega} \right) \frac{\partial \omega}{\partial x_j} \right] \quad (2.27)$$

where the various closure coefficients appearing in the above equations are defined as,

$$\begin{aligned}
\alpha &= \frac{13}{25}, \beta^* = \frac{9}{100}, \sigma = \frac{1}{2}, \sigma^* = \frac{3}{5}, Pr_t = \frac{8}{9} \\
\sigma_d &= \begin{cases} 0, \frac{\partial k}{\partial x_j} \frac{\partial \omega}{\partial x_j} \leq 0 \\ \sigma_{d0}, \frac{\partial k}{\partial x_j} \frac{\partial \omega}{\partial x_j} \leq 0 \end{cases}, \sigma_{d0} = \frac{1}{8} \\
\beta &= \beta_0 f_\beta, \beta_0 = 0.0708, f_\beta = \frac{1 + 85\chi_\omega}{1 + 100\chi_\omega} \\
\chi_\omega &= \left| \frac{\Omega_{ij}\Omega_{kj}\widehat{S}_{ki}}{(\beta^*\omega)^3} \right|, \widehat{S}_{ki} = S_{ki} - \frac{1}{2} \frac{\partial u_m}{\partial x_m} \delta_{ki}
\end{aligned} \tag{2.28}$$

with the rotational strain rate tensor is defined as: $\Omega_{ij} = \frac{1}{2} \left(\frac{\partial u_i}{\partial x_j} - \frac{\partial u_j}{\partial x_i} \right)$.

For a successful turbulent computation the combination of the numerical algorithm and the turbulence model should be able to resolve the entire turbulent spectrum. Though hierarchal models of turbulence models like Direct Numerical Simulations (DNS) and Large Eddy Simulation (LES) achieve this, they have a requirement of high grid density which limits their role in industrial applications of the nature considered in this work. In the thesis unsteady computations have been performed in a hybrid RANS-LES mode, more popularly called as Detached Eddy Simulation (DES). The idea of DES is to compute the attached boundary layer in a RANS mode and the outer detached eddies in the LES mode. The original DES model due to Spalart [53] is based on a one-equation model. In the present case the underlying concept is extended to the k - ω turbulence model. In [53] the DES model it is proposed that the distance from the wall, d , is taken as the minimum of RANS turbulent length scale and the cell length: $\Delta = \max(\Delta x, \Delta y, \Delta z)$ i.e.

$$\tilde{d} = \min(d, C_{des}\Delta) \tag{2.29}$$

where Δx , Δy and Δz denote the cell length in the three dimensions. The constant C_{des} is calibrated and usually set equal to 0.65 [54]. In the boundary layer $d < C_{des}\Delta$ and the turbulent model has a RANS like behavior. Away from the wall surface, depending on the grid size, the model operates in the LES mode when $d > C_{des}\Delta$.

This modification can be easily achieved for the k - ω model by recognizing that $l_t = k^{1/2}/\beta^*\omega$ is the turbulent length scale and then setting,

$$\tilde{l}_t = \min (l_t, C_{DES}\Delta) \quad (2.30)$$

as the turbulent length scale to be used in the determination of the eddy viscosity. The turbulent dissipation term in the k equation becomes,

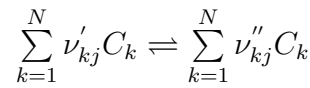
$$\frac{\partial (\bar{\rho}k)}{\partial t} + \frac{\partial (\bar{\rho}\tilde{u}_j k)}{\partial x_j} = \bar{\rho}\tau_{ij} \frac{\partial \tilde{u}_i}{\partial x_j} - \frac{k^{3/2}}{\tilde{l}_t} + \frac{\partial}{\partial x_j} \left[\left(\mu + \sigma^* \frac{\rho k}{\omega} \right) \frac{\partial k}{\partial x_j} \right] \quad (2.31)$$

with this modification. Away from the wall boundary where $l_t < C_{des}\Delta$, the turbulent length scale is set to the grid size, decreasing the dissipation which results in a decrease in turbulent kinetic energy. This in turn reduces the turbulent eddy viscosity, μ_t , reducing the modeled viscosity component in the momentum equation. Thus, allowing the flow to go unsteady. The result is that a part of the turbulence is resolved with the remainder being modeled.

2.3 Chemical Kinetics and Turbulence Chemistry Interaction

In the computation of reacting flows, a main focus is the evaluation of the chemical reaction source term that appears in each species equation and thereby accounting for the reaction heat release in the energy equation. The combustion is dependent on the turbulence and the chemistry defining the species consumption and production. In the literature a number of turbulence chemistry interactions models are available that describe the turbulent combustion process. The Eddy Break Model [55]; [56], G-equation model [57]; [58], the Bray-Moss-Libby model [59]; [60] and probability density function models [61]; [62]; [63] and in situ adaptive tabulation (ISAT) [64] are some examples of models which account for turbulence chemistry interaction. The present work makes use of a finite rate Arrhenius chemistry model to evaluate the species source term and is evaluated based on the filtered quantities described in the earlier sections. The mixing at the sub-grid scale is accounted by the specification of the turbulent Schmidt number. As the larger than grid size turbulence is resolved

by making use of the DES turbulence model described earlier, mixing by turbulent length scales larger than grid size are accounted for in the numerical methodology. Reactions generally proceed through the formation of multiple reactive intermediate species and possibly through different or parallel pathways. The overall reaction can be represented through a series of elementary reactions collectively called the reaction mechanism. Consider a multi-step reaction mechanism for N species reacting through M reaction steps. Each reaction in the multi-step reaction mechanism can be represented by a generic reaction,



where C_k is the k th species taking part in the chemical reaction whose stoichiometric coefficients for the forward and backward reactions are ν'_{kj} and ν''_{kj} respectively. The enforcement of mass conservation gives,

$$\sum_{k=1}^N \nu'_{kj} W_k = \sum_{k=1}^N \nu''_{kj} W_k \quad (2.32)$$

with W_k denoting the molecular weight of a species.

In terms of the concentration of the species, $[M_k] \equiv \rho Y_k / W_k$, the above equation becomes, $\sum_{k=1}^N (\nu'_{kj} - \nu''_{kj}) M_k = 0$. The reaction rate from the law of mass action is given by, $R_k = k_r \sum_{j=1}^N [M_j]^{\nu_j}$, where k_r is the reaction rate and ν_j is the order of the k th species as it appears in the reaction. For a reaction with both forward and backward reactions, the rate of concentration of species from the j th reaction can be obtained from the above definition as,

$$\dot{w}_j = \frac{d}{dt} [M_j] = k_{fj} \prod_{i=1}^N [M_i]^{\nu'_{ij}} - k_{bj} \prod_{i=1}^N [M_i]^{\nu''_{ij}} \quad (2.33)$$

where k_{fj} and k_{bj} are the forward and backward reaction rates. For some reactions at high pressures the concentration of species which do not participate in the reaction or third bodies may help in promoting the reaction rate. The third body while remaining

inert helps in the elementary reaction without itself undergoing any change in its concentration. In this case the third body concentration is taken into account as,

$$\dot{w}_j = \frac{d}{dt} [M_j] = k_{fj} [M_{m,j}]^\sigma \prod_{i=1}^N [M_i]^{\nu'_{ij}} - k_{bj} [M_{m,j}]^\sigma \prod_{i=1}^N [M_i]^{\nu''_{ij}} \quad (2.34)$$

where $[M_{m,j}]$ is the concentration of the third body participating in the j th reaction. The power of the third body concentration, σ , is set to 1 if third body reaction is present or to zero if there is no third body reaction. The third body in a chemical reaction mixture is the constituents of the mixture. The constituents can act with different catalytic efficiencies, that is, some species are more effective than the others in acting as third bodies. This is taken care of by the multiplicative factor called catalytic efficiency, z , for each species in the mixture. For example, species which do not act as third bodies have $z = 0$. The concentration $[M_{m,j}]$ of the third body in the reaction rate can be obtained as,

$$[M_{m,j}] = \sum_{i=1}^N z_i [M_i] \quad (2.35)$$

for j th chemical reaction.

If all the catalytic efficiencies are equal to 1.0, the the above equation can be written as,

$$[M_{m,j}] = \sum_{i=1}^N [M_i] = \frac{P}{RT} \quad (2.36)$$

which clearly depicts the dependence of third body concentration on pressure. For example for bimolecular reactions, at low pressures the concentration of third body is low, therefore, for a reaction which relies on third body collisions the reaction rate is slow. For higher pressures the concentration is higher and the collision with the third body occurs instantaneously. Thus, at high pressures reaction rate does not depend on the concentration of third body.

The overall production of the k th species by all the chemical reactions can then be expressed in terms of individual reaction rates as,

$$\dot{\omega}_k = W_k \sum_{j=1}^M (\nu''_{kj} - \nu'_{kj}) \dot{w}_k \quad (2.37)$$

and the global conservation of mass dictates that,

$$\sum_{i=1}^N \dot{\omega}_i = 0 \quad (2.38)$$

which states the sum of individual species reaction rates should sum to zero.

The reaction rates for backward and forward reactions in Eq. 2.33 are given by the Arrhenius formula. Arrhenius(1889) postulated that only molecules possessing energy exceeding a threshold, the activation energy (E_a), participate in chemical reaction. Based on this postulate, a specific reaction rate of the form:

$$k_f = AT^b \exp\left(-\frac{E_a}{RT}\right) \quad (2.39)$$

is used for the forward reaction based on the Arrhenius law. The exponential term signifies the fraction of all the molecules that possess energy greater than the activation energy to participate in chemical reaction. The pre-exponential factor (A) contains additional information about spatial configuration of the molecules during the reaction while the temperature exponent (b) only modifies the temperature dependence. The constants in the Arrhenius equation make up the chemical kinetic picture of a reaction. To describe the chemical mechanism for a reactive flow is to provide the values of these constants for the various elementary reactions that make up the reaction. The factors control the rate of reaction i.e. the speed at which combustion occurs to convert the reactants into product species. In general these quantities are specified only for the forward reaction while that of the backward reactions are obtained through thermodynamics as,

$$k_{bj} = \frac{k_{fj}}{\left(\frac{p_a}{RT}\right)^{\sum_{k=1}^N \nu_{kj}} \left(\frac{\Delta s_j^0}{R} - \frac{\Delta h_j^0}{RT}\right)} \quad (2.40)$$

where $p_a = 1$ bar. The terms Δs_j^0 and Δh_j^0 are respectively the entropy and enthalpy change occurring in going from the reactants to the products for the j th chemical reaction.

The Arrhenius constants in the reaction rate definition accounts for the temperature dependence. However, as indicated earlier, the reaction rate for a given chemical

reaction is also dependent on the pressure through the third body concentration. The intermediate activated complex formed from the reactants is converted to products through collision with the third body. The collision rate is proportional to the third body concentration which is pressure dependent as seen in Eq. 2.36. The pressure dependence of kinetic reaction rates is accounted through fall-off forms which define an intermediate fall-off form based on the low and high pressure limits. In general the low pressure and high pressure behavior of chemical reactions is related through algebraic relations called the fall-off forms. For example, the Lindemann fall-form provides the kinetics reaction rate for fall-off of region based on the low (k_0) and high pressure k_∞ limits through the following expression,

$$k = k_\infty \frac{p_r}{1 + p_r} \quad (2.41)$$

where the reduced pressure, p_r , is defined as, $p_r = k_0 [M]/k_\infty$.

In the work done in this dissertation the Tsang and Heron [65] fall-off forms have been employed. Similar to the Lindemann form, it relates the low pressure and high pressure reaction rates to define the reaction rate in the fall-off region. The relations for the reaction rate are,

$$k = \frac{k_0 k_\infty}{k_0 + k_\infty/[M]} F \quad (2.42)$$

$$\log F = \log F_C / (1 + (\log k_0 \times M/k_\infty)^2)$$

where the quantity, F_C in the above expression is called the broadening factor and is defines based on the Troe fall-off form definition:

$$F_C = (1 - a_1) \exp(-T/a_2) + a \exp(-T/a_3) + \exp(-a_4/T)$$

with a_1 , a_2 , a_3 and a_4 provided as inputs for the formula.

2.4 Thermo-Chemistry

In order to close the equations of motion additional constitutive relations have to be provided for both non-reacting and reactive flows. To enable the equations to

apply for a general set of formulations including perfect gas, incompressible liquids, real gases, the equation of state is described as an arbitrary equation of state as,

$$\rho = \rho(p, T) \quad (2.43)$$

which in the case of perfect gas states that the density is related to the pressure and temperature through the gas constant, R . The perfect gas assumption is used for both reaction and non-reacting flows in this chapter. The gas constant for a multi-species mixture is obtained as: $R = \mathcal{R}/\mathcal{W}$ where \mathcal{R} is the universal gas constant equal to $8314J/(kg \text{ mol } K)$ and \mathcal{W} , given by,

$$\frac{1}{\mathcal{W}} = \sum_{i=1}^N \frac{Y_i}{W_i} \quad (2.44)$$

is the mean molecular weight. In the case of reacting flow the $N + 5$ equations again use the above ideal gas law to close the equation set. For reacting flows the concentration the relation for the mole fraction is $X_k = Y_k \mathcal{W}/W_k M$ The summation of the species mass fraction and mole fraction over all the species is a constant owing to mass conservation. Therefore,

$$\begin{aligned} \sum_{i=1}^N Y_i &= 1 \\ \sum_{i=1}^N X_i &= 1 \end{aligned} \quad (2.45)$$

are again statements of mass conservation.

2.4.1 Transport Properties

Transport properties define the mass, viscous and thermal diffusivity of the flow. For each species the properties vary with temperature with particularly strong variation for reacting flows which see high temperatures. Non-reacting flows without heat addition in general do not exhibit significant change in temperatures an transport properties are nearly constant.

Apart from individual species transport properties the Navier-Stokes equations need a mixture property in order to compute the viscous vector. In this section the transport property evaluation that is adopted is discussed. In the implementation multiple approaches are available to evaluate the transport properties. The most appropriate method is adopted depending on the type of flow.

For non-reacting flows with air as the working medium the molecular viscosity is calculated through Sutherlands law [66]:

$$\frac{\mu}{\mu_0} = \left(\frac{T}{T_0} \right)^{3/2} \frac{T_0 + S_1}{T + S_1} \quad (2.46)$$

where S_1 is a constant which for air assumes the value $S_1 = 110K$ and μ_0 is reference viscosity at temperature T_0 (for air $\mu_0 = 7.30975 \times 10^{-3}$ at $T_0 = 273K$). The thermal conductivity is obtained based on the definition of the Prandtl number.

The values of molecular viscosity and thermal conductivity of species in a reacting flow are calculated from logarithmic fit of experimental data or from kinetic theory (Gordon *et al.*, 1984). The expressions for the species molecular viscosity and thermal conductivity are,

$$\left. \begin{array}{l} \ln \mu \\ \ln \kappa \end{array} \right\} = A \ln T + \frac{B}{T} + \frac{C}{T^2} + D \quad (2.47)$$

where the constants are provided as tabular data over a range of temperatures.

The mixture molecular viscosity is prescribed by the use of a semi-empirical Wilkes mixing law (Wilke 1950) as modified by Bird *et al.* (1960). Wilkes formula for mixture viscosity is given by:

$$\mu = \sum_{k=1}^N \frac{X_k \mu_k}{\phi_k} \quad (2.48)$$

where $\phi_k = \sum_{k=1}^N X_k \left[1 + \sqrt{\frac{\mu_k}{\mu_j}} \left(\frac{W_j}{W_k} \right)^{1/4} \right]^2 \left[8 \left(1 + \frac{W_k}{W_j} \right) \right]$.

For the mixture thermal conductivity, the combination averaging formula due to Mathur *et al.* (1967) is used,

$$\kappa = \frac{1}{2} \left(\sum_{k=1}^N X_k \kappa_k + \frac{1}{\sum_{k=1}^N X_k / \kappa_k} \right) \quad (2.49)$$

in the viscous flux vector.

The diffusion velocity appearing in the viscous flux vector of the species conservation equation and the energy equation also has to be prescribed. In general the multi-component diffusion equation which describes the diffusion in multi-species mixtures is computationally intensive to solve. In order to overcome this difficulty a simpler approximation is used in computations. The diffusion velocities for molecular diffusion of species in a binary mixture based on Fick's law offer an alternate and simpler form for computational purposes. The diffusion velocity due to Fick's law is [67],

$$Y_k V_k = -D_k \nabla Y_k \quad (2.50)$$

where $D_k = \sum_{i \neq k}^N \frac{1-X_k}{X_k/D_{ki}}$ is the mass diffusivity of the k th species with D_{ki} being the binary diffusion coefficient of species k into i . Binary diffusion coefficients are calculated from kinetic theory using the Chapman-Enskog theory and Lennard-Jones potentials (Reid, Prausnitz and Sherwood 1977) [68],

$$D_{ki} = \frac{0.0266T^{3/2}}{pW_{ki}^{1/2}\sigma_{ki}^2\Omega_D} \quad (2.51)$$

where W_{ki} is the reduced molecular weight: $W_{ki} = 2(1/W_k + 1/W_i)^{1/2}$ and σ_{ki} is a characteristic length given by $\sigma_{ki} = \frac{1}{2}(\sigma_k + \sigma_i)$ with σ_i being the force constant. The quantity ω_D is the dimensionless collision integral for diffusion that is determined from a Lennard-Jones potential as: $\Omega_D = (T_{ki}^*)^{-0.145} + (1/2 + T_{ki}^*)^{-2}$ where $T_{ki} = \frac{k_B T}{\varepsilon_{ki}} = \sqrt{\frac{k_B T}{\varepsilon_k}} \sqrt{\frac{k_B T}{\varepsilon_i}}$ and $k_B = 1.380650e - 23$ is the Boltzmann constant. T_{ki}^* is the reduced temperature and depends on the characteristic energy of interaction between species k and i .

Substituting Fick's law into the species conservation equation gives,

$$\frac{\partial \rho Y_k}{\partial t} + \nabla \cdot (\rho \vec{u} Y_k) = \dot{\omega}_k + \nabla \cdot (\rho D_k \nabla Y_k) \quad (2.52)$$

which can be summed over all species to yield,

$$\frac{\partial \rho \sum_{k=1}^N Y_k}{\partial t} + \nabla \cdot \left(\rho \vec{u} \sum_{k=1}^N Y_k \right) = \sum_{k=1}^N \dot{\omega}_k + \nabla \cdot \left(\rho \sum_{k=1}^N D_k \nabla Y_k \right) \quad (2.53)$$

as the global mass conservation equation.

By making use of earlier identities, Eq. 2.38 and Eq. 2.45, for reaction rates and species mass fractions we obtain,

$$\frac{\partial \rho}{\partial t} + \nabla \cdot (\rho \bar{u}) = \nabla \cdot \left(\rho \sum_{k=1}^N D_k \nabla Y_k \right) \quad (2.54)$$

as the global species mass conservation equation.

For the present formulation the last term is in general not zero unless all the binary diffusion coefficients are equal. One approximate method to circumvent this difficulty is to solve the global mass conservation equation and $N - 1$ species conservation equations. The last species mass fraction follows from $Y_N = 1 - \sum_{k=1}^{N-1} Y_k$. This formulation absorbs all the inconsistencies introduced by Fick's law in obtaining the species diffusion velocity. By subtracting all the 1 to $N - 1$ species conservation equations from the global mass conservation equations yields,

$$\frac{\partial \rho Y_N}{\partial t} + \nabla \cdot (\rho \bar{u} Y_N) = \omega_N + \nabla \cdot (\rho D_N \nabla Y_N) + \nabla \cdot \left(\rho \sum_{i=1}^{N-1} (D_N - D_i) \nabla Y_N \right) \quad (2.55)$$

as the equation for the n th species. There are two uncertainties with the above equation: the last term is unphysical and can act as source or sink resulting in numerical difficulties.

A better way to solve the problem of global mass conservation is to augment the species diffusion velocity with a correction velocity to account for the inconsistencies introduced by Fick's law [67]. This is done as,

$$\frac{\partial \rho Y_k}{\partial t} + \nabla \cdot (\rho \bar{u} Y_k) = \omega_k + \nabla \cdot (\rho (V_k + V^c) Y_k) \quad (2.56)$$

where V_c appearing in the mass diffusion term is correction velocity. By summing up all the species conservation equations we obtain:

$$\sum_{k=1}^N (V_k + V^c) Y_k = 0 \quad (2.57)$$

which gives the correction velocity after making use of Fick's law as:

$$V^C = - \sum_{k=1}^N D_k Y_k \quad (2.58)$$

which according to Peters [57] has smaller effect for turbulent flames but important for laminar flames.

2.4.2 Thermodynamic Properties

The specific heats enthalpy and entropy are required for each of the multi-species components taking part in the chemical reaction in order to compute the reaction heat release. The thermodynamic properties can be obtained in multiple sources. For non-reacting flows where there is no significant change in temperature they are assumed constant but for reacting flows they are temperature dependent. In the present work these thermodynamic quantities are obtained by making use of Gordon and McBride (1996) [69] polynomial curve fits are used for reacting flows. These curve fits are based on experimental data and expresses as,

$$\begin{aligned} \frac{C_p^0}{R} &= a_1 T^{-2} + a_2 T^{-1} + a_3 + a_4 T^1 + a_5 T^2 + a_6 T^3 + a_7 T^4 \\ \frac{h^0}{RT} &= -a_1 T^{-2} + a_2 T^{-1} \ln T + a_3 + \frac{a_4}{2} T^1 + \frac{a_5}{3} T^2 + \frac{a_6}{4} T^3 + \frac{a_7}{5} T^4 + \frac{b_1}{T} \\ \frac{s^0}{RT} &= -a_1 T^{-2} - a_2 T^{-1} + a_3 \ln T + a_4 T^1 + \frac{a_5}{2} T^2 + \frac{a_6}{3} T^3 + \frac{a_7}{4} T^4 + b_1 \end{aligned} \quad (2.59)$$

where the constants are tabulated for each species over a range of temperatures of interest.

2.5 Numerical Scheme

The numerical solution of the fluid dynamic equations described in previous section requires robust and accurate numerical procedures. In the present work a preconditioned dual time algorithm [70] for a finite volume based solver has been used. The fluid dynamic equations in the dual time formulation have an additional pseudo time derivative in addition to the physical derivative terms. The pseudo time iterations are performed to drive out the errors in the transient and ensure convergence in physical time. The pseudo-time derivative may be chosen in order to achieve the process in a fast and robust manner. The preferred method is to choose an appropriate

unsteady preconditioning matrix that multiplies the pseudo time derivative. In this way convergence difficulties arising due to disparate time scales (based on acoustic, $u + c$, and particle, u , velocities) is overcome, particularly for low Mach flows.

The additional pseudo time derivative of the dual time formulation acts as an agent for the preconditioning. The algorithm marches in time by performing inner iterations over pseudo time between outer or physical iterations. On convergence of the inner pseudo iterations, the pseudo time derivative vanishes and the equations reduce to the original form with the physical time derivative. The pseudo time derivative can be added using the conservative variable vector, Q . By using chain rule we can transform the conservative variable vector Q into the primitive variable sector $Q_p = (p, u, v, w, T, Y_k, k, \omega)^T$ and obtain the Jacobian Γ_p . The transformation in this fashion results in Q_p being the unknown vector obtaining which is the goal of computations. The Jacobian Γ_p which multiplies the pseudo time derivative contains differentials of the conservative variables with respect to the Q_p vector. Preconditioning this system involves replacing the ρ_p term with the term ρ'_p which defines a new inverse pseudo speed of sound. This preconditioning matrix is preferred over the physical Jacobian for faster convergence and accuracy. The equations of motion reduce to,

$$\Gamma_p \frac{\partial Q_p}{\partial \tau} + \frac{\partial Q}{\partial t} + \nabla \cdot (\vec{F} - \vec{F}_v) = H \quad (2.60)$$

with the additional pseudo time derivative.

In the finite-volume method the entire fluid space is divided into non-overlapping control volumes, Ω , each surrounded by the control surface $\delta\Omega$. The control volumes surround the unknowns at cell centers, hence, called the cell-centered finite volume method. These control volumes are usually supplied by a preprocessor as an input to the solver. The control volumes used in this work are typically quadrilaterals for two-dimensional and hexahedral elements for three-dimensional problems. The average value of the fluid property is stored at the cell center while the edges of the cell act as

the faces of the control volume. To solve the above equation numerically, we integrate the equation over the control volume Ω ,

$$\int_{\Omega} \left(\Gamma_p \frac{\partial Q_p}{\partial \tau} + \frac{\partial Q}{\partial t} \right) dV + \int_{\Omega} \nabla \cdot (\vec{F} - \vec{F}_v) dV = \int_{\Omega} H dV \quad (2.61)$$

which forms the basis of the finite volume formulation. By defining an average value over the control volume for both the primary and conservative variable set, we can convert the first integral into a perfect differential,

$$\int_{\Omega} \left(\Gamma_p \frac{\partial Q_p}{\partial \tau} + \frac{\partial Q}{\partial t} \right) dV = \left(\bar{\Gamma}_p \frac{\partial \bar{Q}_p}{\partial \tau} + \frac{\partial \bar{Q}}{\partial t} \right) \Omega \quad (2.62)$$

where the quantities, \bar{Q} and \bar{Q}_p are the average values over the control volume,

$$\bar{Q}_p = \frac{1}{\Omega} \int_{\Omega} Q_p dV \quad \bar{Q} = \frac{1}{\Omega} \int_{\Omega} Q dV$$

with Ω defining the control volume.

The second term, the convective integral, can be converted into a surface integral by using Greens theorem:

$$\int_{\Omega} \nabla \cdot (\vec{F} - \vec{F}_v) dV = \oint_{\delta\Omega} (\vec{F} - \vec{F}_v) \cdot \vec{n} dS \quad (2.63)$$

where \vec{n} , as defined earlier, is the normal vector to the control volume surface, $\delta\Omega$, enclosing the control volume Ω . The third integral is replaced by the average source term vector,

$$\bar{H} = \frac{1}{\Omega} \int_{\Omega} H dV \quad (2.64)$$

which is the source term evaluated based on the control volume averages.

Substituting the above derivations results in,

$$\left(\bar{\Gamma}_p \frac{\partial \bar{Q}_p}{\partial \tau} + \frac{\partial \bar{Q}}{\partial t} \right) \Omega + \oint_{\delta\Omega} (\vec{F} - \vec{F}_v) \cdot \vec{n} dS = \bar{H} \Omega \quad (2.65)$$

as the integral form of the equations of fluid motion applicable to reacting and non-reacting equations.

Now, we divide the surface into K distinct non-overlapping control faces of finite area, so that the above integral becomes:

$$\left(\overline{\Gamma}_p \frac{\partial \overline{Q}_p}{\partial \tau} + \frac{\partial \overline{Q}}{\partial t} \right) \Omega + \sum_{k=1}^K \left(\vec{F} - \vec{F}_v \right)_k \cdot \vec{n}_k S_k = \overline{H} \Omega \quad (2.66)$$

with $(\vec{F} - \vec{F}_v)_k$ viewed as the average value of the fluxes over the control surface. It remains to be decided how the fluxes on each control surface are determined which is the Riemann problem. An approximate Riemann solver or an algebraic constitutive flux formula is used for this purpose, for example, that due to Roe [71]. In Eq. 2.66, we replace the divergence of inviscid and viscous fluxes with a discrete operator which will be discussed in the next section followed by a discussion of the time discretization.

2.5.1 Spatial Discretization

As mentioned earlier the fluid space is divided into discrete control volumes and we need to define the computation of the inviscid and viscous fluxes at the control surface. The inviscid fluxes can be evaluated using an approximate Riemann solver in which the normal flux, $F_{nk} = \vec{F} \cdot \vec{n}_k$ at the face k is calculated from the numerical flux vector,

$$\begin{aligned} F_{nk} &\equiv \frac{1}{2} (F_{nL} + F_{nR})_k - \frac{1}{2} \left| \frac{\partial F_{nk}}{\partial Q} \right| (\delta Q)_k \\ F_{nk} &\equiv \frac{1}{2} (F_{nL} + F_{nR})_k - \frac{1}{2} \left| \frac{\partial F_{nk}}{\partial Q_p} \frac{\partial Q_p}{\partial Q} \right| \frac{\partial Q}{\partial Q_p} (\delta Q_p)_k \end{aligned} \quad (2.67)$$

where the subscripts L and R on F_n and Q_p denote the left and right side of the surface k respectively. The first term in the numerical flux is a central difference operator and the second term is a traditional artificial dissipation term that is introduced in the approximate Riemann solver. The artificial dissipation term is defined in terms of the conservative variable vector, Q , but rewritten in terms of terms of the primitive variables, Q_p . By employing the definition of the preconditioning matrix the numerical flux reduces to,

$$F_{nk} \equiv \frac{1}{2} (F_{nL} + F_{nR})_k - \frac{1}{2} \left| \frac{\partial F_{nk}}{\partial Q_p} \Gamma_{pk}^{-1} \right| \Gamma_{pk} (Q_{pR} - Q_{pL})_k \quad (2.68)$$

which shows only the artificial dissipation term is modified.

Following which using the identity, $|(\partial F_{nk}/\partial Q_p) \Gamma_{pk}^{-1}| \Gamma_{pk} = \Gamma_{pk} |\Gamma_{pk}^{-1}(\partial F_{nk}/\partial Q_p)|$ and defining the flux Jacobian in the normal direction as $A_{pn} = \frac{\partial F_n}{\partial Q_p}$,

$$F_{nk} \equiv \frac{1}{2} (F_{nL} + F_{nR})_k - \frac{1}{2} \Gamma_{pk} |\Gamma_{pk}^{-1} A_{pnk}| (Q_{pR} - Q_{pL})_k \quad (2.69)$$

is the numerical flux equation. By dropping the subscript n on the flux vector as well as Jacobians and by assuming all the terms represent the quantities in the normal direction we obtain,

$$F_k \equiv \frac{1}{2} (F_L + F_R)_k - \frac{1}{2} \Gamma_{pk} |\Gamma_p^{-1} A_p|_k (Q_{pR} - Q_{pL})_k \quad (2.70)$$

as the flux at control surface k . Substituting for the above inviscid flux in the Navier-Stokes equations in the integral form we have,

$$\begin{aligned} \left(\bar{\Gamma}_p \frac{\partial \bar{Q}_p}{\partial \tau} + \frac{\partial \bar{Q}}{\partial t} \right) + \frac{1}{\Omega} \sum_{k=1}^K \left[\frac{1}{2} (F_L + F_R) - \frac{1}{2} \Gamma_p |\Gamma_p^{-1} A_p| (Q_{pR} - Q_{pL}) \right]_k S_k \\ - \frac{1}{\Omega} \sum_{k=1}^K \vec{F}_{v,k} \cdot \vec{n}_k S_k = \bar{H} \end{aligned} \quad (2.71)$$

with the viscous terms also rewritten as a face flux. Observing the discretization, we realize that the dissipation is now dependent on the preconditioning matrix and the flux Jacobians. Accordingly, care should be taken to define the matrix $\Gamma_p |\Gamma_p^{-1} A_p|$ to ensure proper amount of artificial dissipation. In this work the preconditioning strategy outlined in Merkle and Venketeswaran [72] has been used, which has been verified to provide the correct amount of artificial dissipation. The inviscid fluxes in the present work are discretized using an upwind flux-difference splitting scheme that uses the Roe [71] approximate Riemann solver. The dissipation matrix can be rewritten as,

$$\Gamma_p |\Gamma_p^{-1} A_p| = R_p |\Lambda_p| R_p^{-1} \quad (2.72)$$

where Λ_p is the eigenvalue matrix and R_p is the right eigenvector matrix. For the Roe flux difference splitting scheme the eigenvalue matrix and the eigenvector matrix are computed based on the Roe averaged variables,

$$\begin{aligned}\rho_{LR} &= \sqrt{\rho_L}\sqrt{\rho_R} \\ u_{LR} &= \frac{u_L\sqrt{\rho_L} + u_R\sqrt{\rho_R}}{\sqrt{\rho_L} + \sqrt{\rho_R}} \\ h_{LR} &= \frac{h_L\sqrt{\rho_L} + h_R\sqrt{\rho_R}}{\sqrt{\rho_L} + \sqrt{\rho_R}}\end{aligned}\quad (2.73)$$

where ρ_{LR} , u_{LR} and h_{LR} are the Roe averaged variables for density, velocity and enthalpy. The matrix Λ_p contains the eigenvalues of the system which are no longer the physical eigenvalues of the system but are based on the definition of the preconditioning system.

Considering the possibility of the eigenvalues going to zero at sonic conditions, the present modified system employs the Harten entropy fix [73]. This modification is particularly important in the present work since nozzle flows at off-design conditions are dominated by shocks. To avoid unphysical solutions in the above system a small amount of dissipation is added by modifying the eigenvalues, λ , as follows:

$$|\lambda| = \begin{cases} |\bar{\lambda}|, & |\bar{\lambda}| > \delta \\ \frac{\bar{\lambda}^2 + \delta^2}{2\delta}, & |\bar{\lambda}| < \delta \end{cases}\quad (2.74)$$

where $\bar{\lambda}$ is the arithmetic average and δ is the difference of the eigenvalues on either side of the face.

Following the flux reconstruction procedure at the face, it remains to be discussed how the values on the face of the control volume are computed from the cell-centers. For a first order scheme, we simply set the variable value at face equal to the corresponding cell. For a higher order system we use a reconstruction procedure to compute the variable value at the face based on the surrounding cell data. The reconstruction methods compute the face value by a Taylor series expansion give by,

$$Q_{p,face} = Q_{p,cell} + \nabla Q_{p,cell} \cdot \Delta \vec{r} + \dots\quad (2.75)$$

where the primitive variable vector on face $Q_{p,face}$ is computed based on the cell center value $Q_{p,cell}$ and the cell gradient $\nabla Q_{p,cell}$ with $\Delta\vec{r}$ denoting the vector from the cell center to the face center. The gradient $\nabla Q_{p,cell}$ is computed using either the linear least square technique or Green-Gauss reconstruction technique [74]. The Green-Gauss method employed in the present work is discussed next.

Green-Gauss gradient reconstruction: The Green-Gauss reconstruction technique constructs gradients by integrating around the boundary of a closed control-volume based on Green's theorem. This control volume is typically a dual control volume surrounding the cell center comprised of either the surrounding cell-centers or the face centers. In our approach we make use of the face centers for reconstruction since the face center values can be obtained as an arithmetic average of node values. The node values are computed based on the surrounding cell values using an inverse weighted averaging. Thus, the cell itself with volume, Ω , and surface boundary, $\delta\Omega$ acts as the dual control volume. From Greens theorem the average gradients over a control volume can be written as,

$$\nabla\overline{Q_p} = \frac{1}{\Omega} \int_{\Omega} Q_p dV = \frac{1}{\Omega} \int_{\delta\Omega} Q_p \vec{n} dS = \frac{1}{\Omega} \sum_{k=1}^K Q_{p,k} \vec{n}_k S_k \quad (2.76)$$

where S_k and \vec{n}_k are the face area and normal vector respectively with $Q_{p,k}$ obtained as the arithmetic average of the node values.

Gradient Limiter: In the case of flows with strong gradients such as shocks, the above second order formulation to obtain the face values may lead to instabilities, and additional dissipation mechanisms are required. For a computation the solution accuracy can be improved by employing a flux limiter function that can eliminate the unphysical oscillation or wiggles in the solution that occur near strong discontinuities. In the literature many forms of limiters have been employed both as cell based and face based limiter. The present work employs a limiter due to Barth [75]. This limiter has been implemented as a cell based limiter as generally face based limiters are

considered to be ineffective [76]. In the limited form the face values are reconstructed as follows,

$$Q_{p,face} = Q_{p,cell} + \phi \nabla Q_{p,cell} \cdot \Delta \vec{r} \quad (2.77)$$

where ϕ is the cell limiter. The goal is to compute the largest admissible value of ϕ while invoking monotonicity principle which states that the value of the cell should lie within maximum and minimum of neighboring cell values. This puts the following,

$$\begin{aligned} Q_{p,\min} &= \min(Q_p, Q_{p,neighbors}) \\ Q_{p,\max} &= \max(Q_p, Q_{p,neighbors}) \end{aligned} \quad (2.78)$$

as limits on the cell-centered values.

For each point on the control volume of the cell, which is the face center, compute the reconstructed face value of the primitive variables as outlined in the previous section. The limiter can then be obtained as,

$$\phi = \begin{cases} \min \left(1, \frac{Q_{p,\max} - Q_{p,cell}}{Q_{p,face} - Q_{p,cell}} \right), & Q_{p,face} - Q_{p,cell} < 0 \\ \min \left(1, \frac{Q_{p,\min} - Q_{p,cell}}{Q_{p,face} - Q_{p,cell}} \right), & Q_{p,face} - Q_{p,cell} > 0 \\ 1, & Q_{p,face} - Q_{p,cell} = 0 \end{cases} \quad (2.79)$$

with the various terms as defined as earlier. The limiting procedure applied as shown above is effective in removing spurious oscillations from the solution but the discontinuous nature of the limiter can hinder the solution accuracy [77]. The limiting process also reduces the accuracy of the local face reconstruction from second order to first order in the vicinity of shocks.

The discretization of the viscous terms is completed by using the Greens theorem again. The viscous vector $F_{vk}^{\vec{r}}$ computed on the k th control surface requires computation of gradients at the face. The Green-Gauss reconstruction technique is employed with a control volume comprising of the face nodes and the adjacent cell centers. The node values used in the gradient computation at face centers are obtained as a inverse distance weighting of the adjacent cell values.

After having described the spatial discretization of the conservation equations, we can now define the discrete divergence operator,

$$\begin{aligned} \nabla_D \cdot (\vec{F} - \vec{F}_v) = \frac{1}{\Omega} \sum_{k=1}^K \left[\frac{1}{2} (F_L + F_R) - \frac{1}{2} \Gamma_p |\Gamma_p^{-1} A_p| (Q_{pR} - Q_{pL}) \right]_k S_k \\ - \frac{1}{\Omega} \sum_{k=1}^K \vec{F}_{v,k} \cdot \vec{n}_k S_k \end{aligned} \quad (2.80)$$

comprising of the algebraic flux operators for the inviscid and viscous flux vectors. Substituting for the above into the integral form of the Navier-Stokes equations gives,

$$\left(\bar{\Gamma}_p \frac{\partial \bar{Q}_p}{\partial \tau} + \frac{\partial \bar{Q}}{\partial t} \right) + \nabla_D \cdot (\vec{F} - \vec{F}_v) = \bar{H} \quad (2.81)$$

as the final form of the equations with spatial discretization defined.

2.5.2 Temporal Discretization

The time marching method utilized in the present work includes the additional of a pseudo time derivative or more commonly referred to as the dual-time procedure. The pseudo time derivative defined based on the primitive variable set allows us to compute the fluid variables of primary interest from which other quantities like enthalpy can be calculated directly. The pseudo derivative also acts as an agent for preconditioning which allows us to control the convergence behavior of the algorithm. Thus, the preconditioned pseudo time term has been designed to find the solution to the physical equation set apart from controlling the artificial dissipation that appears in the numerical flux for the inviscid flux.

In the present work, we employ a second order implicit scheme for the physical derivatives:

$$\frac{\partial \bar{Q}}{\partial t} = \frac{3\bar{Q}^{n+1} - 4\bar{Q}^n + \bar{Q}^{n-1}}{2\Delta t} \quad (2.82)$$

where n represents the time level in physical time.

The pseudo time derivative is replaced by an Euler implicit difference. Replacing these terms in Eq. 2.81 by the appropriate discretization, we obtain,

$$\left(\frac{\bar{\Gamma}_p \bar{Q}_p^{k+1} - \bar{Q}_p^k}{\Delta \tau} + \frac{3\bar{Q}^{n+1} - 4\bar{Q}^n + \bar{Q}^{n-1}}{2\Delta t} \right) + \nabla_D \cdot (\vec{F} - \vec{F}_v)^{k+1} = \bar{H}^{k+1} \quad (2.83)$$

where the subscript k represents the running variable for pseudo time iterations. The pseudo iterations are performed within each physical iteration from level n to $n + 1$. The physical time level $n + 1$ is, therefore, equivalent to the pseudo time level $k + 1$ and is updated after the pseudo iterations meet the convergence criterion. After regrouping all the pseudo time terms on the left hand side, the equation reads,

$$\frac{\bar{\Gamma}_p \bar{Q}_p^{k+1} - \bar{Q}_p^k}{\Delta \tau} + \frac{3\bar{Q}^{k+1} - \bar{Q}^k}{2\Delta t} = - \left(S_t^k + \nabla_D \cdot (\vec{F} - \vec{F}_v)^{k+1} - \bar{H}^{k+1} \right) \quad (2.84)$$

with the first term on the right hand side,

$$S_t^k = \frac{3\bar{Q}^k - 4\bar{Q}^n + \bar{Q}^{n-1}}{2\Delta t} \quad (2.85)$$

representing the physical time derivative.

In order to solve the equation, the inviscid, viscous and source terms at the time level $k + 1$ have to be linearized. Accordingly we have,

$$\begin{aligned} (\nabla_D \cdot \vec{F})^{k+1} &= (\nabla_D \cdot \vec{F})^k + \nabla A_{p,i} \cdot \Delta Q_p \\ (\nabla_D \cdot \vec{F}_v)^{k+1} &= (\nabla_D \cdot \vec{F}_v)^k + \nabla A_{p,v} \cdot \Delta Q_p \\ \bar{H}^{k+1} &= \bar{H}^k + D \Delta Q_p \end{aligned} \quad (2.86)$$

where $A_{p,i} = \partial \vec{F} / \partial Q_p$, $A_{p,v} = \partial \vec{F}_v / \partial Q_p$ and $D = \partial \bar{H} / \partial Q_p$ are the inviscid flux, viscous flux and source Jacobians [78]. On substituting the above expressions into Eq. 2.84 and rearranging the terms,

$$\left(\frac{\bar{\Gamma}_p}{\Delta \tau} + \frac{3}{2\Delta t} \frac{\partial \bar{Q}}{\partial \bar{Q}_p} - D + \nabla \cdot (A_{p,i} - A_{p,v}) \right) \Delta Q_p = - \left(S_t^k + \nabla_D \cdot (\vec{F} - \vec{F}_v)^k - \bar{H}^k \right) \quad (2.87)$$

to obtain the final form of the implicit equation that needs to be solved.

The left hand side has within it details which determine the convergence behavior of the algorithm whereas the right hand side encompasses the transient conservative

equations of motion which determine the physics. As is the case with dual-time procedures, the solution $\left(S_t + \nabla_D \cdot (\vec{F} - \vec{F}_v) - \overline{H}\right)^k$ approaches the desired solution $\left(S_t + \nabla_D \cdot (\vec{F} - \vec{F}_v) - \overline{H}\right)^{n+1}$ in the limit as, $Q_p^{k+1} \rightarrow Q_p^k$ i.e. as the inner pseudo iterations converge. In case of steady computations the running variable n becomes redundant.

The left hand side as obtained above has to be inverted in order to obtain the solution change ΔQ_p . Owing to the wide banded nature of the matrix, this is usually done by an approximate factorization scheme like ADI, LU or line-Gauss Seidel (LGS). The line Gauss-Seidel scheme as described in [78] has been employed in the present case.

2.6 Boundary Conditions

The application of the Navier-Stokes equations requires the specification of boundary conditions for non-periodic problems. The solution depends strongly on the boundary conditions. The choice of boundary conditions is motivated by the physics of the problem of interest. A physical boundary condition specifies the behavior of one or several dependent variables at the boundary. For example, in the case of the plug nozzle which draws air from a plenum, the specification of total pressure and total temperature boundary conditions along with the velocity angles is sufficient.

In the current formulation the boundary conditions are implemented implicitly. To apply boundary conditions exactly at a boundary an additional ghost cell is associated with each boundary cell. The addition of the ghost cells allows the boundary cell to be treated like interior cells. It allows the boundary cell unknown primary variable vector to be computed along with the interior cells. Consider the two cells interior to the boundary b and $b+1$ and the associated ghost cell g . By specifying the ghost cell values, the ghost cell forces the boundary condition at the boundary face. This leads from the fact that the boundary face values are reconstructed based on the ghost and adjacent values. If Ω_g denotes the solution vector in the ghost cell, then it is

constructed based on the reference or prescribed variable vector, Ω_{ref} and the flow variables from the flow field, Ω_b . Therefore,

$$\Omega_g = \Omega_{ref} + \Omega_b \quad (2.88)$$

which on evaluation implicitly at the new time level $n + 1$ gives,

$$\Omega_g^{n+1} = \Omega_{ref}^{n+1} + \Omega_b^{n+1} \quad (2.89)$$

as the equation describing the flow variables in the ghost vector.

Applying Taylor's series expansion, the ghost and boundary vectors become:

$$\begin{aligned} \Omega_g^{n+1} &= \Omega_g^n + \frac{\partial \Omega_g}{\partial t} \Delta t = \Omega_g^n + \frac{\partial \Omega_g}{\partial Q_g} \Delta Q_g \\ \Omega_b^{n+1} &= \Omega_b^n + \frac{\partial \Omega_b}{\partial t} \Delta t = \Omega_b^n + \frac{\partial \Omega_b}{\partial Q_b} \Delta Q_b \end{aligned} \quad (2.90)$$

where Q_g and Q_b are the primitive variable vector for the ghost and boundary cells. The Jacobians $\partial \Omega_g / \partial Q_g$ and $\partial \Omega_b / \partial Q_b$ need to be evaluated depending on the boundary condition. The reference vector Ω_{ref}^{n+1} is a constant for steady computations while for unsteady computations it can be a constant or time dependent depending on the boundary under consideration. Substituting the above expressions we obtain,

$$\Omega_g^n + \frac{\partial \Omega_g}{\partial Q_g} \Delta Q_g = \Omega_b^n + \frac{\partial \Omega_b}{\partial Q_b} \Delta Q_b + \Omega_{ref}^{n+1} \quad (2.91)$$

which can be rearranged to compute the change in ghost cell solution as,

$$\Delta Q_g = \left(\frac{\partial \Omega_g}{\partial Q_g} \right)^{-1} \left[\frac{\partial \Omega_b}{\partial Q_b} \Delta Q_b + (\Omega_{ref}^{n+1} + \Omega_b^n - \Omega_g^n) \right] \quad (2.92)$$

which now becomes part of the equation set to be solved. This general formulation can now be applied to any boundary condition that is encountered. In the next subsection we discuss the common boundary conditions encountered and the definitions of the Jacobians used.

2.6.1 Entropy, Total Enthalpy and Flow Angle at the Inlet

The total pressure, total temperature and flow angle inlet is used primarily for the plug nozzle computations in this work. Additionally the species mass fractions

are also prescribed at the inlet for combustion applications. By knowing the total pressure and temperature we can obtain the total enthalpy and entropy at the inlet for an ideal gas as,

$$\Delta s_g = c_p \ln \frac{T_g}{T_1} - R \ln \frac{p_g}{p_1} \quad (2.93)$$

where p_1 and T_1 are some reference temperatures. The stagnant enthalpy relation is,

$$h_g^0 = c_p T + \frac{1}{2} (U_g)^2 \quad (2.94)$$

where U_g is the magnitude of velocity in the ghost cell with T_g and p_g as the temperature and pressure respectively. The two angles α and β define the incoming flow direction. To implement the boundary condition the solution of the ghost vector is defined as, $\Omega_g = (s_g, \alpha_g, \beta_g, U_g, h_g^0, Y_{k,g})$ with $Q_g = ((p_g, u_g, v_g, w_g, T_g, Y_{k,g}))$ defined as the primary variable vector in the ghost cell. The reference vector is defined as: $\Omega_{ref} = (s_{ref}, \alpha_{ref}, \beta_{ref}, 0, h_{ref}^0, Y_{k,ref})$ while the boundary cell vector is give by, $\Omega_b = (0, 0, 0, U_b, 0, 0)$ for which the primary variable vector becomes, $Q_p = ((p_b, u_b, v_b, w_b, T_b, Y_{k,b}))$. The Jacobians can the obtained as,

$$\frac{\partial \Omega_b}{\partial Q_b} = \frac{\partial (0, 0, 0, U_b, 0, 0)}{\partial (p_b, u_b, v_b, w_b, T_b, Y_{k,b})} = \begin{pmatrix} 0 & 0 & 0 & 0 & 0 & 0 \\ 0 & 0 & 0 & 0 & 0 & 0 \\ 0 & 0 & 0 & 0 & 0 & 0 \\ 0 & \frac{u_b}{U_b} & \frac{v_b}{U_b} & \frac{w_b}{U_b} & 0 & 0 \\ 0 & 0 & 0 & 0 & 0 & 0 \\ 0 & 0 & 0 & 0 & 0 & 0 \end{pmatrix} \quad (2.95)$$

$$\frac{\partial \Omega_g}{\partial Q_g} = \begin{pmatrix} -\frac{R}{p_g} & 0 & 0 & 0 & 0 & \frac{c_p}{T_g} \\ 0 & -\frac{v_g}{u_g^2 + v_g^2} & \frac{u_g}{u_g^2 + v_g^2} & 0 & 0 & 0 \\ 0 & -\frac{u_g w_g}{(U_g)^2 \sqrt{u_g^2 + v_g^2}} & -\frac{v_g w_g}{(U_g)^2 \sqrt{u_g^2 + v_g^2}} & \frac{\sqrt{u_g^2 + v_g^2}}{(U_g)^2} & 0 & 0 \\ 0 & \frac{u_g}{U_g} & \frac{v_g}{U_g} & \frac{w_g}{U_g} & 0 & 0 \\ 0 & u_g & v_g & w_g & c_p & 0 \\ 0 & 0 & 0 & 0 & 0 & 1 \end{pmatrix} \quad (2.96)$$

for the inlet boundary condition.

2.6.2 Outlet Boundary Condition

For the outlet the back pressure becomes the physical choice for the reference solution vector, $\Omega_{ref} = (p_{back}, 0, 0, 0, 0, 0)$. The rest of the components come from the internal flowfield, $\Omega_b = (0, u_b, v_b, w_b, T_b, Y_{k,b})$. The ghost cell boundary condition vector is defined as $\Omega_g = (p_g, u_g, v_g, w_g, T_g, Y_{k,g})$. Then the Jacobians are given by,

$$\frac{\partial \Omega_g}{\partial Q_g} = \frac{\partial (p_g, u_g, v_g, w_g, T_g, Y_{k,g})}{\partial (p_g, u_g, v_g, w_g, T_g, Y_{k,g})} = I \quad (2.97)$$

$$\frac{\partial \Omega_b}{\partial Q_b} = \frac{\partial (0, u_b, v_b, w_b, T_b, Y_{k,b})}{\partial (p_b, u_b, v_b, w_b, T_b, Y_{k,b})} = \begin{pmatrix} 0 & 0 & 0 & 0 & 0 & 0 \\ 0 & 1 & 0 & 0 & 0 & 0 \\ 0 & 0 & 1 & 0 & 0 & 0 \\ 0 & 0 & 0 & 1 & 0 & 0 \\ 0 & 0 & 0 & 0 & 1 & 0 \\ 0 & 0 & 0 & 0 & 0 & 1 \end{pmatrix} \quad (2.98)$$

for the outlet boundary condition.

2.6.3 Inviscid Wall

The inviscid wall requires that the velocity be tangential at the wall. This requirement can be obtained by setting the normal cell velocity at the ghost and the boundary cell equal to each other but opposite in sign. The velocity component that is tangential to the wall have the same magnitude and direction for the ghost and boundary cell. Thus, the ghost cell velocity \vec{u}_g and boundary cell velocity \vec{u}_b are related through the wall normal \vec{n}_W as,

$$\vec{u}_b - \vec{u}_g = 2(\vec{u}_b \cdot \vec{n}_W) \vec{n}_W \quad (2.99)$$

The rest of the values of the ghost cell are set equal to the adjacent cell boundary values. Therefore, the reference solution vector is equal to zero. The boundary cell vector is then defined as,

$$\Omega_b = \begin{pmatrix} p_b, u_b - 2(u_b n_x + v_b n_y + w_b n_z), v_b - 2(u_b n_x + v_b n_y + w_b n_z), \\ w_b - 2(u_b n_x + v_b n_y + w_b n_z), T_b, Y_{k,b} \end{pmatrix} \quad (2.100)$$

where n_x , n_y and n_z are the three components of the unit normal vector to the wall, \vec{n}_W pointing into the flowfield. Consequently, we obtain the Jacobians as,

$$\frac{\partial \Omega_g}{\partial Q_g} = \frac{\partial (p_g, u_g, v_g, w_g, T_g, Y_{k,g})}{\partial (p_g, u_g, v_g, w_g, T_g, Y_{k,g})} = I \quad (2.101)$$

$$\frac{\partial \Omega_b}{\partial Q_b} = \begin{pmatrix} 1 & 0 & 0 & 0 & 0 & 0 \\ 0 & 1 - 2n_x^2 & -2n_x n_y & -2n_x n_z & 0 & 0 \\ 0 & -2n_x n_y & 1 - 2n_y^2 & -2n_y n_z & 0 & 0 \\ 0 & -2n_x n_z & -2n_y n_z & 1 - 2n_z^2 & 0 & 0 \\ 0 & 0 & 0 & 0 & 1 & 0 \\ 0 & 0 & 0 & 0 & 0 & 1 \end{pmatrix} \quad (2.102)$$

for the inviscid wall boundary condition.

2.6.4 Viscous Wall Boundary Condition

For viscous internal flow computations, the velocity at the wall is zero. This requirement can be fulfilled by observing that,

$$\vec{u}_g + \vec{u}_b = 0 \quad (2.103)$$

where \vec{u}_g and \vec{u}_b are defined as earlier. The boundary cell vector and ghost cell vector are defined as $\Omega_b = (p_b, -u_b, -v_b, -w_b, T_b, Y_{k,b})$ and $\Omega_g = (p_g, u_g, v_g, w_g, T_g, Y_{k,g})$ respectively. From this the Jacobians can be obtained as,

$$\frac{\partial \Omega_g}{\partial Q_g} = \frac{\partial (p_g, u_g, v_g, w_g, T_g, Y_{k,g})}{\partial (p_g, u_g, v_g, w_g, T_g, Y_{k,g})} = I \quad (2.104)$$

$$\frac{\partial \Omega_b}{\partial Q_b} = \frac{\partial (p_b, -u_b, -v_b, -w_b, T_b, Y_{k,b})}{\partial (p_b, u_b, v_b, w_b, T_b, Y_{k,b})} = \begin{pmatrix} 1 & 0 & 0 & 0 & 0 & 0 \\ 0 & -1 & 0 & 0 & 0 & 0 \\ 0 & 0 & -1 & 0 & 0 & 0 \\ 0 & 0 & 0 & -1 & 0 & 0 \\ 0 & 0 & 0 & 0 & 1 & 0 \\ 0 & 0 & 0 & 0 & 0 & 1 \end{pmatrix} \quad (2.105)$$

for the viscous wall boundary condition.

CHAPTER 3. NUMERICAL SIMULATION OF SHROUDED PLUG NOZZLE

Supersonic flight requires the development of technologies which can make operation commercially as well as environmentally viable. In this regard the aviation industry is investing resources in developing technologies both for the airframe as well as the propulsion system which will make this possible. A technology solution that has been proposed [4] recently for the propulsion system is that of the high-flow bypass concept by GAC discussed in the introduction of the thesis. The concept uses both a plug inlet and plug nozzle combined with a unique flow path design as shown in Fig. 3.1. It is intended for efficient performance both from the view point of aerodynamic and noise characteristics particularly in the supersonic flight regime. An existing turbofan engine [6] is employed as the core of the propulsion system working with the flow ingested through the plug inlet and exhausted by the plug nozzle outlet. In the shrouded plug arrangement, the engine is exhausted via the core (primary) flowpath within a barrel-type shroud of near constant radius, using a plug center body to choke and supersonically expand the jet flow. An annular nozzle, bounded between the nacelle cowling and primary shroud, is used to expand tertiary matching flow from the nacelle bypass stream. The nacelle bypass provides additional low-boom shaping options for the nacelle, and, in particular, is used to increase the inlets stream capture tube and to circularize the nacelle around non-axisymmetric external engine protuberances as shown in Fig. 3.1. The shrouded plug nozzle which forms a part of the this concept becomes an important component whose characteristics have to be studied. It is unique from traditional designs in that the shroud extends to a considerable portion of the plug (56% of plug length).

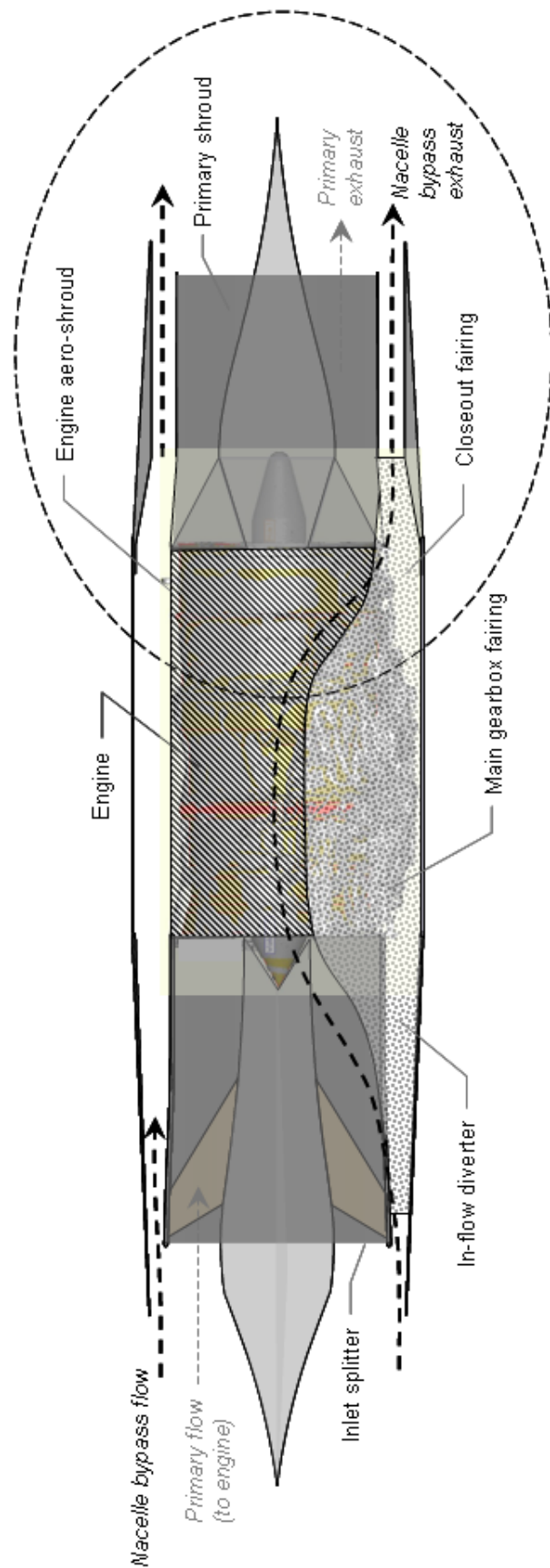


Figure 3.1. Low sonic boom propulsion system concept. Dashed ellipse shows the co-annular plug nozzle.

3.1 Introduction

Compared to a more conventional Laval-type convergent-divergent nozzle, the shrouded plug nozzle offers aerodynamic, structural, and installation benefits that make it a potentially attractive option for supersonic applications. For example, the off-design aerodynamic characteristics of the shrouded plug may allow the nozzle to operate at highly over-expanded conditions that would render a traditional Laval-type configuration unusable. This capability could obviate the need for mechanically complex variable geometry by delivering outstanding supersonic performance and acceptable off-design characteristics. In addition to permitting straight-forward integration with the nacelle bypass nozzle system (Fig. 3.1), the simplicity of the shroud barrel provides other valuable design options. For instance, the length of the barrel can be matched against the surface divergence characteristics of the nozzle plug to provide excellent supersonic performance and an optimally expanded jet stream that minimizes the exhaust contribution to the vehicle sonic boom signature.

A long shroud barrel also serves to isolate the primary nozzle exhaust from that of the bypass, shielding each of the streams from cross-interference, particularly at off-design operation. Because of the physical separation between the two exhaust streams, each can be analyzed, within reason, independent of the other, simplifying the numerical assessment of the configuration. A better understanding of the fundamental characteristics unique to each of the exhaust streams can then be obtained without extensive cross-coupling confounding the results, and explains why the focus of the present computational work is on the shrouded plug nozzle characteristics.

The nozzle behavior is determined by the operating conditions which in turn are related to the flight path of the vehicle. The plug nozzle derives its working medium from the core turbine outlet as well as the bypass stream outlet as seen in Fig. 3.1. The inlet conditions, therefore, are determined by the flow ensuing from the turbine core as well as the bypass stream. The total pressure and total temperature of the issuing gases prescribe these conditions. The total pressure can be characterized using

Nozzle Pressure Ratio (NPR) which is defined as the ratio of total pressure at the inlet to the ambient pressure.

The shrouded plug nozzle considered here has a design NPR of 6.23. When used in actual supersonic transport applications its operation will range from low NPR's at take-off conditions to design NPR at supersonic cruise. The simulations are designed with a requirement to understand these flow characteristics in the complete spectrum of nozzle pressure ratios. To understand the details of these flowfields, the present work draws on experimental data that is available from the static tests of a sub-scale model conducted at Purdue University in the Bi-Annular Nozzle Rig (BANR) [79]; [80]. Figure 3.2 shows a cut-away view of the test model for the static sea level experiments which is also the geometry used for simulations. The cut-away view shows clearly a shroud around the plug that extends downstream of the throat. Experimental data have been acquired from the model hardware that incorporated the hot vitiated core air to simulate turbine exit conditions and an annular cold air stream to simulate fan exhaust [40].

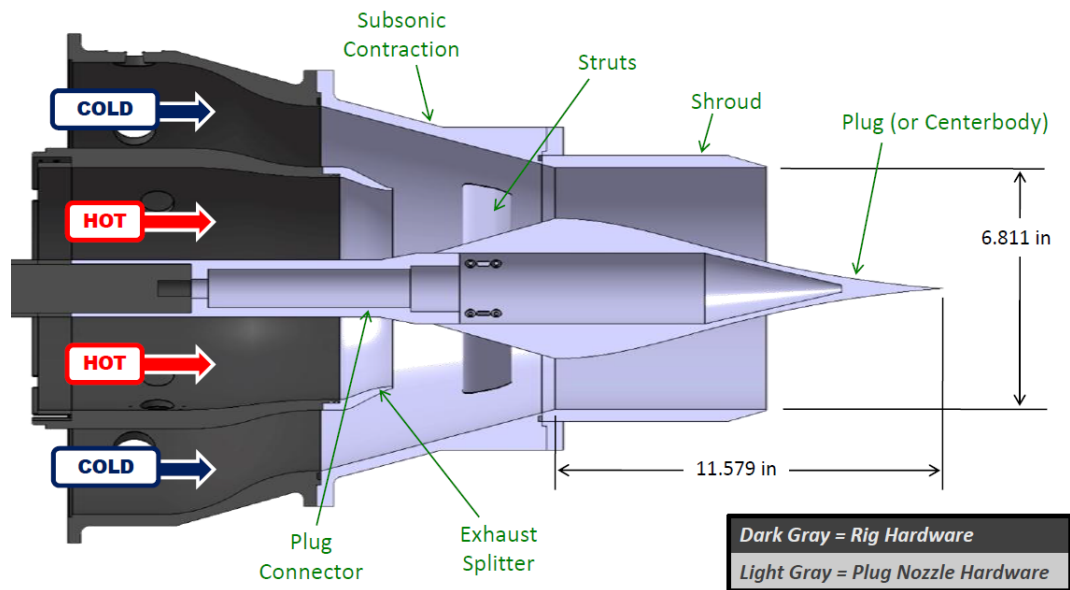


Figure 3.2. Cut-away view of the sub-scale model of the shrouded plug nozzle.

The shroud provides a Converging-Diverging(C-D) passage for the gases issuing from the core and bypass stream separated by an exhaust splitter. The presence of the external shroud is likely to result in a deviation from plug nozzle behavior and a return to C-D nozzle characteristics. After the core and fan streams merge at the trailing edge of the splitter, the compound stream is accelerated by the converging passage between the plug nozzle and the outer shroud until it reaches the throat. At low nozzle pressure ratios, the throat remains unchoked and the flow decelerates subsonically in the divergent section. At moderate to high nozzle pressure ratios, the flow chokes and accelerates supersonically before shocking down to meet the back pressure. This supersonic expansion followed by a shock system often leads to unsteadiness in the flowfield at low NPR's [30]. The unsteadiness drives an oscillating pressure distribution on the plug in the separation region that follows the shock. At the design NPR condition the plug nozzle operates at nearly shock-free conditions with supersonic outflow. In its passage from unchoked operation to shock-free conditions the nozzle might exhibit a multitude of shock structures typical of such geometrical configurations as a function of operating conditions. Thrust optimized parabolic C-D nozzles in rocket applications [34] are particularly known to exhibit two distinct regimes depending on the separation characteristics. In the Free Shock Separation (FSS) regime the flow over the nozzle wall is separated following the shock. In the Restricted Shock Separation (RSS) the flow reattaches on the nozzle wall enclosing a separation bubble.

The computations in conjunction with the experiments are specifically designed with a requirement to understand the shock physics as well as the unsteady characteristics over the entire NPR range. At these various conditions, companion computational results are compared against these experimental data to augment the findings and to provide additional understanding of the flow characteristics. This symbiosis of experiments and computations helped in verifying and validating the computational findings as well as gaining valuable insight into the performance of the nozzle.

The plug nozzle is analyzed using both axisymmetric and three-dimensional (3-D) computations. For each analysis, a brief description of the computational domain and the boundary conditions is followed by a discussion of the salient features of the nozzle aerodynamics starting from the off-design (low) NPR to design (high) NPRs. The primary focus of the present chapter is to shed light on the aerodynamic behavior of the shrouded plug nozzle configuration and to prepare for more complex reacting flows. In the process both available experimental data and computations are used. As will be seen this computational study in conjunction with experiments not only helps in validating the computational data but also result in useful insights further augmenting experimental data. In fact, the computations were used as a basis for designing the experiment. To begin with, in order to understand the measured data we discuss briefly the experimental configuration and the instrumentation available.

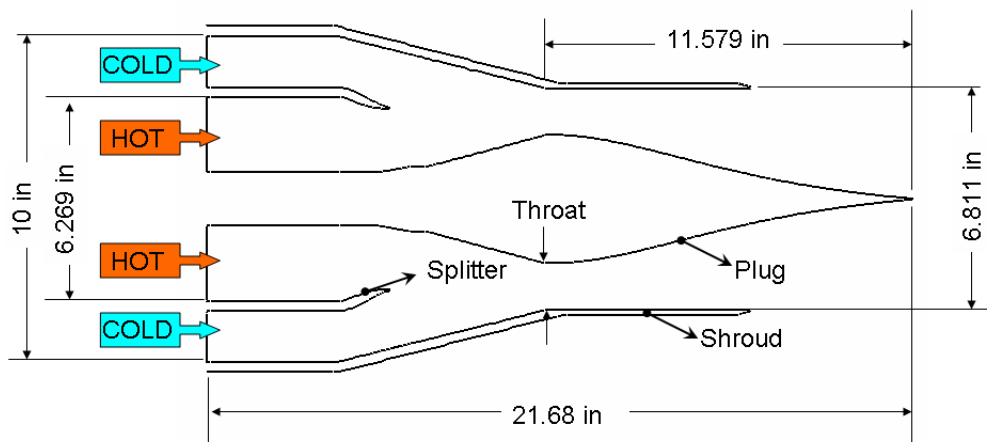
3.2 Experimental Configuration

Figure 3.3 shows a line diagram of the plug nozzle based on the model shown in Fig. 3.2. This is also the geometry that is used for computations. Also shown is a close-up of the plug nozzle near the throat region showing a sharp corner at the throat. The hot flow inlet of the plug draws in hot vitiated air from the nozzle rig to simulate conditions from a turbofan engine core flow and the cold flow inlet draws in air from the blow-down tank of the nozzle rig. The experimental set-up uses a quad-strut arrangement for structural integrity of the nozzle during operation. The aerodynamically designed struts are situated in the subsonic converging part of the nozzle so as to minimize disturbances downstream. The BANR is a blowdown test facility capable of feeding test hardware up to 25 kg/s air flow at pressures roughly 10 times atmospheric and vitiated core stream temperatures on the order of 700°C. The testing of 1/5th to 1/7th scale exhaust nozzles intended for SSBJ applications acted as the primary motivation for designing the BANR facility, with provisions for

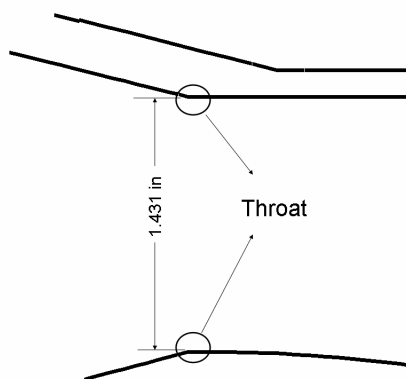
conducting mixer/ejector-type nozzle experiments necessitating that the BANR be a dual-stream (bi-annular) rig.

The rig also has sufficient instrumentation to measure incoming flow conditions to the nozzle. The total pressure and total temperature at the nozzle inflow plane are measured using upstream rakes. The total pressure rakes present at four azimuthal locations had four ports each which measured the radial variation. The mass averaged total pressure, based on bypass and core stream massflow, was reported in the experiments and is used as input to the computations. In addition the total temperature specified at the inlets was used as input for the subsonic inlet condition.

The plug nozzle configuration is provided with a host of instrumentation as shown in Fig. 3.4. To obtain the steady pressure distribution, pressure taps were installed at axial locations along the length of both the plug and shroud surfaces at three azimuthal locations. The choice of three azimuthal locations allowed the tangential variation to be captured to some extent. To measure any unsteadiness in the flow, high frequency Kulite pressure transducers were also placed on the shroud surface. The layout of the static pressure taps as well as the high frequency transducers is shown in 3.4. In the schematic shown it is evident that the azimuthal location at 45° had the best axial resolution of 0.5 inch. The static pressure taps at this azimuthal location are used extensively throughout this work to validate and verify the computations. Schlieren and shadowgraph images, which are of immense help in understanding the flow structure and, in particular, to identify shock shapes and recirculation zones, were also made during experimental operation. The experiments used both vertical and horizontal configurations of the knife-edge in the schlieren set-up. The vertical knife-edge helped to identify horizontal gradients whereas the horizontal knife edge helped identify the vertical gradients. By using a transparent perspex shroud, shadowgraph images within the nozzle section were captured. These were particularly useful when the shock was inside the shroud. The schlieren images identify the first gradient of density while the shadowgraph captures the second gradient of density. Although the mode of operation of schlieren and shadowgraph are different the ultimate goal of



(a) Line diagram of cross section of nozzle.



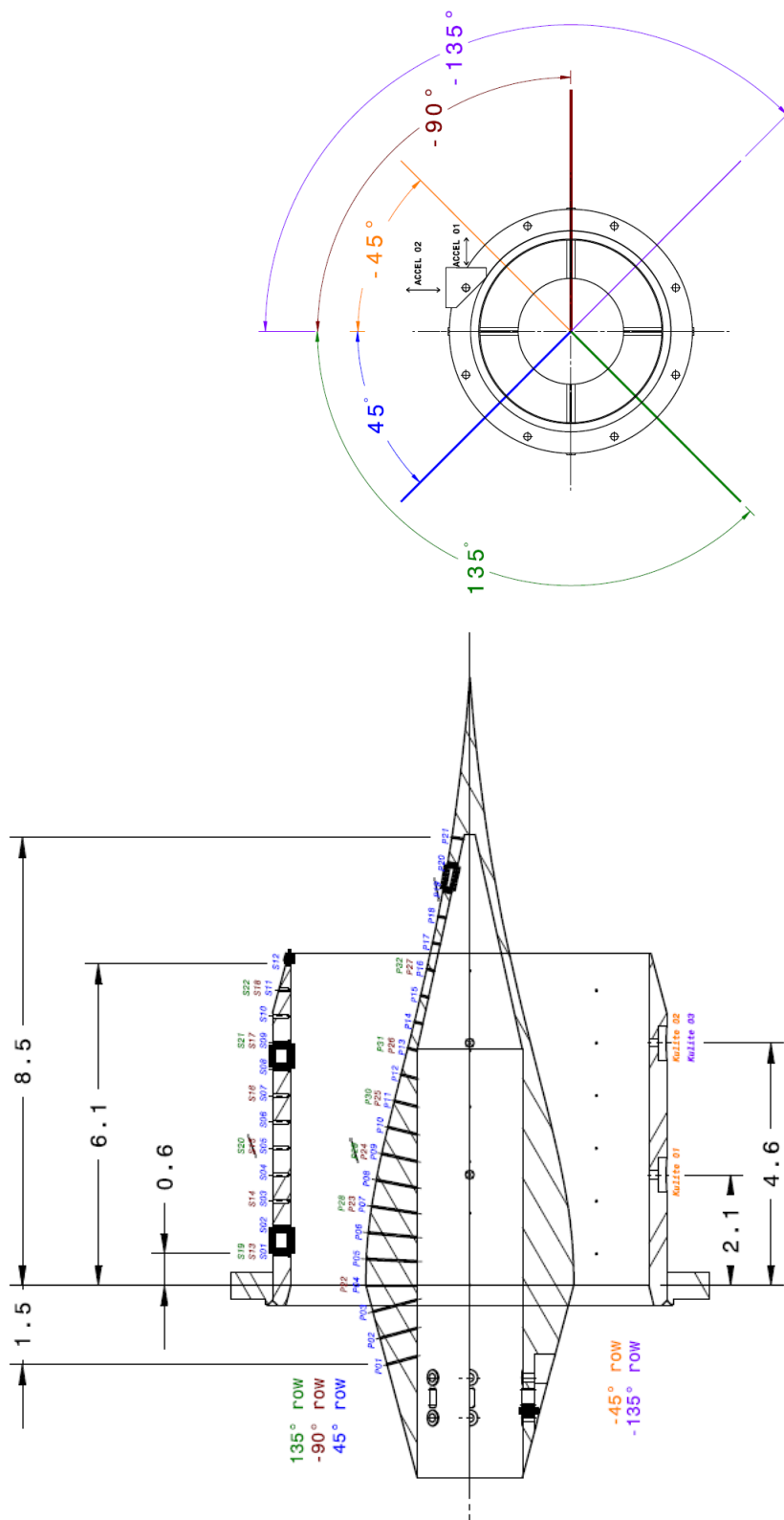
(b) Close-up of throat area showing sharp corner.

Figure 3.3. Schematic of nozzle used for computations along with detail of throat area showing sharp corner.

both is to understand the flow structure. The BANR rig has a force measurement system that allowed for the measurement of thrust forces and side-loads. This is done through a calibrated load cell stand which is mounted behind the nozzle. The measurement system allowed the measurement of axial thrust.

The first series of plug nozzle hot-fire and cold flow tests occurred immediately after the BANR became operational. The primary focus of this first round of tests was to gather quantitative and qualitative data pertaining to the unsteady aerody-

dynamic phenomena resulting from operation at off-design (low nozzle pressure ratio) conditions. A series of sixteen additional hot-fires were conducted as a part of the study to understand performance of plug nozzle. A core stream temperature of 1000F and bypass ratio (BPR) of three were targeted and roughly achieved for each hot-fire. The data has been documented in the M.S. theses of Tapee [40] and Cummings [41]. Key rig validation and performance data were gathered for all tests and presented and analyzed in the M.S. thesis of Sandroni [80]. Data from both the experimental campaigns have been used to validate the computations.



(a) Schematic of instrumentation layout on nozzle. Dimensions in inches. (b) Angle reference for instrumentation layout.

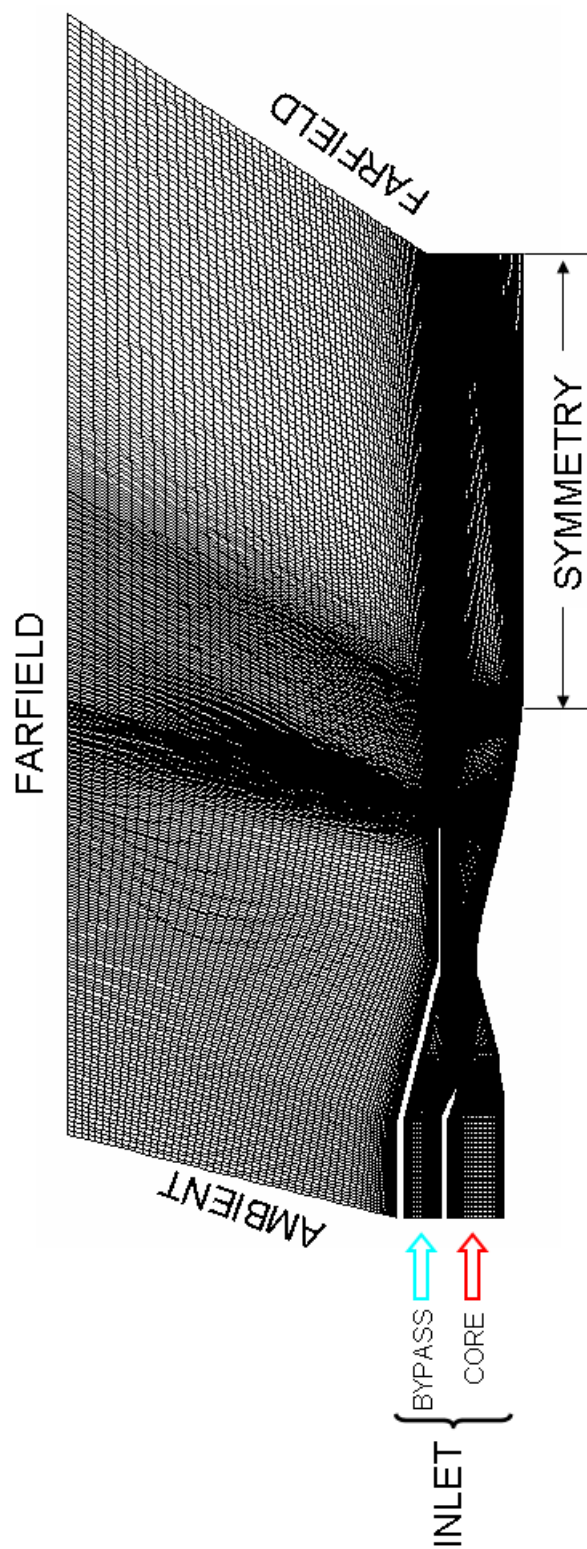
Figure 3.4. Schematic showing the instrumentation available on the plug as well as the shroud surface.

3.3 Axisymmetric Computations

Axisymmetric computations provide a fast and efficient means of computing the shrouded plug nozzle flowfield. We exploit the axisymmetric bore of the plug nozzle to perform the computations which lay the foundation for 3-D computations. To begin we discuss the computational domain, boundary conditions and the solution set-up. This is followed by a discussion of computational results and their comparison to data.

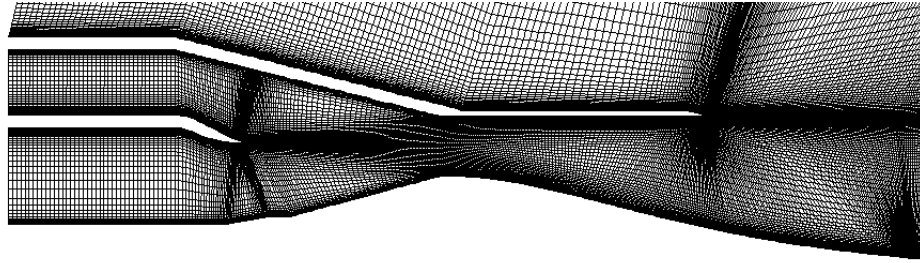
3.3.1 Computational Domain and Boundary Conditions

The computational domain and grid used for the simulations is shown in Fig. 3.5 and Fig. 3.6. The upper plot shows the overall domain while the lower plot shows some details of the grid in the plug nozzle region where the flow phenomena of primary interest take place. The computational domain starts several throat diameters upstream of the nozzle throat. The core and bypass flows remain separated by an exhaust splitter similar to the one in the experiments until the streams reach the beginning of the plug convergence. This allows computations to be conducted with either hot or cold flow in the core stream to mimic conditions in the experiments. One difference between the computational simulations and the experimental set-up is that the quad-strut arrangement that holds the plug in place can not be included in the axisymmetric computations. The strut is unlikely to have a major effect on the nozzle flowfield as it has been aerodynamically designed and is located in the subsonic, convergent section of the nozzle.

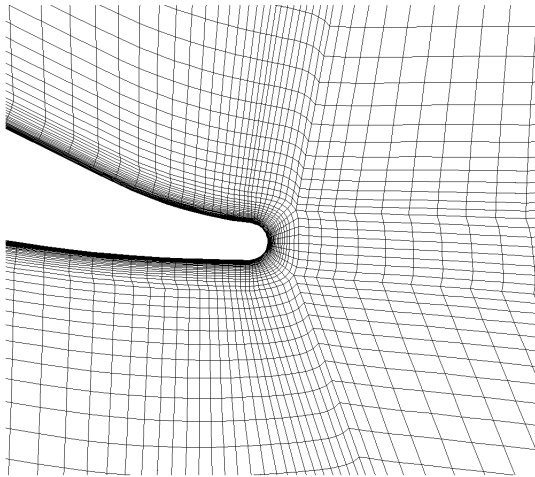


(a) Computational domain for axisymmetric computations.

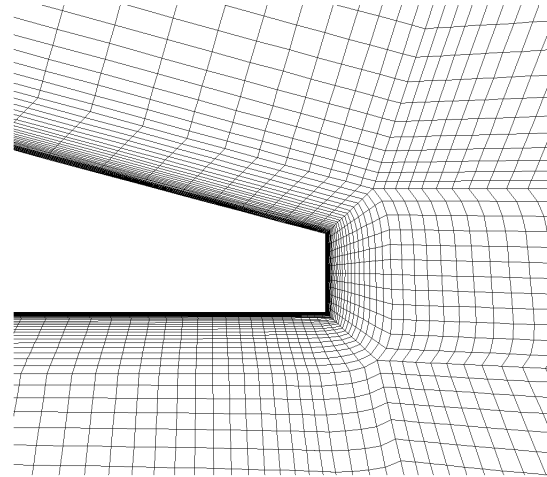
Figure 3.5. Computational domain and grid for axisymmetric computations. Boundary conditions are treated as shown. The plug nozzle walls are treated as no-slip wall.



(a) Detail of grid in the nozzle.



(b) Grid near the splitter tip.



(c) Grid near the shroud tip.

Figure 3.6. Details of grid near the splitter tip and shroud tip.

The computational domain also includes a region outside the nozzle to enable the near-field plume of the nozzle to be computed and compared with experiment. In addition this external domain enables physically meaningful downstream boundary conditions when the outflow is subsonic.

In terms of grid structure, a C-grid of quadrilateral elements is wrapped around the shroud and the exhaust splitter. The rest of the domain employs an H-grid of quadrilateral elements. The grid has 79,000 grid points with the first grid point from the wall specified in order to have a $y^+ < 1$ for a Reynolds number on the order of 100,000. The nozzle section had 120 grid points in the transverse direction to the flow and 400 grid points in the axial direction to the flow. From the throat to the plug tip sufficient resolution was provided to allow for shock capturing. As mentioned earlier,

the best axial resolution in the experiments is at the 45° azimuth which had pressure taps every 0.5 *inch*. There were approximately 10 grid points between adjacent static pressure taps on the plug and shroud in the computation. This allowed the shock location to be determined if it were to occur between the static pressure taps in the experiments.

The boundary conditions at the inlet of both the core and bypass flow streams were specified as reservoir (stagnation temperature and stagnation pressure) conditions with zero flow angle. In the experiments, the mass flow rate was controlled in such a manner as to be able to match the stagnation pressure in the core and bypass streams as closely as possible. The nozzle pressure ratio (NPR), defined as the ratio of upstream total pressure to ambient pressure, is therefore the same for both streams. During the experiment, the rakes showed minor differences in total pressures between the nozzle inlets and separate NPRs are reported for the experiments to document these small differences [40]. From these two NPR measurements for the core and bypass, a mass-weighted average NPR reported in experiments was used for the computations. In the experiments, the bypass stream was always unheated (cold) whereas measurements were made with both heated (hot) and unheated (cold) fluid temperatures in the core stream. In analogous fashion, separate hot- and cold-flow simulations were also done in the computations. For all cold flow streams, the stagnation temperature in the computations was taken as 244 K, based on an average temperature observed in all the experimental runs. The core flow temperatures for the hot flow cases are specified along with the NPR throughout this chapter.

Farfield boundary conditions (inflow or outflow depending on local conditions) are specified on the outer periphery of the external boundary. The hot-flow cases were treated as two-species computations to distinguish the hot core flow from the cold fan stream in the downstream region where they begin to mix. In all cases, the fluid was treated as a perfect gas with the properties of air. On solid surfaces, no-slip boundary conditions are specified and symmetry conditions are imposed on the jet centerline. An upstream turbulence intensity of 10% is prescribed at the core and bypass flow

inlets. The inlet turbulent dissipation is specified such that the turbulence intensity drops by 10% over the length of the nozzle. All computations were performed in parallel using 48 processors. The boundary conditions at the various boundaries are also denoted graphically in Fig. 3.5.

The experimental data have been obtained by static sea level tests of the sub-scale model. For the steady computations the initial condition was set to ambient sea level static conditions at low NPRs. Convergence difficulties were encountered in propagating the strong shock during the first few steady iterations through the converging diverging section for NPR above 2.5. In this case the steady computations were started with total pressure and total temperature conditions in the nozzle section till the exit. The rest of the domain was prescribed ambient conditions.

Kulite pressure data from the experiments indicated that some unsteadiness was present at low NPR conditions. In addition, steady computations showed that shock/boundary layer interactions were present at all NPRs, suggesting the likelihood of unsteady shock oscillations [21]; [30] and local large-scale motions in separated regions and shear layers. As a final indication of unsteadiness, the residuals in the high NPR steady computations converged ten or more orders of magnitude while at low NPRs, the convergence deteriorated somewhat, until for the lowest pressure ratio calculated, $\text{NPR} = 1.26$, the residuals dropped only five orders. Representative convergence rates for three cases showing this degradation are given in Fig. 3.7.

In view of these observed unsteadiness at low NPR's and the analogous reduction in convergence level, to provide a first-order assessment of the unsteadiness a sequence of time-accurate computations using the dual-time stepping algorithm were also performed. In general, the unsteady simulations at moderate and high NPRs converged to the same steady solution as that obtained with the steady algorithm, however, at low NPRs, stationary shock oscillations were observed following an initial transient. The axisymmetric unsteady analyses are discussed after the steady computations and provide a first approximation of the large-scale fluctuations in the flowfield while also serving as a precursor to 3-D, unsteady computations given later.

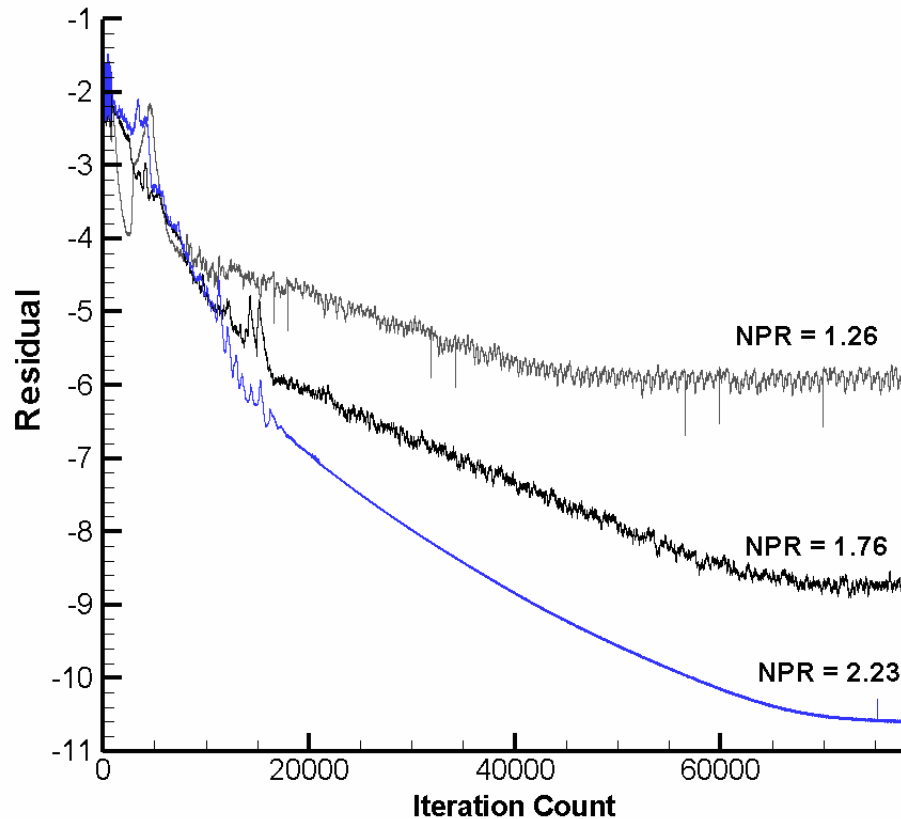


Figure 3.7. Convergence of steady axisymmetric computations at low NPRs.

3.4 Axisymmetric Steady Analysis

The NPR range the plug nozzle would see when employed in service depends upon flight speed, being a minimum when the aircraft is on the runway and a maximum at supersonic cruise. It is therefore important to understand in detail the variety of flow regimes the nozzle undergoes. Accordingly, non-reacting flow simulations have been performed conditions. As indicated earlier, the presence of the external shroud results in an added dimension of shock-boundary layer interactions at subsonic NPR's because of the diverging section. This feature is commonly seen in planar transonic diffusers [29]; [22]; [25] at off-design conditions, however, the same flow phenomena are absent in conventional plug nozzles which do not employ an outer shroud.

The next sections discuss the salient features of the nozzle aerodynamics starting from the design (high) NPR followed by off-design (low) NPR's. The following analysis makes extensive use of numerical schlieren pictures which have been constructed from the computational results using the density gradient field portrayed on a linear (as opposed to axisymmetric) field. The schlieren pictures are contour plots of the absolute values of the gradients at the grid nodes.

3.4.1 Global Shock Structure

We begin by comparing computational and experimental results at the design nozzle pressure ratio in Fig. 3.8 which provides a comparison of the computational schlieren on the bottom left along with an experimental schlieren photograph on the bottom right obtained by using a vertical knife edge. The top figure gives a global view of the flowfield in the nozzle section. Both the experimental and computational schlieren results are for hot-flow conditions (stagnation temperatures of 738 K and 244 K in the core and fan streams respectively) and a NPR of 6.12. The computational results show both the subsonic and supersonic portions of the nozzle along with the near-field plume, while the experimental result with the aluminum shroud shows the flow downstream of the shroud and the near-field plume.

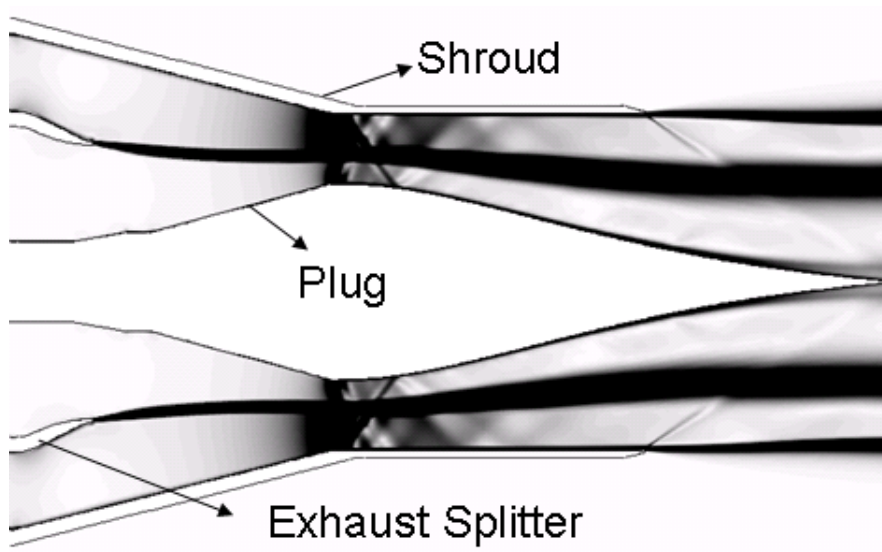
An ideally contoured supersonic plug nozzle allows exact expansion to ambient conditions and produces a uniform one-dimensional flow at the exit plane for the design NPR. Both the experimental and computational results indicate that the present plug-shroud combination and NPR give essentially this condition. In addition, the close resemblance between the computations and the experiments verifies that the computations are qualitatively correct. Both plots show that the flow expands nearly uniformly to ambient conditions as the jet emerges from the shroud. A Mach wave emanating from the end of the shroud and impinging on tip of the plug surface can be clearly seen in the experimental schlieren. The corresponding Mach wave in the

computational schlieren is quite visible in the outer, cold stream, but still remains faintly visible after it crosses the shear layer between the hot and cold streams.

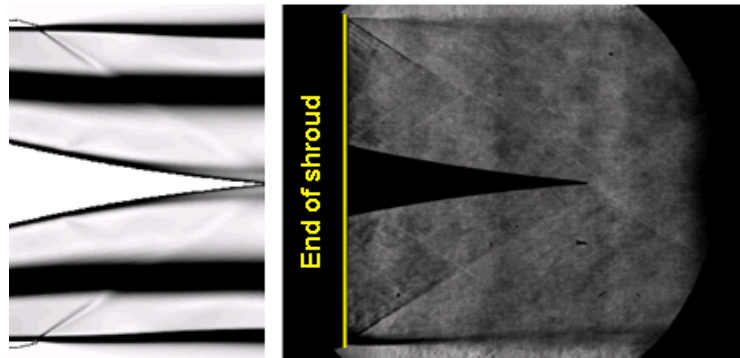
The computations show the exit Mach number reaches 1.75 and the Mach wave at the shroud exit indicates that the nozzle flow does not undergo any turning as it exits the shroud. The computational schlieren also shows a mixing layer that originates at the exhaust splitter tip and propagates downstream. This is a feature that is standard in the computations at all NPR's with hot core flow and cold bypass flow where the density difference between the two streams produces a density gradient that is visible in the schlieren plots. The mixing layer emanating from the shroud tip due to the velocity gradient is also visible in the schlieren images. In addition, the flowfield at design conditions is observed to be steady both in experiments as well as computations without any severe fluctuations.

The off-design characteristics of the nozzle are dominated by complex shock/shock and shock/boundary layer interactions as, for all but very low NPR's, the flow remains choked and over-expands inside the divergent portion of the nozzle thereby introducing shock waves that bring the pressure back up to ambient conditions. The experimental campaign conducted covered a range of NPR's for both hot and cold core flow in order to comprehend the flow structure by means of schlieren and shadowgraph images. In the following, the computational schlieren images are presented first for their ease of understanding and then compared with their experimental counterparts for qualitative agreement at off-design NPR's in the following section.

To understand the details of the flow, steady computations at a series of off-design NPR's were performed and are summarized in Fig. 3.9 by means of computational schlieren and Mach number contours. The steady computations help in gaining insight into the salient shock structure without delving into the shock dynamics, which will be discussed later. The schlieren images for the cold core flow case show a clear progression of the shock in the diverging section as the NPR is increased from 1.26 to 5.01. The cold core flow case without the shear layer, as in the case of hot flow in Fig. 3.8, allows a clear view of the nozzle internal flow structure.



(a) Computational schlieren



(b) Comp. Schlieren

(c) Experimental schlieren

Zoom

Figure 3.8. Computational schlieren compared to experimental schlieren at $NPR = 6.12$.

Starting from Fig. 3.9(a), the shock in the $NPR = 1.26$ case exhibits a normal shock like structure with a large separated flow region on the plug as well as the shroud surface. Additional detail in the throat region are given in Fig. 3.10. At this NPR the Mach number upstream of the shock is about 1.25 and the situation is similar to that seen in transonic diffusers at low subsonic NPR's [22]. The separation zone covers the entire plug and causes a monotonically increasing pressure distribution on

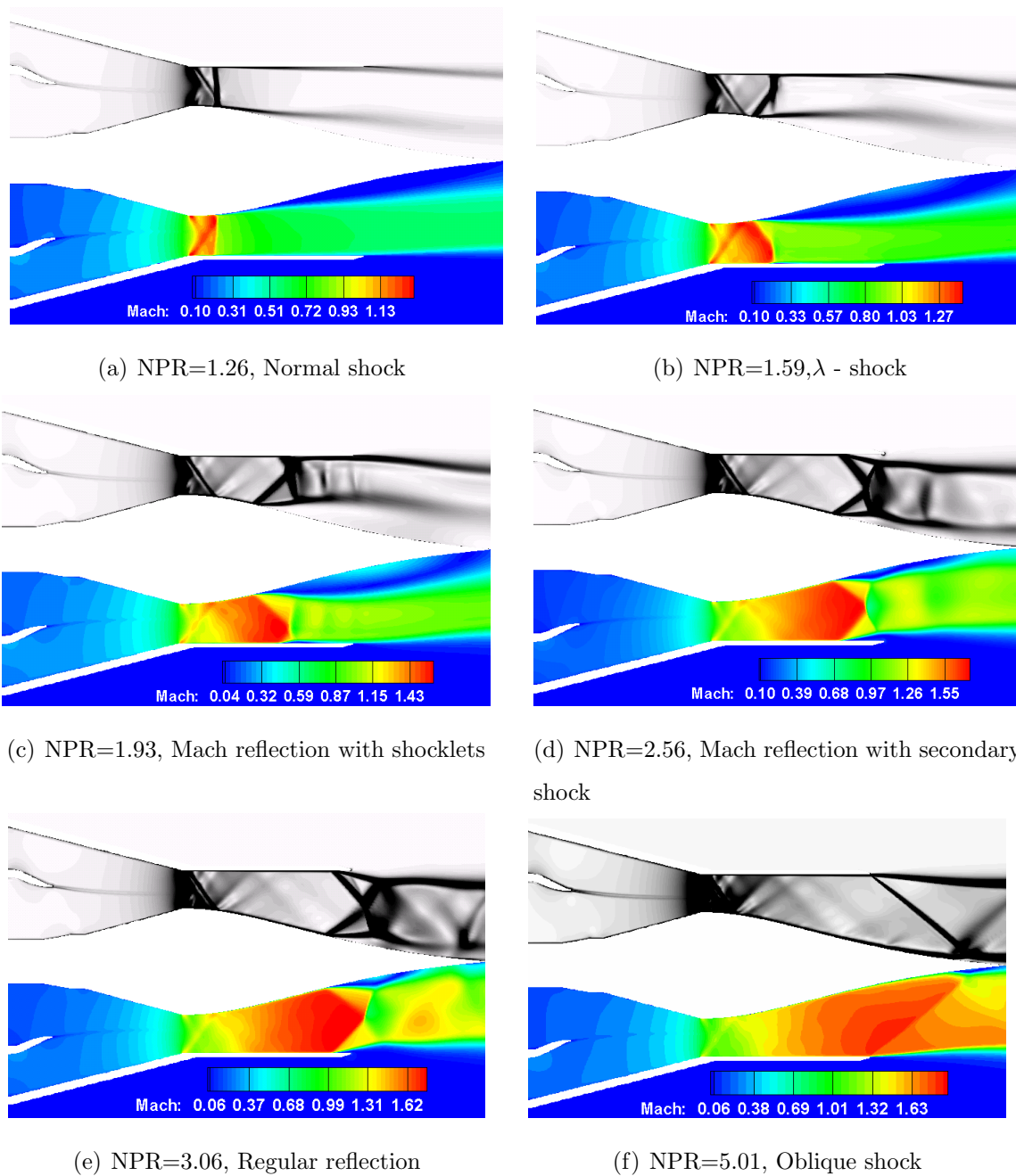


Figure 3.9. Computational schlieren (top half) and Mach number (bottom half) for progressing NPRs depicting shock structure.

the plug surface as shown later. This is typical of the free shock separation regime where the flow following the shock is separated from the nozzle wall and does not reattach. Another feature that can be discerned from the computational schlierens at

all NPR's is the presence of an expansion fan at the corner between the intersection of the subsonic contraction and the shroud. The shrouded plug nozzle considered here has a sharp change in slope at the throat as discussed with reference to Fig. 3.3.

The detail is seen more clearly in Fig. 3.10 showing near throat region. At all NPR's the flow over-expands just aft of the throat through this expansion fan. As the flow negotiates the sharp turn from the subsonic contraction to the diverging section it passes through the sonic condition and forms a small supersonic bubble at the throat. The flow compresses again in a short distance as it slows down within this small supersonic region. The flow then again expands finally to shock down in the diverging section. The impingement of the expansion fan on the plug surface causes a slight increase in pressure on the plug surface aft of the impingement location. Evidences of this expansion fan are present in all NPR solutions as well as in the static pressure distributions discussed later. The supersonic region near the throat would not have been present if the throat contour were gradually varying instead of containing a sharp corner.

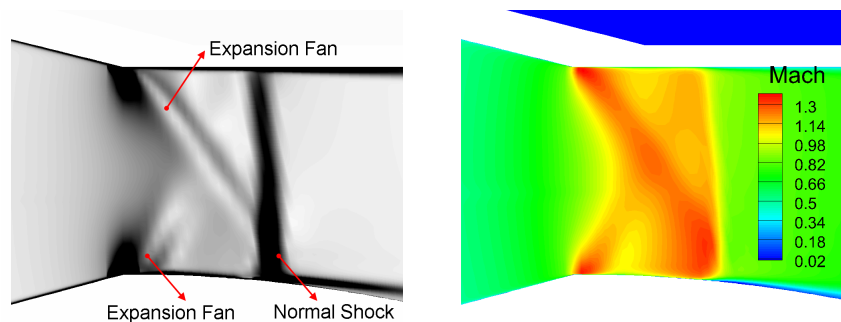


Figure 3.10. Near throat region computational schlieren (grayscale) and Mach number (rainbow) at $NPR = 1.26$.

Returning again to Fig. 3.9, results for the slightly higher NPR of 1.59 are shown in Fig. 3.9(b). The Mach number upstream of the shock reaches 1.44 and the flow undergoes shock-induced flow separation. At this point a weak lambda-shock pattern is observed to be developing as seen in the close-up view of the computational schlieren in Fig. 3.11 which shows only the near-shock region. The flow at the shroud separates

and reattaches immediately forming a small recirculation zone while the flow is fully separated over entire length of the plug. Also clearly seen in Fig. 3.11 is the expansion fan impinging on the plug.

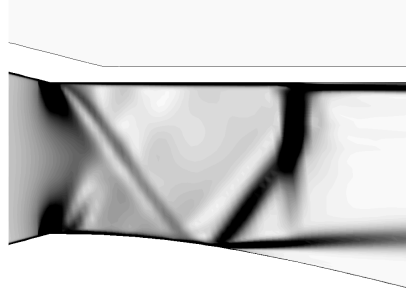


Figure 3.11. Computational schlieren showing lambda shock and expansion fan impinging on plug at $NPR = 1.59$.

For the $NPR = 1.93$ shown in Fig. 3.9(c) with a large local view in Fig. 3.12. Since the flow at the throat is indifferent of the NPR, the present close-up only shows the shock location. The shock structure generates a lambda pattern at the plug while a weak lambda pattern enclosing a recirculation zone is seen at the shroud surface. The shock is modified in the vicinity of the walls. The pressure rise at separation results in compression waves propagating in the supersonic part of the boundary layer. These waves coalesce into an oblique shock (the first part of the lambda) which intersect the shock at a triple point from which emanates the reflected shocks (second part of lambda). Stemming from the triple point, the oblique reflected shock fits the angle of the fluid downstream with the fluid aft of normal shock. The velocity difference between these zones generates a slip line that emerges from the triple point. Also notice the presence of weak shocks or shocklets in the region aft of the shock in the main stream. These weak shocks seem to be a manifestation of the natural converging-diverging passage formed downstream of the shock by the recirculation zone on the plug.

The shroud flow at this NPR is still attached with a small recirculation bubble just downstream of the shock. The shocks at these low NPR's are accompanied by

a relatively large recirculation zone on the plug. The nozzle is, therefore, still in the FSS regime.

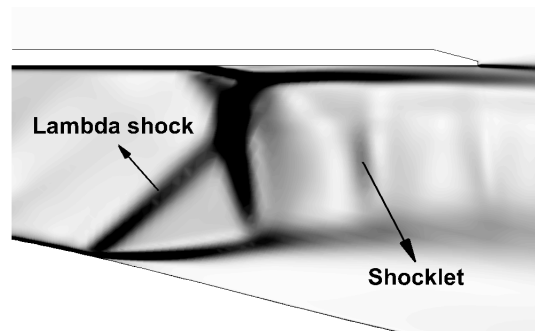


Figure 3.12. Computational schlieren showing lambda shock and shocklets in mean flow at $NPR = 1.93$.

For NPR's above 2.25 (Fig. 3.9(c) through 3.9(f)), the restricted shock separation is the mode of separation on the plug. In the mid-NPR range (2.25 to 3.1) a Mach reflection is present on both the plug and the shroud surfaces as seen in Fig. 3.9(d) for an NPR of 2.56 and in close view of Fig. 3.13(a). The computational schlieren show a shock/boundary layer interaction analogous to that observed in planar supersonic nozzles [15, 31]. The shock structure consists of oblique shocks starting from both the plug and shroud surfaces. These two oblique shock structures anchor a normal Mach stem in the mean flow and the shock structure exhibits Mach reflection [81]. The flow adjacent to the walls undergoes a considerable amount of turning with the Mach number upstream of the normal shock region being approximately 1.7 in this case. The separated flow on the plug reattaches downstream, thus, exhibiting a restricted-shock separation (RSS) character.

As the NPR is increased the length of the normal portion of the shock decreases until the oblique shocks from the shroud and plug occupy the entire cross section where they finally intersect and undergo a regular reflection [81] at a NPR of about 3.06 as shown in Fig. 3.9(e) and the close-up view of Fig. 3.13(b). The flow separates on the shroud surface and entrains ambient air.

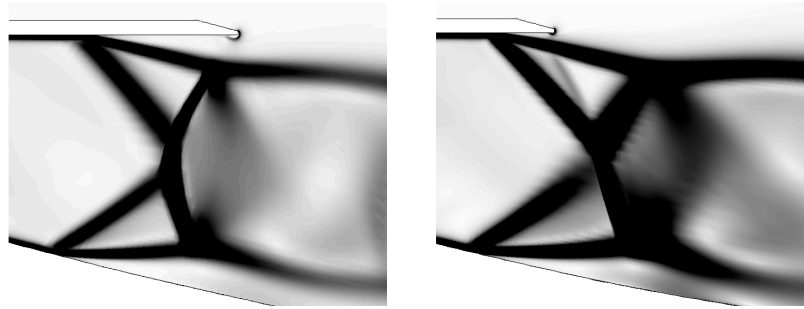


Figure 3.13. Computational schlieren showing Mach reflection at NPR = 2.56 (left) and regular reflection at NPR = 3.06 (right).

At NPR's above 3.1 the shock structure on the plug is similar to the shock/boundary layer interaction that is seen in oblique shocks incident on flat plates [82]. The incident oblique shock at these NPR's is generated close to the shroud surface tip with the flow on the shroud still separated. The turbulent boundary layer on the plug surface is distorted as it sees an adverse pressure gradient across the incident oblique shock. These distortions are propagated upstream through the subsonic boundary layer which separates ahead of the shock. A separation shock exists at the separation point. The shock pattern on the plug surface encloses a recirculation bubble.

At a nozzle pressure ratio of about 4.0, the shroud shock moves to the end of the shroud and there appears to be no separation from the shroud at this condition. The oblique shock emanating from the end of shroud now travels across the entire stream. It is incident on the recirculation bubble adjacent to the plug surface while the separation shock from the plug surface hits the free shear layer outside the nozzle. The oblique shock continues to move downstream as the NPR is increased enclosing a recirculation zone that continues into the wake of the plug.

Increasing the NPR to 5.01 continues to weaken the separation shock (Fig. 3.9(f)). Figure 3.14 shows a close-up view of the plug exit region for an NPR of 5.01 with the shock structure showing the incident and reflection shock.

A conventional plug nozzle (without an external shroud) primarily achieves expansion to ambient conditions by means of a centered expansion fan generated at the

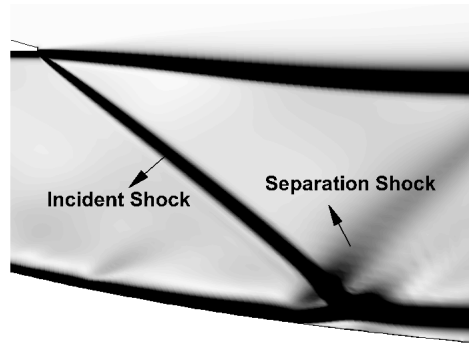


Figure 3.14. Computational schlieren showing oblique shock from shroud tip impinging on plug surface at $NPR = 5.01$.

nozzle tip under quiescent ambient conditions. At design conditions the flow expands to ambient conditions with the expansion fan terminating at the plug tip (Fig. 1.1). At NPR's below design the expansion fan hits at shorter distances on the plug and reflects as a compression wave. The compression wave in turn reflects as an expansion fan from the free stream. This expansion/compression continues till the plug end. It is important to note that in the shrouded case unlike an expansion fan emanating from the throat of a conventional plug nozzle an oblique shock emanates from the shroud tip of the shrouded plug nozzle. The shrouded plug nozzle does not exhibit the interaction with the ambient that is seen in a conventional plug nozzle at NPR's below design. The oblique shock traverses downstream as the NPR is increased until it eventually ceases to exist with only a shroud tip Mach wave at the design $NPR = 6.23$ as was shown previously in Fig. 3.8 remains. The shrouded plug nozzle, therefore, behaves as a conventional plug with a Mach wave at the exit plane only at its design point.

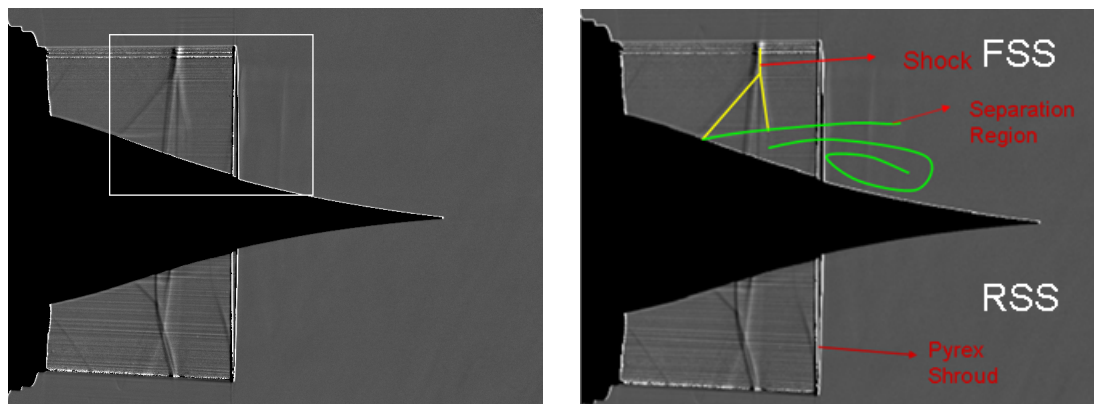
3.4.2 Computational Vs. Experimental Shock Pattern

The above discussion gives an overall view of the motion of the shock structure as the nozzle pressure ratio is increased from low to high values. Now, we compare the predicted shock patterns at specific NPRs with observed shock patterns taken from

the experimental schlieren and shadowgraphs at similar NPRs. An important consideration to bear in mind in the comparisons as well as in the interpretation of the experimental images is that the experimental images contain information corresponding to the three-dimensional (axisymmetric) character of the flow. The experimental images are generated by the integral of the first derivative (schlieren) or second derivative (shadowgraph) of the density along the light path as it passes through every radius along a particular line of sight. Therefore, they collapse the three dimensionality of the flow onto a 2D plane. In contrast to this, the computational schlieren images are taken in a two-dimensional sense with the incident light rays propagating through only a single plane of the axisymmetric solution. The comparisons in this section are all for cold flow conditions with equal stagnation temperatures in the core and fan streams.

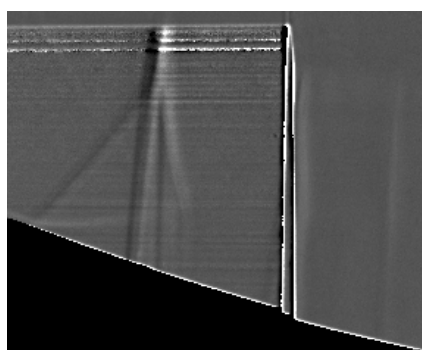
The first comparison is shown Fig. 3.15 for an experimental shadowgraph at NPR = 2.14 and a computational schlieren at a NPR of 2.11. The experimental results are given twice. The photograph on the top left shows the original shadowgraph, while the one on the top right shows the same shadowgraph with some characteristic flow features superimposed to enhance understanding. These experimental shadowgraphs were taken through the pyrex glass shroud so that a larger portion of the flow in the divergent section could be seen. Note that the outline of the pyrex shroud is clearly seen in the shadowgraph. Because of the pyrex shroud, these shadowgraphs can only be obtained for cold flow (the fan temperature equal to the core temperature). The schlieren and the shadowgraph images can be compared with regard to shock structure as both replicate it in a similar fashion.

Looking first at the experimental shadowgraph image in Fig. 3.15(a) with the aid of the graphical interpretation in the photo to the right, the presence of an oblique shock emanating from the plug can be clearly seen. This shock causes the boundary layer to separate from the plug surface (note the faint horizontal line on the upper surface of the plug). After leaving the plug surface, the shock propagates across

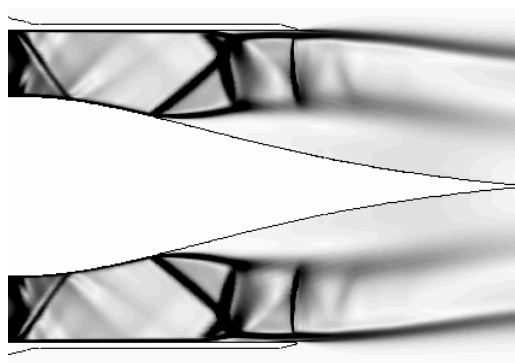


(a) Experimental Shadowgraph

(b) Experimental Shadowgraph with schematic



(c) Shadowgraph view of rectangular region marked in (a)



(d) Computational schlieren

Figure 3.15. Computational schlieren compared to experimental Shadowgraph at $NPR = 2.11$.

the annulus and intersects the inviscid shock. The inviscid shock moves toward the shroud surface where it forms a lambda shock.

A similar oblique shock and separation region on the plug surface can be seen in the computational schlieren on the bottom of Fig. 3.15. One difference between the two results is that the experimental image shows a distinct vertical line between the two legs of the lambda shock that is not present in the computation. This additional line, however, is the foot of the circular shock leg on the circumference of the pyrex

shroud that has been collapsed onto a line in the 2-D plane and is an artifact of the 3-D image, not a feature of the flowfield.

The computational schlieren also shows a secondary shock just downstream at the end of the shroud that, at first appearance, does not appear to be present in the experimental image. Close inspection of the enlarged portion of the experimental shadowgraph in Fig. 3.15(c) showing a close up of the flow field marked by a rectangle in Fig. 3.15(a), however, also reveals the presence of a secondary shock in the upper half plane at nearly the same axial location at the end of the shroud. The close-up shows both the shock in the diverging section and the secondary shock just downstream of the exit. Also the computational schlieren shows the presence of separation off the shroud which cannot be distinguished in the experimental shadowgraph. However, the separation wake can be seen in the experiments as well as the computations. Overall, the computational visualizations agree well with the experimental images and the characteristics described by both the experiment and the computation are indicative of the flow characteristics that are observed at these low NPR's.

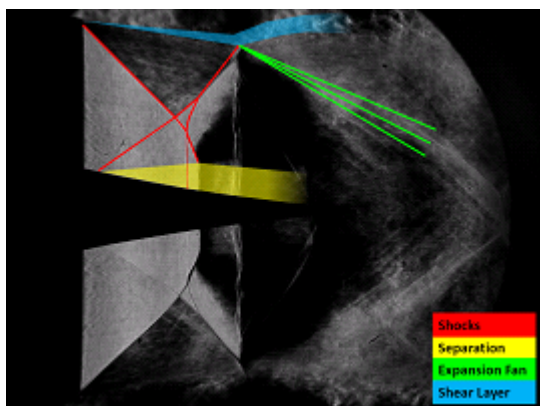
Finally, note that the upper and lower halves of the experimental shadowgraph exhibit differences suggesting the presence of a weak three-dimensionality in the flow at this NPR. As discussed later, this particular NPR of 2.11 lies in the transition from FSS to RSS. In the shadowgraph picture above it appears that the upper half of the nozzle is in the free shock separation regime whereas the lower half is in the restricted shock separation regime. This asymmetrical flow separation has been observed during the transition regime [33]; [83] in experiments on rocket nozzles and has been studied extensively [31]; [34]; [83] as it is considered to be responsible for the side-loads on nozzles. The axisymmetric computations clearly cannot replicate this non-symmetric effect but are still helpful in predicting the character of the flow as well as in understanding the flow physics. Capturing the asymmetric features at these NPR's requires 3-D computations which are discussed later. In the case of the supersonic shrouded plug nozzle this asymmetry seems to exist only in this narrow range between 2.0 and 2.25 where the transition occurs. This will be confirmed later

from the experimental static pressure distributions and dynamic pressure data which are analyzed in the following sections.

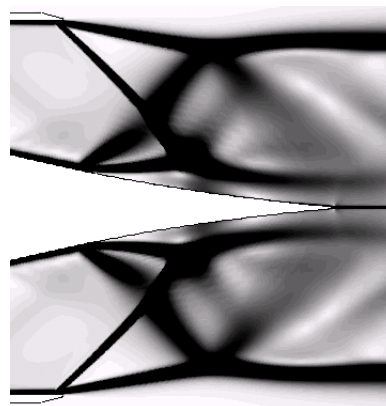
Figure 3.16 provides a similar comparison of computation and experiment at a higher NPR of 3.73 to show the manner in which the shock structure and flow separation regions compare. These results are again for cold flow. In contrast to the previous figure, the experimental results in Fig. 3.16 are schlieren images taken with both horizontal and vertical knife edges at the same conditions. The photograph in the upper left of Fig. 3.16 corresponds to the vertical knife edge orientation while that for the horizontal knife edge orientation is seen in the lower two photos. Note that these schlieren images are taken with a metal shroud so that only the portion of the flowfield outside the shroud can be seen in the experimental images.

The vertical knife edge results in schlieren that is very clear and is nearly symmetric from top to bottom. A schematic of the shocks, expansion fans, separation regions and shear layers is superimposed on the top half of the photo while the lower half is left untouched to provide an unobstructed view of the photo. The schlieren with the horizontal knife edge is somewhat less distinct, so the complete photo is shown on the lower left, and is then again repeated on the lower right with the flow characteristics superimposed for interpretative purposes. Again, the comparison between the computational schlieren and the experimental schlieren images shows a close resemblance at this higher nozzle pressure ratio. Though it is not evident in the schlieren images, the flow reattaches on the plug implying that the flow exhibits a restricted shock separation.

In the schlieren images from the experiments the orientation of the knife-edge determines the direction in which the density gradients are captured. The schlieren with the vertical knife-edge (upper left of Fig. 3.16) captures horizontal gradients and clearly shows the incident and separation shocks. The schlieren with the horizontal knife edge (lower photos in Fig. 3.16) depicts vertical gradients and also captures the recirculation zone created by the plug shock. The horizontal knife-edge schlieren also shows the presence of a shear layer emanating from the shroud tip and the separation



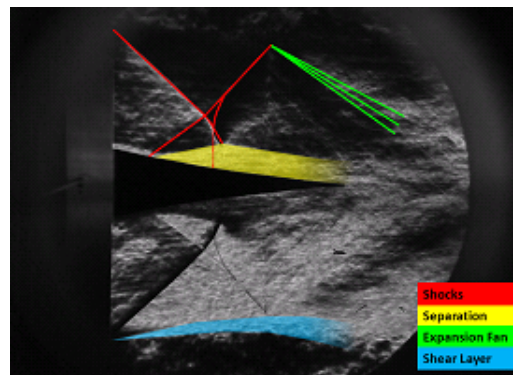
(a) Experimental schlieren with schematic depicting $\partial\rho/\partial x$.



(b) Computational schlieren.



(c) Experimental schlieren depicting $\partial\rho/\partial y$.



(d) Experimental schlieren with schematic depicting $\partial\rho/\partial y$.

Figure 3.16. Computational schlieren compared to experimental schlieren at $NPR = 3.73$.

shock reflecting as an expansion fan at the free surface. The computational schlieren clearly replicates these salient flow features. Another important observation that can be made from the experimental schlieren is the axisymmetric nature of the shock justifying the use of axisymmetric computations to accurately predict flow physics.

3.4.3 Pressure Distribution

The use of both experimental as well as computational results helped in obtaining an understanding of the associated shock physics at various NPR's. In particular, the presence of free shock separation and restricted shock separation regimes were recognized. The shock structure towards the high end of the NPR spectrum showed an oblique shock impinging on the plug surface. In order to further confirm these flow regimes it is instructive to look at the static pressure distributions on the plug as well as the shroud surface. As seen earlier in Fig. 3.4, the experimental set-up had the facility to measure static pressures at three azimuthal locations of 45° , 135° and -90° to the vertical, looking counter-clockwise from upstream of the nozzle. This allowed for a reasonable resolution of any three-dimensionality in the tangential direction. The row of static pressure probes at 45° azimuth had the maximum number of static pressure probes with 0.5 inch resolution on both the shroud and plug surfaces. Figure 3.17 shows the static pressure distribution obtained from the experimental data at a low (1.26, Fig. 3.17(a), 3.17(b)), moderate (2.56, Fig. 3.17(c), 3.17(d)) and a high (5.01, Fig. 3.17(e), 3.17(f)) NPR. These correspond to the free shock separation, restricted shock separation and shroud tip shock separation regimes outlined in the previous section respectively. The left row of figures is for the plug and the right row is for the shroud. The x -axis has been non-dimensionalized by the length of the plug from the throat to the tip with $x/L_{plug} = 0$ as the throat. The pressure has been non-dimensionalized with the total pressure upstream. The plots for both the shroud and plug show a fairly axisymmetric flow structure except for minor variations close to the shock. Thus, it seems reasonable to use axisymmetric computations to understand the global nature of shrouded plug nozzle flowfields. The pressure probe at the throat in the -90° azimuthal direction shows a comparatively lower pressure than the pressure probe at 45° which is directly in the wake of one of the struts.

It is evident from the plots that some of the details cannot be discerned by looking at them alone. In fact the drop in pressure below ambient at the throat is not entirely

clear without the help of internal flow measurements. Note that the fourth pressure tap from the throat at the $x/L_{plug} = 0.18$ position in the NPR of 2.56 and 5.01 cases (Fig. 3.17(c) and Fig. 3.17(e)) appears to have malfunctioned. It shows an increase in pressure instead of monotonic decrease from the throat till the shock due to expansion. The computations, however, show a strong local pressure excursion at the throat as well as the increase in pressure at $x/L_{plug} = 0.18$. Detailed analysis of the computations show that this pressure excursion is real at the throat and that it arises as the result of the corner in the plug shown in Fig. 3.8(c). This scenario shows that accurate computations help explain the physics and interpret the experimental methodology.

The series of figures, Fig. 3.18 to Fig. 3.20 show the plot of predicted static pressure distribution on the shroud and plug surface compared to the measured data. Also shown in the plots are the computational schlieren from steady computations in order to correlate the shock physics with the static pressure distribution. The throat is located at $x/L_{plug} = 0$ and the pressure and the y and x co-ordinates have been scaled by the upstream total pressure and the plug length, respectively.

As the nozzle exhibits a multitude of shock structures and separation regimes with increasing NPR, it is important that the ability to predict the static pressure be quantified for the entire range. Hence, the figures show a progression of NPRs compared to data. In Fig. 3.18 all the NPR's shown correspond to that of the free shock separation regime for NPR's below 2.0. The shock transitions from a normal shock at NPR of 1.26 to a lambda shock at NPR of 1.93. First, looking at the NPR of 1.26 plot for the plug we notice a dip in static pressure at $x/L_{plug} = 0.1$ which lies in between two data points. The flow then expands to form a shock after which the static pressure rises monotonically. The two data points lie on the predicted pressure distribution giving credence to the predictions. This dip in pressure would not be recognized if the data were (Fig. 3.17(a)) analyzed independently.

For the free shock separation regime at the low NPR end the results show an increase in the static pressure distribution aft of the shock. The pressure increases

monotonically both on the shroud as well as the plug surface. It may be noted that the pressure at the plug throat is below 0.528 times the inlet total pressure indicating the presence of the supersonic region following the expansion fan at the throat. This was discussed earlier in context with the shock structure occurring due to the sharp corner at the throat. Also evident in the static pressure distributions is the slight increase in pressure when the expansion fan formed at the throat hits the plug at $x/L_{plug} = 0.1$. An experimental data point at the peak of the pressure rise (Fig. 3.18(c) and Fig. 3.18(e)) further confirms its presence. Also the same increase in pressure is seen on the shroud surface both from the experiments as well as the computations. The static pressure distribution is close to the measured data at all three NPRs in Fig. 3.18 both on the plug and shroud surface. The shock position has been captured accurately and the rise on pressure aft of the pressure predicted accurately for all NPRs. The separation region length which extends over the entire plug after the shock is also predicted accurately. It appears though that the static pressure is over predicted by a few percent in the recirculation zone.

Figure 3.19 shows pressure distribution in the restricted shock separation regime for NPRs 2.23, 2.56 and 3.06. At these nozzle pressure ratios the shock transforms from a Mach reflection into a regular reflection mode as seen earlier. In the case of RSS regime, the pressure rises aft of the first leg of the lambda shock and then forms a plateau which ends when the reflected shock, the second leg of the lambda shock hits the recirculation bubble. Immediately after this the pressure increases till the reattachment point and then monotonically decreases as the flow expands downstream of reattachment. For example, in the case of $NPR = 3.73$ the pressure forms a plateau after the shock till the oblique shock hits the recirculation bubble ($x/L_{plug} = 0.75$), then continues to increase till the reattachment point ($x/L_{plug} = 0.85$) and then decreases downstream of reattachment. The computed static pressure distribution is very close to the data. Again at all the NPR's shown the shock location is predicted accurately. The static pressure distribution on the shroud surface is also similar to the experi-

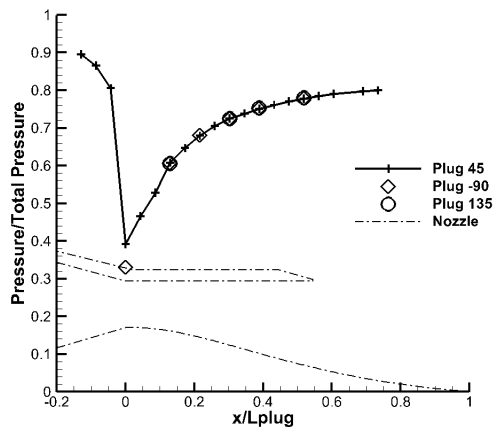
ments. The static pressure increases aft the shock on the shroud as long as the shock remains upstream of the shroud tip.

In the final figure of the series, Fig. 3.20, the two NPR's shown exhibit shock structure similar to oblique shock reflection on a flat plate [82]. In the present case the oblique shock formed at the shroud tip reflects of the plug surface. The pressure on the plug in this cases decreases as the flow expands in the diverging section before rising aft of the reflection shock. As in the previous case the pressure plateau exists till the oblique shock impinges on the recirculation bubble. At both the NPR's shown the predicted pressure distribution matches exactly with the data in predicting the shock location and extent of the recirculation bubble.

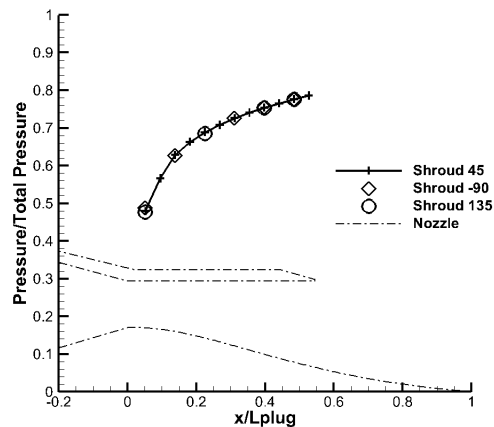
For all NPRs above 2.0 and between 2.25 for cold core flow the experiments showed a step change in the evolution of the static pressure on the plug as well as the shroud surface. This can be seen when we look at the wall pressure data for experiments corresponding to NPR of 2.04 with cold core flow as an example. Figure 3.21 shows the NPR variation during the course of the experiment as well as the plug and shroud wall pressure evolution. The observation window for which the static pressure is plotted is shown in Fig. 3.21(a). The figure also shows a schematic of the plug and shroud along with the position of static pressure probes at the 45° azimuthal position. Each static pressure probe is identified by a colored diamond with the corresponding color for the pressure plot. The static pressure probes for show a step change in the pressure corresponding to the FSS/RSS transition. The FSS/RSS transition has been observed in experiments earlier[38, 41, 42] with nozzles for rocket applications. In earlier work it was noticed that when the NPR is increased during the experimental run the FSS/RSS transition occurred and when the NPR is reduced from a higher value, the RSS/FSS transition was observed. This indicated the presence of a hysteresis regime in the transition. In the present case the mass flow rate was increased to achieve the required NPR, held constant to obtain the data and then the mass flow rate cutoff abruptly (as shown in Fig. 3.21(a)). Hence, the FSS/RSS transition could be observed but the RSS/FSS transition is not clearly captured. Nevertheless, it can

be assumed that present nozzle also shows the hysteresis effect as is the case with supersonic nozzles. Also of interest is that the transition event occurs simultaneously at the shroud and the plug. This shows that it is associated with the entire shock front and not necessarily a local phenomenon in which the flow on the plug alone reattaches after transition. An analysis of the experiments showed that the FSS/RSS transition also occurred in the NPR range 2.0-2.25 for the experiments.

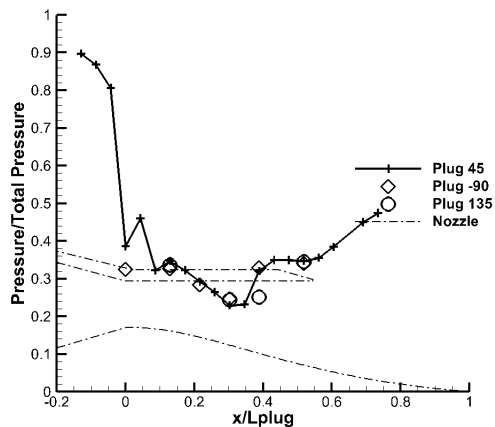
In Figs. 3.21(d) and 3.21(e) the wall pressure measured at the three azimuthal locations on the plug wall before and after the transition for NPR of 2.04. Also shown in the figure is the prediction from the computations which agree with the FSS regime. Figure 3.21(d) shows that the flow is axisymmetric just before the transition. Figure 3.21(e) which is after the transition event shows that the flow is separating asymmetrically. The axisymmetric assumption allows the FSS regime to be captured as seen in Fig. 3.21(f). The steady computations were unable to predict any hysteresis but only showed the shock transitioning into the RSS regime at about a NPR of 2.15. Thus it seems that in order to better understand the hysteresis regime complete 3-D computations are required in the NPR range of 2.0 to 2.25 where the transition occurs. The axisymmetric computations still help in understanding the shock structure in major part of the NPR spectrum where the flow is axisymmetric.



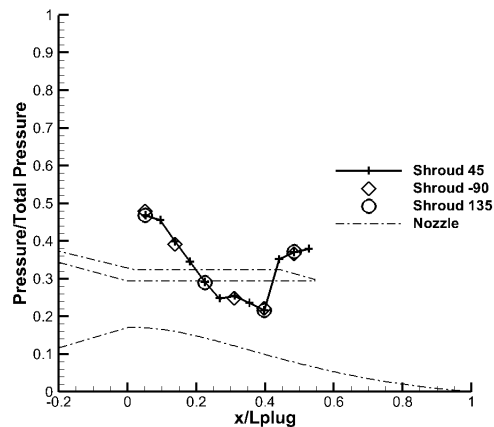
(a) NPR = 1.26, Plug.



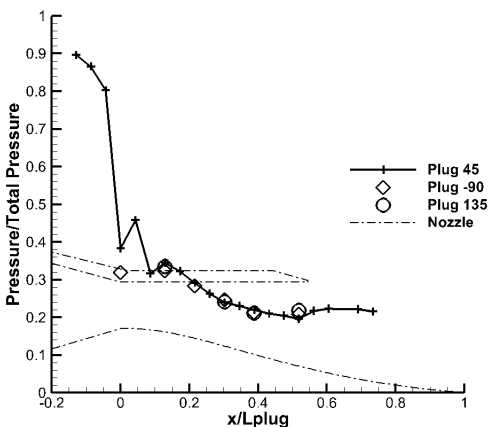
(b) NPR = 1.26, Shroud.



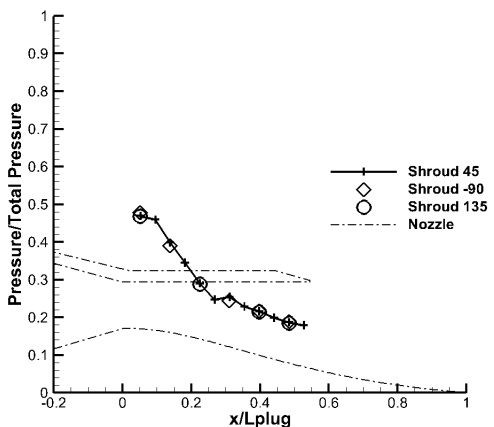
(c) NPR = 2.56, Plug.



(d) NPR = 2.56, Shroud.

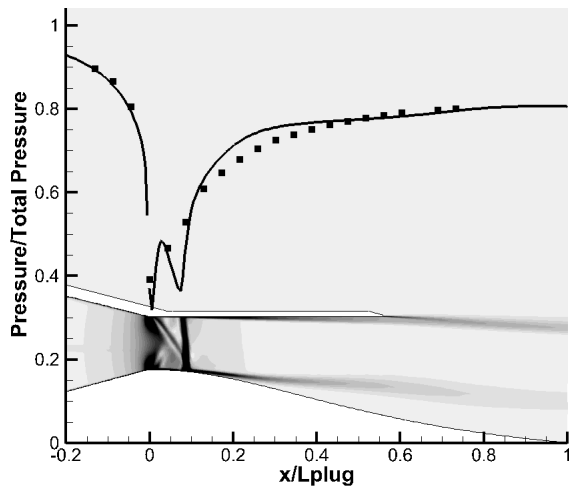


(e) NPR = 5.01, Plug.

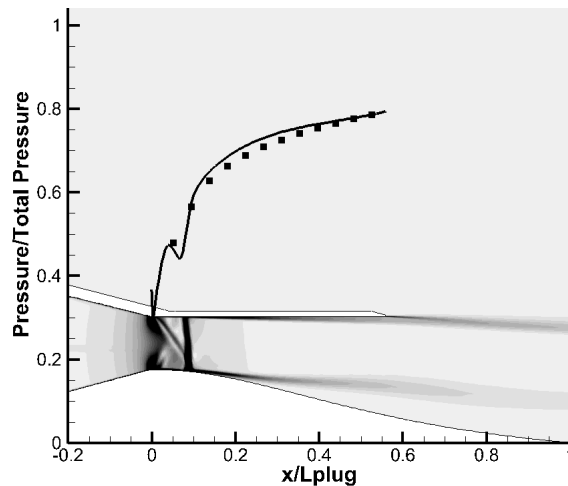


(f) NPR = 5.01, Shroud.

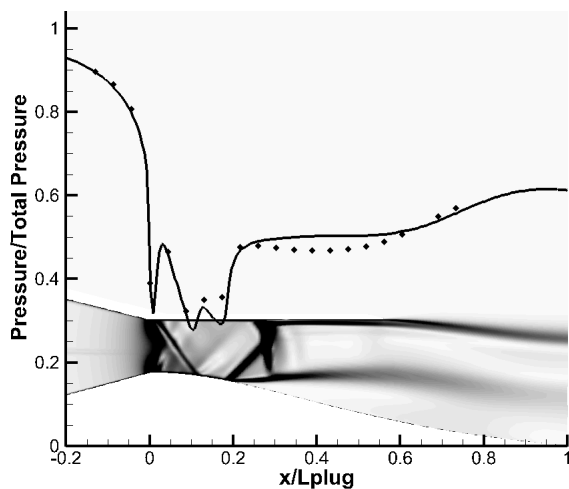
Figure 3.17. Normalized Static Pressure from data showing axisymmetry.



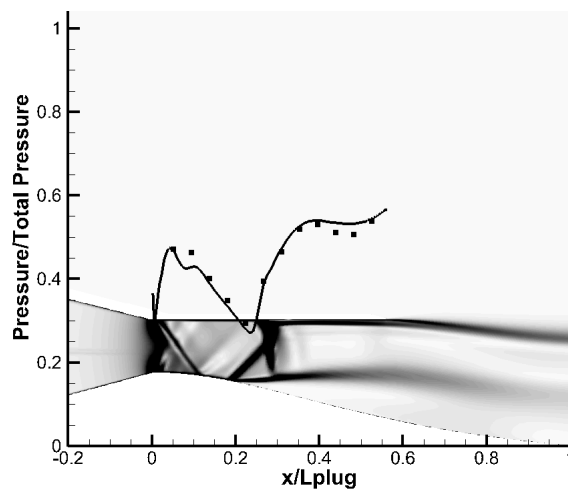
(a) NPR = 1.26, Plug.



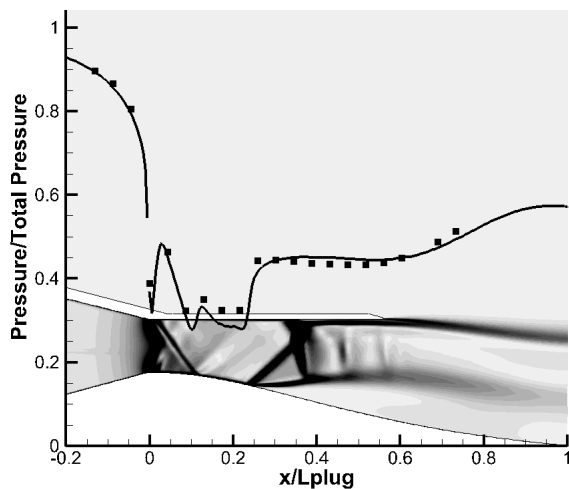
(b) NPR = 1.26, Shroud.



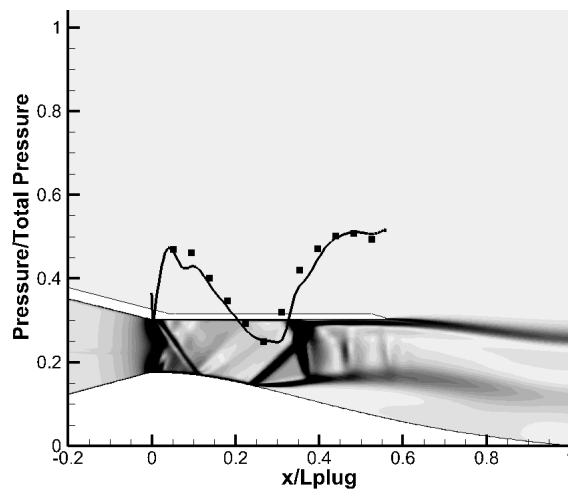
(c) NPR = 1.76, Plug.



(d) NPR = 1.76, Shroud.

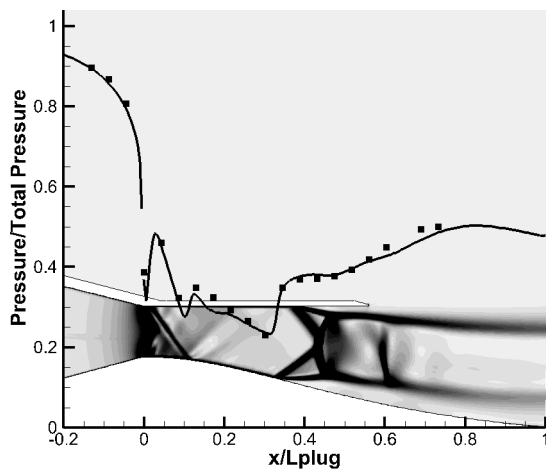


(e) NPR = 1.93, Plug.

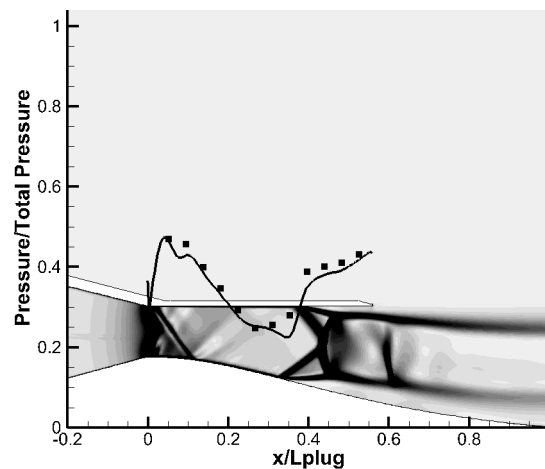


(f) NPR = 1.93, Shroud.

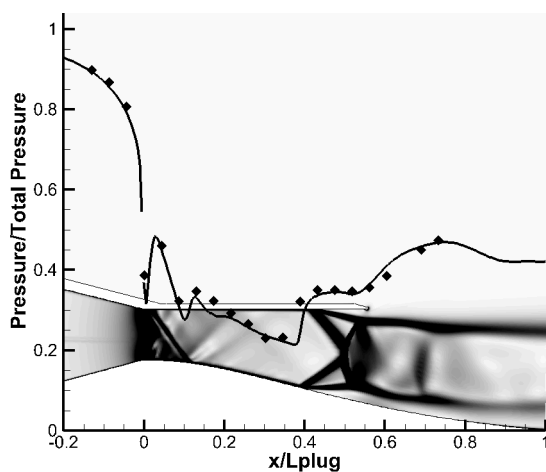
Figure 3.18. FSS normalized Static Pressure distribution on plug and shroud superimposed on computational schlieren, line - computations, square - experiment data point.



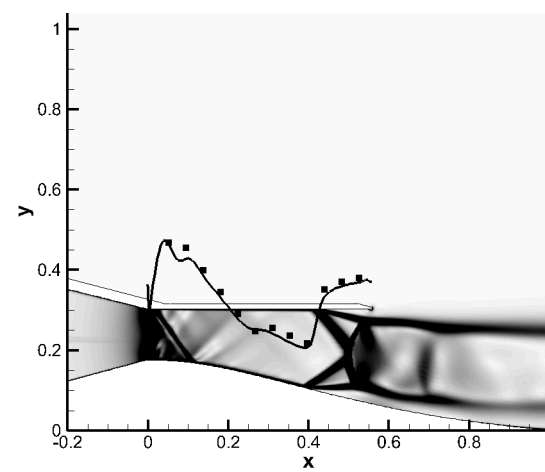
(a) NPR = 2.23, Plug.



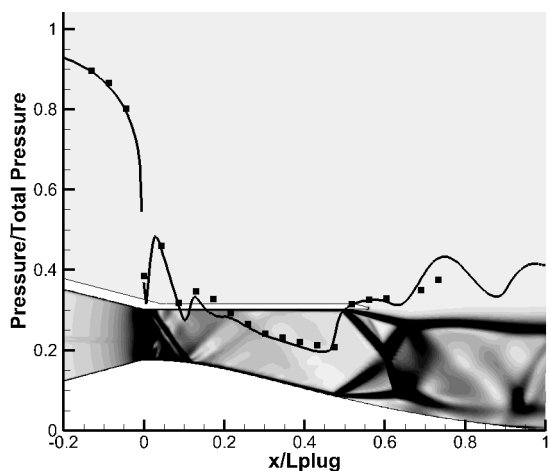
(b) NPR = 2.23, Shroud.



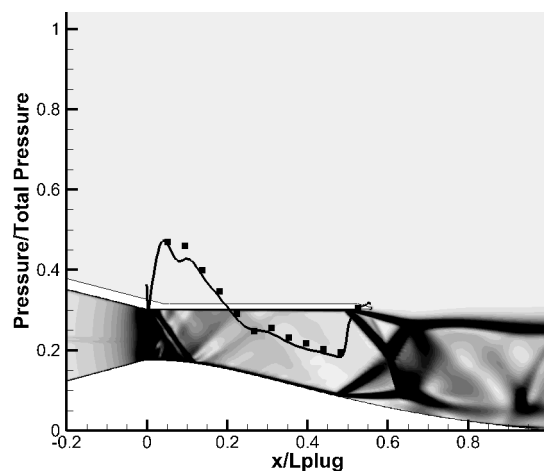
(c) NPR = 2.56, Plug.



(d) NPR = 2.56, Shroud.

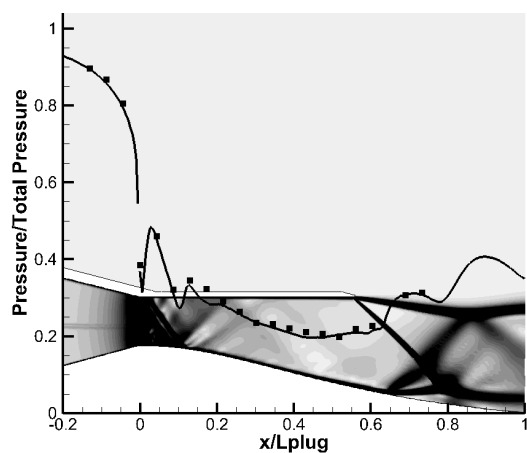


(e) NPR = 3.06, Plug.

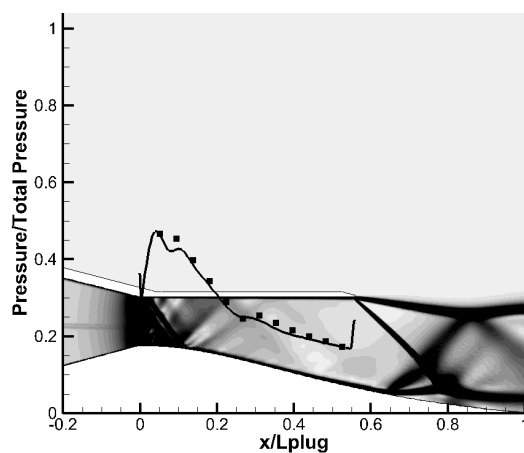


(f) NPR = 3.06, Shroud.

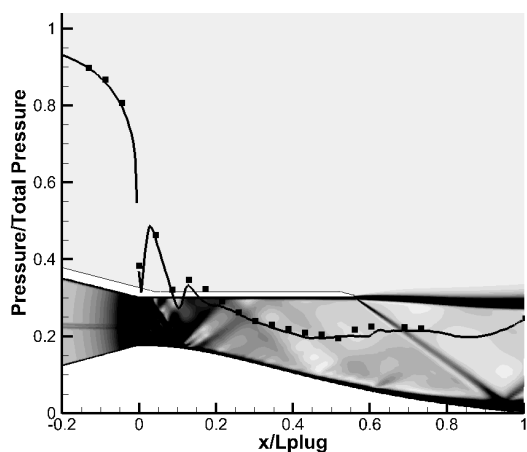
Figure 3.19. RSS regime normalized Static Pressure distribution on plug and shroud superimposed on computational schlieren, line - computations, square symbol - data point.



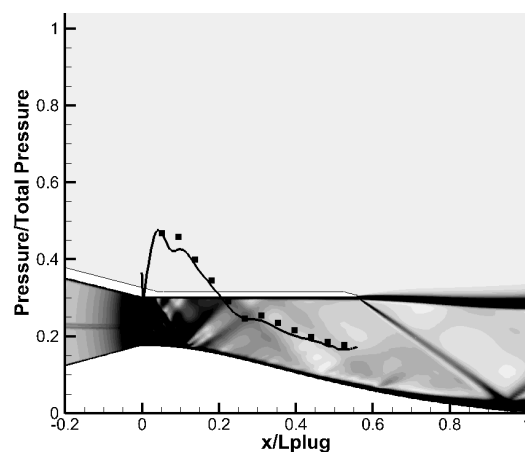
(a) NPR = 4.01, Plug.



(b) NPR = 4.01, Shroud.

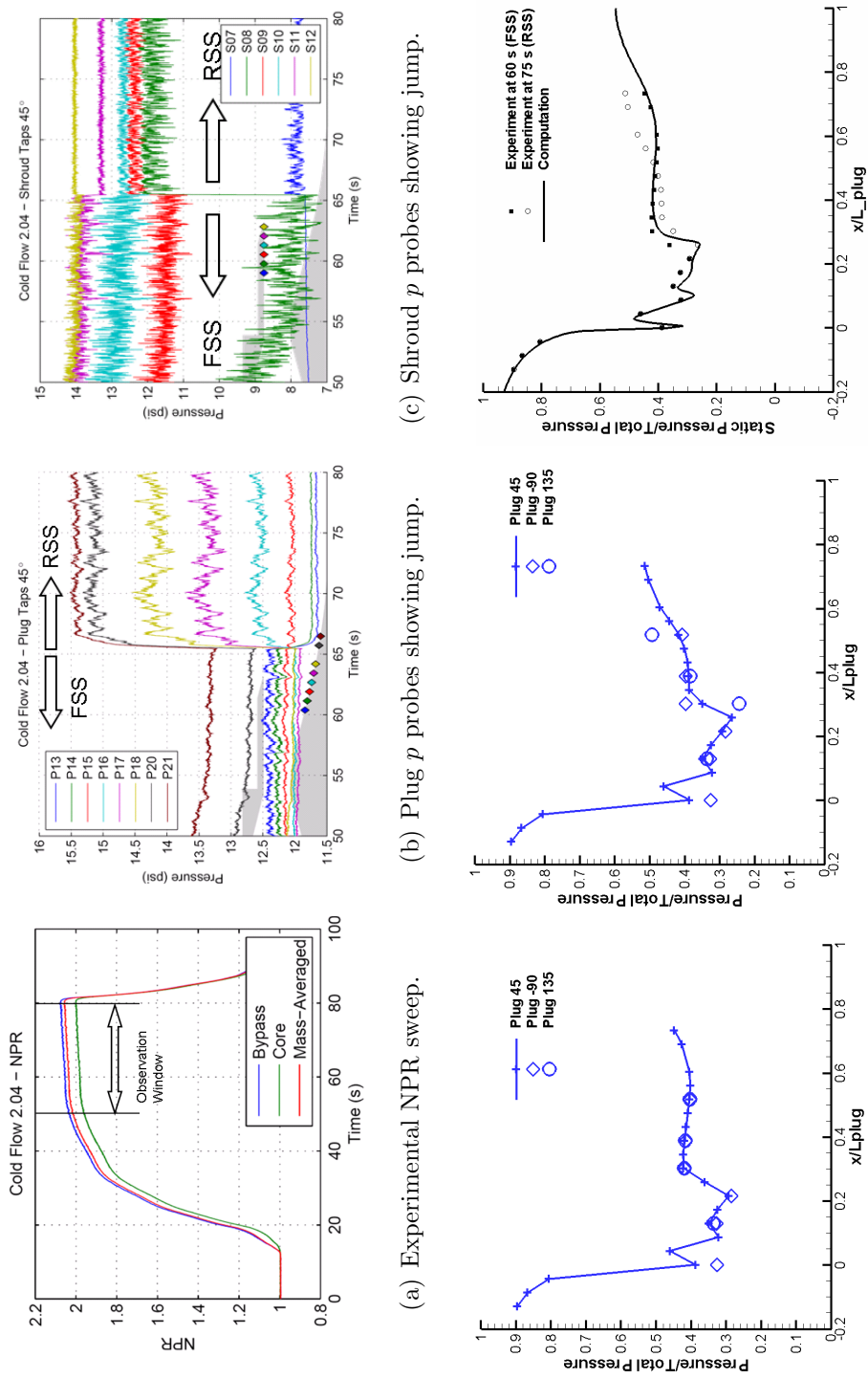


(c) NPR = 5.75, Plug.



(d) NPR = 5.75, Shroud.

Figure 3.20. Oblique shock regime normalized Static Pressure distribution on plug and shroud superimposed on computational schlieren, line - computations, square - experiment data point.



(a) Experimental NPR sweep.

(b) Plug p probes showing jump.

(c) Shroud p probes showing jump.

(d) Pressure dist. on plug before jump.

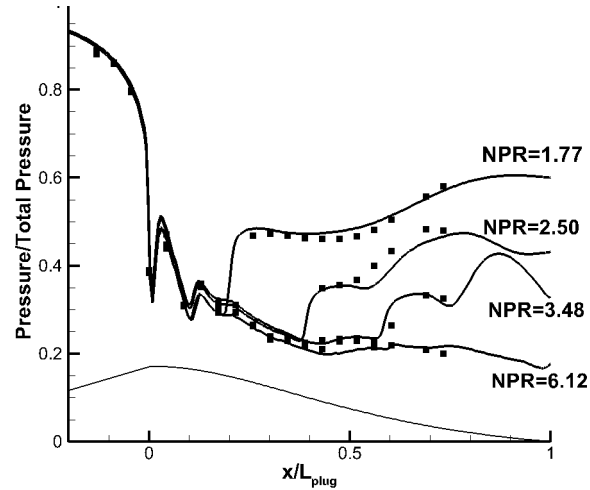
(e) Pressure dist. on plug after jump.

(f) Pressure predicted Vs. data.

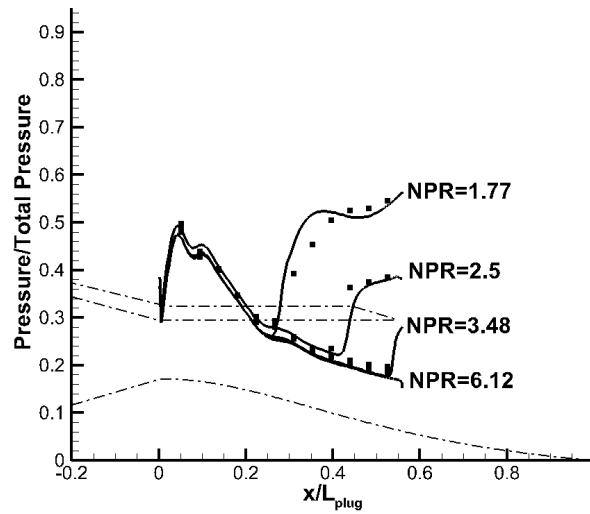
Figure 3.21. Static pressure on plug and shroud exhibits sudden jump at NPR of 2.04 due to transition from FSS to RSS.

Figure 3.22 shows the static pressure distribution on the plug and the shroud surfaces for hot core flow from steady computations as the NPR progresses. The plots also show the experimental pressure distributions obtained through static pressure taps located axially along the plug and shroud at the 45° azimuth which provided the best resolution. Also shown in the plots are the schematic of the shrouded plug nozzle with dash-dot lines for reference. The progression of shocks is seen as the NPR is increased. The axisymmetric computations predict the shock location on the plug as well as the shroud accurately. Also the static pressure distribution matches closely with the experimental observations at all NPR's. However, the predicted static pressures in the FSS regime at low NPR's are higher than the experimentally observed values. At moderate and higher NPR's ($\text{NPR} > \sim 2.25$) where the restricted shock separation regime sets in, the predicted values are close to the experimentally observed results. From the plots it can be seen that the static pressure distributions are those of the FSS regime till a NPR of 2.11 and thereafter show the RSS pressure distribution when the recirculation zone reattaches on the plug, thus confirming the observations made earlier on the shock structure at various NPR's using experimental and computational schlieren. For hot core flows the shock location is downstream of the cold flow case at the same NPR. In the case of hot flows the issuing gases from the core have lower ratio of specific heat (1.33) compared to the cold flow case (1.4).

Earlier the presence of secondary shock or shocklets was observed in the comparison of schlieren and shadowgraph at NPR of 2.11 in Fig. 3.15. These shocklets appear as normal shock across the entire flow cross section in the Schlieren. Again these normal shocks are a manifestation of the three-dimensional nature of the schlieren photographs. The discussion with reference to Fig. 3.9(c) that these secondary structures are due to the converging diverging passage created by the separation zone on the plug surface. The same can be discerned by comparing the pressure distribution at the horizontal centerline at the plug nozzle. In Fig. 3.23 the pressure distribution and the Mach number along the centerline are shown. At a NPR of 1.76, there is a weak shock after the normal shock. For $\text{NPR} = 1.93$, the static pressure and the



(a) Plug (line - comp., symbol - expt.)

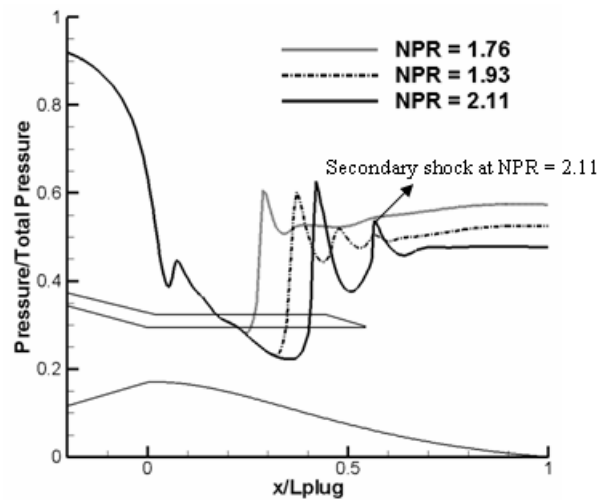


(b) Shroud (line - comp., symbol - expt.)

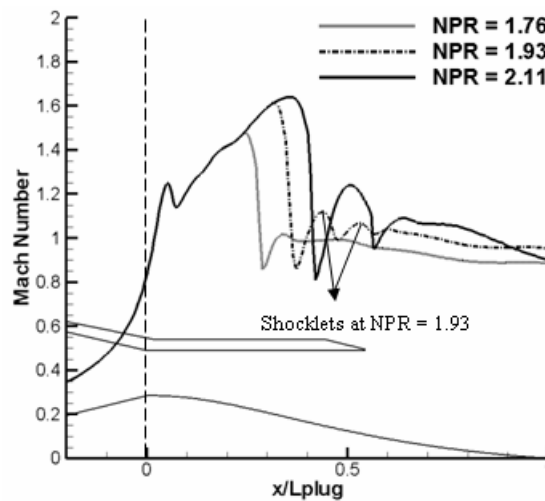
Figure 3.22. Normalized Static Pressure distribution for hot core flow with varying NPR.

Mach number show two distinct peaks with the Mach number going above 1, showing the presence of two weak shocks after the strong shock. As the NPR is increased to 2.11, a second distinct peak in Mach number of about 1.2 shows the presence of a secondary shock in the mean flow. As pointed out earlier, in the case of $NPR = 1.93$ the flow on the shroud is attached whereas at $NPR = 2.11$ the shroud flow is

separated constricting the mean flow area further and thereby resulting in a stronger shock.



(a) Mach number at centerline



(b) Pressure at centerline

Figure 3.23. Mach number and pressure at constant radius location passing through the center of the throat.

3.5 Unsteady Characteristics

The experimental data in conjunction with the steady computational results have been able to explain the flow regimes observed in the shrouded plug nozzle. In particular, comparison of the experimental and computational flow structures by means of schlieren and shadowgraphs shows that good agreement can be obtained through axisymmetric computations. The steady pressure agreement with data further confirm the effectiveness of axisymmetric computations. A dominant shock turbulent boundary layer interaction is present in the entire operating regime except at design conditions. The interactions of shocks with a turbulent boundary layer results in a temporally varying pressure on the adjacent surfaces [27]; [26]. The unsteadiness is primarily driven by shock oscillations in the diverging section and has been observed in experiments with transonic diffusers [21]; [25] with shock/boundary layer interaction at subsonic NPR's. In literature the shock oscillations have been attributed to multiple mechanisms as discussed in the introduction.

In this section we perform preliminary computations to assess the capabilities of axisymmetric unsteady simulations in predicting the pressure oscillations in the nozzle. In doing so we form the basis for unsteady analysis of the complete geometry in the coming sections. As will be seen in the following discussion, the peak frequency of pressure oscillations is a constant for NPR's which fall in the FSS regime. Accordingly, the axisymmetric unsteady computations are performed at a single NPR of 1.59 to verify if the simulations can make accurate predictions. The section begins by discussing the Kulite data obtained from experiments. This discussion is included here to extend the discussion in Tapee [40] where the trend was stated. As will be shown, it is possible to do this before discussing unsteady computations in lieu of what has been discussed in the previous section with regard to shock physics and steady pressure distribution on the plug. Following this discussion the results from the unsteady computations are presented.

3.5.1 Analysis of Experimental Data

The experimental set-up had three Kulite high-frequency absolute pressure transducers on the aluminum shroud as shown in Fig. 3.4. These transducers sampled the pressure on the shroud surface at 20 *kHz*. The resulting high-frequency data was studied for its frequency content by a power spectral density (PSD) obtained by means of Welch's method, which is based on the periodogram estimate and a strategic use of windowing functions. The PSD is an estimate of the power carried by the pressure wave per unit frequency. Figure 3.24 shows the PSD estimate at six NPR's for cold core flow run of the nozzle. The PSD of all three Kulite pressure transducers at the corresponding NPR is shown in the same plot. The positions of the Kulite on the shroud were discussed with reference to Fig. 3.4. Briefly, Kulite 01 is located at $x/L_{plug} = 0.18$ and Kulite 02 and 03 are located at the same axial location of $x/L_{plug} = 0.4$. Kulite 02 and 03 are, however, separated azimuthally by 90°.

A most important parameter in understanding the meaning of the Kulite signal is an assessment of whether they are upstream or downstream of the shock location on the shroud. The location will determine if the Kulite will experience the unsteadiness observed in recirculation zones downstream of the shock location. For the NPR's shown in Fig. 3.24, the shock location relative to the Kulite locations is shown in Fig. 3.25. The nozzle schematic normalized by the plug length is shown as a schematic. The black diamond indicates the shock location for the NPR it is associated with and indicated in the figure. The red triangle symbols indicate the position of the Kulites on the shroud.

For NPR of 1.26 from Fig. 3.25, it is seen that the three Kulites are all downstream of the shock in the recirculation zone. Looking at the PSD in Fig. 3.24(a), we notice that for all three Kulites at NPR of 1.26 the dominant tone occurs at 170 *Hz*. The same peak frequency for all Kulites indicate that the pressure oscillation is independent of axial location on shroud. The shock unsteadiness drives a uniform frequency throughout the nozzle. However, both the downstream Kulites show higher

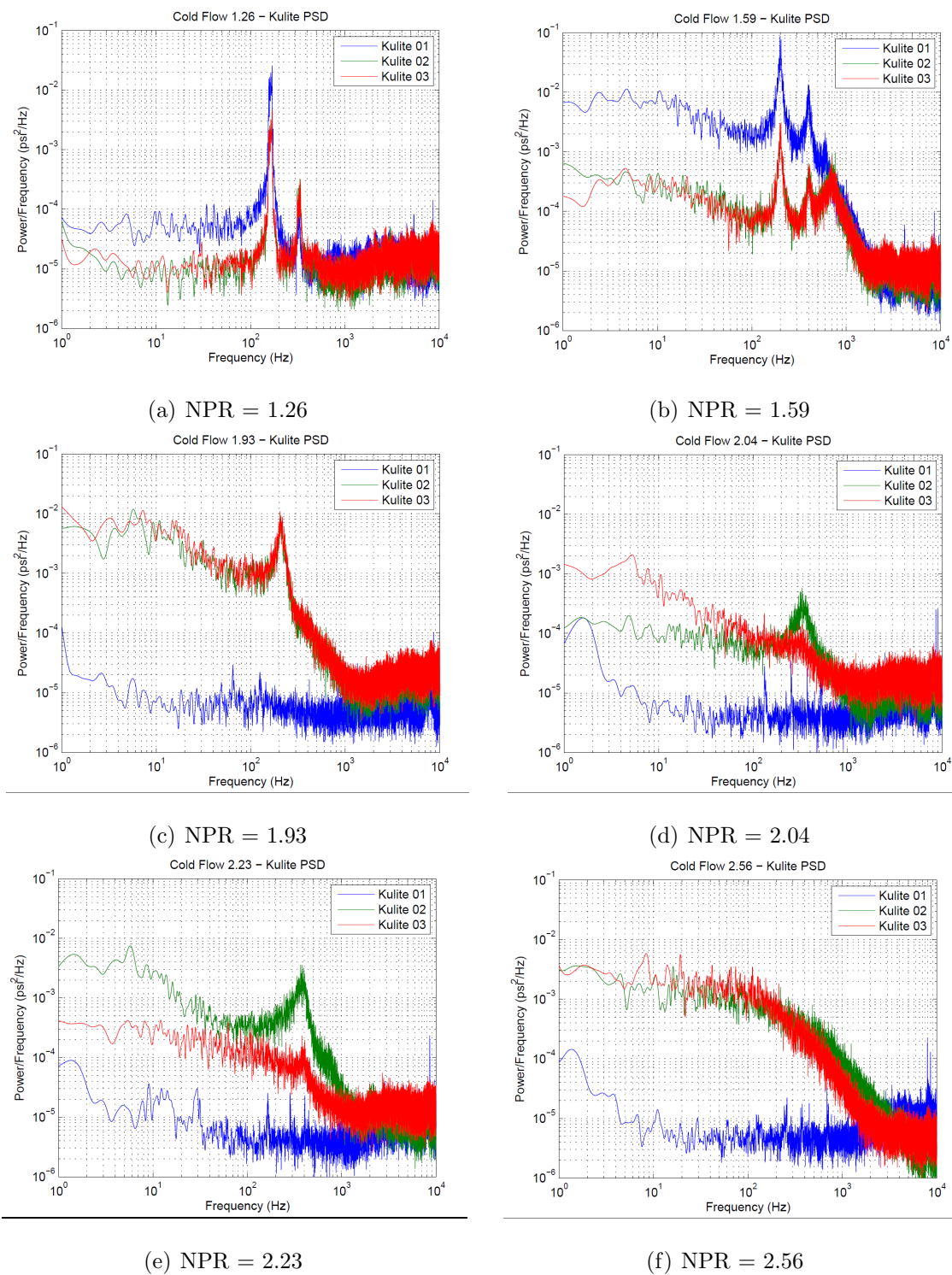


Figure 3.24. PSD measured from Kulite data and its variation with NPR.

power than Kulite 01 as the mean pressure is higher at this location (Fig. 3.18). The same peak at two tangential locations also confirms the symmetry in the flow with respect to the spectral content.

For an NPR of 1.59 the dominant spectral frequency has shifted to 200 Hz for all three Kulites as seen in Fig. 3.24(b). The magnitude of the power spectral density in the case of Kulite 01 is again lower than those of Kulite 02 and 03 which are downstream of Kulite 01. In this case Kulite 01 is at the shock leg where the mean pressure is lower than at Kulite 02 and 03 which are in the recirculation zone. Again the same frequency indicates spatial independence of dominant tone behavior. In general all three Kulites show similar dominant frequency as long as the shock is upstream of the Kulite.

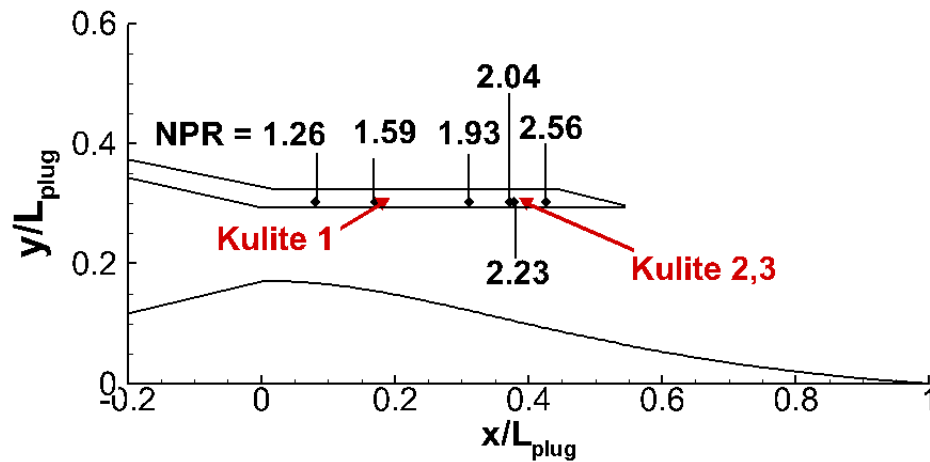


Figure 3.25. Relative position of shock location on shroud with respect to Kulite location as a function of NPR.

At an NPR of 1.93, shown in Fig. 3.24(c) Kulite 01 is upstream of the shock as seen in Fig. 3.25. It shows no dominant tone as it lies within the boundary layer ahead of the shock. Kulites 02 and 03 which are downstream of the shock show a dominant frequency again at 200 Hz similar to the NPR of 1.59. The dominant frequency for the FSS regime (NPR < 2.0) is found to be a constant at 200 Hz except at NPR of 1.26. Also, the magnitudes of the power spectra for Kulite 02 and 03 are equal

indicating the flow is tangentially symmetric at low NPRs, thus giving further weight to using axisymmetric computations. A single dominant frequency in the recirculation zone for the FSS regime also suggests the presence of a single mechanism driving the pressure oscillation in the plug nozzle.

For an NPR of 2.04 (Fig. 3.24(d)) the shock has moved almost to the location of Kulite 02 and 03 . In this case again Kulite 01 is upstream of the shock as seen in Fig. 3.25 and the dominant frequency component has shifted above 300 *Hz*. Unlike at low NPRs, the power of Kulite 02 is higher than that of Kulite 03, which indicating a possible asymmetry at this NPR.

Similar behavior is seen at an NPR of 2.23 in Fig. 3.24(e) where the shock is even closer, but still upstream of Kulite 02 and 03. As noted earlier in the discussion on static pressure distributions starting from NPRs of 2.0 the boundary layer on the nozzle wall transitions from being fully separated (FSS) to reattached (RSS) in the NPR range range of 2.0 and 2.25 and the flow is observed to be asymmetric (Fig. 3.15 and Fig. 3.21) in this transition regime. A part of the plug can exhibit RSS while the rest of the plug is in the FSS regime.

The last PSD of Fig. 3.24 is at an NPR of 2.56 and exhibits considerable energy content but no peak frequency. At this NPR the nozzle has transitioned into the RSS regime. Literature [82] suggests that RSS regime exhibits a dominant frequency due to shock unsteadiness. However, as the the shock has moved downstream of the Kulites as seen in Fig. 3.25, the Kulites are unable to capture the spectral content. Thus, the dominant frequency cannot be obtained for the RSS regime from the available probe locations. The dominant frequency trend is summarized in Fig. 3.26 as a function of nozzle operation condition. It is clear from the plot that except at the lowest NPR (1.26), the frequency remains constant for NPR's less than 2.0 and increases gradually as the nozzle transitions into the RSS regime starting at an NPR of 2.0.

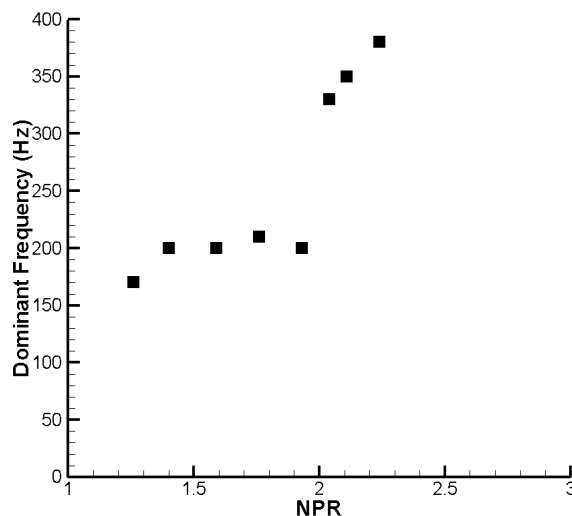


Figure 3.26. Kulite frequency variation with NPR.

3.5.2 Axisymmetric Unsteady Analysis

In many unsteady flows the dominant frequency in the flowfield can be associated with a time or length scale determined by the operating condition or geometry. In shock dominated flows, however, it is not clear which characteristic length and time scales are to be used [82]; [38]; [39]. The plug nozzle frequency analysis data showed a dominant frequency of 200 *Hz* for NPR's below 2.0 except at NPR 1.26. The constant frequency suggests that independent of the operating condition a common source drives the pressure oscillation in the plug nozzle. Therefore, it is reasonable to study a single operating condition to understand the unsteady flow physics in this constant frequency regime. In this section we analyze a single NPR of 1.59 to assess the ability of unsteady axisymmetric computations to predict pressure oscillations on the nozzle wall. The case of NPR 1.26 is also considered due to the difference in observed Kulite frequency from the higher NPR's. The unsteady computations performed here help to get an initial estimate which forms a basis for full unsteady 3-D computations. This will help in assessing the usefulness of the axisymmetric representation.

The unsteady computations in this section are done on the same axisymmetric grid used for steady computations described with reference to Fig. 3.5. The preconditioned dual-time stepping algorithm is adopted with the inviscid and viscous fluxes constructed as discussed in Chapter 2 of this thesis. The preconditioning matrix employed is particularly suited for low Mach number flow like separation regions[REF]. The $k - \omega$ model is employed in the hybrid RANS/LES mode by using a turbulent length scale switch to allow turbulent structures larger than the grid to be resolved. The boundary conditions are the same as those employed in steady computations. The inlet boundary conditions are set to the measured stagnation conditions both at the core and bypass stream inlets. An upstream steady turbulence intensity of 10% is prescribed at the core and bypass flow inlets. The inlet turbulent dissipation is specified such that the turbulence intensity drops by 10% over the length of the nozzle.

The unsteady computations are performed with the initial condition set to ambient. The use of physically relevant initial conditions helps in understanding the transient evolution of the flow. As shown in the following discussion, the time history of the flow can be used to decide when flow statistics can be obtained. The flow statistics collected from the computations can then be compared and used in conjunction with available data to study unsteadiness in the flow field. The time-averaged results of unsteady computations allow direct comparison of flow field with steady pressure data.

The unsteady computations in the dual-time context are performed with an outer physical time step and inner pseudo iterations within each physical time. The CFL of the inner iterations based on acoustics is set to 1.0. Numerical experiments with 5 and 15 inner iterations did not show any significant differences in solution. Hence, the inner iteration count is set to five which caused the inner iteration residual to drop by two orders of magnitude. Based on considerations of solution accuracy and computational time this was considered sufficient. The physical time step is set to $1\mu s$

to resolve pertinent time scales and is clearly sufficient to resolve 200 Hz oscillations seen in experiments.

The unsteady computations proceed through an initial transient during which the shock in the diverging portion of the flow is established. Following this transient, the shock should stabilize about a mean position in the diverging section around which it oscillates driving pressure oscillations on the plug and shroud walls.

In order to visualize the entire unsteady computation we can rely on representing a flow quantity at a given spatial location as a function of time using a space-time contour plot. The space time plot is obtained by taking the pressure data along a line in the axial direction, for example the plug wall, and plotting its response with respect to time. This helps to summarize important parameters of the unsteady computations in a single plot. The locations covered by these plots depend upon the feature of interest. In the present case the pressure variation on the plug and shroud walls along with the mean flow are of interest for understanding the unsteadiness related to the shock oscillations in the diverging section. In Fig. 3.27 the locations over which the space time plots are made is shown. The location on the plug and shroud are denoted by PP' and SS' and extend from the throat to the end of the shroud and to the plug tip respectively. In order to understand variations in the middle of the flow path an additional mid-plane section, denoted by MM' in the schematic is also considered. The mid-plane section passes through the center of the throat and extends from the throat to the plug tip at constant radius.

Figure 3.28 shows the space-time pressure contours on the plug(left) and shroud (right) walls as a function of time for the $NPR = 1.59$ case. The plots clearly demonstrate the the flow in the divergent section is unsteady. The plots help discern several flow features in the nozzle section. The darker colors correspond to regions of low pressure while the lighter colors correspond to high pressure. Starting at the lower left of the plug plot (Fig. 3.28(a)) a sudden jump from low to high pressure is seen at an $x/L_{plug} = 0.3$. This change in color is indicative of the shock location. Downstream of the shock location the pressure is high, upstream it is low. Between this zero

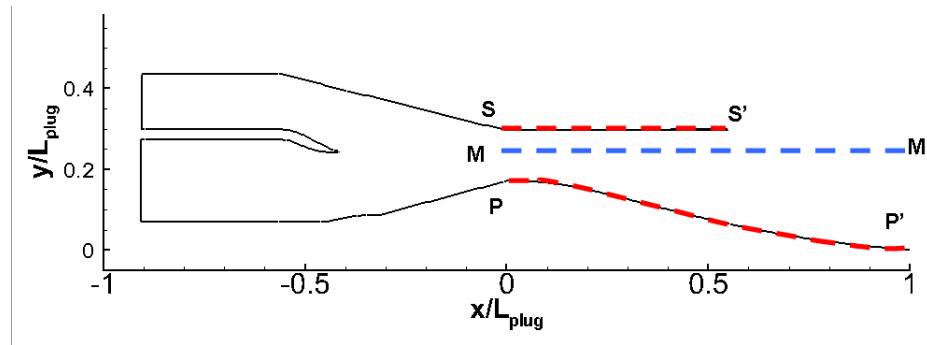


Figure 3.27. Schematic of locations at which space-time plots are shown, plug(PP'), shroud(SS') and mid-plane(MM').

and approximately $1.5ms$ this color streak is seen to move upstream (to the right) ultimately reaching an x/L_{plug} of 0.1 near the throat. At about $2ms$ it suddenly jumps slightly downstream and then again returns towards the throat. Following this the shock alternately jumps downstream at an x/L_{plug} of 0.2 before again moving upstream in a quasi-periodic fashion. The time interval between 0 and $220ms$ corresponds to a starting transient while that beyond $220ms$ represents a nearly stationary periodic oscillation. A similar pattern is seen in the pressure contour of the shroud (Fig. 3.28(b)), except that the shock is further downstream of the throat, varying from an x/L_{plug} of 0.1 to 0.3. The lower portion of the plots show the initial transient which lasts for about $220ms$ as is documented later. Most dominant feature is the shock unsteadiness in the diverging section. The shock motion follows a saw-tooth like pattern at a low frequency. The shock is demarcated by a strong change in pressure in the plots. The shock oscillation amplitude predicted by axisymmetric computations appears to be large and is more than 10% at some instants in time.

The streaks in the space-time plot are indicative of acoustic waves propagating along the shroud and plug walls. Streaks with a positive slope correspond to waves moving in the downstream direction while streaks with a negative slope correspond to acoustic waves moving in the upstream direction. On the plug we can observe acoustic signals generated at the shock foot propagating in the downstream direction. Most

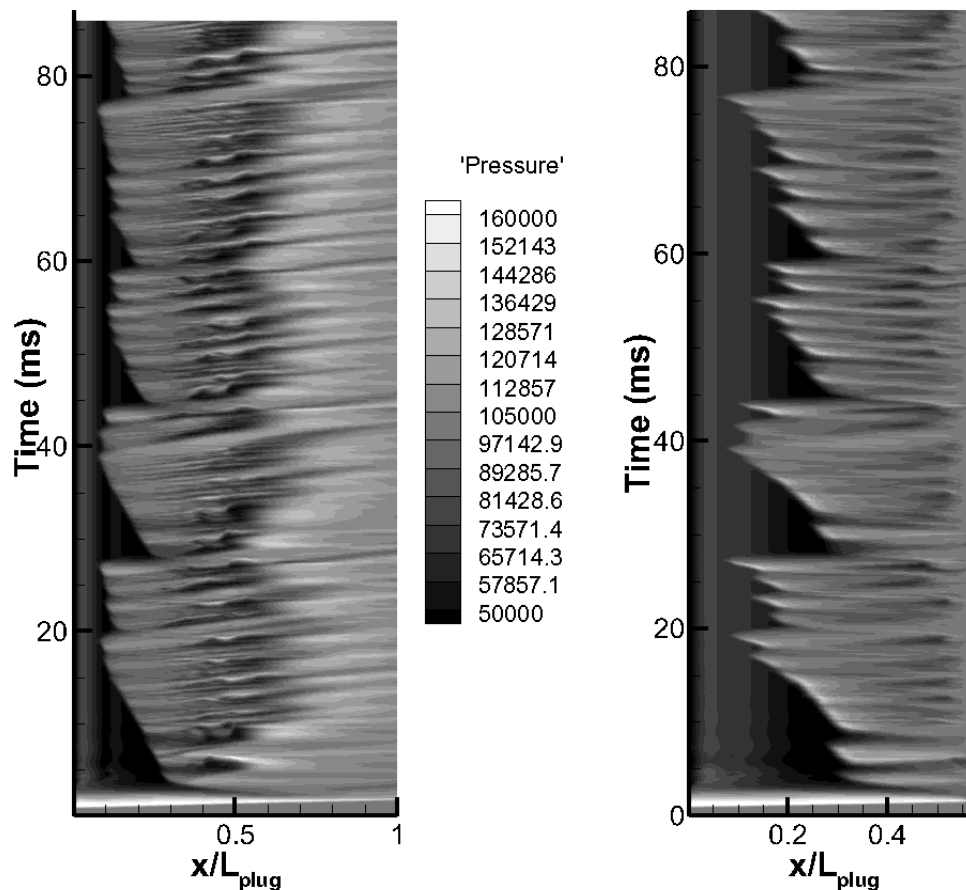


Figure 3.28. Space time plot of pressure on the plug(left) and shroud(right) of the nozzle at NPR of 1.59.

of the pressure disturbance on the shroud propagate in the upstream direction and appear to originate at the nozzle exit. Note that these waves are traveling faster than the downstream propagating ones.

Figure 3.29 shows the space-time plot at a constant radius location in the mid-plane section, MM' of the nozzle. In the mid-plane space-time plot the acoustic disturbances propagate in both directions. Again the origin for upstream and downstream propagating waves appears to be the nozzle exit. These disturbances have been observed earlier in experimental work related to transonic diffuser channels [25]; [22].

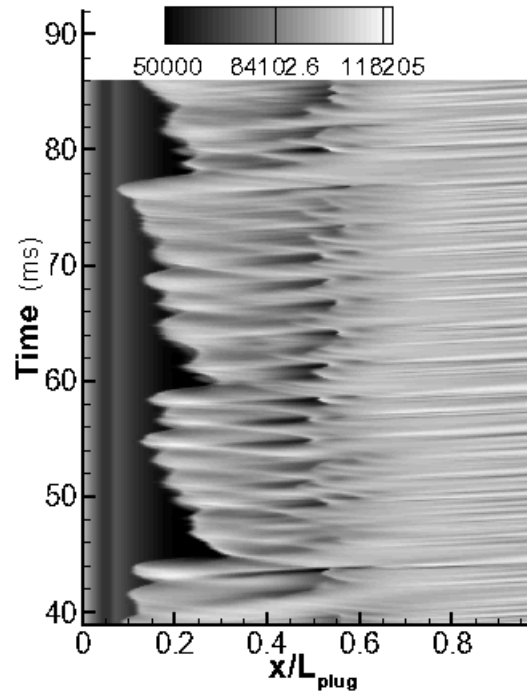


Figure 3.29. Space time plot of pressure oscillation at mid-plane of the nozzle.

In Fig. 3.30 the variation of the pressure is shown at different axial locations on the shroud and plug wall. The locations shown on the shroud wall coincide with the location of the Kulites in the experimental nozzle. All the plots have been start from the beginning of the computation and the transient portion is demarcated by a vertical line and letter 'T'. In all locations the pressure signal appears to be unsteady. The initial transient shows two large amplitude oscillations in pressure which last for about $10ms$ in Fig. 3.30(e). In order to reduce the effect of the transient on the statistics obtained the transient is considered after a period of $10ms$ from this point. The plots at location $x/L_{plug} = 0.18$ on the plug show three instants of drastic pressure drop ($35ms$, $45ms$ and $50ms$) when the shock moves past these locations and creates supersonic conditions. Otherwise this location lies in the separated regime. These instants are associated with the largest shock motion amplitude also seen in Fig. 3.28(a). The same holds for the shroud location but in this case the shock

moves downstream more frequently. All other locations show an oscillatory pressure response typical of nozzles.

The spectral content from the location at $x/L_{plug} = 0.18$ on the plug and the shroud are studied using a periodogram estimate and are shown in Fig. 3.31. Both the figures show a peak frequency of 60Hz compared to Kulite frequency of 200Hz . The peak frequency, though different from the measured value, points to an important conclusion, that the disturbances on the shroud and plug have the same peak frequency. This helps in extending the Kulite frequency observed on the shroud to the plug also. It is to be reminded that the Kulite data was available only on the shroud and not the plug.

To allow for a direct comparison to data we present the time averaged solutions of unsteady computations in Fig. 3.32 and Fig. 3.33. Both the figures are obtained after averaging for a period of 64 ms. In Fig. 3.32 the schlieren from steady computations is shown in the bottom half while the time averaged solution is shown in the upper half. The time averaged computations exhibit all the salient features of steady computations. The supersonic region near the throat and expansion fan are present. The shear layers appear thicker due to the large resolved eddies in unsteady computations. The shock in unsteady computations is weaker than that in steady computations. The recirculation zone appears larger in unsteady computations due to its dynamic nature. In unsteady computations the constant recirculation zone of the steady computations is replaced by a vortex shedding pattern. The recirculation zone is therefore of varying size. Also seen at the exit is a weak disturbance of considerable thickness. This weak shock is in fact the shocklets that are formed in the mean flow at the exit. As described earlier the recirculation zone provides a natural converging passage which causes the appearance of the shocklets. The steady pressure distribution in Fig. 3.33 shows that the shock location is predicted close to the data for the plug but the recirculation zone pressure is not recovered accurately on the plug and the shroud. This may be due to the axisymmetric assumption in the computation. Though the steady flow is axisymmetric as predicted and matched by

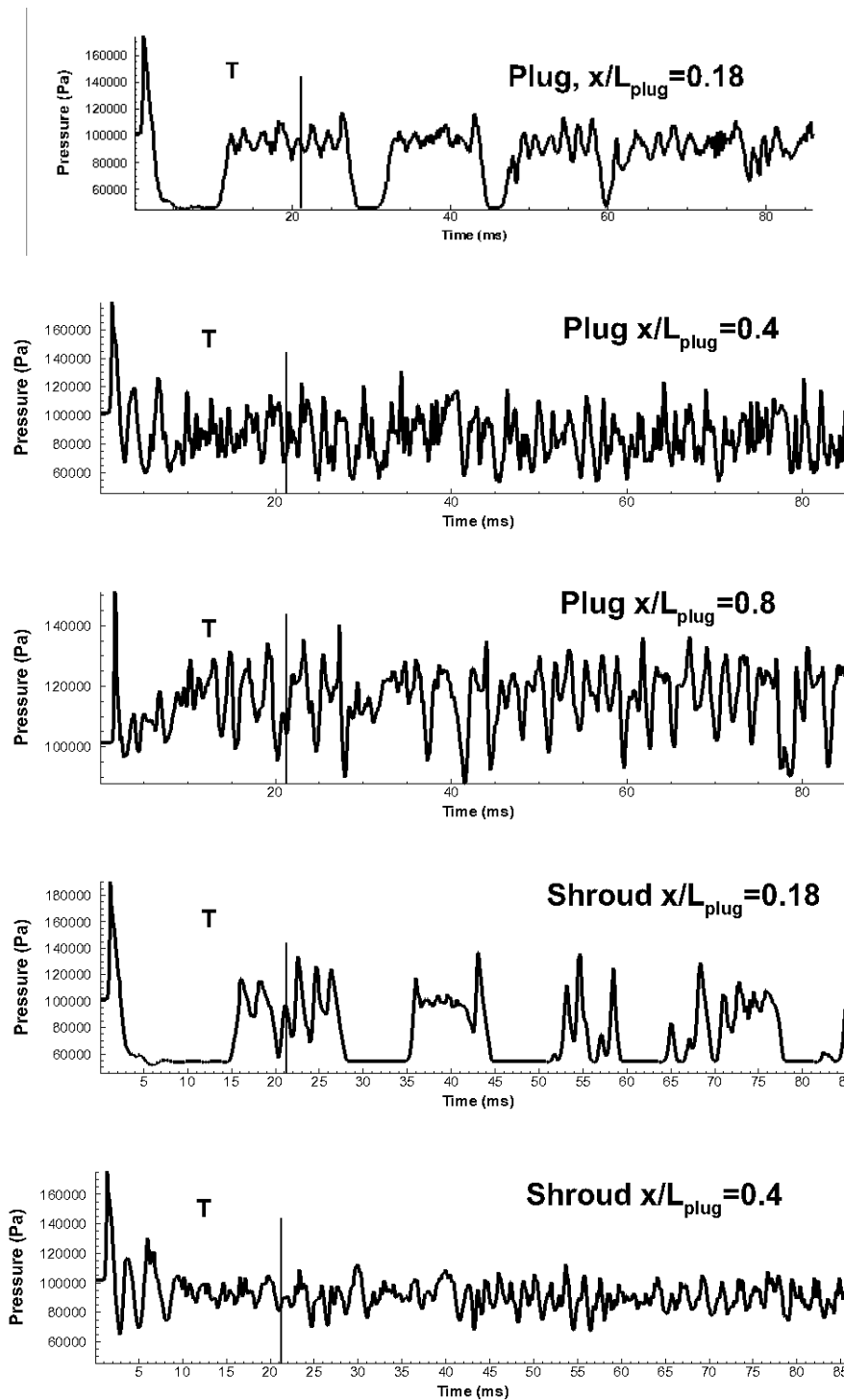


Figure 3.30. Pressure oscillations on the plug and shroud for NPR of 1.59 at locations indicated on the plot.

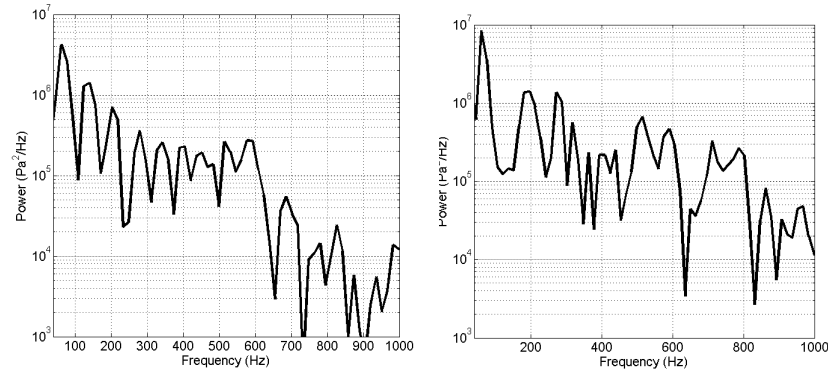


Figure 3.31. PSD estimate for location $x/L_{plug} = 0.18$ for the plug(left) and shroud(right) taken from the duration $22ms$ to $86ms$ showing a peak at $60 Hz$.

steady computations with data, the unsteady flow in the separation region may not be axisymmetric. As shown later, the predictions improve considerably for the NPR of 1.59 case when the axisymmetric assumption is dropped. This 3-D unsteady analysis may help explain why the predicted frequency and the static pressure distribution on the plug and shroud are not close to data.

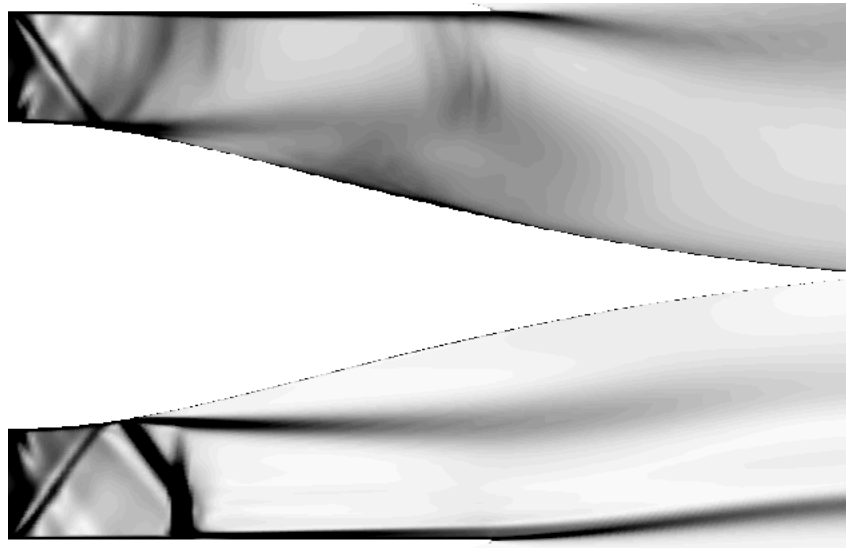


Figure 3.32. Time averaged schlieren from unsteady computations (top half) compared to steady computations (bottom half).

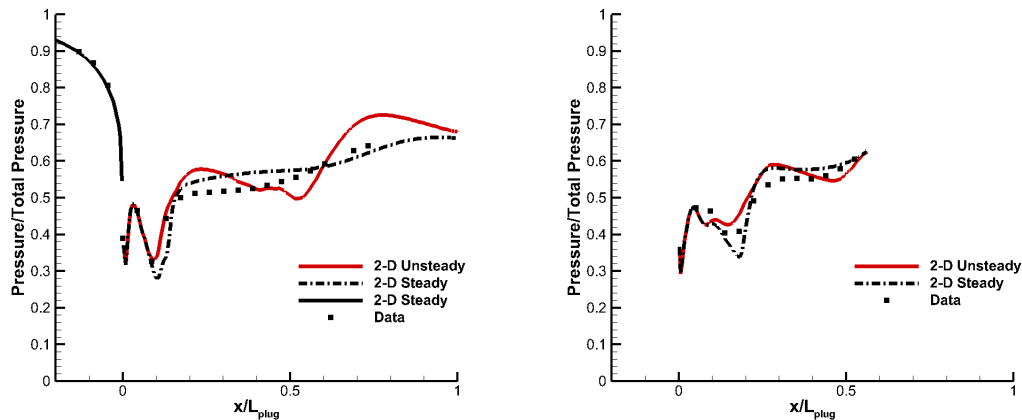


Figure 3.33. Time averaged pressure from unsteady computations compared to steady computations and data for NPR of 1.59.

As an additional case, the axisymmetric computations are considered at NPR of 1.26. Kulite data suggested that NPR of 1.26 showed a lower frequency of 170Hz and might merit additional analysis. The solution is set up as described previously in the context of NPR of 1.59 except that the cold flow inlet stagnations conditions correspond to NPR of 1.26. The computations begin with a transient following which the flow is established in the diverging section. In Fig. 3.34 the space time contour plot for the pressure variation on the plug (PP') and shroud (SS') are shown. The unsteadiness in the case of NPR of 1.26 appears to be periodic in contrast to NPR of 1.59. The shock motion, demarcated by strong pressure rise, is seen both on the plug as well as the shroud surface. The acoustics on the plug and shroud are similar to the case of NPR of 1.59. On the plug the disturbances propagate in the downstream direction whereas on the shroud they appear to propagate in the upstream direction.

The variation of pressure on the plug and shroud surface is shown in Fig. 3.35 for different locations as indicated on the plots. In all the plots the transient is seen to exist for the first 11ms of the computation. This zone is demarcated by a vertical line and indicated by the letter 'T'. All the plots shown reflect the periodic nature of

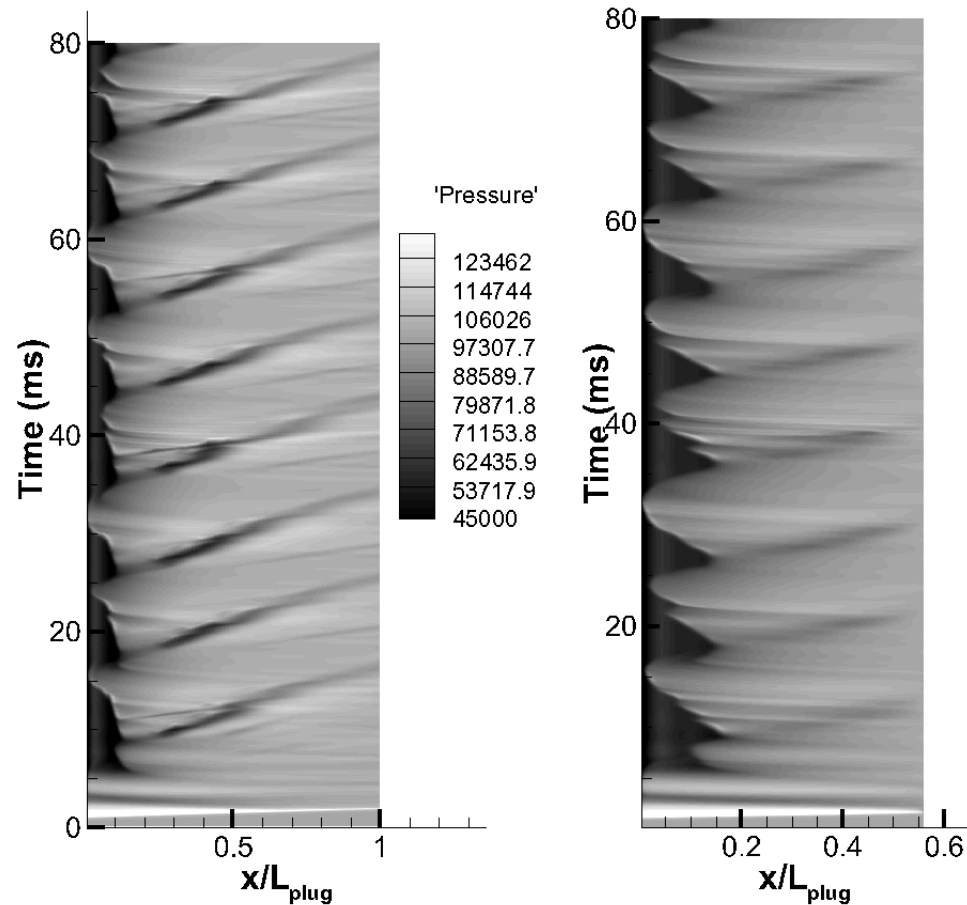


Figure 3.34. Space time plot of pressure on the plug(left) and shroud(right) of the nozzle at NPR of 1.26.

the flow which was seen in Fig. 3.34. The pressure at the locations $x/L_{plug} = 0.18$ which is close to the shock location drops when the shock moves upstream of this location and shows low frequency oscillations till the shock moves downstream. The other location shows a rise in pressure when the recirculation zone on the plug wall is shed. Figure 3.36 shows the PSD estimate at the location $x/L_{plug} = 0.18$ on the plug and the shroud. This PSD estimate was obtained by sampling the data at 10000Hz for period from 11ms to 80ms . In both cases a peak frequency of 110Hz is seen which is closer to the Kulite frequency of 170Hz .

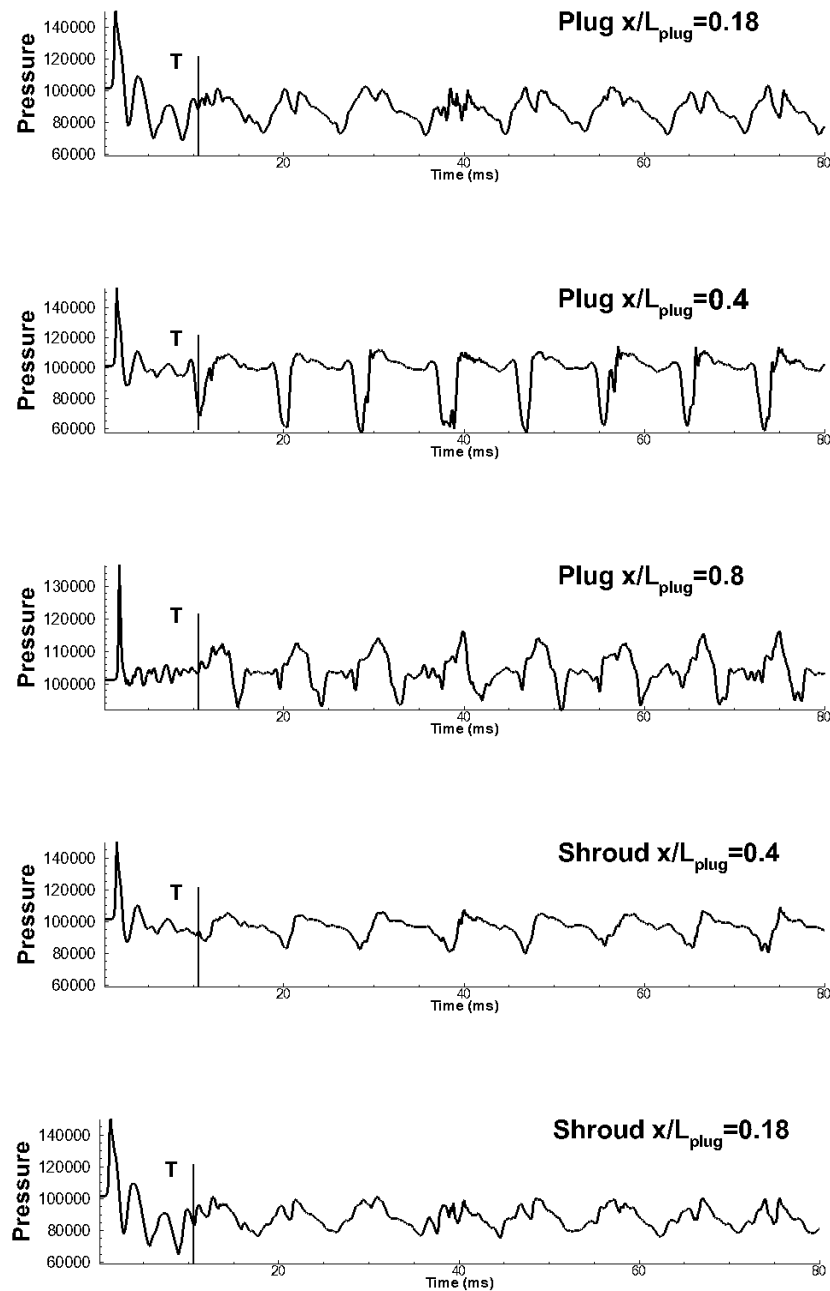


Figure 3.35. Pressure oscillations on the plug and shroud for NPR of 1.26 at different locations.

In Fig. 3.37 and Fig. 3.38 the time averaged schlieren and pressure distribution on the plug are shown. The time averaging has been performed for a period of

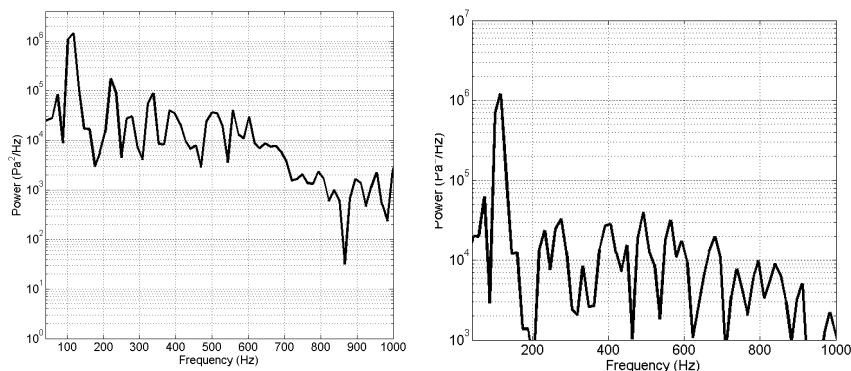


Figure 3.36. NPR=1.26, PSD estimate for location $x/L_{plug} = 0.18$ for the plug(left) and shroud(right) taken from the duration 11ms to 80ms showing a peak at 110 Hz.

69ms after the transient. The schlieren shows a weaker shock compared to the steady result due to shock oscillations in the diverging section. The separation region appears to be larger in size compared to the steady computations. The predicted pressure from time-averaged computations matches closely with data and steady computations both on the plug and the shroud surface. Thus, it appears that the assumption of axisymmetric flow holds at this NPR, which is validated when we look at 3-D unsteady analyses.

3.6 Three-Dimensional Computations

The axisymmetric computations along with the experimental data helped in shedding light on the separation pattern observed in shrouded plug nozzles. The axisymmetric computations proved to be sufficient for the major part of the NPR spectrum except in the transition regime from FSS to RSS. This occurred after an NPR of 2.0 and below 2.25 according to the data. The three-dimensional computations will ascertain whether axisymmetric computations are sufficient to predict shrouded plug nozzle flowfields at least in the regime where the flow is axisymmetric. A compari-

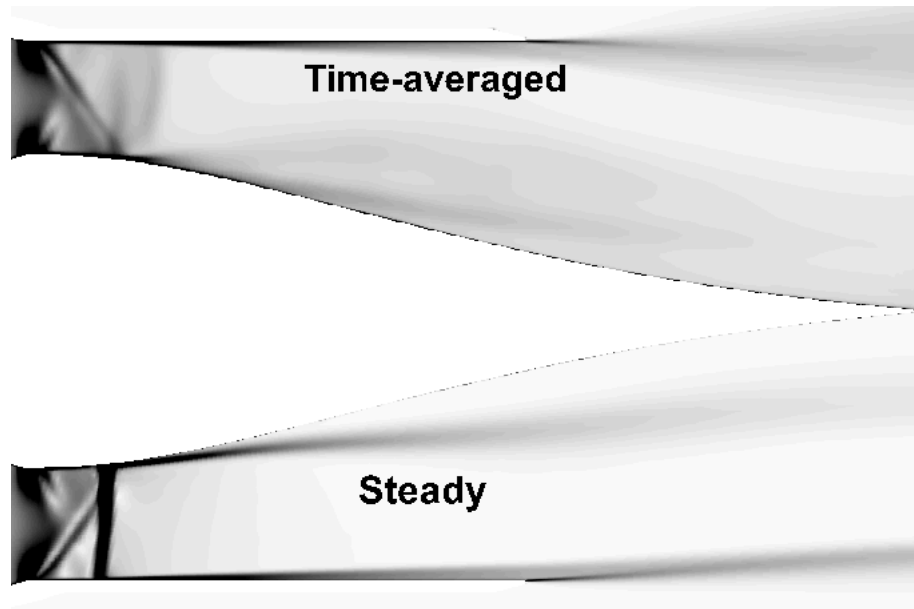


Figure 3.37. Time averaged schlieren from unsteady computations (top half) compared to steady computations (bottom half).

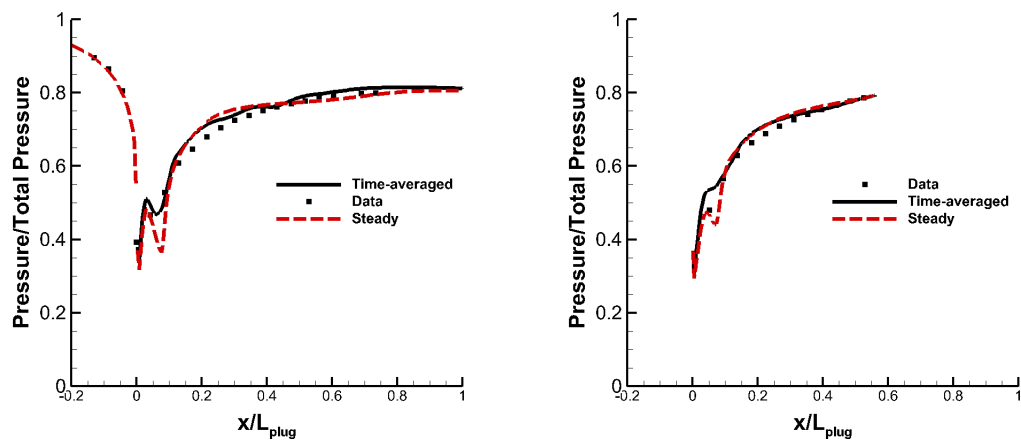


Figure 3.38. Time averaged pressure from unsteady computations compared to steady computations and data for NPR of 1.26.

son of three dimensional computations with axisymmetric computations might give insights into the modeling of flows with strong shock physics.

Accordingly, this section focuses on three-dimensional computations of the shrouded plug nozzle concept. The section begins with a description of the computational domain and boundary conditions employed followed by a discussion of the computational results. Again, extensive use of measured data is used to ascertain the accuracy of the computations. During the discussion focus is shown in comparison of the 3-D result to the axisymmetric case. Mainly with a view to understand if the axisymmetric assumption is sufficient for studying this flowfields. For cases where deviations from axisymmetry occurs further analysis is carried out.

3.6.1 Computational Domain and Boundary Conditions

The computational domain consists of the two flow streams (core and bypass) as well as an ambient grid field. The ambient grid for the three-dimensional computations is similar in extent to that of the axisymmetric computational domain. The computational domain extends four nozzle throat diameters laterally to the shroud and six nozzle throat diameters in the axial direction aft of the plug tip.

For 3-D computations two grids were employed considering the duration for unsteady computations. The grid on which axisymmetric computations were performed is capable of resolving the shock structure and the pressure distribution on the plug. The axisymmetric grid had 79000 cells in the entire domain. The 3-D dimensional counterpart of the axisymmetric grid obtained by revolving the axisymmetric grid about the axis using a total of 80 azimuthal planes will have more than 6 million cells. Accordingly, two grids are used: one which will retain the resolution of the axisymmetric grid in the entire nozzle section and a coarser grid without sacrificing the resolution in the diverging section and the boundary layer.

The plug nozzle geometry poses a particular difficulty in generating a grid compared to the axisymmetric case. The tip of the plug converges to a point at the end and poses a singularity for laying a cartesian or cylindrical grid. The grid for the three-dimensional computations, therefore differed from that of the axisymmetric grid

Table 3.1 Comparison of two 3-D grids.

Feature	Grid 1	Grid 2
Nozzle	264×70×80	340×130×80
Ambient	73×90×80	73×140×80
Diverging section	150×70	200×130
Δy	$7E - 6 \cdot D_t$	$7E - 6 \cdot D_t$
No. of cells	$\approx 2,050,000$	$\approx 4,600,000$

only in the treatment of the centerline. In practice a plug tip will have a finite base, in a similar fashion a negligible portion ($< 0.1\%$) of the plug tip was clipped to leave it with a small bluntness. As mentioned two grids were generated for the plug nozzle geometry with the clipped plug tip. Table 4.1 contrasts the two grids. In the table the grid resolution for the nozzle (inlet to plug tip), ambient and diverging section are provided. Grid 1 is about half the size of grid 2 and is generated without significant differences in handling axial and boundary layer resolution in the diverging section. A total of 80 tangential planes were used based on two competing considerations of overall grid size and the requirement that the aspect ratio ($\Delta x/R\Delta\theta$) of grids close to the plug tip is not greater than 100. The first grid point from the wall lies such that the $y^+ < 1$ with enough grid points for boundary layer resolution. The entire grid is constructed of hexahedral elements. A C-grid wraps around both the plug and the shroud for the boundary layer while the rest of the domain is made up of an H-grid. The grid for the centerline is obtained by laying hexahedral elements from the plug base to the domain farfield.

The grid for 3-D computations is shown in Figs. 4.36 and 4.37. In the first figure the quarter grid in the computational domain is shown. Also, shown is the multi-block topology of the grid in order to show in some detail the mechanics of the grid. Each of the blocks is made up of a cartesian grid consisting of hexahedral elements. The grid generation is done efficiently by working with a quarter of the

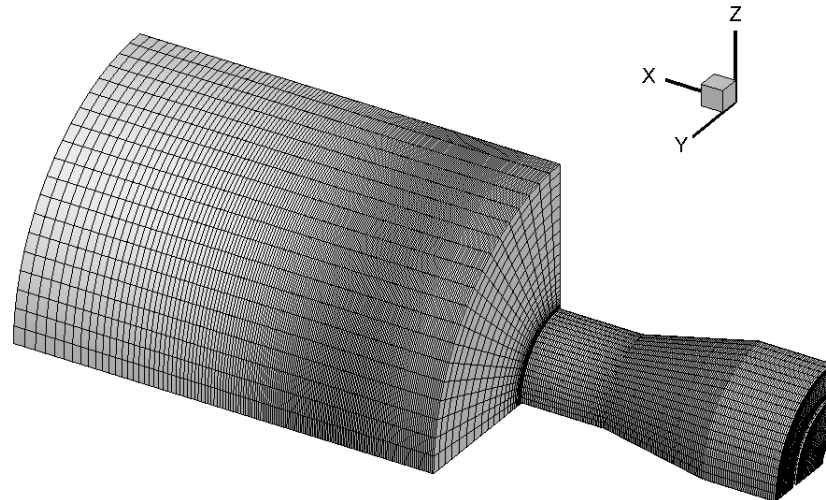
domain. Figure 4.37 shows the grid within the nozzle section without the exterior grid to give some detail within the converging-diverging section of the plug nozzle. Also, shown in the figure is the detail of how the centerline grid extends from the plug base. In Fig. 3.40(b) the plug surface is shown on the left while the multi-block cartesian topology which replaces the centerline singularity is shown on the right. This centerline block extends all the way to the outlet. The above treatment for the computational domain is similar for both grid 1 and 2. The difference between both grids occurs only in the longitudinal section as seen in Table 4.1. The grid in the diverging section for grid 1 and grid 2 is compared in Fig. 3.41.

Similar to the axisymmetric computations, total pressure and cold flow total temperature boundary conditions are specified at the inlet, the walls are treated as adiabatic no slip walls. All the boundaries away from the nozzle are treated as farfield conditions. As the experiments are performed at static sea level conditions the farfield boundaries correspond to sea level static. This allows a direct comparison of the three-dimensional predictions with the experimental data.

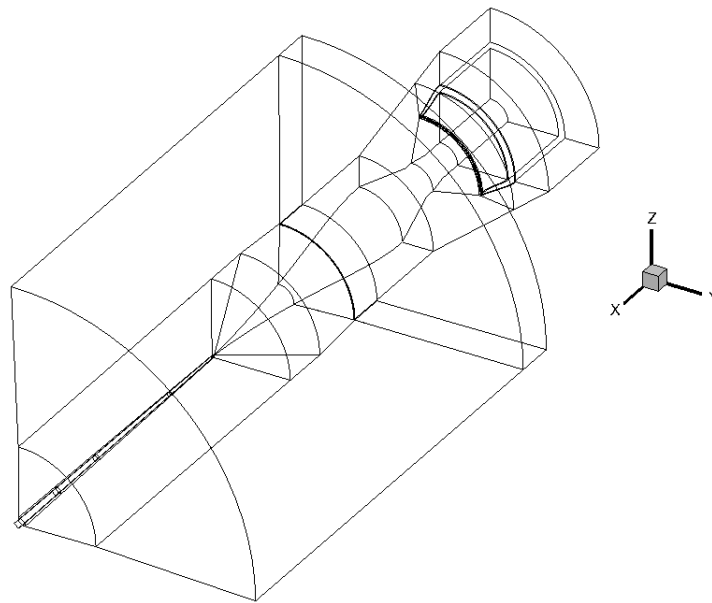
3.7 Three-Dimensional Steady Analysis

In this section we discuss the steady three-dimensional computations and compare them with the axisymmetric computations. The results in the previous section suggested that the axisymmetric assumption holds reasonably well for plug nozzle flowfields for all NPR's except those in the transition regime. As the axisymmetric computations were able to identify the shock physics we restrict our comparisons to pressure distributions. The shock structure will follow once the static pressure distributions match. The 3-D computations will further help in understanding the asymmetry in plug nozzle flowfields.

The convergence characteristic of the steady RANS computations is shown in Fig. 3.42 for grid 1. Similar convergence was obtained for grid 2. The cell limiter active in the vicinity of the shock deteriorates the convergence at all NPR's. The



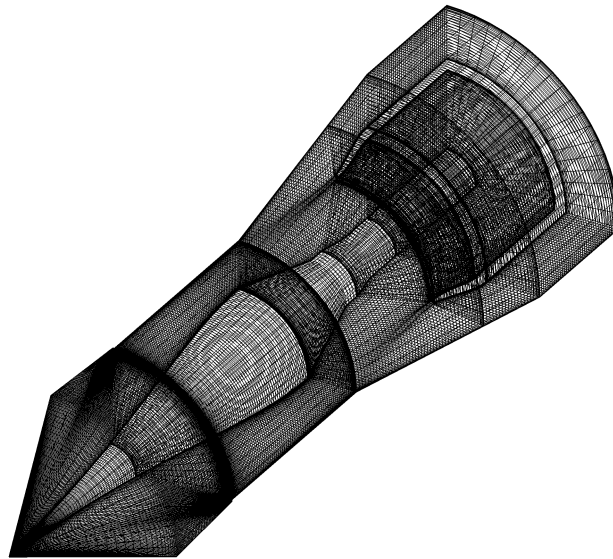
(a) Quarter grid of the nozzle



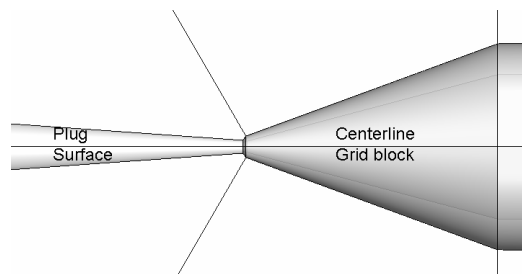
(b) Multi-block topology of quarter grid

Figure 3.39. Quarter grid for three dimensional computations.

convergence improves as the separated region decreases in the flowfield with increasing NPR with the highest NPR in the plot showing 5 orders of drop in residual. At low NPR of 1.26 due to the large recirculation zone on the plug wall, the computations



(a) Quarter grid detail in the nozzle section without exterior grid



(b) Detail of topology near the plug tip

Figure 3.40. Quarter grid for three dimensional computations.

show periodic convergence to about two orders of magnitude, an indication that the flow is probably unsteady. In contrast to axisymmetric computations a larger number of cells are in the recirculation zone for 3-D computations which is inherently unsteady and prevents uniform convergence even at high NPR's.

Both the 3-D grids, the coarser and the finer grid discussed earlier, are employed. The coarser grid is referred to as grid 1 has half the number of gridpoints in grid 2. Grid 2 is derived from the axisymmetric grid. Grid 1 had similar resolution as grid 1 in the boundary layers and in the diverging section of the plug where the shock

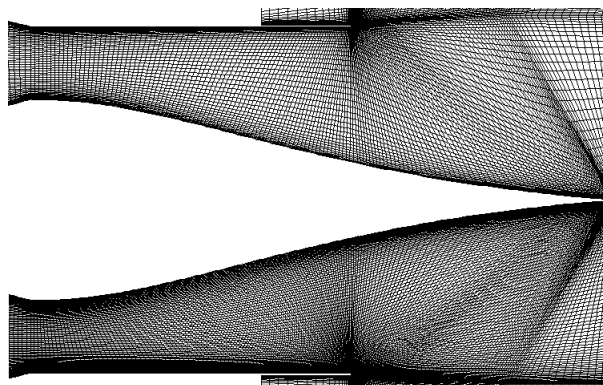


Figure 3.41. Grid in the axial direction in the diverging section compared for grid 1(top) and grid 2(bottom).

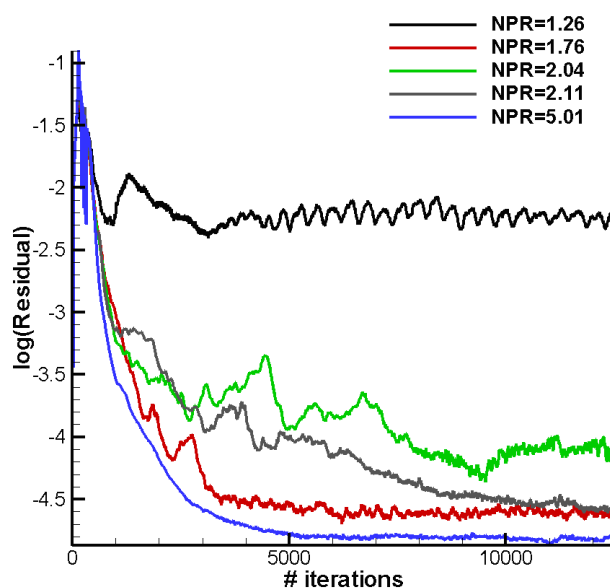


Figure 3.42. Convergence of steady 3D computations.

resides. The computations are executed for the same NPR's that were analyzed in axisymmetric case. Figure 3.43 shows the static pressure distribution on the plug and shroud wall for two NPRs: 1.76 in the FSS regime and 3.73 in the RSS regime. In the plots results from three computations are compared against data - 3-D steady computation on grids 1 and 2 as well as the axisymmetric steady computation. The pressure distributions from 3-D computations are taken from four azimuths on the

plug and the shroud walls and are shown in the same plot in Fig. 3.43. For both the NPR's the static pressure distributions from all three computations coincide with each other and also match closely to the data. This leads to the first conclusion that the shock location does not vary from grid 1 to 2 in the 3-D computations either in the FSS and RSS regimes. The 3-D results for both the grids are shown at four different azimuthal positions which overlap with each other showing that the 3-D computations also predict the axisymmetric nature of flowfield. In general the same result was obtained for all the NPR's that were studied using 3-D analysis on both grids. The shock location as well as the extent of the separation region are predicted very well.

Primary differences from axisymmetric computations were observed in the transition regime from FSS to RSS which is expected to occur between 2.0 and 2.25 based on experimental data. Figure 3.44 shows the pressure distribution from 3-D computations again compared to axisymmetric computations and data for NPR of 2.04 and 2.11. In both plots the data correspond to the time before the transition occurs during experimental operation (Fig 3.21) i.e. in the FSS regime. In the case of NPR of 2.04 grid 2 is able to predict the shock location and separation region both on the plug and shroud wall and match closely with axisymmetric computations and data. Grid 1 predicts a completely different pressure distribution than data or axisymmetric computations as well. The case of NPR of 2.11 shows an opposite prediction for behavior with respect to grid 1 and grid 2. The predictions from grid 1 are closer to the data than grid 2. Also, in all the plots the pressure distributions from all four azimuth locations mentioned earlier are shown. Clearly, all the four locations collapse to single line for both grids. Thus, 3-D computations also predict axisymmetric flow for the transition regime. It is not entirely clear why a grid change results in different shock predictions. Separation zones are observed to have the property precessing while shedding continuously. The asymmetric nature of the plug flow in the hysteresis regime changes the separation region in the azimuthal direction. Thus, as the separation region precesses about the plug the static pressure taps exhibit different regimes

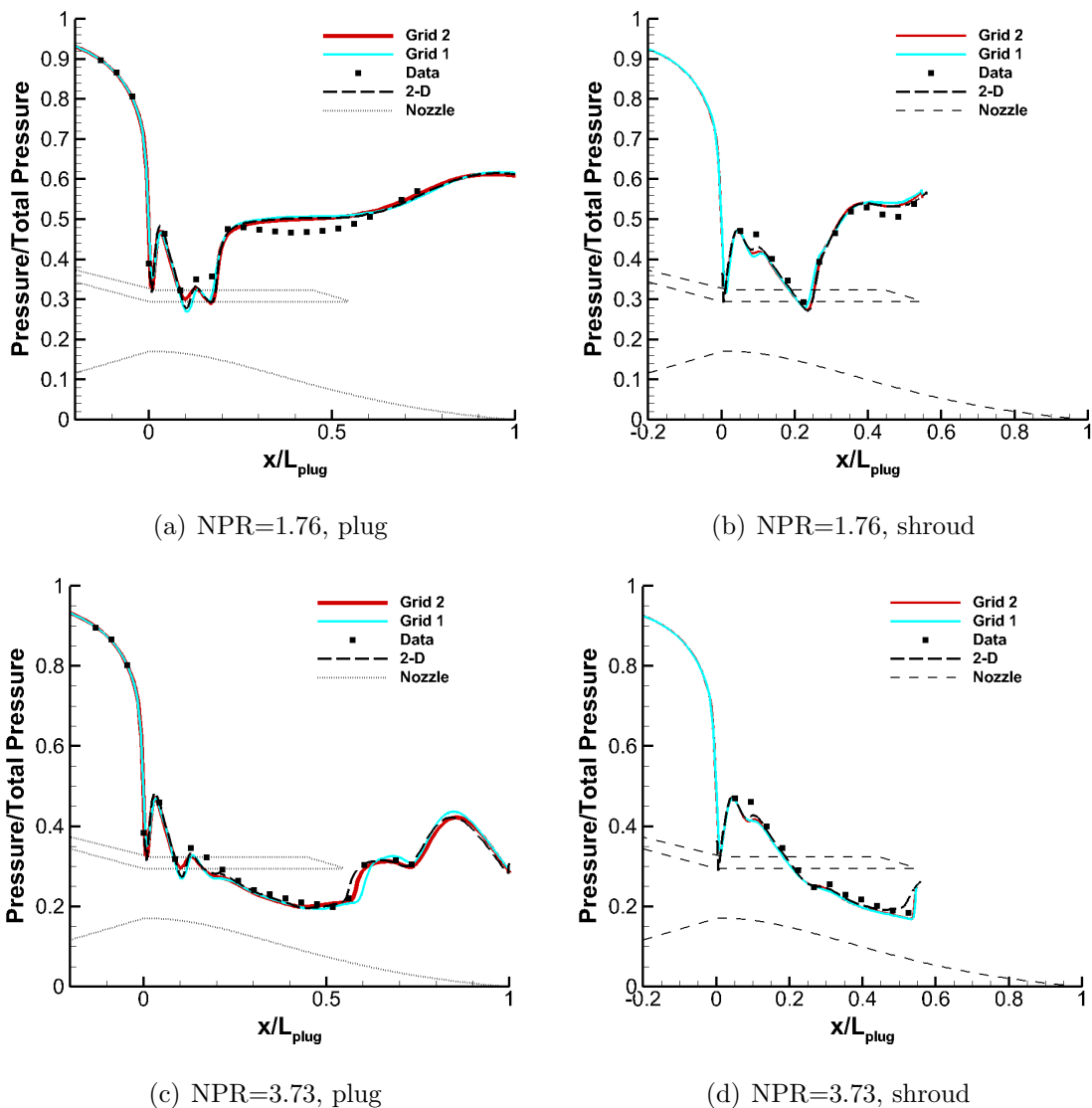


Figure 3.43. Static pressure distribution from 3-D computations on grid 1 and 2 compared to axisymmetric computations and data at NPR of 1.76(FSS) and 3.73(RSS).

at different time instants. The static pressure taps located at three azimuths on the shroud and plug may not be sensitive to this precession of the separation region. This is a likely reason why static pressure distributions do not match.

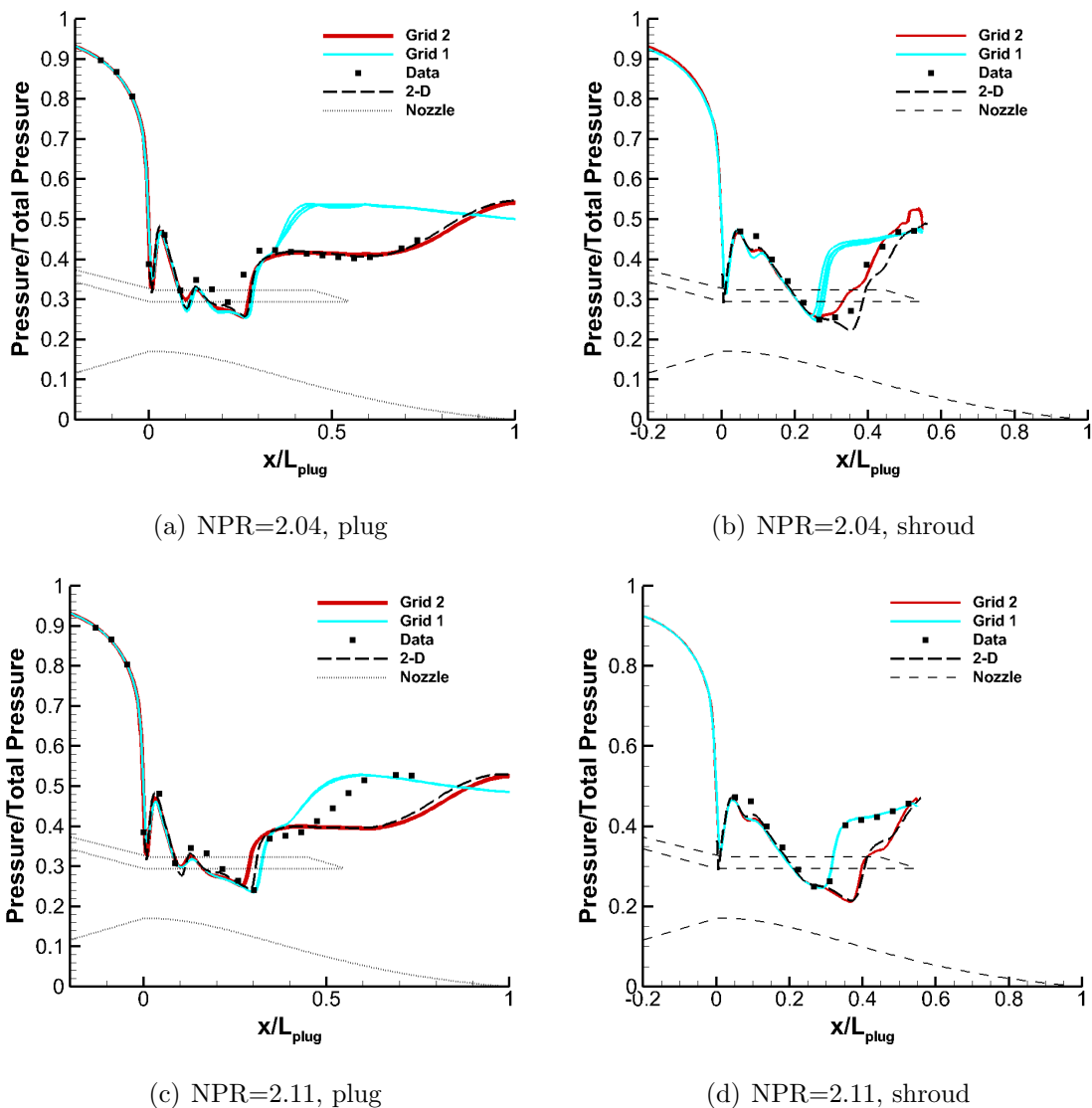


Figure 3.44. Static pressure distribution from 3-D computations on grid 1 and 2 compared to axisymmetric computations and data.

3.8 Three-Dimensional Unsteady Analysis

The unsteady axisymmetric computations showed unsteady shock motion in the diverging portion of the nozzle as one of the important unsteady characteristic of the plug flowfield. The DES model employed in axisymmetric computations showed large amplitudes shock oscillations but fell short of predicting the pressure oscillation

frequency. However, it was able to lay the basis for a preliminary unsteady analysis that shed light on the nozzle acoustics. In this section we contrast 3-D unsteady computations with axisymmetric computations and evaluate their accuracy in predicting nozzle flow physics. The experimental Kulite frequencies showed a frequency around 200 Hz in the FSS regime for NPR's below 2.0. At NPR of 1.26, however, a reduced frequency of 170 Hz was observed. We adopt a similar approach to the axisymmetric unsteady computations and focus our attention on the NPR of 1.59 for which data are available. Also, NPR case of 1.26 is also studied using the unsteady 3-D computations to explore any differences from higher NPR's.

The unsteady computations presented in this section are performed on grid 1 used for steady computations. As pointed earlier, this grid is coarser in a tangential plane than the grid used for axisymmetric computations. The pressure distribution predicted on the plug and the shroud are close to measured data for both NPR of 1.26 and 1.59 as seen in the earlier section. The details of the grid and its contrast to the axisymmetric grid are discussed in conjunction with Fig. 3.41. Again, the preconditioned dual-time stepping algorithm is adopted with the inviscid and viscous fluxes constructed as discussed in CHAPTER 2. The $k - \omega$ model is employed in the hybrid RANS/LES mode by using a turbulent length scale switch to allow larger than grid turbulent structures to be resolved. Similar to the steady computations, the inlet boundary conditions are set to the measured cold flow stagnation conditions both at the core and bypass stream inlets. A constant upstream turbulence intensity of 10% is prescribed at the core and bypass flow inlets. The inlet turbulent dissipation is specified such that the turbulence intensity drops by 10% over the length of the nozzle.

As in the case of axisymmetric unsteady computations, the physical time step is set to $1\mu s$ which is adequate for resolving the 200 Hz tone observed in the Kulite data and for computing turbulent fluctuations in the flow associated with larger time scales. The inner pseudo iteration count is set to 5 which resulted in the inner iteration residual dropping by two orders of magnitude. The inner CFL number based

on the acoustic eigenvalue of the cell is set to 1.0 using the minimum length of the computational cell.

The progress of the solution is monitored as the flow evolves into quasi periodic oscillations. Following this transient, statistics are collected at 10000 Hz frequency to analyze the frequency content for both the NPR's considered here.

3.8.1 Unsteady Results at NPR = 1.59

At an NPR of 1.59 the steady computations were able to predict the shock location accurately and the length of the separation region. Both the steady calculations and the experimental data indicated that the boundary layer on the plug at this NPR case is fully separated as it lies in the FSS regime. The unsteady axisymmetric simulations indicate that the recirculation zone following the shock is unsteady and its dynamics appears to decide the shock motion in the diverging section of the plug. The oscillatory convergence behavior of the steady computations (Fig. 3.42) also suggests the presence of unsteadiness of the flowfield. The following discussion highlights the salient features of the unsteady 3-D computations and the unsteady flowfield.

The initial condition for the unsteady computations again start from uniform quiescent conditions with ambient pressure in the entire domain but with specified stagnation pressure at the upstream boundaries for the core and bypass flow. Upon initiation, this stagnation pressure induces a precursor shock wave that sets the flow in motion in much the manner of a shock tube. The unsteady computations then proceed through a transient period before eventually reaching stationary conditions. Following this transient the mean behavior of the shock physics can be understood. This initial transient is first documented by a series of schlieren contours from beginning of computation and continuing until initial stationary conditions are approached.

Six instantaneous computational schlieren on one tangential plane of the plug are given in Fig. 3.45 to depict the transient behavior. Both the upper and lower

halves of the nozzle diverging section are shown to show the shock motion. The first instant shown at a time of 1 *ms* clearly shows a normal shock in the diverging section. This is the normal shock formed at the inlet from the stagnation boundary conditions and ambient initial pressure. This shock traverses the entire nozzle diverging section before finally exiting. The second snapshot at time 2 *ms* depicts this condition just after the shock has passed out of the diverging section. Once outside the nozzle, the normal shock weakens in strength and is dissipated before it reaches the farfield boundary. Following this initial shock the nozzle remains unchoked for approximately 2 *ms*. At about 5*ms* a weak shock forms in the divergent section as seen in Fig. 3.45(c). At this instant, the nozzle walls are devoid of any separation regions. As time progresses, this normal shock moves upstream and establishes at a position determined by the mean flow in the nozzle. In the process it goes through a regular reflection as seen in Fig. 3.45(d) at $t = 5ms$. Note that the boundary layer behind the shock at this instant has separated and an expansion shock has formed at the throat indicating that the mean flow upstream of the shock has been established.

The instantaneous schlieren at 7.5 *ms* shows that the separation region on the plug has grown considerably and the shock moved much further upstream. The shock location and the size of the recirculation zone appear to be strongly correlated. Also, note the appearance of shocklets close to the exit in the mean flow in Fig. 3.45(e) between the separated boundary layer and the shroud. The recirculation zone provides a natural converging diverging passage aft of the shock allowing the mean flow to go supersonic again, thus resulting in the shocklets seen at the exit. As the recirculation region is shed from the plug wall the shock moves downstream again as seen in Fig. 3.45(f) at $t=8.8ms$. Following this the shock again returns to the upstream position and the process is repeated. Note that the flow appears to be nearly axisymmetric throughout the initial part of the starting transient.

The same transient behavior can be more concisely shown by space-time plot of pressure in the nozzle. The space-time plot allows the entire transient process plus stationary condition to be depicted in a single picture. Figure 3.46 below shows

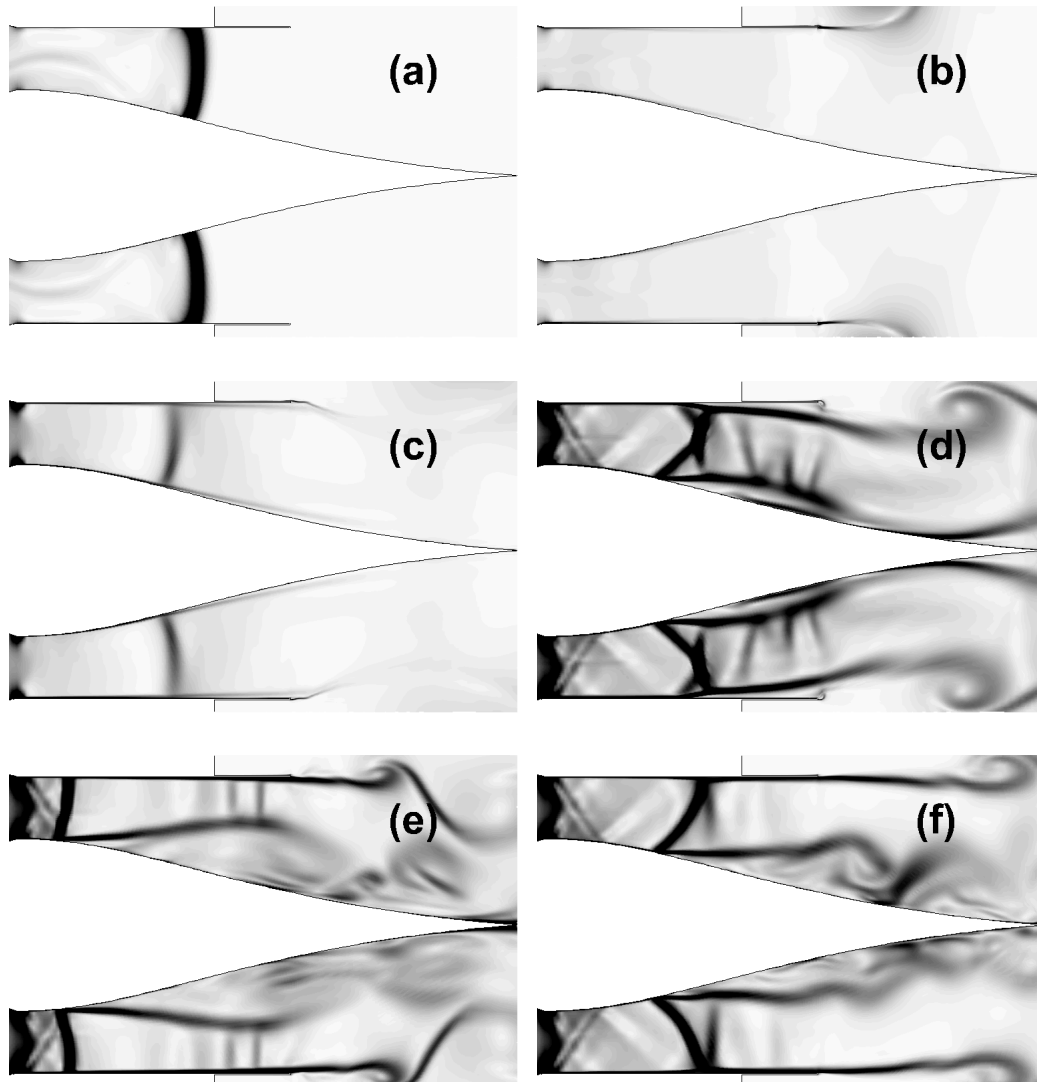


Figure 3.45. Instantaneous schlieren from unsteady computations in a tangential plane depicting the initial transient. Six instants starting at time - a) $1ms$, b) $2ms$, c) $3ms$, d) $5ms$, e) $7.5ms$ and f) $8.8ms$ into the unsteady computation are shown.

the three locations for which the space-time plots are constructed. The line PP' is along the plug wall, line MM' is at a constant radial location passing through the center of the nozzle while SS' is along the inner wall of the shroud. The plots for the plug line, PP' , and nozzle mid-plane line, MM' start from the converging section ($x/L_{plug} = -0.2$) pass through the throat ($x/L_{plug} = 0$) and extend to the

plug tip ($x/L_{plug} = 1.0$). The space-time plot for the shroud, SS' , also starts from $x/L_{plug} = -0.2$ but ends at the shroud tip.

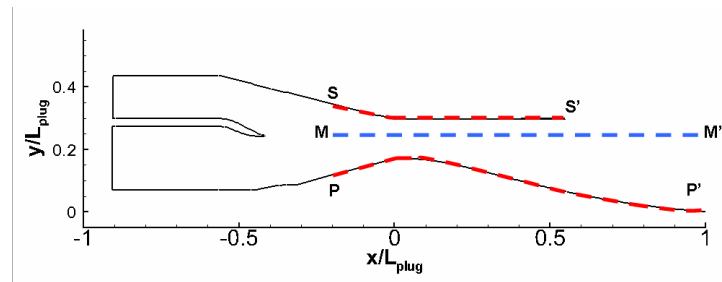


Figure 3.46. Location reference for plug (PP'), mid-plane (MM') and shroud (SS').

The space-time plot for the mid-plane section MM' is given in Fig. 3.47. The black end of the grayscale corresponds to low pressure while the white depicts high pressure. A strong contrast in shade therefore implies a discontinuity (shock wave) in the flow. The time instants at which instantaneous schlieren given in Fig. 3.45 are also marked on the space-time plot for reference. At time zero, the entire nozzle is at ambient pressure and the first disturbance comes from the starting shock which is seen at the bottom of Fig. 3.47. This normal shock sweeps through the nozzle section at approximately constant speed as seen by the light to dark transition that crosses $t=1ms$ (line - a) at about x/L_{plug} of 0.6. This shock is marked by a yellow arrow. Following this shock the throat remains unchoked for a period of time (Fig. 3.45(b)). A shock then forms almost midway through the diverging section at about $5ms$ as shown in Fig. 3.45(c). The shock can be discerned from the contour by noting the region with the strongest change in shade (black to white). The shock instantly moves forward then backward undergoing three oscillations of large amplitude between 5 and $14ms$ and then slowly moves momentarily towards the throat until $t=22ms$ signifying the end of the starting transient.

The results of the initial transient are combined with dynamics in the stationary region in the space-time plot of Fig. 3.48 which is from 0 to $90ms$. According to the locations marked in schematic of Fig. 3.46, Fig. 3.48 shows plots of pressure on the plug,

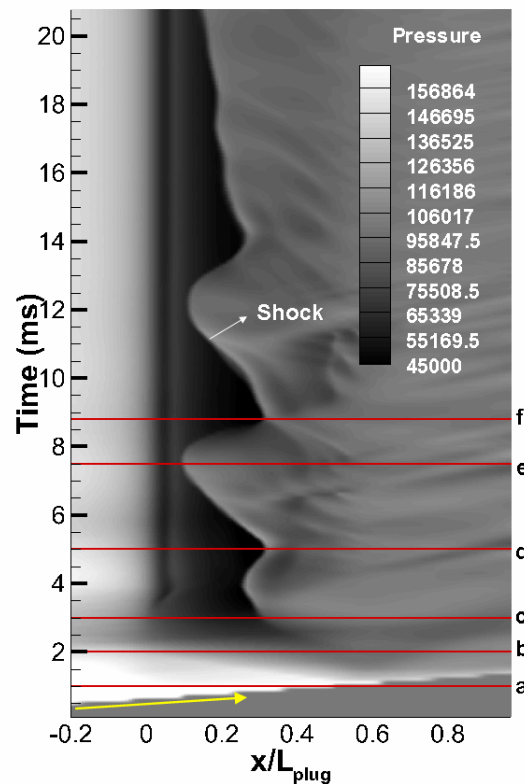


Figure 3.47. Space time plot at MM' location in the plug depicting the transient process and the shock movement. The red lines indicate the time instants at which schlieren images in Fig. 3.45.

shroud and mid-plane for a single azimuth. From these plots it is seen that stationary conditions are reached around $22ms$ after flow start-up. The approximate extent of the transient is marked in the contour plot of the mid-plane. The most prominent flow feature in all the plots is the shock oscillation demarcated by the sharp change in color which is especially precise at the mid-plane. Clearly, three-dimensional unsteady computations do not exhibit the violent oscillations observed in axisymmetric unsteady computations (contrast with Fig. 3.28). The shock amplitude is restricted to approximately 8% of the plug length as compared to axisymmetric computations which showed an amplitude of about 15%. Analyses at different azimuthal positions leads to similar conclusions on shock amplitude.

A strong correlation is observed between the shock movement on the plug, center-line and the shroud indicating the shock front at an azimuthal location moves as one entity with minor radial variations (The sectional views of the plug nozzle confirming this are shown later in Fig. 3.51). It is therefore implied that the pressure oscillation that is driven by shock motion is the same on the plug and shroud. This is important in the extending the analysis of experiments in which pressure was measured on the shroud alone.

The spatial and temporal depiction of the contours of pressure in Fig. 3.48 also allow us to understand the acoustics of the plug nozzle. The space-time plots in the nozzle diverging section clearly exhibits streaks in the region after the shock. These streaks give a sense of direction of propagation of acoustic waves according to the slope of lines. As in axisymmetric unsteady computations we can observe acoustic signals generated at the shock foot propagating in the downstream direction on the plug. The shroud exhibits upstream propagating pressure disturbances which seem to originate at the nozzle exit. The mid-plane space-time plot shows disturbances propagating in both directions which have been marked as 'UA' and 'DA' denoting upstream propagating acoustics and downstream propagating acoustics. These disturbances have been discussed earlier in experimental work related to transonic diffuser channels [25] shown in Fig. 1.4. Thus, the computations appear to predict the correct phenomenon. The acoustic waves generated at the nozzle exit seem to be forming due to the dynamic separation region on the plug wall. As the separation region grows it accelerates the mean flow aft of the shock and between the shroud wall and the shear layer. The flow aft of the shock can reach transonic Mach numbers close to the shroud exit as it passes through this converging portion resulting in the formation of weak discontinuities. These discontinuities propagate upstream and dissipate as they get closer to the shock. Analysis of the entire azimuth of the plug leads to the same conclusions as above for the acoustics.

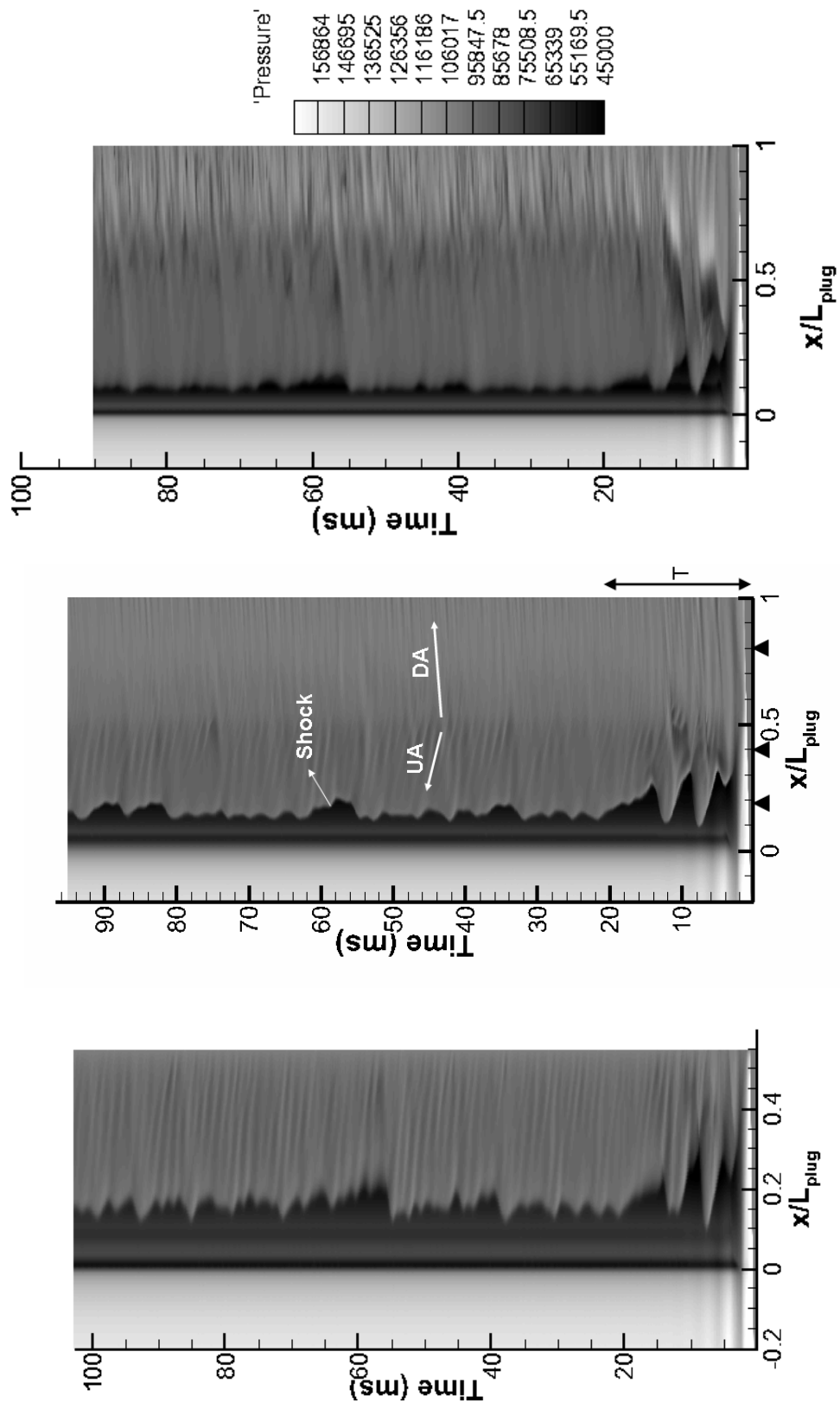


Figure 3.48. Space time plot of pressure on the shroud wall(left), mid-plane(center) and plug wall(right) of the nozzle at NPR of 1.59.

The pressure space-time contour plot in Fig. 3.48 provide some understanding of the mechanics of the shock motion and acoustics in the nozzle. In Fig. 3.49 the variations of pressure on the plug and shroud are shown from the beginning of the computation for five locations. The two locations on the shroud, $x/L_{plug} = 0.18$ and 0.4 shown in the plots coincide with the position of the Kulites on the shroud. Along with these two positions a downstream location of $x/L_{plug} = 0.8$ is also shown for the plug. The location of 0.18 is close to the shock on the shroud while the other location is in the boundary layer. In the case of the plug all three locations are in the recirculation zone. The approximate duration of initial transient has been marked on each plot by the letter 'T'. The initial transient clearly shows strong pressure oscillations due to shock sweeping through the nozzle section before the stationary flow is set up at $220ms$ as discussed earlier with reference to Fig. 3.45. The top plot in Fig. 3.45 which corresponds to the location, $x/L_{plug} = 0.18$ which is near the shock exhibits a low amplitude fluctuation compared to the location $x/L_{plug} = 0.8$ which is close to the plug tip. The locations within the recirculation region on the plug exhibit a low and high frequency. The spectral content of the pressure oscillations is shown in Fig. 3.50. The PSD estimate has been generated by collecting statistics at $10000Hz$ sampling frequency over a period of $80ms$ after the transient. All plots show a peak at $150 Hz$ compared to the Kulite frequency of $200 Hz$ and unsteady axisymmetric frequency of $60Hz$. An additional high frequency appears around $800Hz$ for the plug and shroud in the separation region. A similar analysis at other azimuthal locations found the spectral content to be independent of azimuthal location similar to the Kulite data.

The spectral content at other azimuthal locations showed similar peak frequencies. The instantaneous flowfield, however, may vary from one tangential plane to the other. The flow picture in the diverging section is shown in Fig. 3.51 at four time instants at the same tangential plane. The time instants fall within one period of the Kulite frequency of $200Hz$, thus giving the flow picture over one cycle. The contour plots are schlieren images at equal intervals of $2ms$ starting at $330ms$ into the unsteady

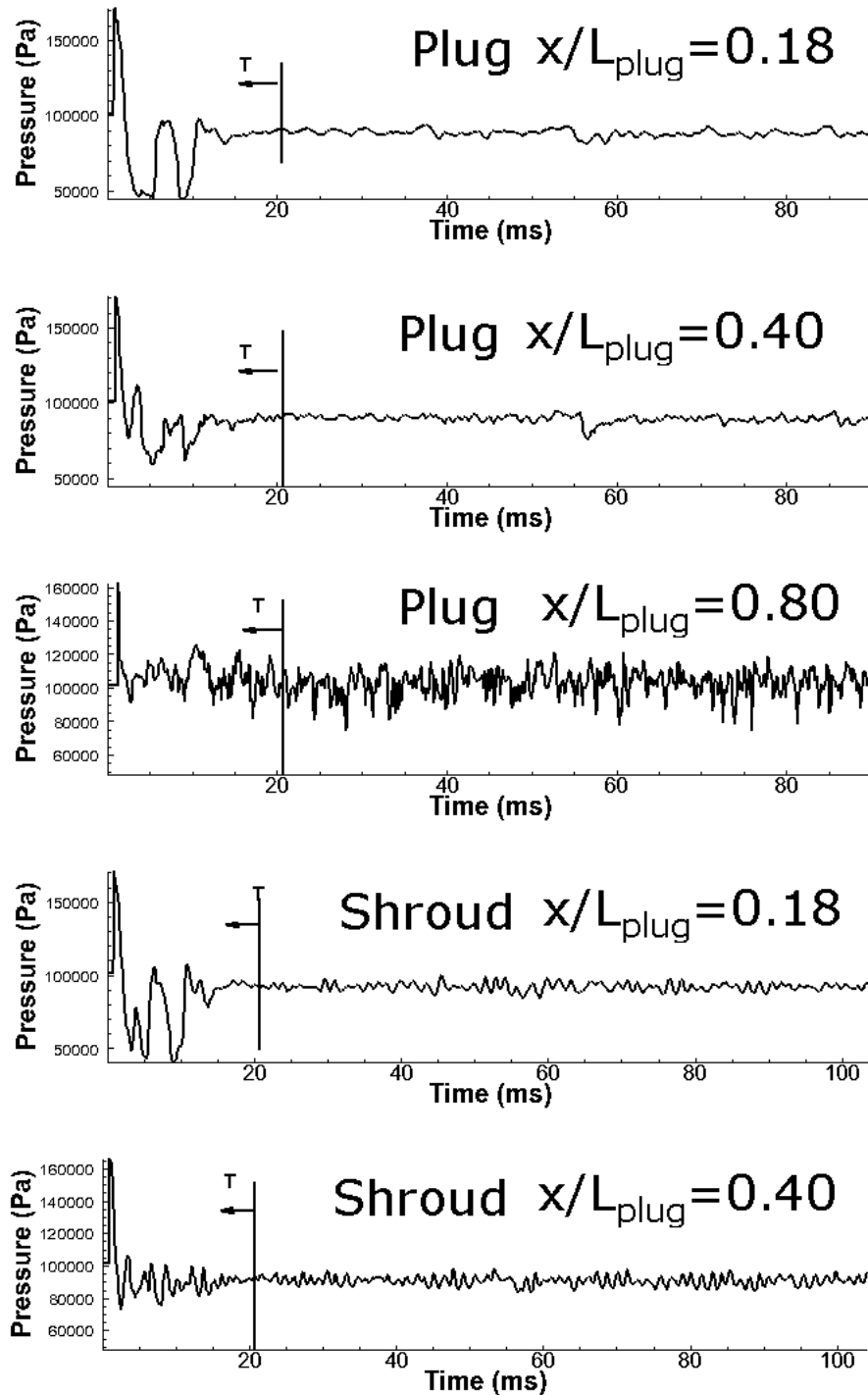


Figure 3.49. Pressure oscillations on the plug and shroud for NPR of 1.59 at the locations indicated on the plug.

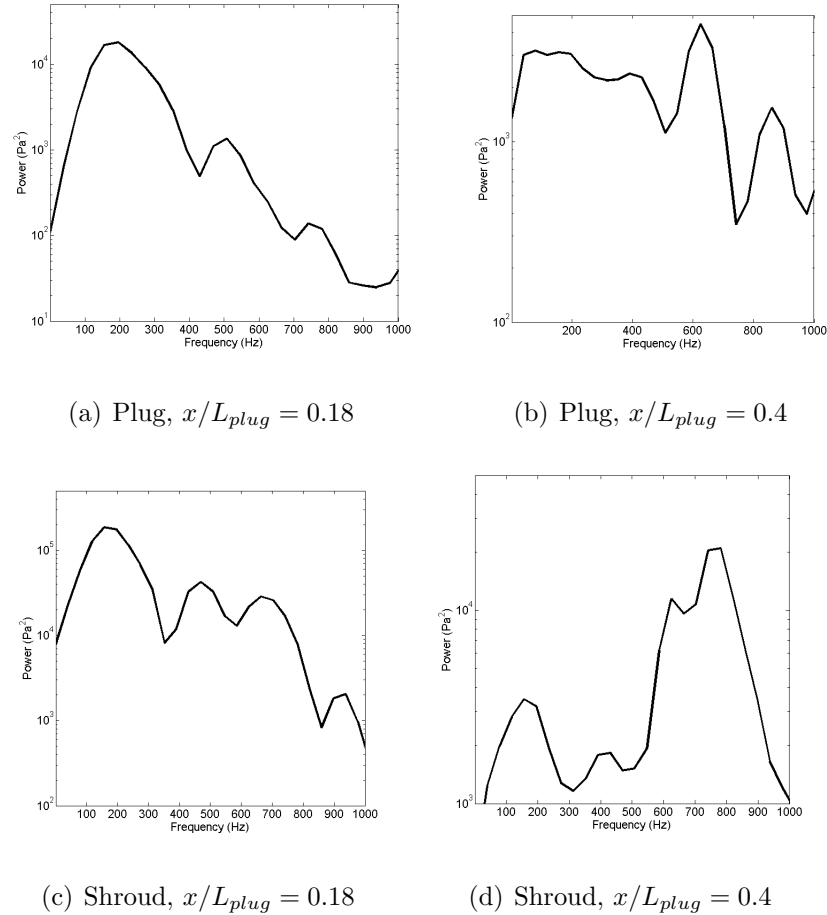


Figure 3.50. Power Spectral density at two locations on plug and shroud for NPR of 1.59.

computation. Comparing the four schlieren images we note that the shock location has not changed significantly. The shock motion occurs at much lower frequency than the pressure oscillation on the plug. Also marked as 'SL' in the plots is the weak upstream propagating acoustic wave. It is seen that the disturbance propagates upstream as time progresses, thus giving a visual confirmation to what has already been observed in the space time plot. Note the asymmetry in the plots from the top half to bottom half which are separated by 180° in the recirculation zone.

The asymmetry in the tangential direction is particularly strong in the behavior of the recirculation zone on the plug wall. This asymmetry is confirmed by looking

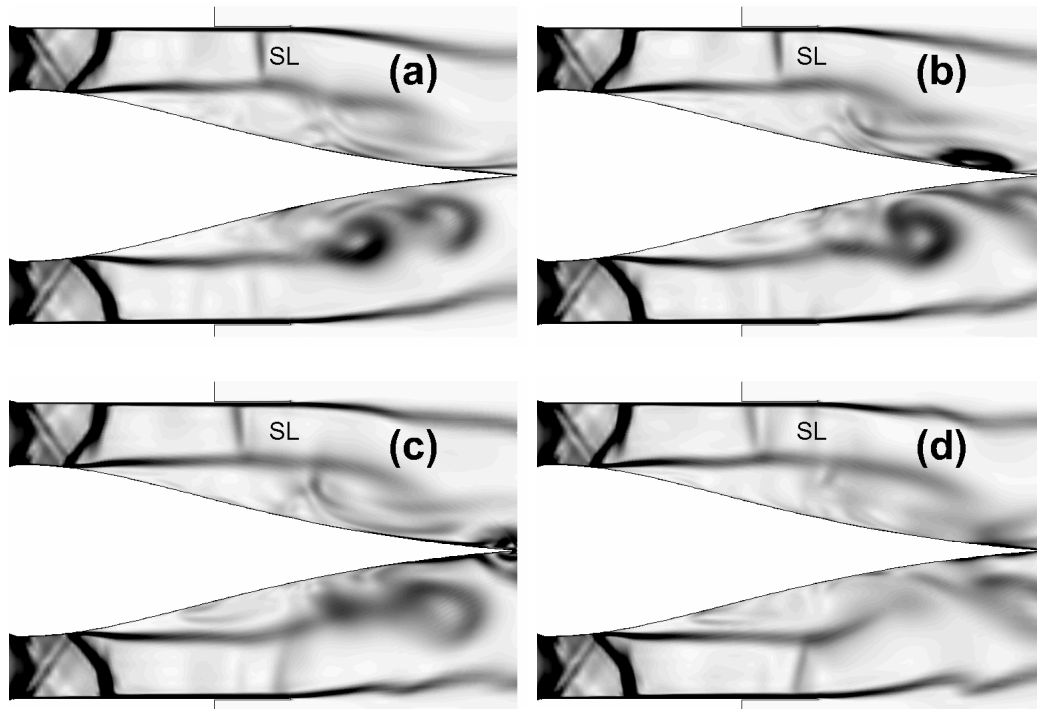


Figure 3.51. Instantaneous schlieren from unsteady computations in a plane. Four instants starting at time, τ are shown - a) τ , b) $\tau+2ms$, c) $\tau+4ms$, d) $t = \tau+6ms$.

at the pressure distribution on the plug and shroud at four different azimuths, in Figs. 3.52 and Fig. 3.53. The azimuthal positions are at 0° , 90° , 180° and 270° an offset of 90° to each other. The pressure distribution from the four azimuthal locations is also compared to the pressure distribution from steady 3-D computations which has been compared against experimental data. The steady 3-D computation which predicted axisymmetric pressure distribution is shown by dotted lines in the plots. The unsteady computations depict strong asymmetry particularly in the separation region. Also, the shock location seems to vary in the tangential direction both on the plug and shroud by a few percent from the mean position seen particularly in the $t = \tau+6ms$ plot. The 3-D unsteady computations predict a variation in the azimuthal direction which cannot be distinguished using axisymmetric unsteady computations.

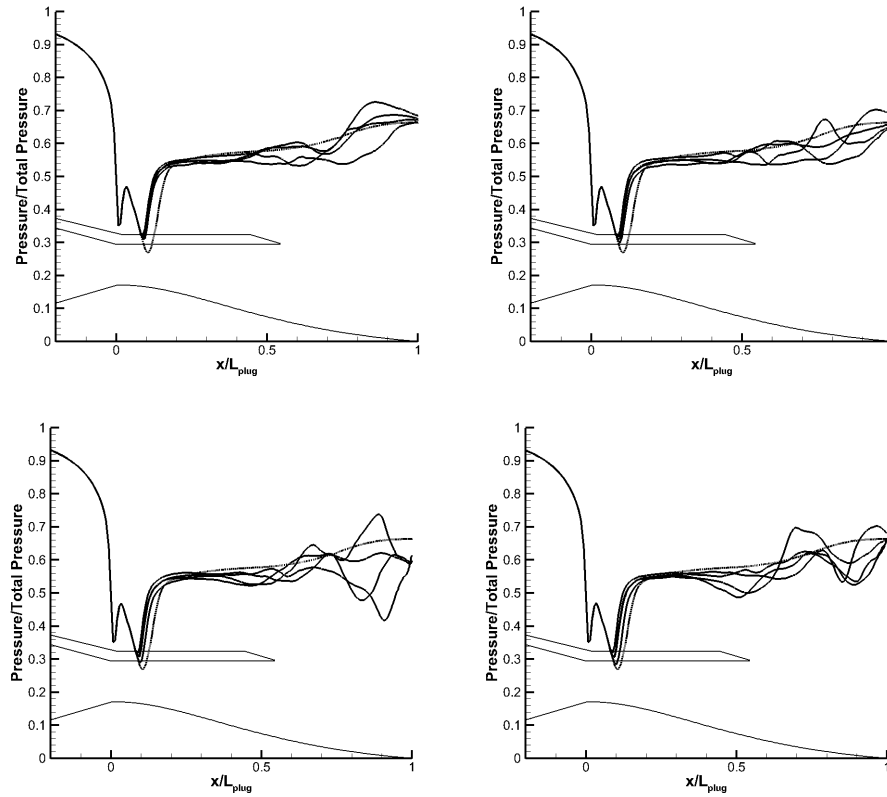


Figure 3.52. Instantaneous pressure distribution (solid) on the plug at four azimuthal locations compared to steady pressure (dotted). Four instants for a frequency of 150 Hz starting at time, τ are shown - a) τ , b) $\tau + 2ms$, c) $\tau + 4ms$, d) $t = \tau + 6ms$.

The data from static pressure probes in the experiments at the three azimuthal locations on the plug as well as the shroud showed that the flow is axisymmetric. The 3-D steady computations also gave the same result. The pressure probes, however, are slow response instruments that give time averaged pressure so it is appropriate to compare the time averaged results from the unsteady computations with experiments. The unsteady computations are averaged over a period of $80ms$ which corresponds to about 16 cycles of the peak Kulite frequency of 200 Hz and shown in Fig. 3.54. The top figure is a comparison of the 3-D time averaged schlieren with its 3-D steady counterpart. Both the plots are compared at a single azimuth. The time-averaged results capture the expansion fan and the supersonic region at the throat section.

The shear layer from the shroud tip appears thicker than the steady computations due to vortex shedding from the tip. The time-averaged static pressure distributions on the plug and shroud are compared in Figs. 3.54(b) and Fig. 3.54(c) with the time-averaged axisymmetric unsteady and 3-D steady computations. For the time-averaged unsteady 3-D computations the pressure distributions from four azimuths are shown as was done earlier (0° , 90° , 180° and 270°). Also shown as symbols are the data from static pressure probes.

The first conclusion is that the pressure distribution at the four azimuths is similar for the 3-D unsteady time-averaged for both plug and shroud. The pressure distributions from the four azimuths collapse to single line in Fig. 3.54. Though the instantaneous pressure on the plug and the shroud was tangentially asymmetric (Fig. 3.52 and Fig. 3.53) the steady flow depicted by time-averaging of the 3-D unsteady computations is axisymmetric similar to the static pressure probe data. The shock location on the plug is predicted close to the data by all the three computations. The pressure in the separation region predicted by the time-averaged 3-D are closer to the data than the time averaged 2-D axisymmetric result. The shock location on the shroud is under-predicted by the 3-D time averaged result but the pressure in the recirculation zone is recovered well compared to the 3-D steady and time-averaged unsteady 2-D axisymmetric computations.

In summary, the unsteady 3-D computations show that the tangentially flowfield is asymmetric particularly in the recirculation region on the plug at $NPR = 1.59$. The steady results constructed by time-averaging the unsteady data predicted axisymmetric flowfield. This is in agreement with both the steady three-dimensional computations as well as the data which showed axisymmetric pressure distribution. The shock motion amplitude in the case of 3-D unsteady computations is smaller than that of 2-D unsteady computations. The frequency predicted by the 3-D unsteady computations is closer to the experimental value than that predicted by the axisymmetric computations implying that 3-D nature of the recirculation is an important aspect for pressure oscillations on the plug.

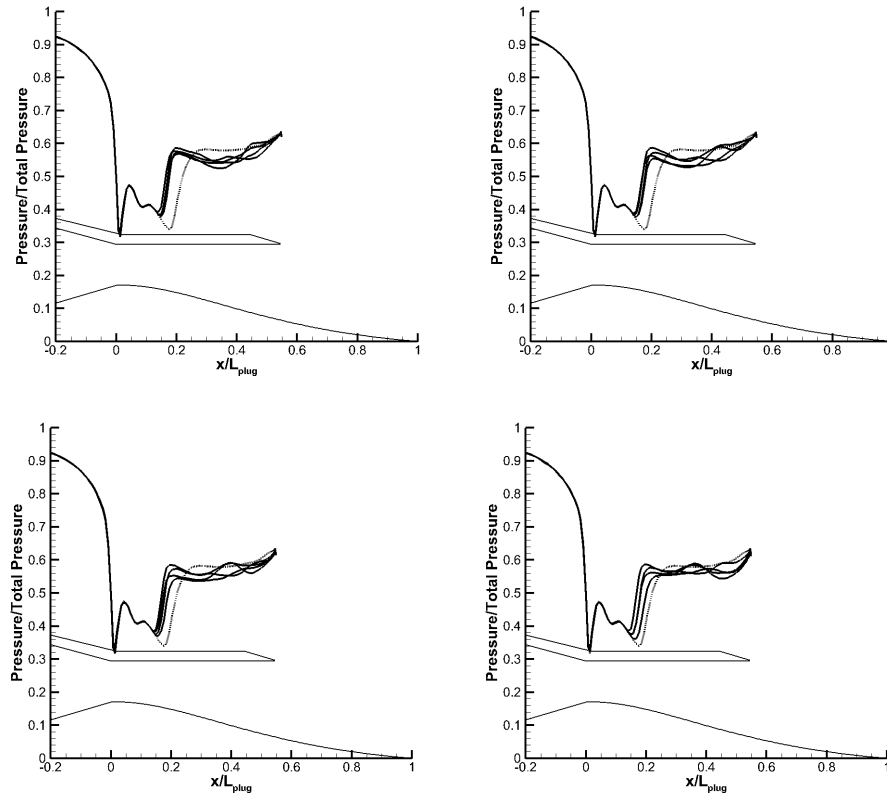


Figure 3.53. Instantaneous pressure distribution(solid) on the shroud at four azimuthal locations compared to steady pressure(dotted). Four instants for a frequency of 200 Hz starting at time, τ are shown - a) τ , b) $\tau+2\text{ ms}$, c) $\tau+4\text{ ms}$, d) $t = \tau+6\text{ ms}$.

3.8.2 Unsteady Results at $\text{NPR} = 1.26$

The Kulite pressure transducers indicated that the peak oscillation frequency reduced to 170 Hz for an NPR of 1.26 . The unsteady axisymmetric computations showed distinct behavior compared to NPR of 1.59 in the form of nozzle unchoking. Figure 3.42 which showed the convergence of Unsteady 3-D computations for $\text{NPR} = 1.26$ also showed oscillatory convergence indicative of unsteadiness in the flow. The unsteady solution is set-up as discussed in the beginning.

As was done for the case of NPR of 1.59 , Fig. 3.55 shows the space-time plots of the pressure on the plug (PP'), shroud (SS') and mid-plane (MM') as indicated in the

schematic in Fig. 3.46. The initial transient behavior is similar to that at NPR pf 1.59. The shock oscillation pattern after the initial transient is highly periodic with large amplitude. A distinct feature of this NPR is that the shock in the diverging section moves upstream of the throat and the plug nozzle remains at shock free conditions. This pattern appears periodically in all the three locations shown in Fig. 3.55.

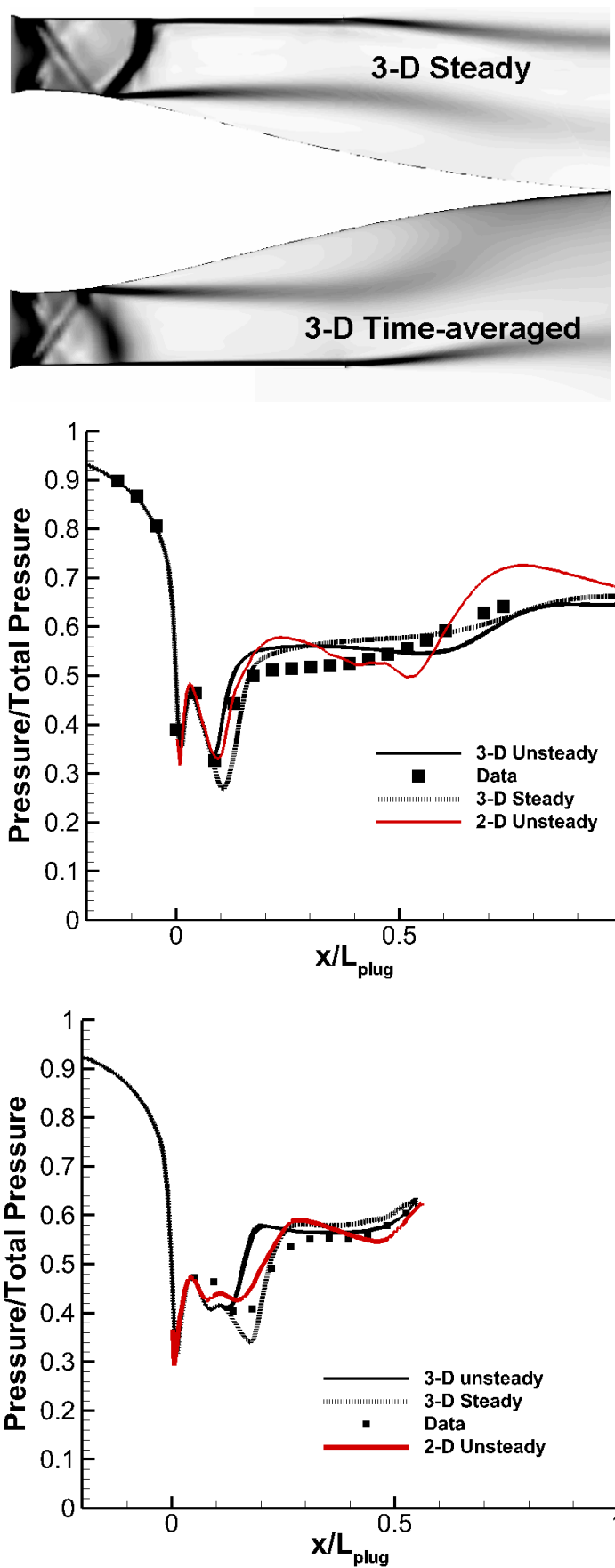


Figure 3.54. NPR=1.59. Time-averaged schlieren from 3-D and 2-D unsteady compared to 3-D steady. Time-averaged Solid lines - avg. unsteady, dotted line - steady computations, symbols - data.

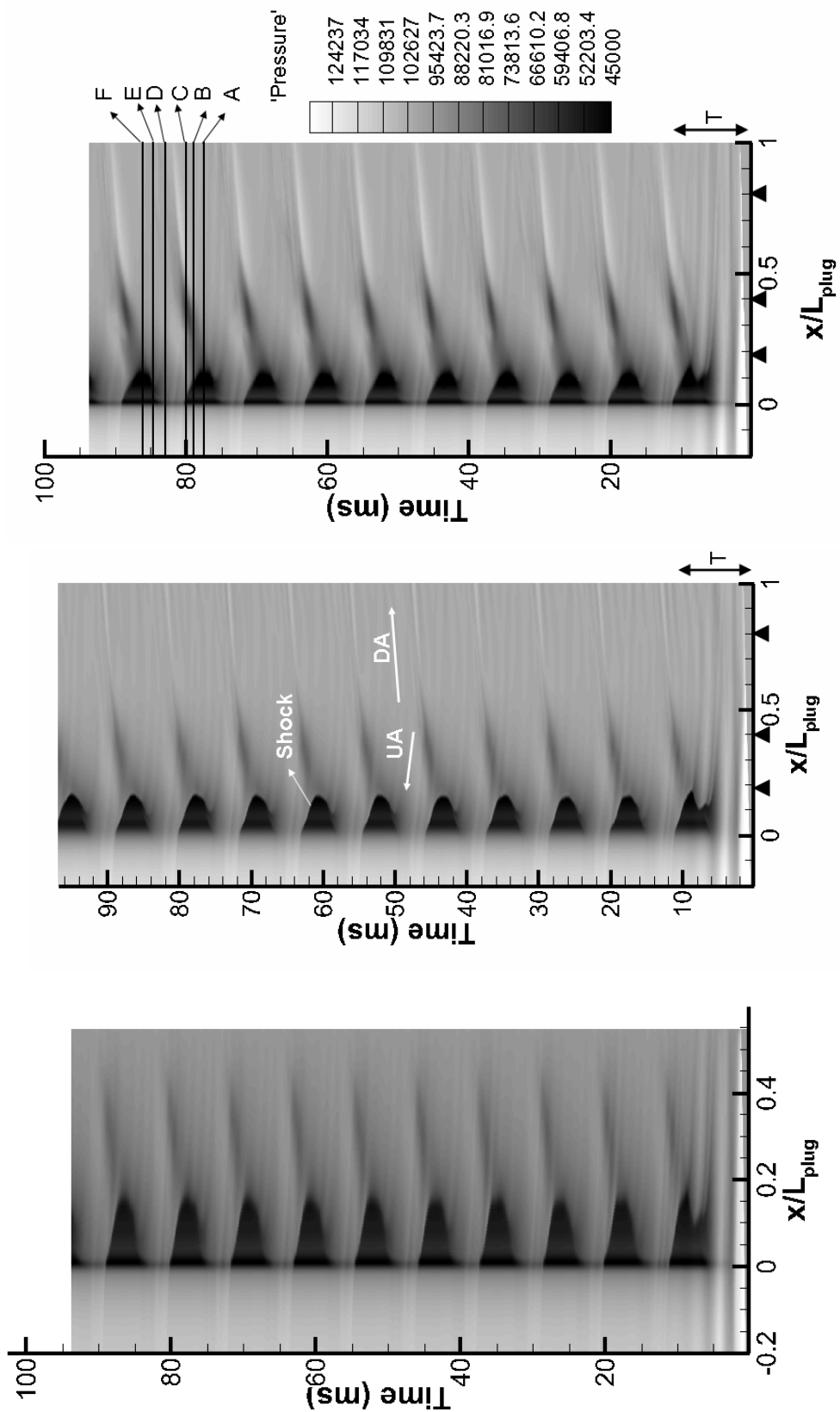


Figure 3.55. Space time plot of pressure on the shroud(left), mid-plane(center) and plug (right) of the nozzle at NPR of 1.26. (Legend for all contours at the end.)

The entire sequence of shock motion in the plug is visualized in Fig. 3.56 by means of a series of instantaneous schlieren images taken from the plane in the nozzle. The schlieren images start from a point where the shock is at its most downstream location. The time instants at which the schlieren images are shown are marked on the right of Fig. 3.55(c). The first picture in Fig. 3.56 shows the shock at its most downstream location with the separation region following the plug contour closely. In the next instant, $15ms$ later, the shock has moved upstream and at the same time the separation region has thickened. At the time instant, $t = \tau + 25ms$, the separation region has begin to roll-up and ready to shed(Fig. 3.56(c)). In Fig. 3.56(d), the shock has moved upstream of the throat and the throat has unchoked. The throat remains at subsonic conditions for the next $18ms$ until another shock is formed in the diverging section. The separation region on the plug wall has shed as shown in Fig. 3.56(e). This shock gains in strength as it performs the downstream leg of the oscillation. It, therefore appears that this periodic behavior is driven by the separation region on the plug. As the separation region changes its size the downstream boundary condition at the nozzle exit varies. The shock location adjusts its position accordingly depending on the downstream condition, thus undergoing oscillations. The shock oscillation amplitude is about 12% of the plug length which is significant compared to higher NPR's.

The upper and lower halves of the unsteady schlieren which are at an offset of 180° are identical to each other except for minor variations. This is unlike the case of NPR of 1.59 in Fig. 3.51 which showed asymmetry in the separation region. The axisymmetric nature of the 3-D unsteady simulations is confirmed when the instantaneous pressure distribution on the plug at four azimuthal locations is shown in the same plot and compared against steady 3-D computations. The steady 3-D computations predicted axisymmetric flow. This is shown in Fig. 3.57 which are for the same time instants shown in Fig. 3.56. The pressure distributions at the four azimuthal locations from the unsteady computations collapses onto a single line proving the axisymmetric nature of the flow. Minor differences are seen in Fig. 3.57(c) in the

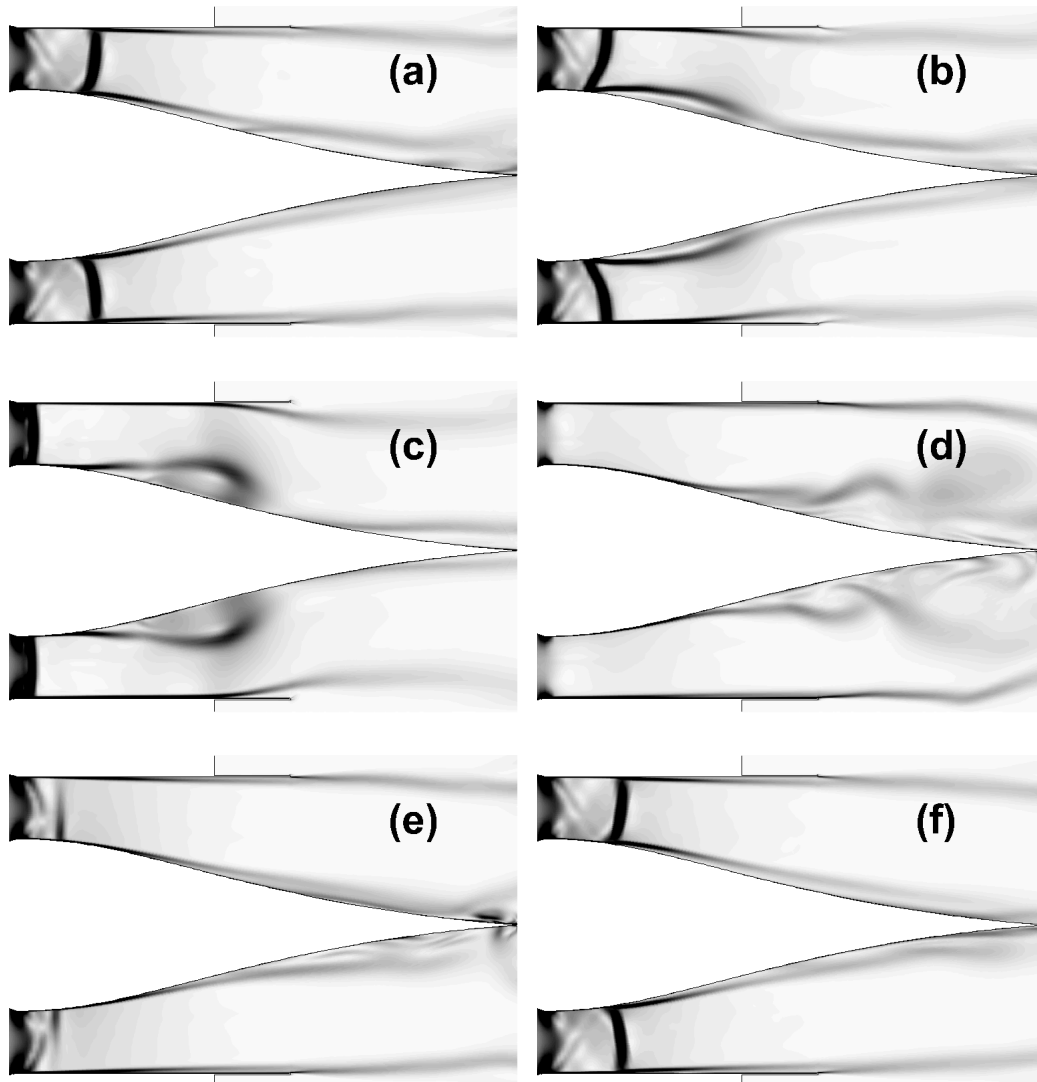


Figure 3.56. Instantaneous schlieren images at a plane in the nozzle depicting shock motion starting from the farthest downstream shock location at time, τ - a) τ , b) $\tau+15ms$, c) $\tau+25ms$, d) $t = \tau+54ms$, e) $t = \tau+72ms$ and f) $t = \tau+86ms$.

position where the separation region exists on the plug (Fig. 3.56(c)). It also appears that the vortex shedding pattern closely matches the movement of the second weak pressure rise seen in Fig. 3.53(d). This can also be seen as a distinct disturbance propagating in Fig. 3.55(c) from the instant when shock is at its most downstream position (marked by A) and propagating downstream along the plug surface. An

analysis of other azimuthal locations confirms the axisymmetric nature of the flow at this NPR and might explain why the axisymmetric unsteady computation gave good predictions. Similarly the shroud pressure distribution was also found to be axisymmetric.

In Fig. 3.58 the pressure oscillation on the shroud and the plug are shown. Clearly, a low frequency periodic behavior is seen at all the locations. A sharp rise is seen in pressure at location $x/L_{plug} = 0.18$ when the shock passes this location and the pressure drops gradually. The pressure at locations 0.4 and 0.8 show a sharp decrease or increase when the acoustic wave generated by the shedding recirculation passes the plug. The power spectral density plots for the location $x/L_{plug} = 0$ on the plug and the shroud are shown in Fig. 3.59. This time the peak lies at a frequency of $120Hz$ in comparison to a frequency of $170Hz$ from Kulite data. The axisymmetric unsteady computations predicted a frequency of $110Hz$. Again, the axisymmetric flowfield of unsteady 3-D computations explains why the axisymmetric computations gave the same frequency at this NPR.

In Fig. 3.57 the variation of pressure in the azimuthal direction for one cycle were depicted. In Fig. 3.57 the shock location can be seen to oscillate about the mean position which is given by the shock location of the steady 3-D computations. The time-averaged flowfield from the unsteady computations will provide the steady picture. Figure 3.60 compare times averaged results from 3-D unsteady computations with their 2-D counterpart. The time-averaged result have been obtained by averaging unsteady result over a period of $80ms$ after the initial transient. Also shown is the data from experiments and 3-D steady computations. Starting at the top with the comparison of the 3-D steady schlieren compared to the time-averaged 3-D unsteady schlieren picture, the salient flow features match. The expansion fan and the supersonic conditions at the sharp corner are present in both results. The shock from time-averaged 3-D unsteady computations appears at a downstream location compared to the steady 3-D computations. The separation region over the plug in the time-averaged case is larger than the steady part which can be explained in part due

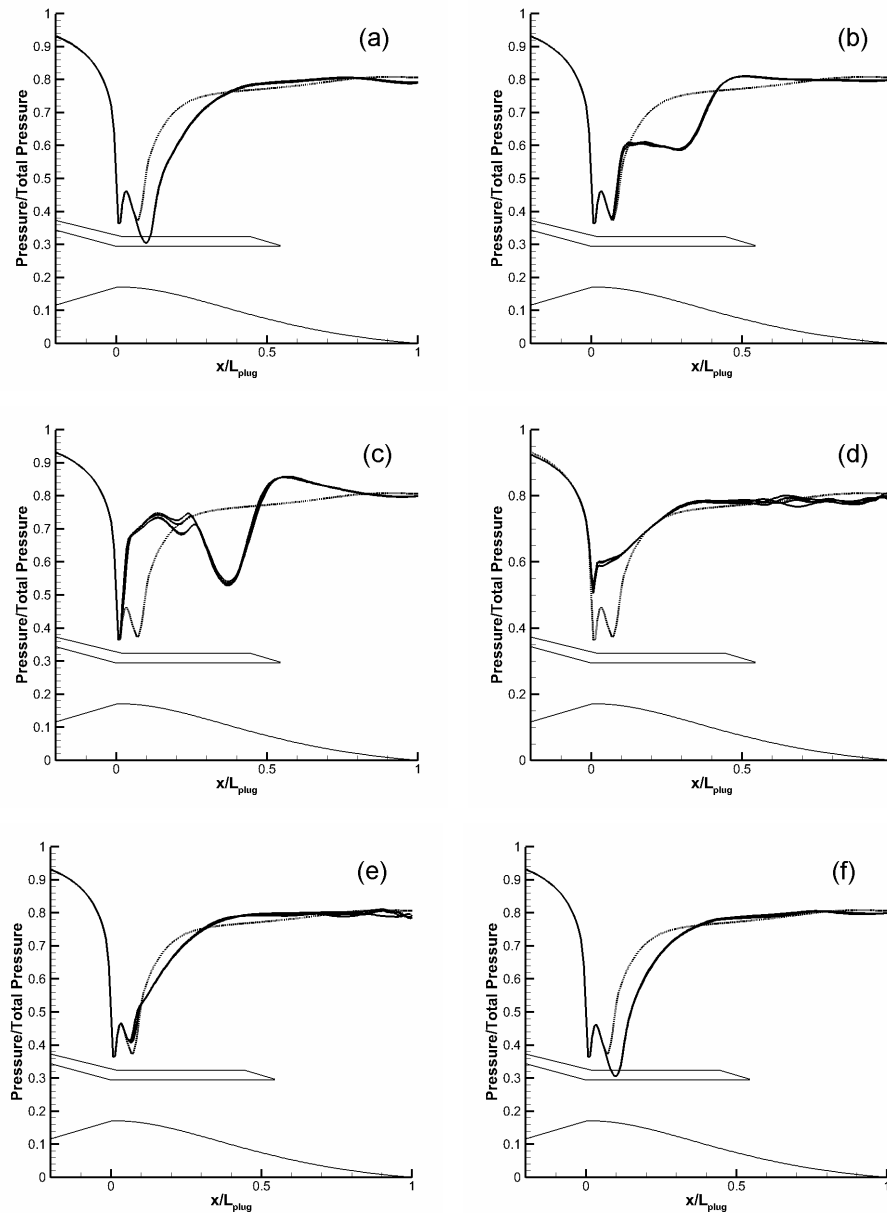


Figure 3.57. Instantaneous pressure distribution (solid) on the plug surface at four azimuthal locations compared to steady pressure (dotted) during a cycle of shock motion starting from the farthest downstream shock location at time, τ - a) τ , b) $\tau + 15ms$, c) $\tau + 25ms$, d) $t = \tau + 54ms$, e) $t = \tau + 72ms$ and f) $t = \tau + 86ms$.

to the dynamic recirculation zone seen in Fig. 3.57. Following the schlieren comparison in Fig. 3.60, plots of pressure distribution on the plug and shroud surface are

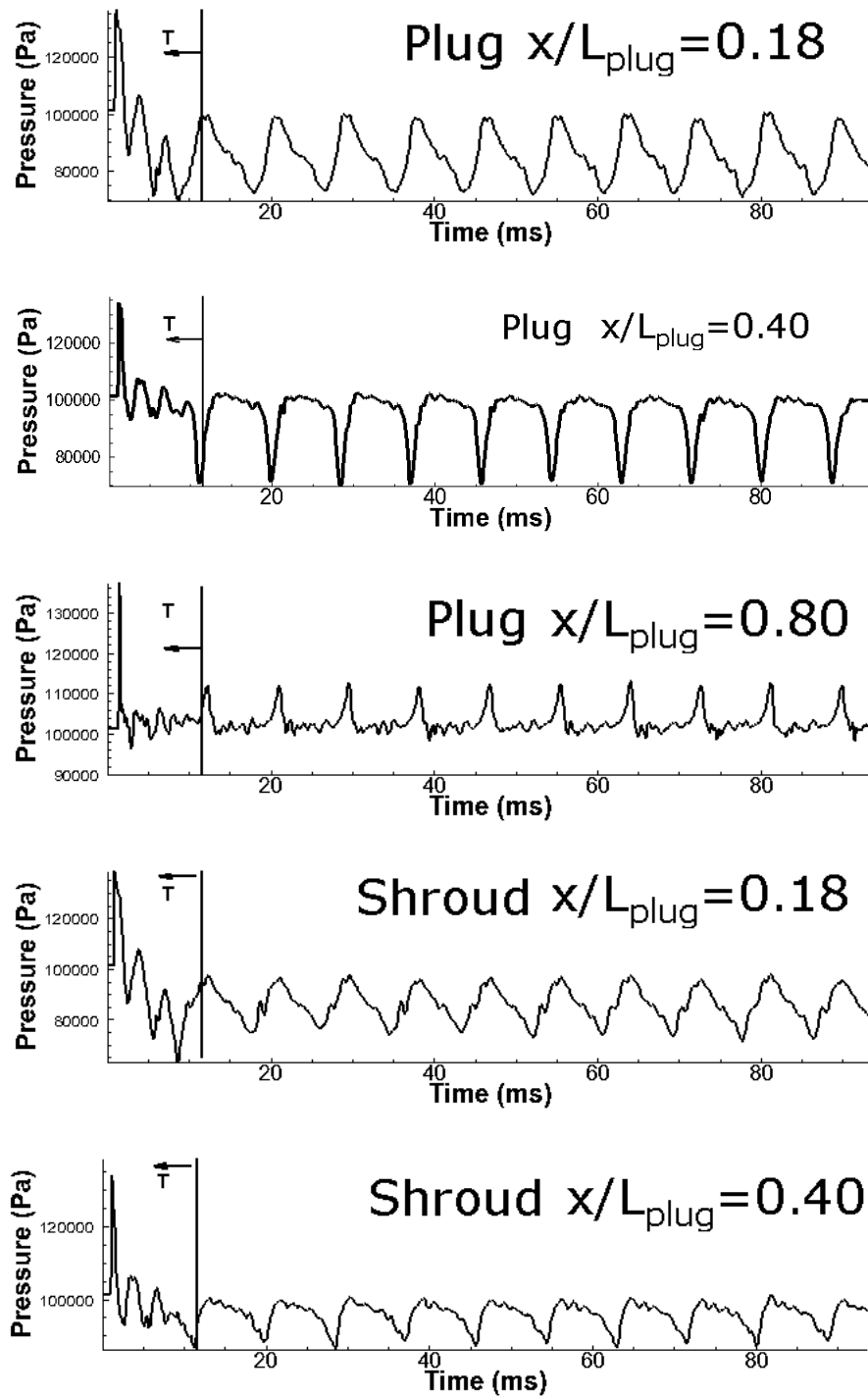


Figure 3.58. Pressure oscillations on the plug and shroud for NPR of 1.26.

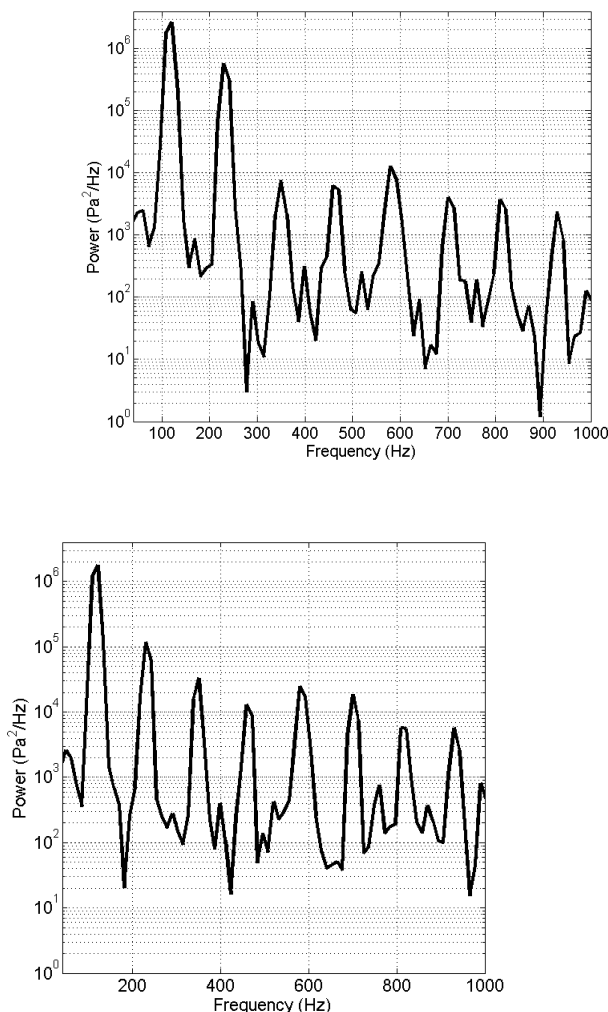


Figure 3.59. Power Spectral density at $x/L_{plug} = 0.18$ on plug(top) and shroud(bottom).

given. In both figures the pressure distribution at four azimuthal locations, each offset by 90° is shown from the time-averaged 3-D unsteady. The pressure distribution from the steady computations is also presented for comparison. The pressure distribution for the four azimuthal locations from the 3-D unsteady computations again overlap each other. Again, time-averaged unsteady three-dimensional computations also predict axisymmetric flow after time averaging similar to NPR case of 1.59. The pressure distribution on the plug as well as the shroud closely match with the data as

well as the 2-D time averaged data. Schlieren from time-averaged 3-D unsteady data show a weaker shock compared to steady data. This is also evident from the weak pressure rise compared to steady computations in Fig. 3.60.

The 3-D unsteady computations showed a cycle of shock oscillation characterized by shock free conditions in the diverging section. The oscillations occurred at a more regular interval compared to the axisymmetric unsteady computations. These are aspects which cannot be captured using steady computations. Transonic diffusers at very low NPR's have shown shock free conditions during shock oscillation cycles [25]; [22] (Fig. 1.4). The flowfield is tangentially symmetric for 3-D unsteady computations which explains the frequency match with unsteady axisymmetric computations. The frequency of 120Hz predict by 3-D unsteady computations is the same at any location aft of the shock on the plug and shroud wall. The Kulite frequency of 170Hz on the shroud can therefore be extended to plug surface which did not have any Kulite instrumentation. The shock free conditions for the shock oscillation cycle might explain the lower frequency of 170Hz from Kulite data compared to higher NPR's. The time-averaged data from both unsteady 3-D and axisymmetric computations matched closely with the data on both the plug and the shroud.

3.9 Performance Analysis

The flux of gases at a nozzle exit causes a thrust (F) or reaction force on the nozzle structure. This being the sole duty of the nozzle it is important that its performance be quantified against an ideal nozzle thrust. The nozzle discharge coefficient (C_d) and the thrust efficiency (η_F) are important performance metrics for a nozzle. The discharge coefficient C_d is the ratio of the measured mass flow rate to the theoretical mass flow rate that can be achieved for a given throat area. The thrust efficiency is the ratio of the measured thrust to the ideal thrust that can be obtained. It is usually determined in terms of the ratio of measured thrust coefficient to the ideal thrust coefficient. The thrust coefficient (C_f) can be thought of as representing the

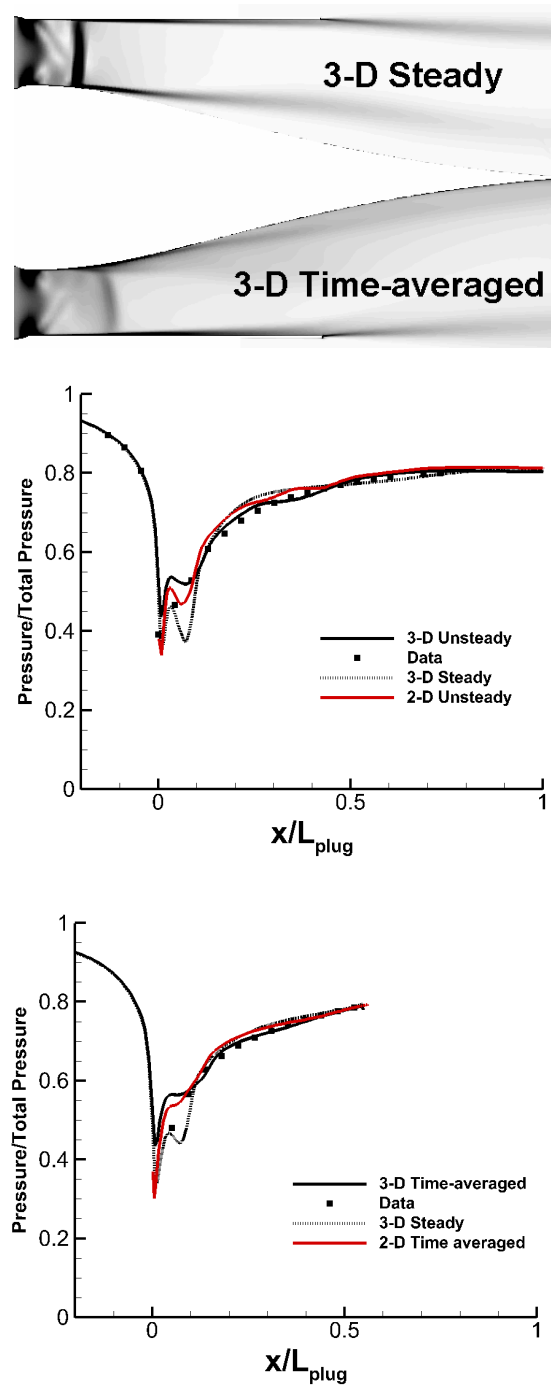


Figure 3.60. NPR=1.26. Time-averaged schlieren from 3-D and 2-D unsteady compared to 3-D steady. Time-averaged Solid lines - avg. unsteady, dotted line - steady computations, symbols - data.

amplification of thrust due to the gas expanding in the supersonic nozzle as compared to the thrust that would be exerted if the nozzle chamber pressure acted over the throat area alone. Both of these parameters are deduced from the computational results in this section. The relatively close agreement between the steady axisymmetric computations and the three dimensional computations, allows us to work with axisymmetric predictions for the performance analysis. The experimental data are obtained from the work of Chase [41] who reported both metrics, C_d and η_F for the nozzle.

The ideal nozzle thrust is achieved when the exiting gases expand in a one-dimensional fashion. Due to losses associated with over-expansion or under-expansion, this is seldom achieved in an actual nozzle. In over-expanded nozzles the losses due to reduced exit velocity overwhelm those due to the pressure force at exit. In the case of an under-expanded nozzle the pressure force at the exit is lower than ideal. Also, 2-D effects become important in actual nozzles. The thrust coefficient is a standard metric used to measure nozzle performance. The thrust coefficient, C_f , given by,

$$C_f = \frac{F}{p_0 * A_t} \quad (3.1)$$

is a function of gas property, the nozzle throat area, A_t and the operating NPR of the nozzle.

The discharge coefficient (C_d) depends on the working fluid, the nozzle area ratio and the flow conditions. It can also be considered as a metric to express the mass flow rate that can be realized in the nozzle. The viscous losses that occur in the nozzle and the heat conduction at the nozzle surface result in a total pressure loss which result in lower mass flow rate. It is given by,

$$C_d = \frac{\dot{m}_{meas}}{\dot{m}_{theo}} \quad (3.2)$$

with m_{meas} being the measured mass flow rate and m_{theo} being the theoretical mass flow rate.

The discharge coefficient C_d is less than one due to friction associated losses, which result in a drop in total pressure. Since the friction coefficient is also a function of roughness it is likely that area which is not smooth can also cause losses.

The shrouded configuration draws its working fluid from two streams: a hot core stream and a bypass stream. In the presence of two streams it is very difficult to define either C_d or C_f which rely on a definition of ideal condition. The ideal condition depends on the degree of mixing achieved between the two streams. Also even in 1-D flow both the streams may not be choked at the throat. For this reason, two extremes were considered in [41]: entirely unmixed streams and completely mixed streams. The unmixed assumption is employed by considering separate core and bypass streams that share the flow area at the nozzle throat. This data reduction scheme will, therefore, be referred to as 'area-based (*a*-based)'. In contrast, the perfectly mixed assumption employs mass-averaged properties of the entering core and bypass streams to determine flow conditions at the nozzle throat. This data reduction scheme will, therefore, be referred to as 'mass-based (*m*-based)' through the remainder of this document.

The nozzle is operated with 810K for the hot core flow while the bypass stream is at 280K on an average based on experimental data. The core stream properties were determined using the CEA thermo-chemistry code and reported in the experiments. Accordingly, the hot core ratio of specific heats γ is set to 1.33. The solution is set up as discussed earlier in the context of axisymmetric computations.

The computations which do not follow either approach but show partial mixing. For example, Fig. 3.61 shows the radial total temperature variation at the throat normalized by the upstream core total temperature as a function of radial distance normalized by the plug length. The upper portion of the flow is colder due to the bypass stream while the lower portion is at the core temperature. Complete mixing (*m*-based) would have given a uniform total temperature profile at the throat whereas no mixing (*a*-based) would have resulted in a sharp change in temperature at the interface of the two streams. The gradual change in the temperature from the cold

to hot stream through the shear layer shows partial mixing of the streams. Clearly, the results are closer to the unmixed approximation than the fully mixed one. The total temperature profiles were similar across the entire NPR spectrum.

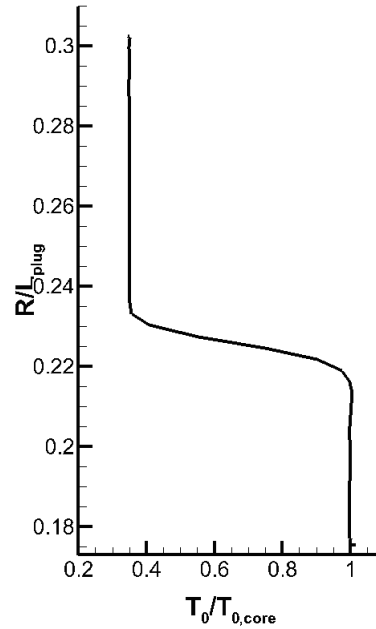


Figure 3.61. Total temperature profile at the nozzle throat normalized by upstream core temperature.

In the following sections we discuss the calculation of the nozzle discharge and thrust efficiencies using results from the steady computations. The calculation of both quantities in experiments and computations is done in a similar fashion and are compared with each other.

3.9.1 Nozzle Thrust Efficiencies

The theoretical exhaust velocities (V_e) of each stream may be determined as,

$$V_e = \sqrt{\frac{2\gamma RT_t}{\gamma-1} \left[1 - \left(\frac{1}{NPR} \right)^{\frac{\gamma-1}{\gamma}} \right]} \quad (3.3)$$

knowing individual stream total temperatures (T_t), ratios of specific heats (γ), specific gas constants (R) and NPR's from 1-D analysis.

In accordance with the altitude compensating nature of the plug nozzle design, perfect expansion of each stream is assumed for all operating conditions, and the theoretical thrust produced by each stream $F_{theor,A-based}$ is then solely comprised of jet thrust:

$$F_{theor,A-based} = (\dot{m}V_e)_{core} + (\dot{m}V_e)_{byp} \quad (3.4)$$

where \dot{m} corresponds to the measured or computed mass flowrate through the stream. Thrust efficiency assuming unmixed streams, $\eta_{F,A-based}$ may then be defined,

$$\eta_{F,A-based} = \frac{F_{z,meas}}{F_{theor,A-based}} \quad (3.5)$$

as the ratio of measured axial thrust $F_{Z,meas}$ to theoretically produced jet thrust.

The assumption of perfectly mixed core and bypass streams naturally leads to an evaluation of nozzle thrust efficiency in terms of the traditional thrust coefficient. The measured thrust coefficient, $C_{f,meas}$ may be determined using Eq. 3.6,

$$C_{f,meas} = \frac{F_{z,meas}}{\bar{p}_t A_{throat}} \quad (3.6)$$

where the stagnation pressure, \bar{p}_t at the nozzle throat (the cross-sectional area of the A_{throat}) is estimated as the mass-average of the core and bypass stream inlet stagnation pressures.

The ideal thrust coefficient ($C_{f,ideal}$) is given by,

$$C_{f,ideal} = \sqrt{\frac{2\bar{\gamma}^2}{\bar{\gamma}-1} \left(\frac{2}{\bar{\gamma}+1}\right)^{\bar{\gamma}+1/\bar{\gamma}-1} \left[1 - \left(\frac{1}{NPR}\right)^{(\bar{\gamma}-1)/\bar{\gamma}}\right]} \quad (3.7)$$

from the mass-averaged ratio of specific heats and the NPR.

Nozzle thrust efficiency assuming perfectly mixed streams $\eta_{F,m-based}$ may be defined,

$$\eta_{F,m-based} = \frac{C_{f,meas}}{C_{f,ideal}} \quad (3.8)$$

as the ratio of the measured thrust coefficient to the ideal thrust coefficient.

The axial thrust force is obtained from the computations as the sum of gas force at the nozzle exit and the integration of pressure on the plug contour taking into account the effect of the environmental pressure on the nozzle. Therefore, we have,

$$F_{thrust} = \dot{m}V_e + (p_{shroudeexit} - p_{atm}) A_{shroudeexit} + \int_{shroudeexit}^{tip} (p_{plug} - p_{atm}) dA \quad (3.9)$$

where the first two terms together are the gas force and the last term is the surface force on the plug.

Axial thrust efficiencies determined from the perfectly mixed and unmixed streams from data and computations are plotted in Fig. 3.62. As one may expect, axial thrust efficiency reaches a maximum at the design NPR.

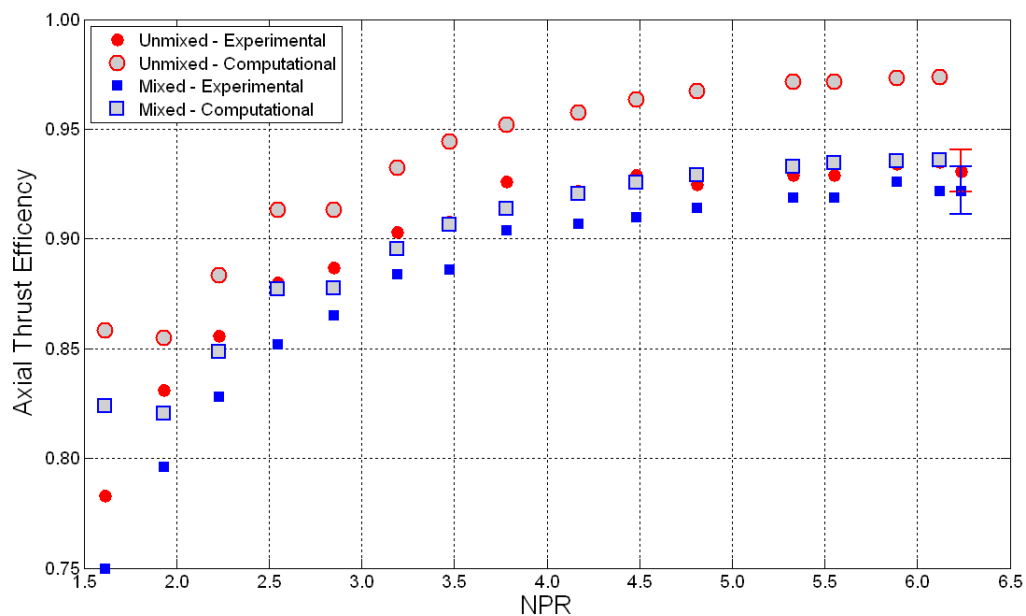


Figure 3.62. Experiment vs. Predicted thrust efficiency: area and mass based.

3.9.2 Nozzle Discharge Coefficient

The area based discharge coefficients have been obtained in [41] assuming choked bypass flow. Assuming a Mach number of unity, the mass flow parameter of the bypass stream $MFP_{8,byp}$ may be written:

$$MFP_{8,byp} = \left[\sqrt{\frac{\gamma}{R}} \left(\frac{\gamma + 1}{2} \right)^{\frac{\gamma+1}{2(1-\gamma)}} \right]_{byp} \quad (3.10)$$

where station 8 is assumed to be the physical throat location per the common notation used in gas turbine literature. The theoretical throat area of the bypass stream $A_{8,byp}$ may be determined as,

$$A_{8,byp} = \left(\frac{\dot{m}\sqrt{T_t}}{MFP_{8,byp}p_t} \right)_{byp} \quad (3.11)$$

with knowledge of the bypass mass flowrate (\dot{m}), inlet total temperature T_t , and inlet total pressure p_t and the assumption of identical throat and inlet stagnation conditions.

The static pressure at the nozzle throat p_8 is determined from the bypass stream total pressure,

$$p_8 = \left[p_t \left(\frac{\gamma + 1}{2} \right)^{\frac{\gamma}{1-\gamma}} \right]_{byp} \quad (3.12)$$

making use of the assumption of choked bypass flow.

The theoretical throat Mach number of the hot core stream $M_{8,core}$ is determined as,

$$M_{8,core} = \left\{ \sqrt{\left[\left(\frac{p_t}{p_8} \right)^{\gamma - 1/\gamma} - 1 \right] \frac{2}{\gamma - 1}} \right\}_{core} \quad (3.13)$$

with the core stream inlet total pressure from Eq. 3.13.

A core stream throat MFP

$$MFP_{8,core} = \left[\sqrt{\frac{\gamma}{R}} M_8 \left(1 + \frac{\gamma - 1}{2} M_8^2 \right)^{\frac{\gamma+1}{2(1-\gamma)}} \right]_{core} \quad (3.14)$$

and theoretical throat area $A_{8,core}$

$$A_{8,core} = \left(\frac{\dot{m}\sqrt{T_t}}{MFP_{8,core}p_t} \right)_{core} \quad (3.15)$$

is determined using Eq. 3.14 and Eq. 3.15, respectively.

An area-based nozzle discharge coefficient $C_{d,A-based}$ may then be defined,

$$C_{d,A-based} = \frac{A_{8,core} + A_{8,byp}}{A_{8,actual}} \quad (3.16)$$

based on the ratio of the sum of core and bypass theoretical throat areas to the physical throat area of the tested plug nozzle $A_{8,actual}$.

The theoretical mass flowrate through the nozzle assuming perfectly mixed streams, $\dot{m}_{theor,m-based}$,

$$\dot{m}_{theor,m-based} = \sqrt{\frac{\bar{\gamma}}{R}} \left(\frac{2}{\bar{\gamma} + 1} \right)^{\bar{\gamma} + 1/2} (\bar{\gamma} - 1) \frac{\bar{p}_t}{\sqrt{\bar{T}_t}} A_{throat} \quad (3.17)$$

is obtained using Eq. 3.17 with mass-averaged parameters.

Mass-based nozzle discharge coefficients ($C_{d,m-based}$) is obtained, .

$$C_{d,m-based} = \frac{\dot{m}_{core} + \dot{m}_{byp}}{\dot{m}_{theor,m-based}} \quad (3.18)$$

by making use of Eq. 3.18

Discharge coefficients determined in this manner are plotted against NPR in Fig. 3.63. The trend in discharge coefficient with NPR from the data appears to closely match that of the thrust efficiency data presented in the previous section aside from the fact the relationship appears more linear over the tested range of NPR's. Again, the maximum discharge coefficient corresponds to the design condition. Computationally determined discharge coefficients are plotted alongside the previously discussed experimentally determined discharge coefficients. The computational results show almost a constant C_d value over the entire NPR range, while measurement show slight increases in C_d with NPR. The computational results are bracketed by the two approaches used in reducing the experimental data.

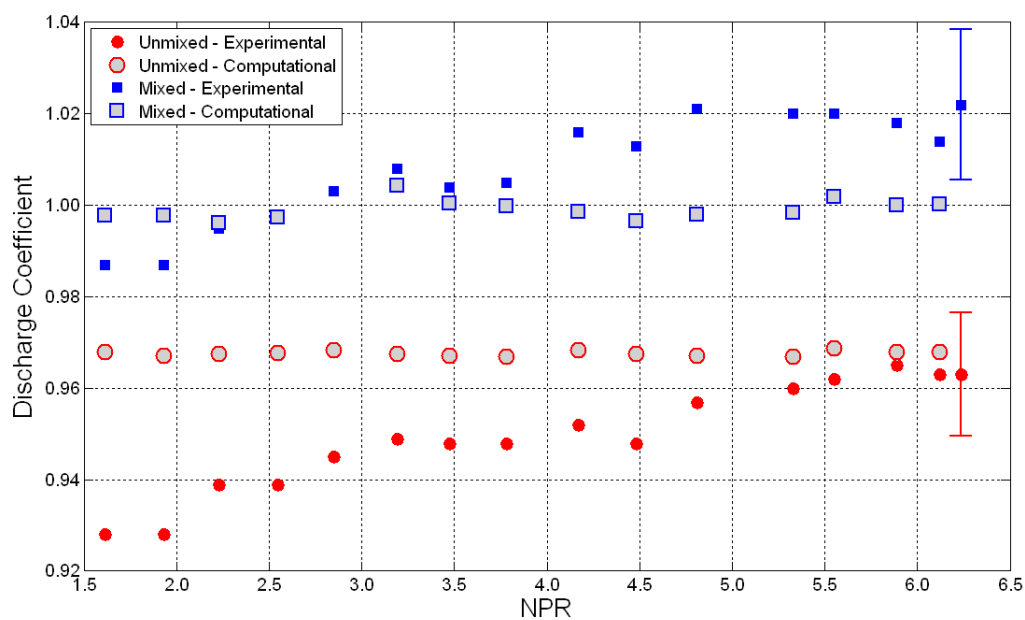


Figure 3.63. Experiment vs. Predicted discharge coefficient: area and mass based.

CHAPTER 4. REACTING IMPINGING JETS OF MMH/RFNA

Hypergolic bipropellants are fuel and oxidizer combination that, upon contact, chemically react and release enough heat to ignite spontaneously. Generally oxides of nitrogen are used as oxidizers, for example nitric acid with dissolved oxides of nitrogen. The fuels are organic compounds like amines, heterocyclic compounds and polyatomic phenols. Hypergolic propellants are used because of their advantages in terms of spontaneous ignition, high density and long term storability at room temperatures while one of the drawbacks being their toxicity. Understanding the combustion of bipropellant combinations will help in developing designs for efficient combustion process and thereby desired performance.

Hypergolic propellant combustion is characterized by an interplay between chemical kinetics and physical processes [50]. Ignition in hypergolics occurs after a finite time delay [84]. This ignition delay for hypergolics determines the behavior of the combustion system [85]. A long time to ignite can lead to catastrophic failure if the accumulated propellants in the chamber detonate at a later time. Ignition is usually followed after a period of diffusion and mixing. The chemical kinetics of the propellant gases in turn determines the global kinetics time scale. The combination or their relative occurrence determines the ignition and flame propagation. The diffusion and mixing properties are characterized by the mass and thermal diffusive properties of the constituent gases while the chemical delay is limited by the chemical mechanism that takes the reactants to the product species.

Combustion of fuel and oxidizer combinations occurs in two phases (i) an induction phase where the fuel and oxidizer mix, react to form an initial species mixture suitable for combustion initiation and (ii) exponential heat release from exothermic gas reactions and combustion. Hypergolic bipropellants are studied typically using

impinging jet configurations where fuel and oxidizer impinge on each other to initiate reaction [48]; [49]; [50].

The use of reactive flow modeling which includes the chemical kinetic mechanism for fuel and oxidizer reaction and accounts for the species property variation with ambient conditions can help in laying a better foundation in extending or interpreting experiments performed using bipropellants. The present chapter studies the combustion of Monomethylhydrazine (MMH) which is considered to be the state of the art in hypergolic fuels and RFNA (Red fuming nitric acid) is a commonly used oxidizer [49]. The species source term is obtained using the finite rate Arrhenius chemistry model which is evaluated using the filtered averaged equations as described in CHAPTER 2. A 25 species and 98 reaction chemical kinetic mechanism is incorporated to account for species formation and consumption leading to the hypergolic heat release [APPENDIX A]. This reaction mechanism was developed as part of the Multiple University Research Initiative (MURI) research program [45]. Prior to this mechanism there was no reduced mechanism available for MMH/RFNA combustion. The work presented here will employ this mechanism throughout this chapter and evaluate its behavior in the context of the impinging reaction jet problem. Due to lack of a reduced mechanism for MMH/RFNA the analysis initially used a reduced mechanism due to Ohminami et al for N_2H_4 and Nitrogen tetroxide (NTO). The MMH/RFNA mechanism will be contrasted with this mechanism primarily with a view to understand chemical time scales.

The combustion behavior of bi-propellant mixtures is strongly influenced by environment in which the combustion occurs [47]; [46]. The thermodynamic and transport properties which determine the convection and diffusion processes are dependent on the ambient conditions. In order to gauge combustion response to ambient conditions a series of computations of gaseous propellants with different initial pressures and temperatures are performed. The initial temperature and pressure of the propellants strongly influences the initial chemical kinetics and hence the overall reaction. For hypergolic propellants it is generally believed that condensed phase reactions

result in sufficient heat release to increase the temperature of a pool of reactants to initiate ignition. Obtaining a precise estimate of this critical temperature above which the reactants are able to overcome the activation energy barrier to undergo chemical reaction is difficult. The global kinetic ignition delay time is believed to be inversely proportional to the pressure of the system. At higher pressures the reactions are initiated instantly compared to low pressures. In general for rocket applications the internal chamber pressure can vary from one atmosphere to a few 10s of atmospheres. In view of this strong dependence on temperature and pressure of the combustion mechanism their effect on combustion is studied and presented here.

Combustion is determined by both mixing and chemical kinetics. The time scale of one in relation to the other will govern the flame initiation and sustenance process. It is instructive to begin the study by understanding the global chemical kinetics time scale by isolating it from the mixing process. To do this we formulate a constant volume combustion problem to understand the global kinetic time scales in the context of the numerical methodology presented in CHAPTER 2. The influence of temperature and pressure on the chemical time scale will be the main interest as part of constant volume combustion problem. Following constant volume combustion problem combustion behavior of impinging jets of gaseous MMH/RFNA jets is discussed. First, the reacting impinging jet is addressed by making a planar assumption. This will serve as a first step towards complete three-dimensional computations presented later. The planar flowfield computations will allow for quick evaluation of the new chemical kinetic mechanism. As the computational time for planar case is considerably smaller compared to three-dimensional computations, we can perform a survey of combustion by varying background gas properties. Both the effect of pressure and differences in mass and thermal diffusivities on combustion behavior will be studied and presented in this chapter. Three-dimensional computations are presented later where the turbulence is treated as three-dimensional and the combustion behavior studied again. In the three-dimensional computations emphasis is laid on flame propagation and its contrast to the planar case.

4.1 Constant Volume Combustion

In order to understand the time scales associated with chemical delay without the complications of mass and thermal diffusion, a simple system is devised. For this we consider a constant volume vessel with a homogeneous mixture of the reactants. This can be easily done in the framework of solving the multi-dimensional fluid dynamic equations for reactive flow by considering a square domain with uniform distribution of grids as shown by the schematic in Fig. 4.1 The surrounding boundary is given as an inviscid wall. As no mass escapes and since the volume remains constant, the density of the system does not change. Hence, the combustion in the closed volume is a constant density process.

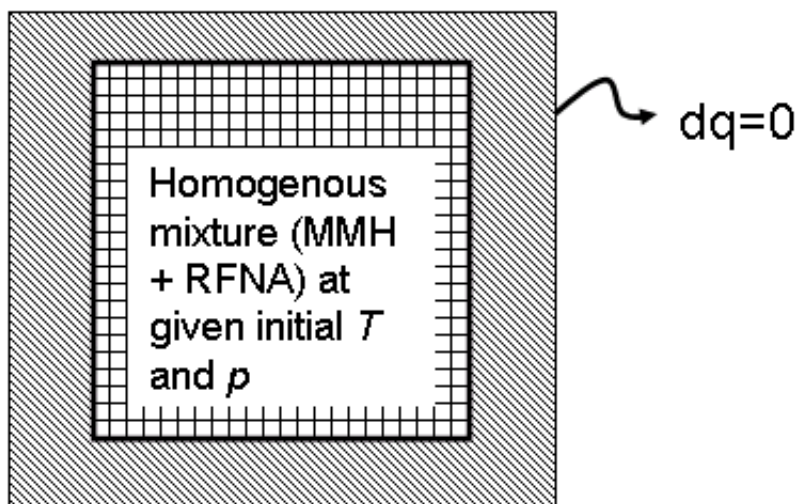


Figure 4.1. Schematic sketch of constant volume combustion computation with no heat conduction at the inviscid walls. A homogeneous mixture of fuel and oxidizer at given temperature and pressure are used as initial condition.

The fluid dynamic system of equations for reactive flow are solved in the entire domain. The turbulence is no longer a factor in determining the flow evolution, so the laminar equations of reactive flow are solved on the uniform grid. The computations are initiated with a homogeneous vapor of fuel and oxidizer at a given temperature and pressure and at zero velocity. Thus, there are no gradients associated with any of the

flow quantities. The result is that the inviscid and viscous fluxes which are dependent on the gradients in the flow drop from the fluid dynamic equations. The chemistry is decoupled from the convection and diffusion associated with a real system and allows us to understand the chemical kinetics of the system. In the resultant equation set, though the mass and momentum equations are retained, they have no significance due to zero velocity and zero gradients. The species conservation and energy equation with their source terms remain. With no heat loss to the surroundings, the internal energy of the system does not change,

$$\frac{de}{dt} = 0 \quad (4.1)$$

and as the density being is constant, the species mass conservation equation reduces to,

$$\rho \frac{\partial Y_k}{\partial t} = \dot{\omega}_k \quad (4.2)$$

with no spatial gradients of any of the flow variables. The species source term determined by using the finite rate Arrhenius chemistry model as described in CHAPTER 2 is employed here. The combustion model is sufficient as the flow is treated as perfectly mixed or homogeneous for the entire duration. The above equations describe the conservation of energy and mass of the 25 species within the constant volume combustion zone. The global kinetic mechanism time scales are strongly dependent on the pressure and temperature and therefore by varying the initial temperature and pressure we can study their effects on delay times. At higher temperatures the species involved in a chemical reaction are able to overcome the activation energy barrier needed for completing the reaction. At low temperatures the steps which initiate reaction are very slow.

Figure 4.2 shows a plot of variation of temperature within the constant volume combustor as a function of time for three initial temperatures: 400K, 600K and 800K. In order to understand pressure dependence we consider two extremes of pressure: 101325Pa and 10132500Pa. A series of six oxidizer to fuel mass (O/F) ratios are also shown in in the plots: 2.0, 1.74, 1.4, 1.2 and 0.8 *i.e.* going from an oxidizer

rich environment to a fuel rich environment. From the plots it is evident that both temperature and pressure strongly influence the hypergolic ignition process. The lowest temperature case of $400K$ did not show any initiation of combustion. During a $20ms$ interval the temperature rises only by a few degrees for all the O/F ratios considered. The higher pressure has no effect on initiating the reaction as well at $400K$.

At the temperature of $600K$ the higher pressure case shows initiation of combustion while there is no combustion at lower pressure. The initiation time increases from just under $5ms$ at O/F = 2.0 to more than $14ms$ at O/F = 0.8. The temperature increases almost exponentially due to the hypergolic heat release spike. The equilibrium temperature reached by the propellant mixture keeps decreasing with O/F as the fuel does not go complete oxidation due to the lower equivalence ratio. The higher temperature of $800K$ shows initiation both at the lower as well as high pressures. In the case of low pressure the oxidizer rich mixture shows an ignition delay time of about $5ms$ whereas at high pressures the ignition occurs almost instantaneously at all O/F. The simple analysis suggests that there is a critical temperature at which the reactions are initiated.

In Fig. 4.3 the consumption of reactant and intermediate species is shown at the top while the formation of products is shown at the bottom for $T = 800K$ and $p = 101325Pa$ with O/F = 2.0. The temperature is also plotted as a reference with the axis on the right. The fuel and oxidizer are completely consumed during the process. The fuel N_2O_4 undergoes a decomposition reaction to give two moles of NO_2 . This reaction is endothermic and therefore the temperature reduces by about $10K$. Following this the NO_2 formed reacts with MMH ($CH_3-NH=NH_2$) to form HONO, an intermediate species. The above reaction is exothermic and results in heating up the homogeneous mixture. During this time there is a rapid build-up of HONO while MMH mass fraction drops for first 10th of a millisecond as seen in Fig. 4.3. Following this the HNO_3 starts undergoing decomposition reaction to form NO_2 which reacts immediately with the MMH to abstract a H to form HONO. Thus,

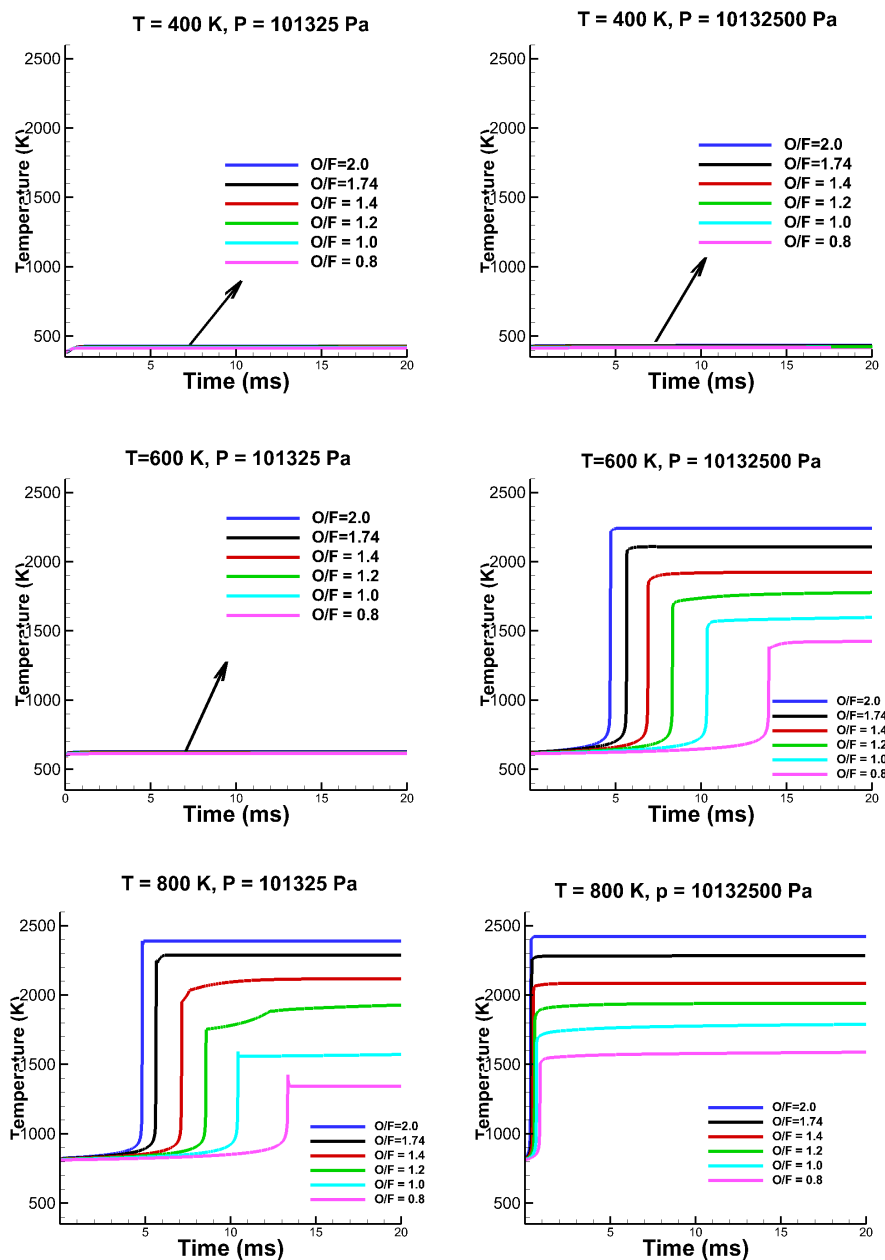


Figure 4.2. Ignition time delay as function of pressure and temperature for various O/F ratios.

increasing amounts of HONO are formed as seen in the plot. During this process the mixture is increasing in temperature as a result of which increased amount of $\text{CH}_3\text{-N=NH}$ or CH_4N_2 is formed due to scission reactions of MMH as seen in the

plot. Fig. 4.4 shows the reaction zone just before and after the heat release. It is seen that the NO_2 concentration starts increasing due to the recombination reaction of the HONO. Close to the heat release event the HNO_3 undergoes decomposition reaction to form HONO. Part of the HONO reacts with MMH while the rest results in NO_2 . Once the mixture has sufficient NO_2 to complete oxidation of CH_4N_2 , the oxidation of MMH is completed. Due to the higher temperatures the elemental nitrogen present in the mixture forms large part of the products as NO while N_2 , CO, CO_2 , H_2O and H_2 form the rest of the product mixture. The reaction initiation and product formation is similar at higher pressures as low pressures although the speeds are faster as noted earlier. As the O/F ratio decreases increasing amount of CH_3 is formed in the products as the fuel is not fully oxidized due to lower oxidizer mass fraction.

The constant volume analysis shows that a critical temperature and pressure exist above which combustion occurs. This has an important bearing for the initial conditions of the two-dimensional computations discussed in the next section. Unless preheated mixtures are not considered the combustion process may not initiate.

4.2 Two-Dimensional Analysis

4.2.1 Introduction

In most hypergolic propellant applications the presence of many physical processes like liquid liquid, condensed phase reactions, rapid gas formation, highly complicated multi-step reaction kinetics etc complicates the analysis. Complete three-dimensional modeling of the various processes at the outset may result in uncertainties due to modeling. A simplified analysis with well established models may result in useful insights. In gas phase reactive processes phase change effects are not present and combustion is determined by a combination of chemical kinetics, turbulence and fluid properties. The impact of reduced chemical kinetic analysis was used in the previous section to obtain preliminary estimate of combustion times. Constant volume combustion analyses like the ones considered in the previous section are dependent only on the

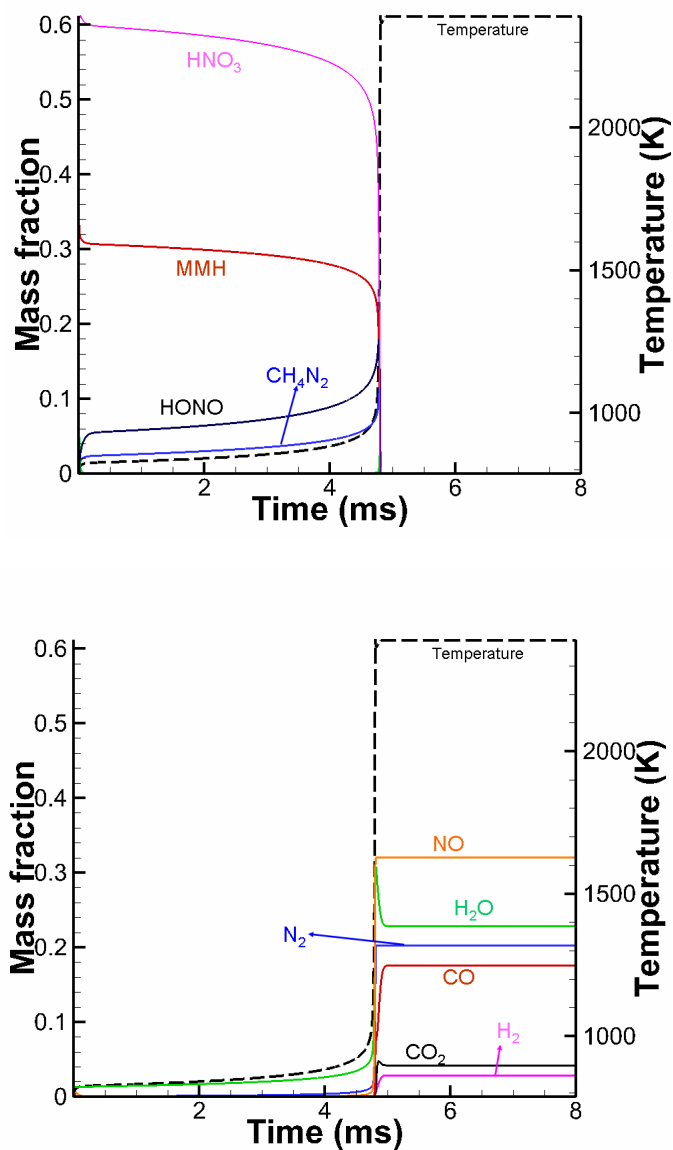


Figure 4.3. Reactant and intermediate species consumption (top) and product formation (bottom) at $T = 800\text{K}$ and $p=101325\text{Pa}$ for $\text{O}/\text{F} = 2.0$. Mass fraction axis on left and temperature axis on right.

initial and final steady state and do not allow for the impact of hydrodynamic phenomena. In real combustion systems, the rate of reaction is combined with that of other processes, such as convection and diffusion to determine combustion behavior.

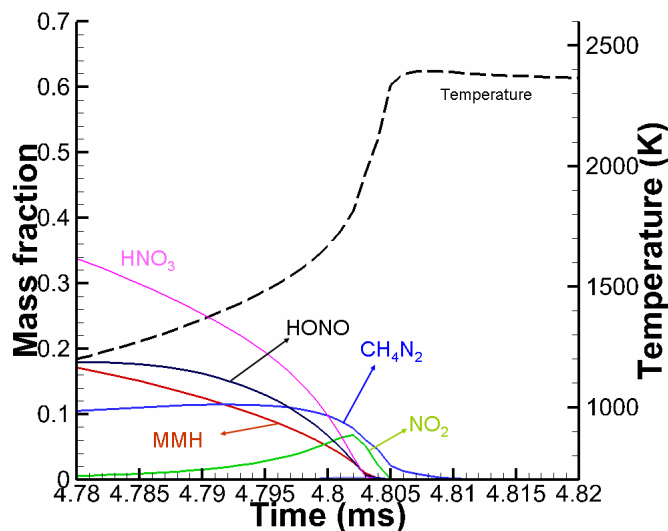


Figure 4.4. Intermediate reaction species formation in the reaction zone, primarily HONO, NO_2 and CH_4N_2 . Mass fraction axis on left and temperature axis on right at $T = 800\text{K}$ and $p=101325\text{Pa}$ for $\text{O}/\text{F} = 2.0$.

As a first step in understanding combustion when RFNA and MMH are brought into contact with each other, we begin by considering a 2-D or planar analysis. Two dimensions enable relatively fine grids to be used and prepare for more costly 3-D computations. They will allow us to evaluate the chemical kinetic mechanism of MMH/RFNA efficiently. As noted above the available chemical kinetics system contains 25 species. The conservation equations presented in CHAPTER 2 are solved here with all the equations along with turbulence closure treated in two-dimensions. This section will lay the basis of three-dimensional studies presented in the next section. With an additional species used in the ambient domain, the system constitutes a total of 32 coupled partial differential equations. Apart from the reduced load of analysis time, 2-D grids allow a parametric survey that can yield important insights. For example the effect of environmental factors such as shown in the following discussion can be studied. The specific geometry has two streams of fuel and oxidizer issuing from the orifices, impinging and reacting in a downstream ambient domain.

This allows the primary focus to be the combustion behavior in the presence of convection and diffusion processes coupled with chemical kinetics. Both these processes dominate combustion behavior in the real gas phase systems.

4.3 Problem Definition

To study the combustion of hypergolic MMH/RFNA the original geometry of the experimental analysis discussed in [48]; [49] is retained excluding the injectors. The fuel, MMH, is drawn in through one orifice while the other orifice has a steady flow of RFNA. In Fig. 4.5 the planar computational domain with the cartesian grid is shown. The computational grid consists of the MMH and RFNA orifices with dimensions similar to that in the experiments. The two orifices which have an included angle of 60° are protruding somewhat into the computational domain. This is similar to what has been done in the experiments. The outer walls of the orifices and the wall between them enclose a cavity with one side open to the ambient region. For the geometry shown the inner dimensions of the MMH ($D_{t,RFNA}$) is $1.4mm$ and that of the RFNA ($D_{t,RFNA}$) slot is $1.5mm$. The length of both inlet channels is $24.4mm$. A rectangular grid is used in the ambient region downstream of the orifices. The length of the computational domain is shown in m in Fig. 4.5. In Fig. 4.6 the geometry detail including the cavity near the inlet channels is shown along with the boundary conditions.

In the experiments the two streams undergo combustion in a large volume downstream of the injectors at atmospheric pressures. In the computations combustion initiation and flame propagation in a region close to the orifices are of interest. The grid dimensions in this near-field region were determined after numerical experiments with a series of domains to allow for the computation of the reacting shear layer while at the same time maintaining a grid density that allowed acceptable computational time. The final computational grid encompassed the two inlet channels plus the external domain show in Fig. 4.5 and was composed of about 79000 quadrilat-

eral elements. The external domain contained 250 grids in the flow direction and 240 grid points in the transverse direction. Both the MMH and RFNA orifice had 144 grid points in the axial direction and 44 grid points in the transverse direction. The boundary layer on the orifice walls is resolved with 20 grid points with the first grid point at $\Delta y = 6.7e - 4D_{t,RFNA}$ for RFNA orifice with diameter $D_{t,RFNA}$ and $\Delta y = 7.1e - 4D_{t,MMH}$ for MMH orifice with diameter $D_{t,MMH}$. This boundary layer resolution resulted in $y^+ < 1$. The details of the grid in the orifice exit sections are shown in Fig. 4.7. A uniform grid is present in the ambient section of the domain as seen in the figure to resolve any recirculation zones or unsteady hydrodynamics.

The boundary conditions employed at the domain boundaries are also given in Fig. 4.5 and Fig. 4.6. Mass flow rate, temperature and composition by mass of the incoming gases are specified at the inlet to both the RFNA and MMH passages. The MMH inlet has 100% by mass of MMH while the RFNA inlet is composed of a homogeneous mixture of 88% HNO_3 , 10% N_2O_4 and 2% H_2O . The flow determined by these inlet conditions passes through these passages. The fuel and oxidizer passes through their respective channels and upon emerging from the exit, impinge upon each other generating a reacting shear layer (if conditions are right) which propagates through the domain till the outlet boundary at the side or bottom of the domain as indicated in Fig. 4.5. The momentum of the two streams entrains ambient air, however, the combustor volume in the experiments extends much larger than the orifice diameter from the orifices so that the effect of the entrained air at the orifices is not significant. To mimic this condition in the computation the top boundary of the domain is treated as an ambient inlet boundary as shown in Fig. 4.5 and marked as 'AI'. This results in very low Mach numbers and nearly uniform static pressure for the present results. The back pressure at the outlets is also set to ambient pressure. The inner and outer walls of the MMH and RFNA orifices are treated as no slip adiabatic walls.

The same chemical kinetic mechanism comprised of 25 species and 98 reactions as used in the zero-dimensional computations described in Section 4.1 is also employed

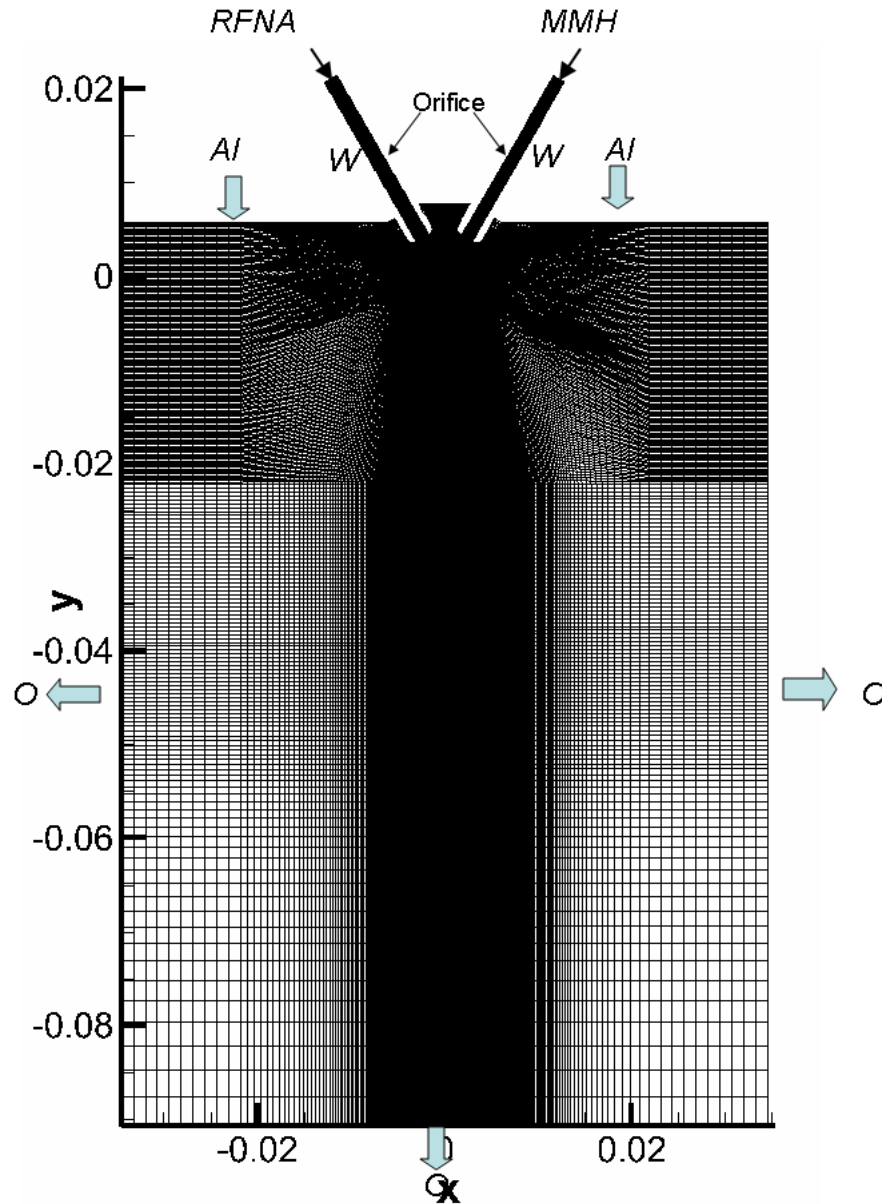


Figure 4.5. Computational domain with grid and details on boundary conditions (RFNA - RFNA inlet, MMH - MMH Inlet, W - Wall, AI - Ambient Inlet, O - Outlet).

here [APPENDIX A]. The ambient gas in the external domain is treated as an additional species, bringing the total to 26 species. As noted later this ambient was

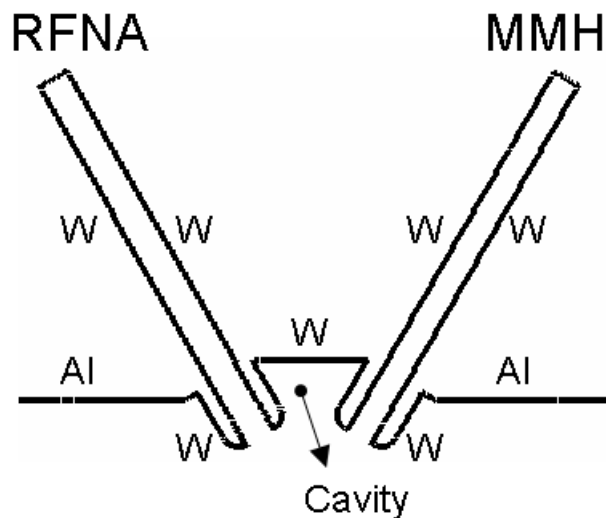


Figure 4.6. Computational domain near RFNA and MMH orifices along with the cavity. Also marked are the boundary conditions (RFNA - RFNA inlet, MMH - MMH Inlet, W - Wall, AI - Ambient Inlet).

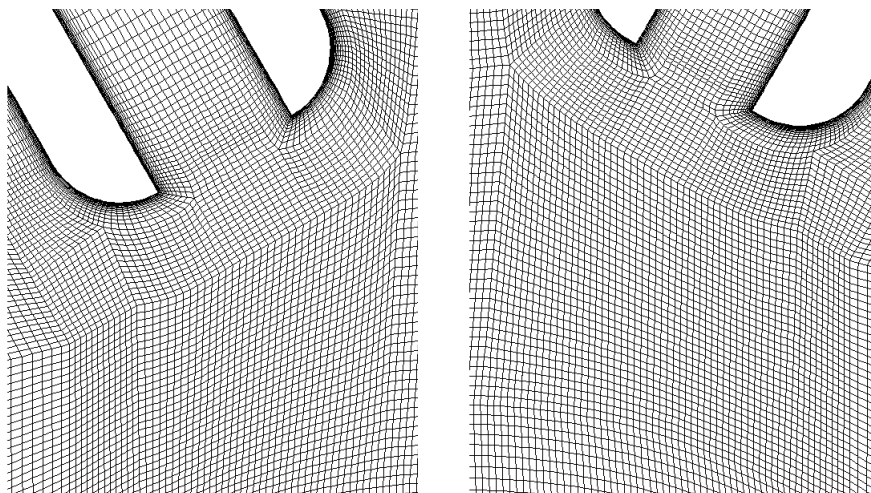


Figure 4.7. Grid details at RFNA orifice exit (left) and MMH orifice exit (right).

treated as an inert and was modeled as either He or Ar. The mass fraction of the last species is determined from the conservation of all species masses.

The coefficients of the polynomial fits describing the species thermodynamic and transport properties are tabulated for different temperature ranges. The properties

are calculated in the computations based on this look-up table. The temperature dependence of species mass and heat diffusion properties have been discussed earlier.

For unsteady computations the initial condition is analogous to the process used for the shrouded plug nozzle flowfields. In the experiments, the combustion chamber is filled with air at room conditions, or in special cases with selected inert fluid at room temperature and pressure. In computational analysis we consider variations in pressure and ambient gas properties as was done in the case of zero-dimensional analysis. To ensure combustion initiates the fuel, oxidizer and the ambient gas are set at $800K$. The choice of $800K$ is also influenced by the zero-dimensional analysis shown in the earlier section where long delay times to ignition for temperatures below $800K$ at both low and high pressures were observed. The elevated ambient temperature was similarly chosen as an aid in ignition, but subsequent results show it has little effect.

Computations have been performed for two ambient pressures, $101325Pa$ and $10132500Pa$. This choice is motivated by the operating conditions of a bipropellant combustion motor of MMH/RFNA as seen in [42]. In addition, two ambient gases are considered with different thermal transport properties: helium and argon. The molecular weight of argon is 10 times that of helium while the thermal conductivity and specific heat of helium are almost 10 times that of argon. Thus, the two ambients provide mediums in which the mass and thermal diffusive properties vary.

The dual-time preconditioning methodology is again used for solving the fluid dynamic equations. For the unsteady computations presented here a physical time of $1\mu s$ is used along with an inner iteration CFL of 1000 chosen to ensure convergence of inner iterations at these low Mach numbers. The inner pseudo iteration count is set to 8 which gave a residual drop of 3 orders of magnitude for the computations shown here.

The mass flow rate boundary conditions prescribed at the MMH and RFNA inlets set up a flow through the two passages which traverses into the ambient domain. The flow goes through an initial transient following which statistics are obtained for study-

ing the combustion process. Time-averaged flow properties are constructed based on these statistics to give a long snapshot of the combustion process. The next sections describe in detail the transient combustion process occurring prior to stationary conditions. In the process the combustion behavior is contrasted for different ambient gases as well as pressures.

4.4 Combustion Behavior

Combustion is initiated by injecting streams of fuel and oxidizer through the two slots as indicated in Fig. 4.5. After emerging from the slots the fuel and oxidizer streams collide developing a shear layer between them as they propagate downstream. The shear layer grows as it propagates through the ambient gas. Due to the species mass gradient between the two streams, mass diffusion occurs at the interface, setting up mixing at the interface. The RFNA stream which is composed of 8% N_2O_4 is at a lower temperature as the decomposition of N_2O_4 into NO_2 is an endothermic reaction. The RFNA stream is in general 50K below the MMH stream, thus setting a thermal gradient at the interface. The constant volume analysis in the previous section showed that there is finite time lag for the gas phase mixture to combust. This time lag is dictated by the chemical kinetics which is dependent on the temperature and pressure. In the case of reacting shear layers an added dimension of convection and diffusion processes complicates the analysis compared to the constant volume combustor. The time to combustion is therefore decided by both kinetics and fluid dynamic processes.

To understand the combustion process in the impinging jet configuration, we consider cases with two different background gases, He and Ar. In both calculations the background gases are at 800K and 101325Pa. The goal is to compare the effect of ambient gas. Then we repeat the analysis for both cases at an elevated pressure of 10132500Pa. Comparing them allows us to deduce the effect on combustion initiation and flame propagation. The lower pressure case is presented first followed by the high pressure case.

Table 4.1 Computations detail for $T=800K$, $p=101325Pa$.

Flow property	Fuel Stream	Oxidizer stream
Gas composition	MMH	RFNA
Temperature(K)	800	800
Mass flow rate($kg/m s$)	0.012	0.02
Density (kg/m^3)	0.7	0.9
Velocity (m/s)	20	18
Thermal conductivity ($W/m - K$)	0.0826	0.0545

Table 4.2 Helium ambient properties.

Flow property	Reference value
Temperature, (K)	800
Pressure, Pa	101325
Density, kg/m^3	0.06
Thermal conductivity, $W/m-K$	0.308
Specific heat at constant pressure, $J/kg-K$	5200

4.4.1 Combustion in Helium Environment at $800K$ and $101325Pa$

The inlet propellant initial conditions for computations at $101325Pa$ are given in Table 1. The O/F ratio is 1.67. Both propellants enter at $800K$ and the inflow velocities are at 18 and $20m/s$. The mass flow rate ratio allowed for most of the flame sheet to be confined to the computational domain and exit through the outlet opposite the orifices. The analysis of the combustion processes is done in two steps. To begin the discussion early time flame initiation and propagation through the domain are presented to document the start-up process. This is followed by results at later times.

Combustion in a helium environment at $800K$ and $101325Pa$ are presented first. The initial transient begins with the oxidizer and fuel streams traversing the propellant passages. Shortly after they emerge, they impinge at a downstream location as shown in Fig. 4.8 by the density contours at the time instant $t=1.4ms$. While inside the fuel passage the MMH stream does not decompose but on the oxidizer side, the N_2O_4 present in the RFNA undergoes an endothermic decomposition reaction to form NO_2 . This decomposition occurs nearly instantaneously as the fuel enters the passages and as the oxidizer stream is composed of NO_2 along with the HNO_3 and H_2O that are initially present. The NO_2 remains dissolved within the HNO_3 and no further reactions occur in the oxidizer stream.

At the impingement location the two gas stream interfaces come into a grazing contact as shown in the density contour plot of Fig. 4.8. The density of the fuel and oxidizer stream are higher than that of the helium and help in distinguishing the contact surface between the two streams.

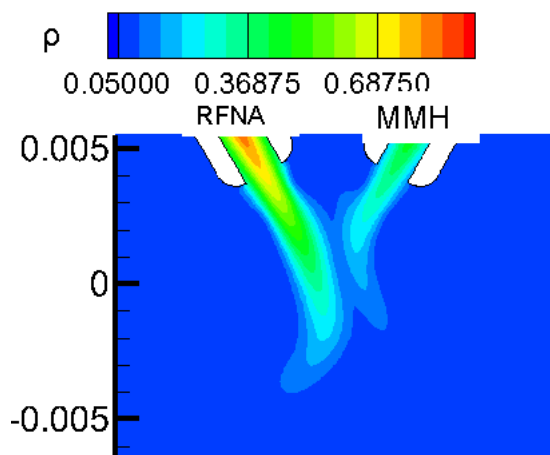


Figure 4.8. Density contours MMH/RFNA streams coming into a grazing contact at $T=800K$, $p=101325Pa$ in helium environment with HNO_3 on left and MMH on right at $t=1.4ms$.

Following this initial impingement, the streams remain in contact as they propagate downstream displacing the ambient helium gas as shown in the sequence in Fig. 4.9. The figure shows HONO mass fraction contours which is formed at the

interface due to the breakdown of HNO_3 . As the HONO is present in the reacting interface between the two streams it helps in visualizing the interface. The contour plots show the region close to the orifices where the ignition occurs along with the cavity enclosed between the two orifices. In the contour plot the HONO formation at time instants of $t=1.4\text{ms}$ (when the two streams come into contact), 2.5ms (an instant mid-way between contact and ignition), 3.3ms (just before ignition) and 3.5ms (just after ignition) are shown along with a streamline from the RFNA orifice marked in white to demarcate the interface between the fuel and the oxidizer. Upon ignition the fuel and oxidizer stream become separated with the gaseous reaction products which form an inert layer between the propellant jets. Clearly, increasing amount of HONO is formed as the propellants propagate downstream with time. The streamline which passes through the center of the HONO mass fraction region helps in distinguishing the fuel side (right) from the oxidizer side (left). The HONO mass fraction reaches above MMH mass fraction at the time instant shown in Fig. 4.9(c) just before ignition. At the instant $t= 3.5\text{ms}$ when ignition occurs, the HONO contour plot shows a region where it has depleted and demarcates the flame location. The ignition consumes both the fuel and the oxidizer in the initial front and lies in between the two streams. Considerable heat release occurs in the 0.2ms time duration before and after ignition.

In the same time duration the contour plots in Fig. 4.9 show the cavity within the orifices beginning to fill with HONO. The fuel and oxidizer streams impinge, they mutually trap helium gas in between them forming a recirculation region between the streams. The recirculation region fills HONO formed at the interface into the cavity and drives the helium out of the cavity. The recirculation region are shown by means of streamlines in Fig. 4.9(c). The recirculation zone which is established in between the orifices is a consequence of the planar assumption. In a three-dimensional geometry the products may escape normal to the plane and not result in the buildup of reactive gases between the orifices.

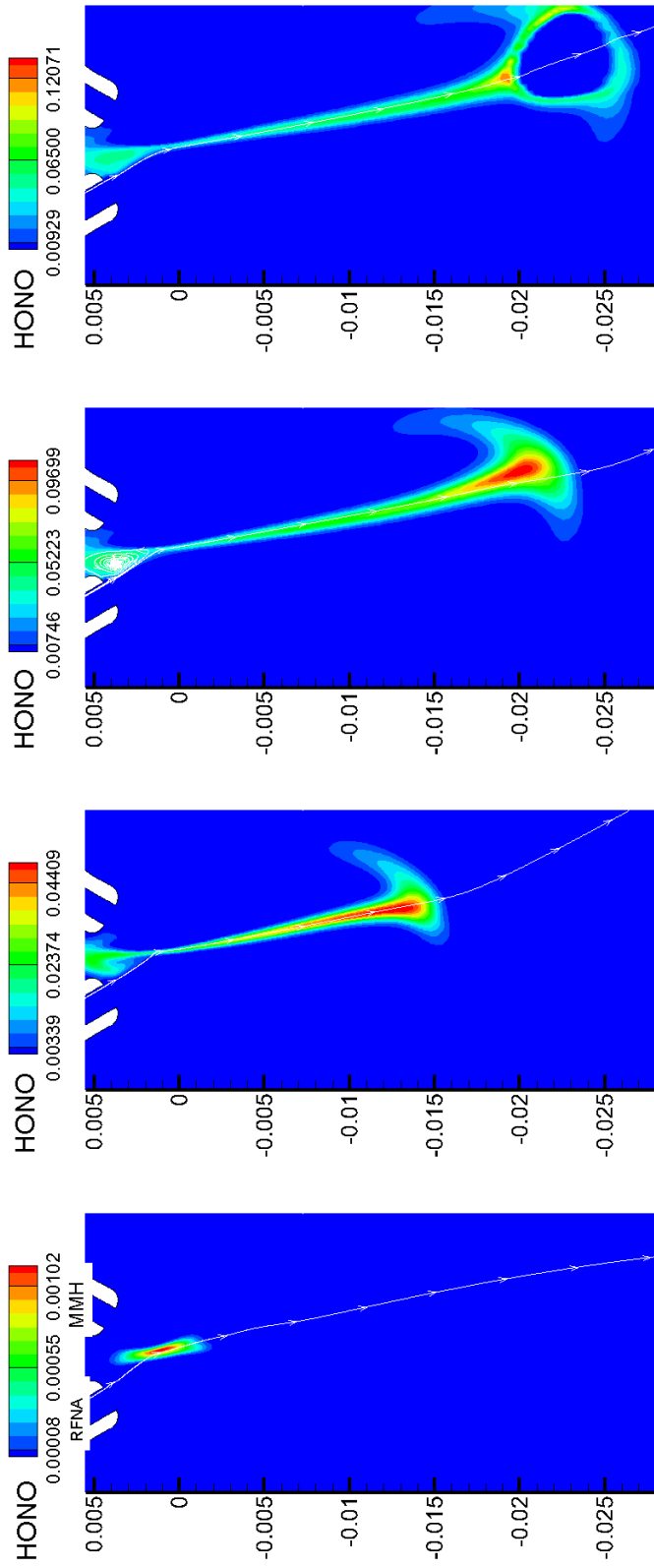
(a) Initial contact, $t=1.4\text{ms}$.(b) Mid-way, $t=2.5\text{ms}$.(c) Before ignition, $t=3.3\text{ms}$.(d) After ignition, $t=3.5\text{ms}$.

Figure 4.9. HONO mass fraction contours showing HONO formation in the reactive interface between the two streams and ignition at $T=800\text{K}$, $p=101325\text{Pa}$ in helium environment. The streamline from the RFNA orifice helps in demarcating the fuel and oxidizer streams.

Figure 4.10 shows contour plots of fuel, oxidizer, temperature and the prominent products of combustion at the point when the ignition occurs at $3.5ms$. The combustion region can be seen in the temperature contour plots where the temperature has reached above $2300K$ compared to the initial temperature of $800K$. The MMH and HNO_3 plots show depletion in mass fraction at this location indicating they have been consumed. The oxidizer stream HNO_3 contours do not show any significant change in concentration till it reaches the flame front. The prominent combustion products are NO , NO_2 , N_2 , H_2O and CO_2 whose contour plots of mass fraction are shown in Fig. 4.10 and Fig. 4.11. The large mass fraction of the oxides of carbon and nitrogen shows oxidation has been initiated. The contour of CH_4N_2 in Fig. 4.11 on the fuel side and around the periphery of the flame shows that the heat release from combustion is causing rapid scission of MMH as it is about to enter the combustion zone.

Figure 4.12 shows an instantaneous snapshot at time $t = 6.1ms$ when the flame has propagated downstream of the ignition location. Again, note that the fuel and oxidizer stream are separated by the wide combustion zone which is the region with high temperature as seen in the temperature contours. The two propellant stream surrounding the flame front also exhibit some instability as they roll-up during propagation through the domain. The cavity in between the two orifices continue to have considerable build-up of HONO.

Starting after this, at $t=6.4ms$ the HONO between the oxidizer and fuel cavity has built up to large enough concentration that it self-ignites generating heat release and a second ignition zone appears in the cavity. In Fig. 4.13 the temperature contour at three instants of time are shown. The region close to the cavity as well as the downstream flame front are shown. The high temperature denotes the combustion zone. The first contour plot shows the ignition event in the cavity region at $t=6.4ms$. The hot gases in the cavity are propagated downstream into the reactive interface from the recirculation zone completing the oxidation of the fuel radicals (most prominently $CH_3-N=NH$). This is seen in the second contour plot in the sequence when the flame is

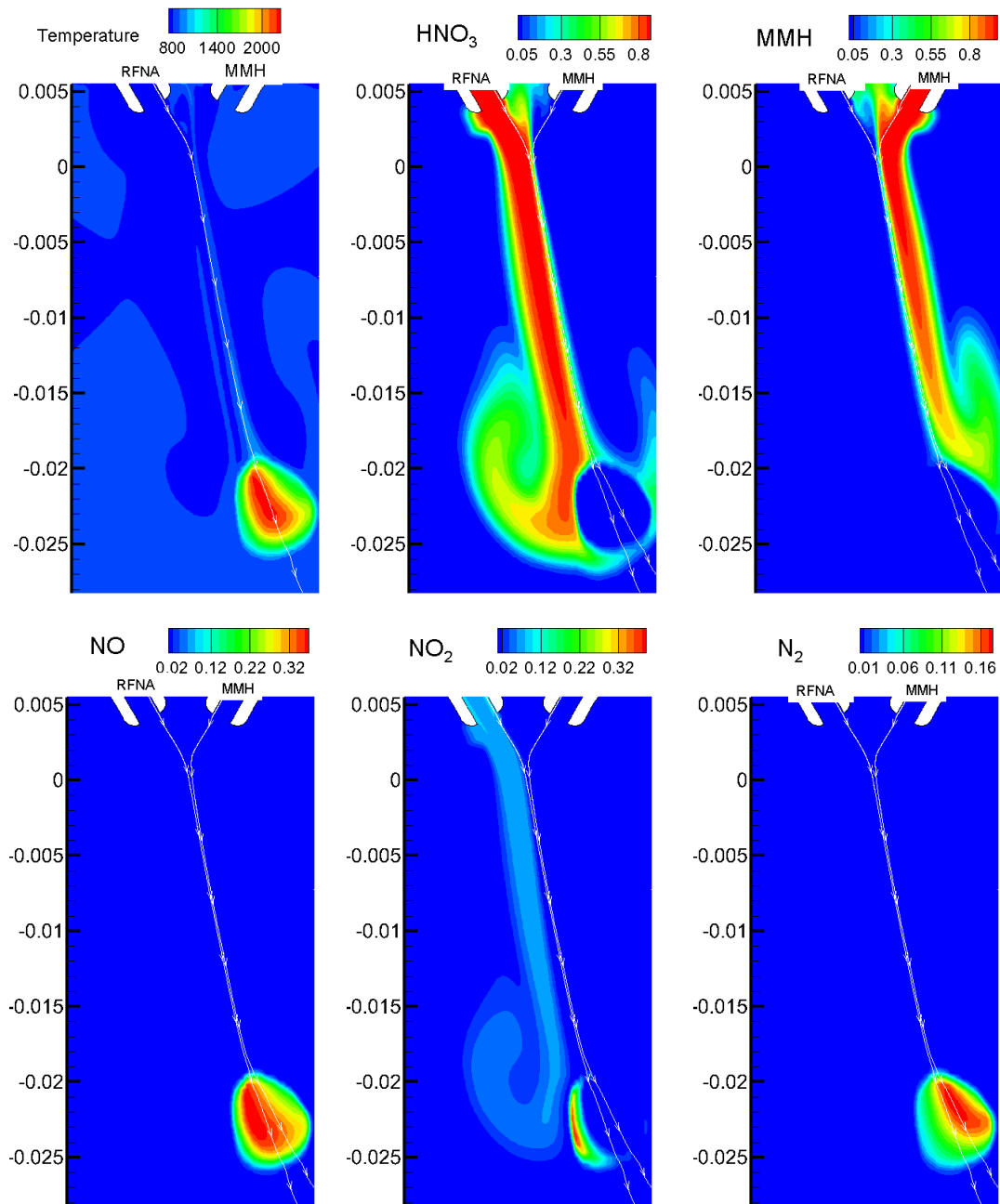


Figure 4.10. Mass fraction of fuel, oxidizer, temperature and prominent products of combustion after ignition at $3.5ms$ at $T=800K$, $p=101325Pa$ in helium environment. The streamline from the RFNA and MMH orifice helps in demarcating the fuel and oxidizer streams.

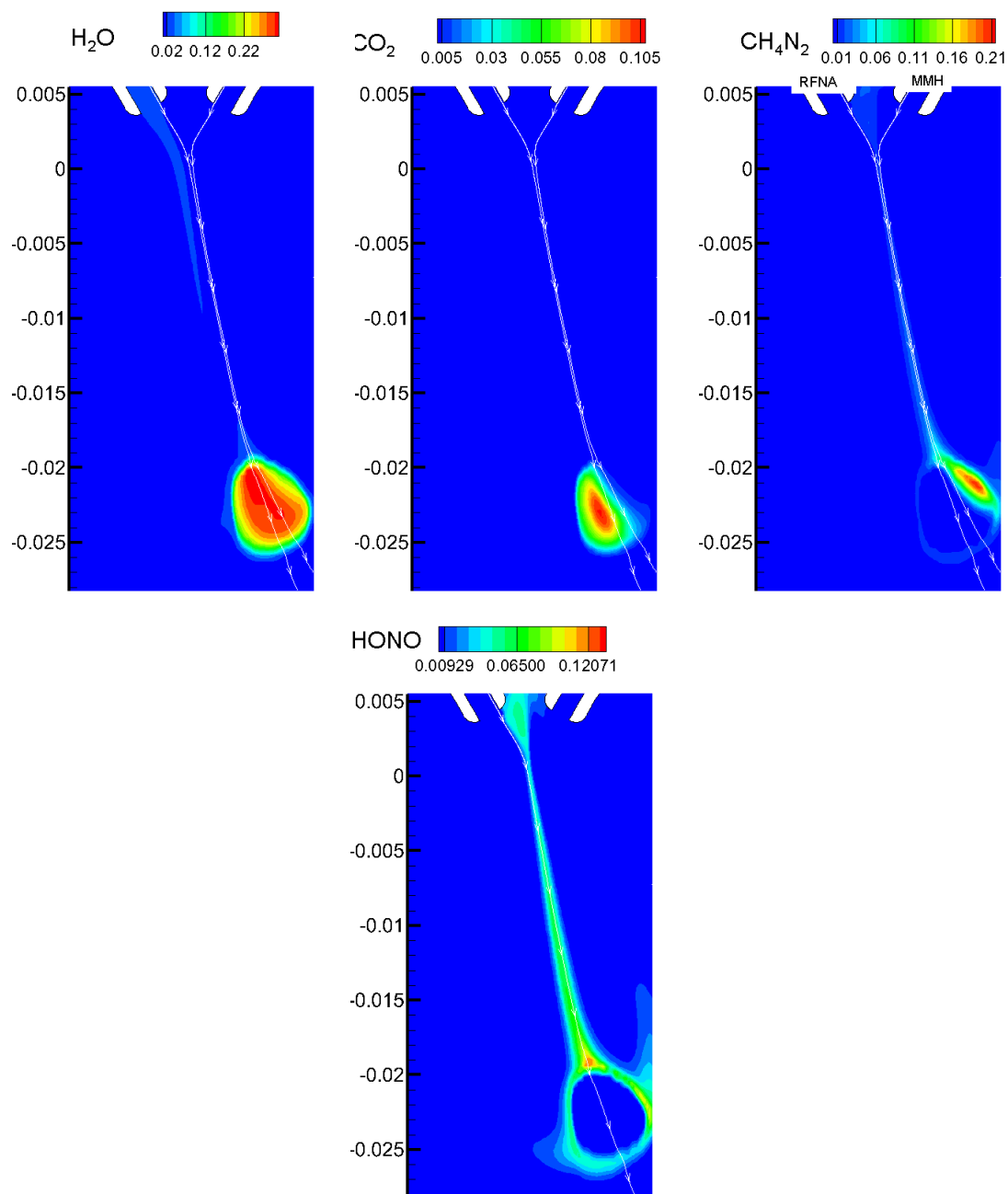


Figure 4.11. Mass fraction of products and intermediate species of combustion after ignition at 3.5ms in helium environment. The streamline from the RFNA and MMH orifice helps in demarcating the fuel and oxidizer streams.

mid-way between the cavity and the downstream flame. The flame front between the

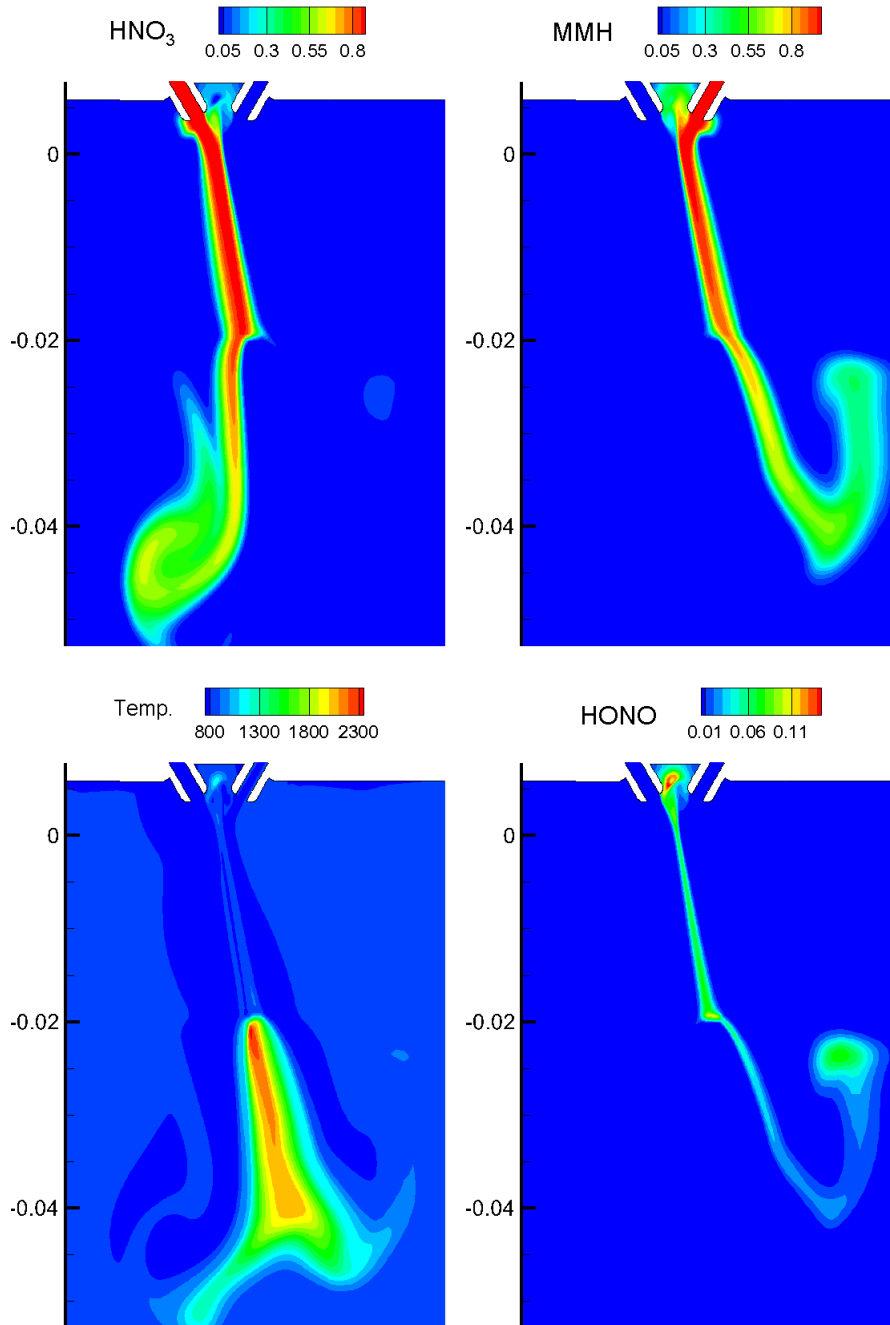


Figure 4.12. Mass fraction of fuel, oxidizer, temperature and HONO at 6.1ms. The flame front is propagating downstream and considerable build-up of HONO in the cavity.

passages now propagates along the entire reactive interface and quickly merges with the flame front that is established earlier. The merged flame fronts then propagate downstream till they eventually exit the domain. The initial combustion zone which existed from a downstream location to the outlet now spans the entire computational domain. The transient phase is essentially complete at time $t=12ms$ and statistics can now be obtained to study combustion

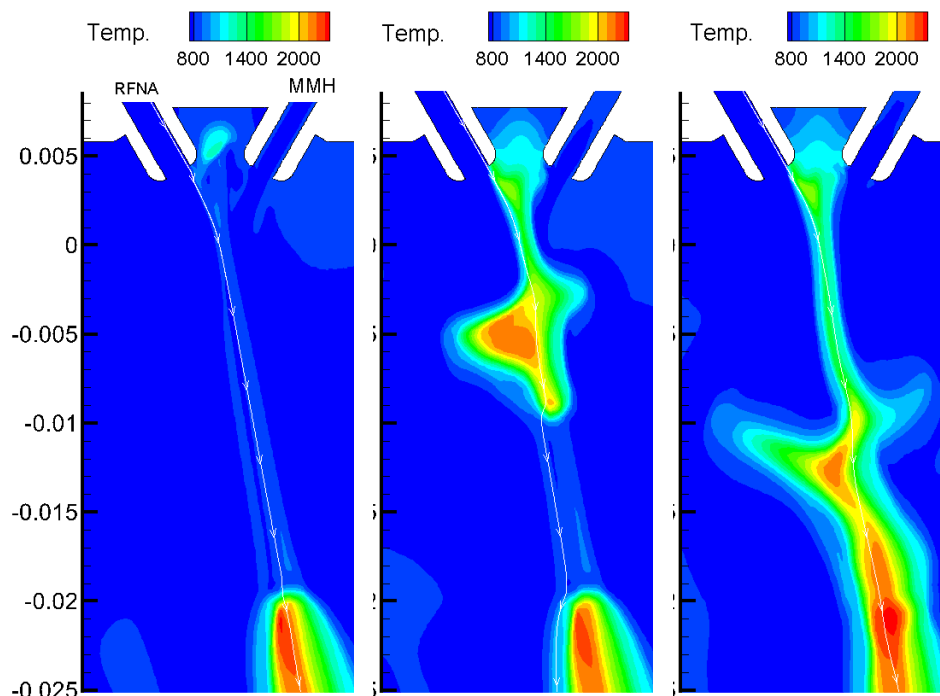


Figure 4.13. Temperature contours at $t = 6.4ms$ when ignition occurs in the cavity, $t= 7.1ms$ when the flame is half way between cavity and downstream flame and at $t=7.6ms$ when the two flame fronts merge.

In Fig. 4.14, Fig. 4.15 and Fig. 4.16 the instantaneous contour plots for the reactant and product species along with temperature are shown at time instant $t=40ms$ after the flame has been set up. The streamlines following the internal edges of the MMH and RFNA orifices are also shown to distinguish reactant streams and the combustion zone. Both the MMH and RFNA streams in the first two contour plots remain laminar without developing any instability and separated by the flame front between them.

The MMH and RFNA are not completely depleted within the computational domain. The temperature is on the order of $1500K$ in the combustion zone which is colder than the temperature for complete combustion. In fact, the contour plot for $CH_3-N=NH$ or CH_4N_2 shows considerable amount of the species in the combustion zone showing that the oxidation of MMH has not proceeded to completion. The flame front is anchored at the RFNA nozzle outer wall closer to the oxidizer as seen from the contour plots of NO.

4.4.2 Combustion in Argon Environment at $800K$ and $101325Pa$

Previous section highlighted the transient process associated with combustion of bipropellant combination of MMH/RFNA in an helium background. Mainly, combustion was initiated at a downstream location followed by a second ignition in the cavity enclosed by the two orifice locations. Following this the two flame fronts merge and the combustion zone is set up along the length of the shear layer. In the present section the combustion process in the helium environment is contrasted with similar results in an argon environment at the same temperature and pressure. The reference properties for the argon are given in Table 4.3. Compared to helium, argon is 10 times denser and thermal diffusivity is 10 times smaller. Again we begin by a discussion of the initial transient followed by instantaneous results after a long time. The conditions at which the fuel and oxidizer stream are fed are similar to the previous case and are listed in Table 4.1. The result of these differences is that (i) the two streams from the orifice diffuse into the denser argon at a slower rate (ii) the lower thermal diffusivity results in less thermal conduction. The boundary conditions and the solution have been set up for the unsteady computation as discussed earlier.

The combustion initiation and flame propagation for MMH/RFNA propellant combinations in argon environment is similar to that of helium but with differences in the behavior of the flame front. These differences are more particularly evident

Table 4.3 Argon ambient properties.

Flow property	Reference value
Temperature, (K)	800
Pressure, Pa	101325
Density, kg/m^3	0.6
Thermal conductivity $W/m-K$	0.0373
Specific heat at constant pressure, $J/kg-K$	520

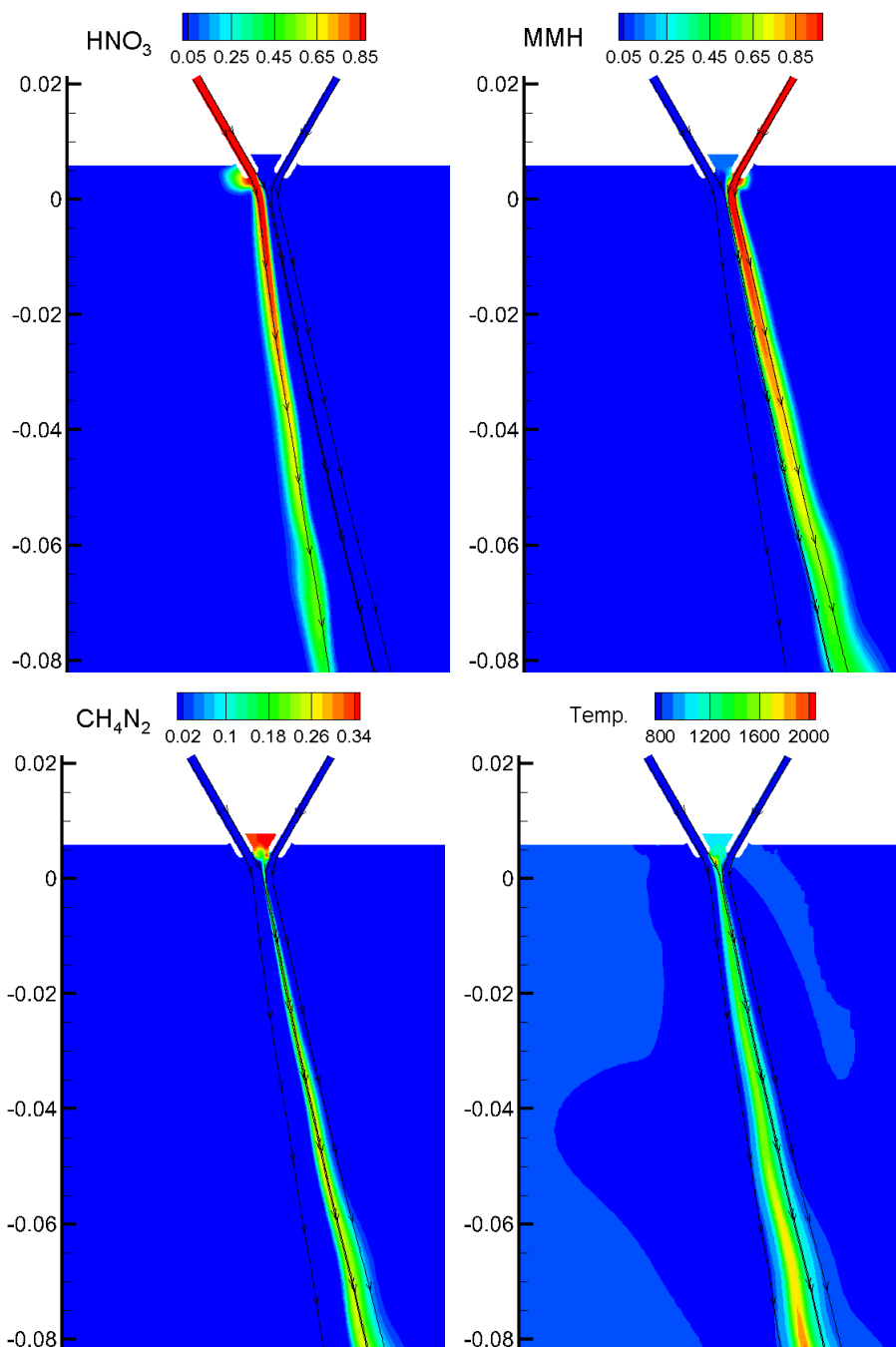


Figure 4.14. Mass fraction of HNO_3 , MMH and CH_4N_2 along with temperature at time $t=40\text{ms}$ after the flame is set up in the domain for helium background at $T=800\text{K}$ and $p=101325\text{Pa}$.

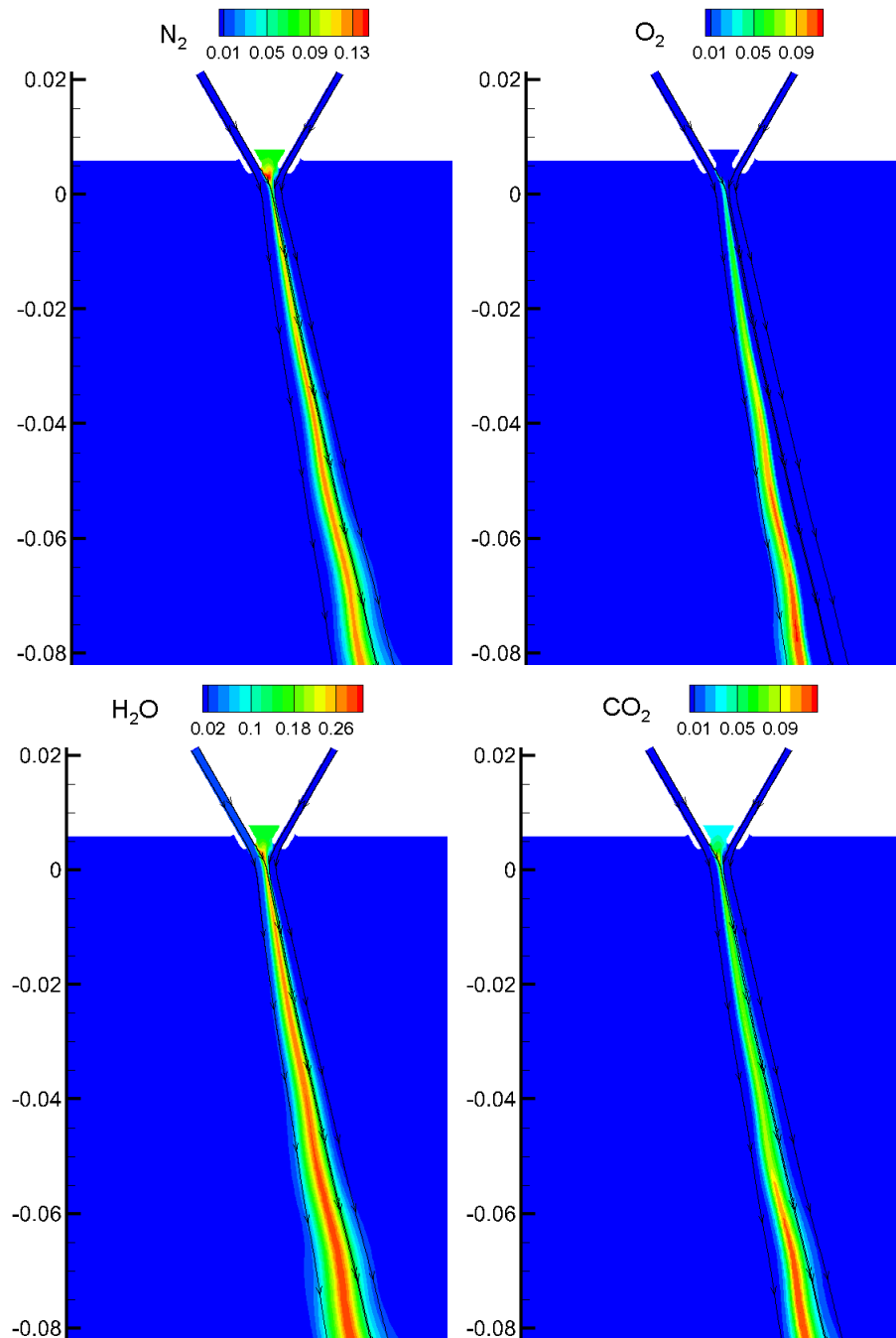


Figure 4.15. Mass fraction of N_2 , O_2 , H_2O and CO_2 at time $t=40ms$ after the flame is set up in the domain for helium background at $T=800K$ and $p=101325Pa$.

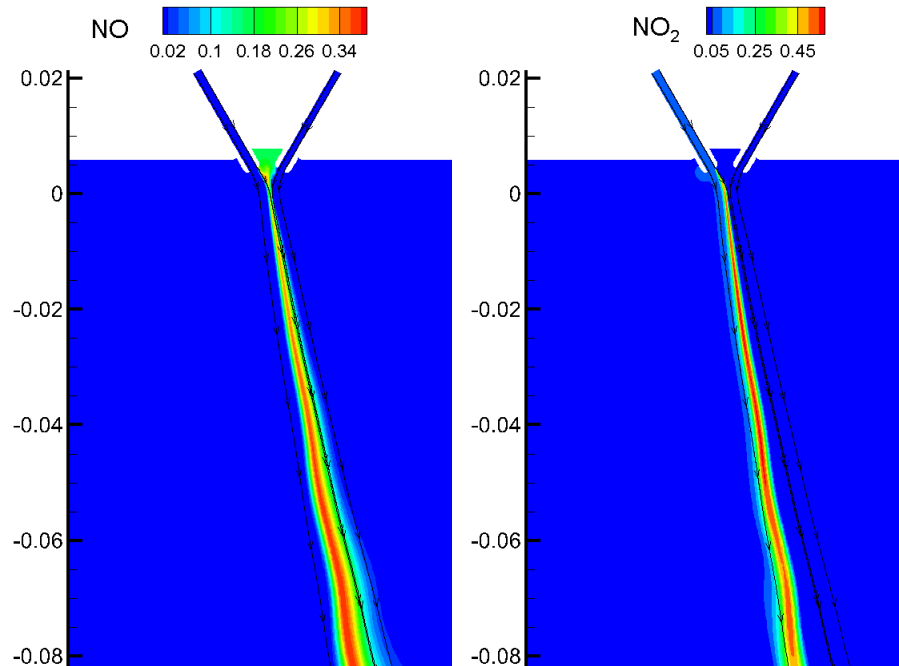


Figure 4.16. Mass fraction of NO and NO₂ at time $t=40ms$ after the flame is set up in the domain for helium background at $T=800K$ and $p=101325Pa$.

when stationary combustion sets in after the initial transient. In this section we contrast the combustion process.

The starting transient in argon is similar to that in helium except that argon being denser than the incoming propellants causes the various events to occur at different times. In Fig. 4.17 the contours of temperature are shown from the instant when the two streams come into contact till the ignition event. A significant instability in the form of roll-up of the initial front is seen (Fig. 4.17). In the sequence four time instants are shown. The temperature in between the interface is seen rising as it propagates downstream due to the heat release associated with the reactions in the interface. When the species mixture in the initial front becomes reaches critical mixture fraction, it ignites(Fig. 4.17(d)). The temperature after heat release rises to about $2100K$ in the flame. The ignition event is associated with large heat release and a compression wave propagates through the domain. Again the heat release

spike occurs at the initial front of the fuel and oxidizer streams. In the case of helium environment the first ignition event occurred at $3.4ms$ from the instant the propellant streams enter the orifices. For argon the first ignition event occurs at $4.6ms$ but is almost at the same axial location. Because of smaller mass diffusivity the diffusion of MMH and HNO_3 into the higher molecular weight argon ambient is slower in comparison to the diffusion of the same into helium.

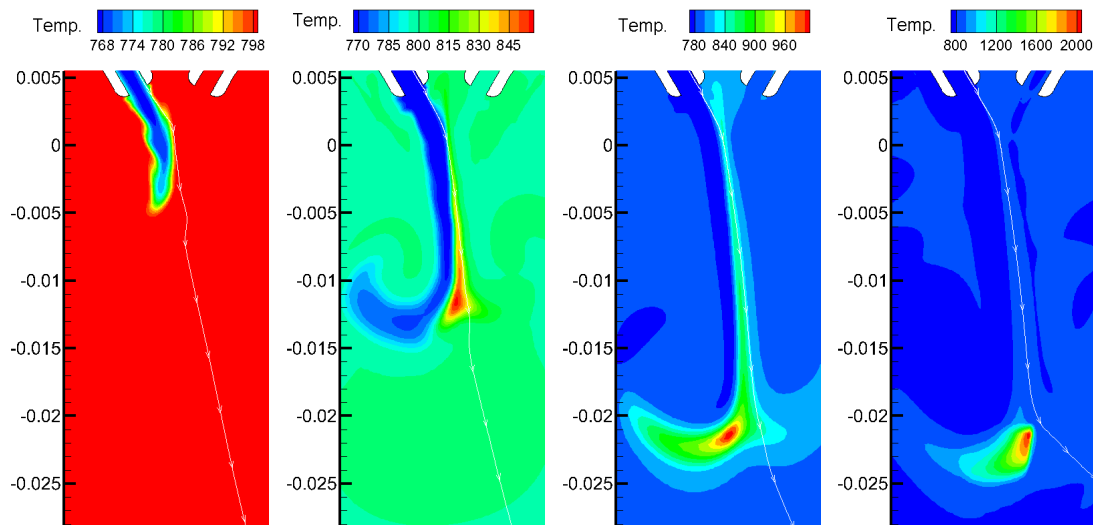


Figure 4.17. argon, $T=800K$, $p=101325Pa$. Series of contour plots of temperature at $t=1.6ms$ (initial impingement), $3.0ms$ (mid-way of impingement and ignition), $4.5ms$ (before ignition) and $4.7ms$ (after ignition) showing the initial combustion process.

In Fig. 4.18 the mass fraction contours of MMH, HNO_3 , NO and H_2O are shown at time instant $t=4.7ms$ just after ignition. The flame front depletes the fuel and oxidizer streams surrounding it. The considerable formation of NO and H_2O show the presence of combustion. The flame front is again anchored at a downstream location as in the case of He ambient and remains there until no external disturbance is imposed.

In Fig. 4.19 the MMH, HNO_3 and H_2O mass fractions along with the temperature contour are shown when the propagating products of combustion reach the downstream. With helium as the background gas the two propellant streams formed a

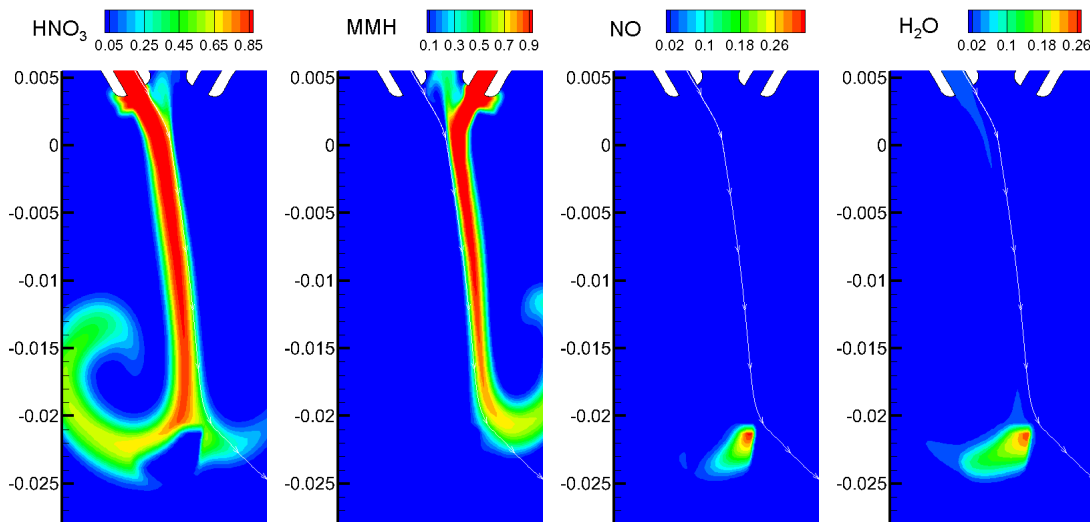


Figure 4.18. Mass fraction contours of HNO_3 , MMH, NO and H_2O after ignition in argon environment at $T = 800\text{K}$ and $p=101325\text{Pa}$ at $t=4.7\text{ms}$.

laminar sheet around the hot gases without developing any instabilities. The combustion zone was confined in between the two outer sheets and the propellants exited without complete combustion. In the case of argon, however, the two propellant streams enclosing the hot gases develop instabilities. Particularly roll up is observed downstream of the ignition location as seen in Fig. 4.19(a) and Fig. 4.19(b) which show the oxidizer and fuel streams depleting as they proceed to the exit. This is in contrast to Fig. 4.14 which shows a laminar sheet of MMH and RFNA enclosing the flame front. The fuel and oxidizer are therefore completely exhausted within the domain because of enhanced mixing. The region of combustion for argon environments is wider than that for helium environments near to the exit.

In the case of the helium environment the hot gases formed at the reactive interface escaped into the cavity between the two orifices because of the recirculation zone between the jet streams. As the cavity was filled lighter gas, the reactive gases (primarily HONO and CH_4N_2) displaced the He. Once the radical concentration reached a critical value combustion occurred in the cavity resulting in a flame that propagated

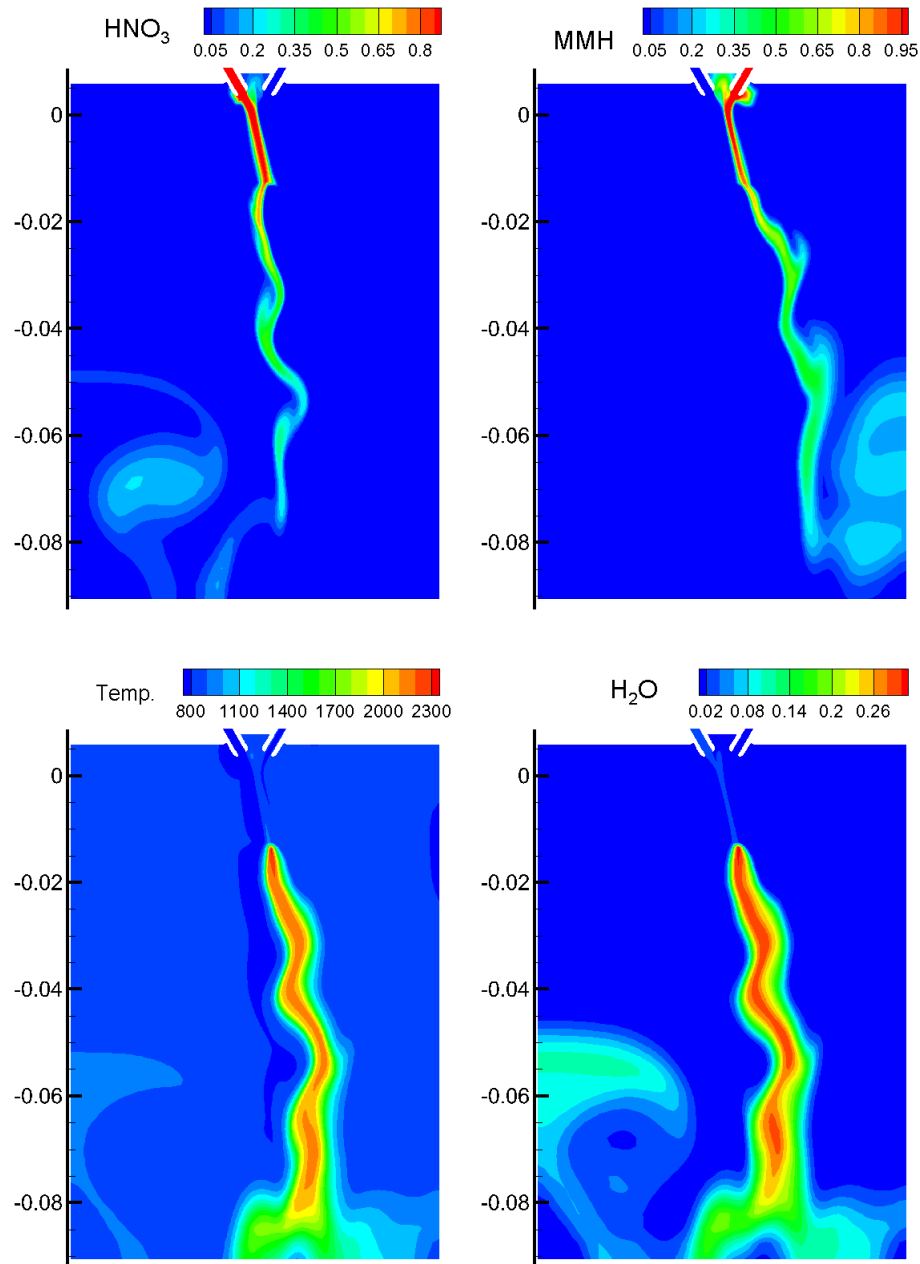


Figure 4.19. Mass fraction contours of HNO_3 , MMH and H_2O along with temperature when the flame front has reached the exit at $t = 24.6\text{ms}$ in argon environment at $T = 800\text{K}$ and $p=101325\text{Pa}$.

downstream and merged with the flame downstream to form a reaction zone spanning the entire domain. In the case of argon, the occurrence of this event is delayed

considerably. This is because of the time required to diffuse the heavier argon from the cavity and establish propellant concentrations that can initiate combustion. Once this cavity region ignites, the flame front again eventually merges with the flame at the downstream location. The temperature contours in Fig. 4.20 show the sequence at $25.8ms$ cavity undergoes ignition, at $26.2ms$ the flame front is propagating downstream and at $26.5ms$ the two flame fronts merge. Following this time instant a combustion zone anchored at the RFNA orifice extends throughout the length of the domain.

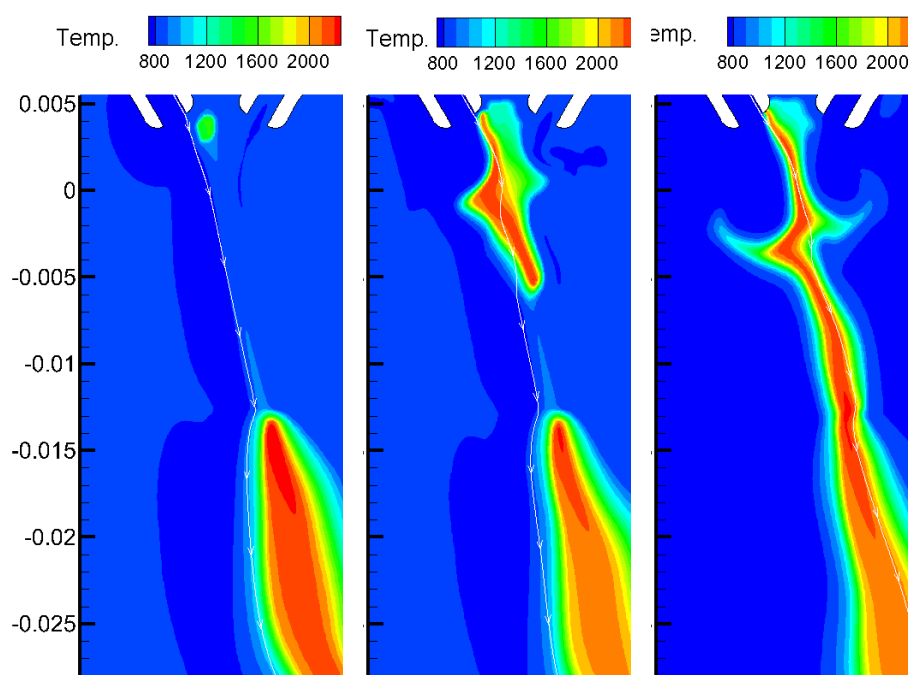


Figure 4.20. Temperature contours at $t = 25.8ms$ when ignition occurs at the cavity, $t = 26.2ms$ when the flame is half way between cavity and downstream flame and at $t = 26.5ms$ when the two flame fronts merge for argon at $T = 800K$ and $p = 101325Pa$.

Figure 4.21 shows an instantaneous contour plot of MMH, HNO_3 , NO and temperature at $t = 40ms$. The MMH and RFNA streams are depleted well within the domain. The fuel and oxidizer streams develop considerable instability, compared to

helium ambient, in the form of shear layer roll-up. This is in contrast to Fig. 4.16. The MMH appears to be exiting from the outlet boundary on the right side.

4.4.3 Combustion at 800K and 10132500Pa

The constant volume combustion analysis, which ignored convection and diffusion, showed that ignition occurred much more rapidly at 100atm than at 1atm for an initial temperature of 800K. High pressure results for impinging stream are given in this section to enable a similar comparison of the effect of pressure for this geometry. As already seen at low pressures the type of ambient gas has significant effect on the combustion process. The initiation processes in argon and helium underwent the same ignition events but they occurred at different times. Following this initial transient the combustion process was characterized by reactive sheet roll-up in argon whereas helium showed a laminar diffusion flame. The issue in the present section is to assess how pressure affects these processes.

As before we again consider both helium and argon ambient environments. The background gas are again at a temperature of 800K but at a pressure of 10132500Pa. Inlet conditions for the MMH and RFNA are given in Table 4.4. The mass flow rates for these calculations are 100 times those at low pressure, while the oxidizer to fuel mass flow rate ratio is kept same.

The transient process at high pressure in helium environment is summarized in Fig. 4.22 and shows a sequence that is qualitatively similar to the one at 1atm. In Fig. 4.22 both the density and temperature contour plots at three instants of time are shown for helium background gas. The density contour plots help in distinguishing the fuel and oxidizer streams from the ambient gas which is at a lower density. The products of combustion are also at lower density due to higher temperatures and merge with the helium in the density plot. In Fig. 4.22 the first time instant shows the two streams after impingement at $t=2.0ms$. The density contours show the two streams have merged and the temperature at their interface is now above the ambient

Table 4.4 Computations detail for $T=800K$, $p=10132500Pa$.

Flow property	Fuel Stream	Oxidizer stream
Gas composition	MMH	RFNA
Temperature(K)	800	800
Mass flow rate($kg/m s$)	1.2	2.0
Density (kg/m^3)	70	90
Velocity (m/s)	20	18
Thermal conductivity ($W/m - K$)	0.0826	0.0545

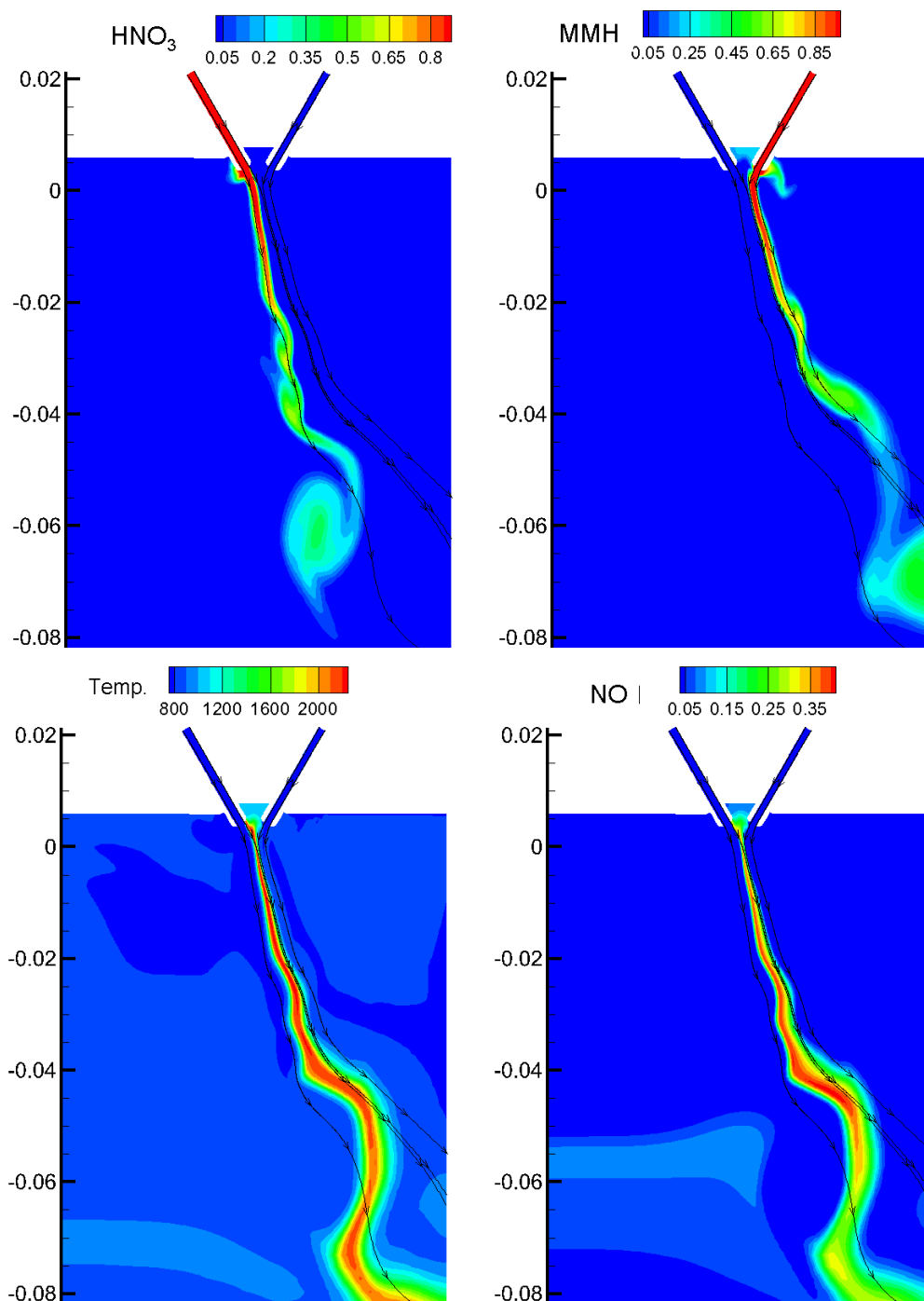


Figure 4.21. Instantaneous contour plots of MMH, HNO_3 , NO and temperature for argon environment at 101325Pa for argon at $T = 800\text{K}$ and $p=101325\text{Pa}$.

due to interface reactions as seen in the temperature contour. Thus, diffusion and chemical reactions have set in. The first contour plot is similar to what is seen at low pressures when the two streams are merged. A reactive interface develops almost immediately when the two streams imping on each other. Once this initial diffusion has resulted in the necessary radical pool for combustion, the ignition event occurs in the reactive zone.

The next instant at $t=2.3ms$ shows combustion at the interface of the two streams. The density contours show the hot product gases filling the interface. The propellant streams are now separated by the combustion zone at the first ignition event. The heat transfer in the interface moves the ignition point to the region in between the two separated streams upstream. This process occurs through the entire length of the interface between the propellant streams before it finally reaches the cavity. The cavity region then undergoes combustion thus a combustion zone eventually separates the MMH and RFNA streams for the entire length. Compared to low pressures this process occurs at the same time for both background gases and also instantaneously in both the helium and argon environments. The flame is seen propagating in between the two streams from the temperature plots. The flame propagation at high pressures appears to occur by a different mechanism compared to low pressures. From the figure it is seen that the hot combustion zone is propagating in the opposite direction to the flow. At high pressures the propellant streams separate from each due to combustion in the interface region. In case of high pressures the first ignition event in the initial front (at $t = 2.3ms$ in Fig. 4.22) controlled by diffusion. Following this the chemistry takes over due to smaller time scales. Thus, the flame propagates quickly through the reactive interface dominating the diffusion process. The ignition sequence occurs almost in a similar fashion for argon. At high pressure the time taken for the ignition to occur in case of helium is $2.3ms$ compared to $2.7ms$ for argon from the start of computation, showing that the ambient gas has almost no effect on time for combustion initiation at high pressures. Recall that these values were $3.5ms$ for

helium and 4.5ms for argon at 1atm. So the initiation process occurs approximately 50% faster in helium and 70% faster in argon at these high pressures.

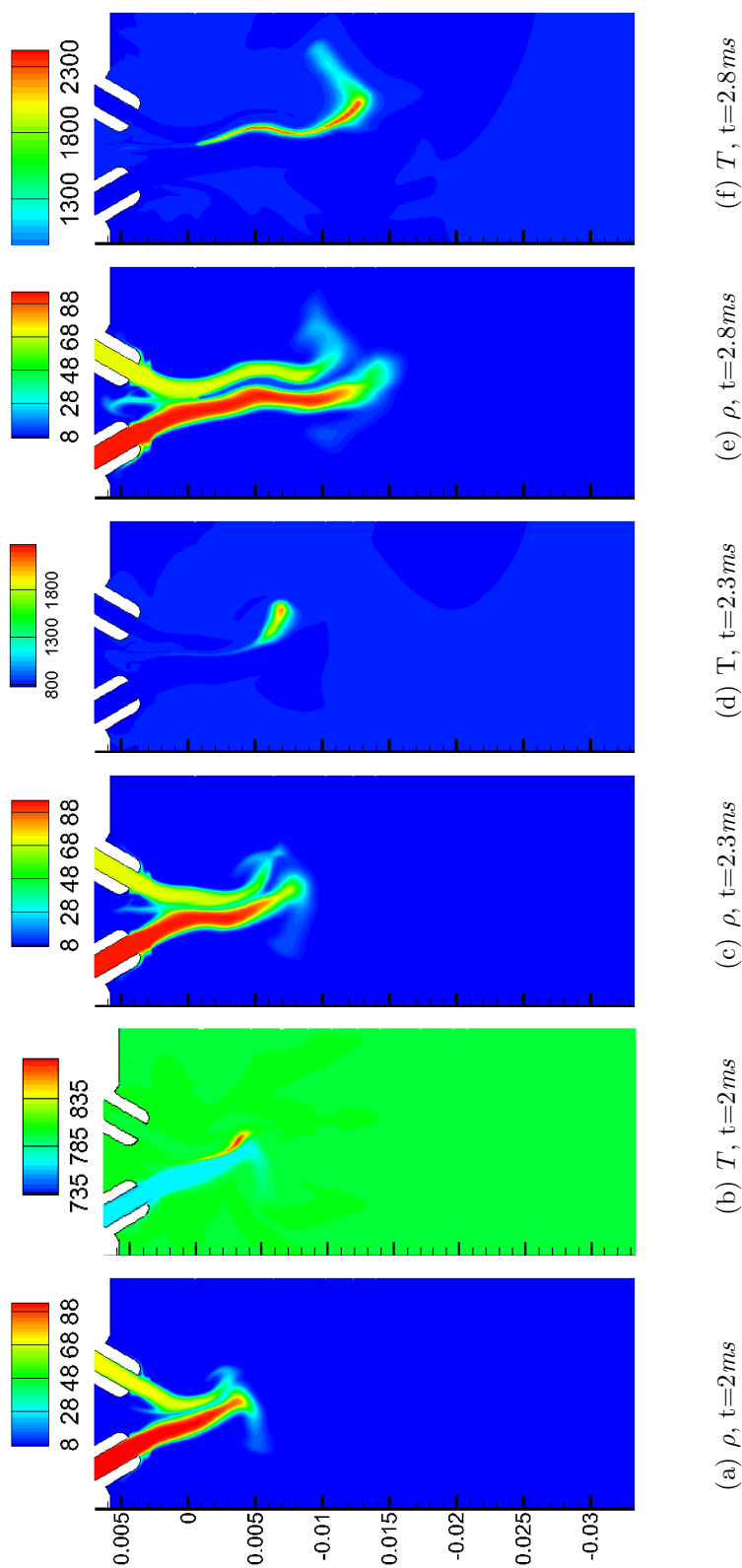


Figure 4.22. Instantaneous contour plots of density and temperature for helium at 10132500 Pa showing flame propagation between the fuel and oxidizer interface for three instants of time $t = 2 \text{ ms}$, 2.3 ms and 2.8 ms for helium background gas at $p = 10132500 \text{ Pa}$.

At later times, the combustion region between the two streams prevents them from mixing and combustion. In the case of He the two streams remain separated by the combustion zone for the entire length of the domain. For argon environment which is at a higher density compared to the propellants instabilities in the form of roll-up of outer fuel and oxidizer streams appear resulting in enhanced mixing. The combustion front reaches the outlet of the domain at $10ms$ for helium compared to $20ms$ for argon. Again, this is due to the faster diffusion of propellants in the lighter helium environment compared to argon. Following the end of the transient, statistics can be obtained to study time averaged properties.

Figures 4.23 and 4.24 show the instantaneous combustion in argon and helium environment at $t= 40ms$ to illustrate that flowfield at later instants of time.

4.4.4 Comparison of Time-Averaged Results

In the previous section the transient combustion process was described leading to stationary flow for both argon and helium environments at low and high pressures. At both pressures the stationary combustion zone extends from the oxidizer outer wall to the outlet boundary condition. At low pressures the time instants at which various ignition events occur are different for helium and argon environments because of the longer time scales for heat release compared to diffusion processes. At high pressures the chemical time delay dictates the combustion. The instants at which stationary conditions were obtained in the unsteady combustion were described previously. In comparison to helium the argon gas induces more unsteadiness. In the present section time averaged properties (averaged over $20ms$) after stationary combustion is established are compared for the ambient conditions considered earlier.

We begin the section by comparing the low pressure case for argon and helium environments. In Fig. 4.25 and Fig. 4.26 the contour plots for fuel, oxidizer, product gas NO and temperature are shown for the ambient domain for helium on the left and argon on the right. The first difference is that in argon the propellants are depleted

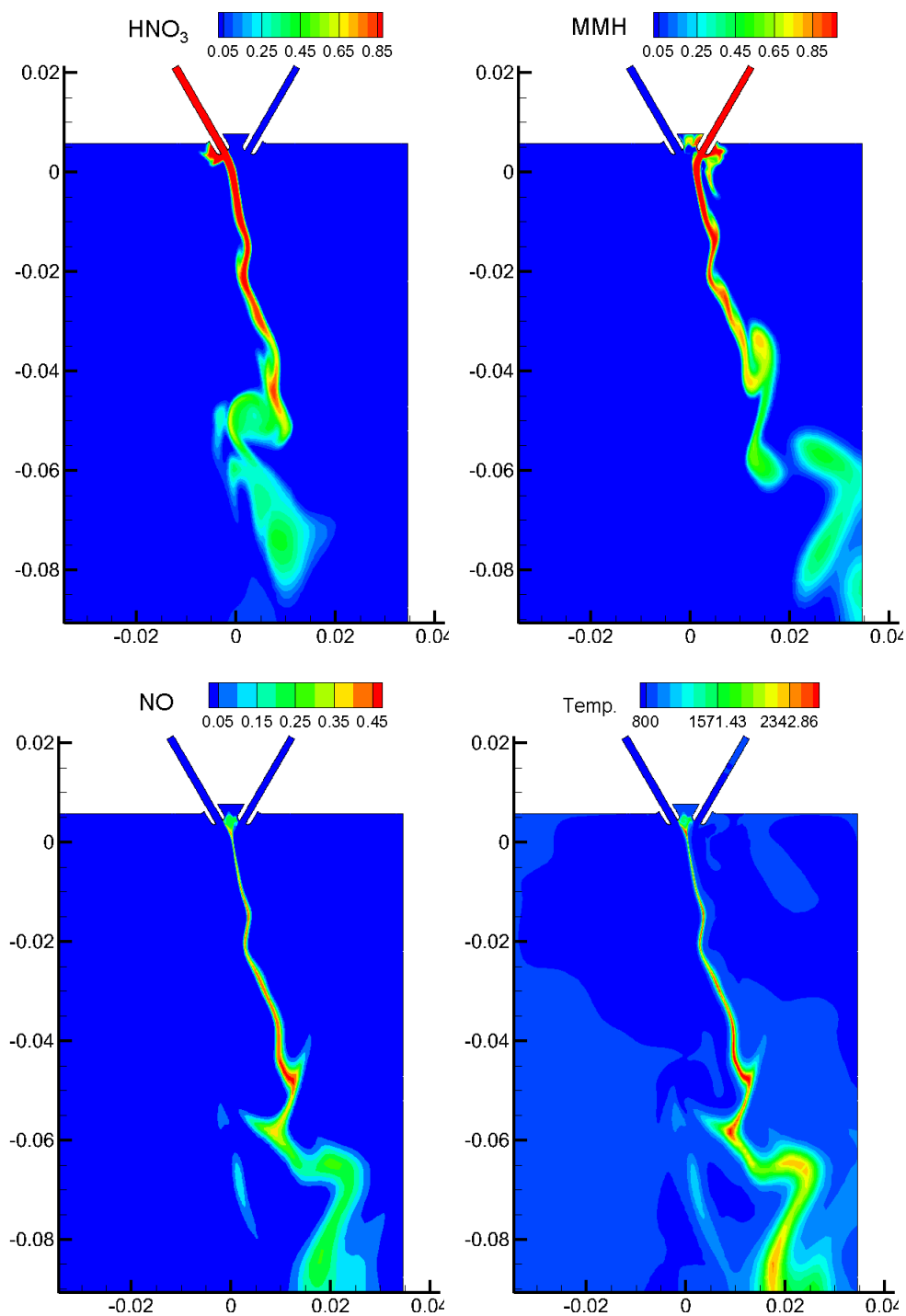


Figure 4.23. Mass fraction contours of MMH, HNO₃ and NO along with temperature for argon at $t=40ms$, $10132500Pa$.

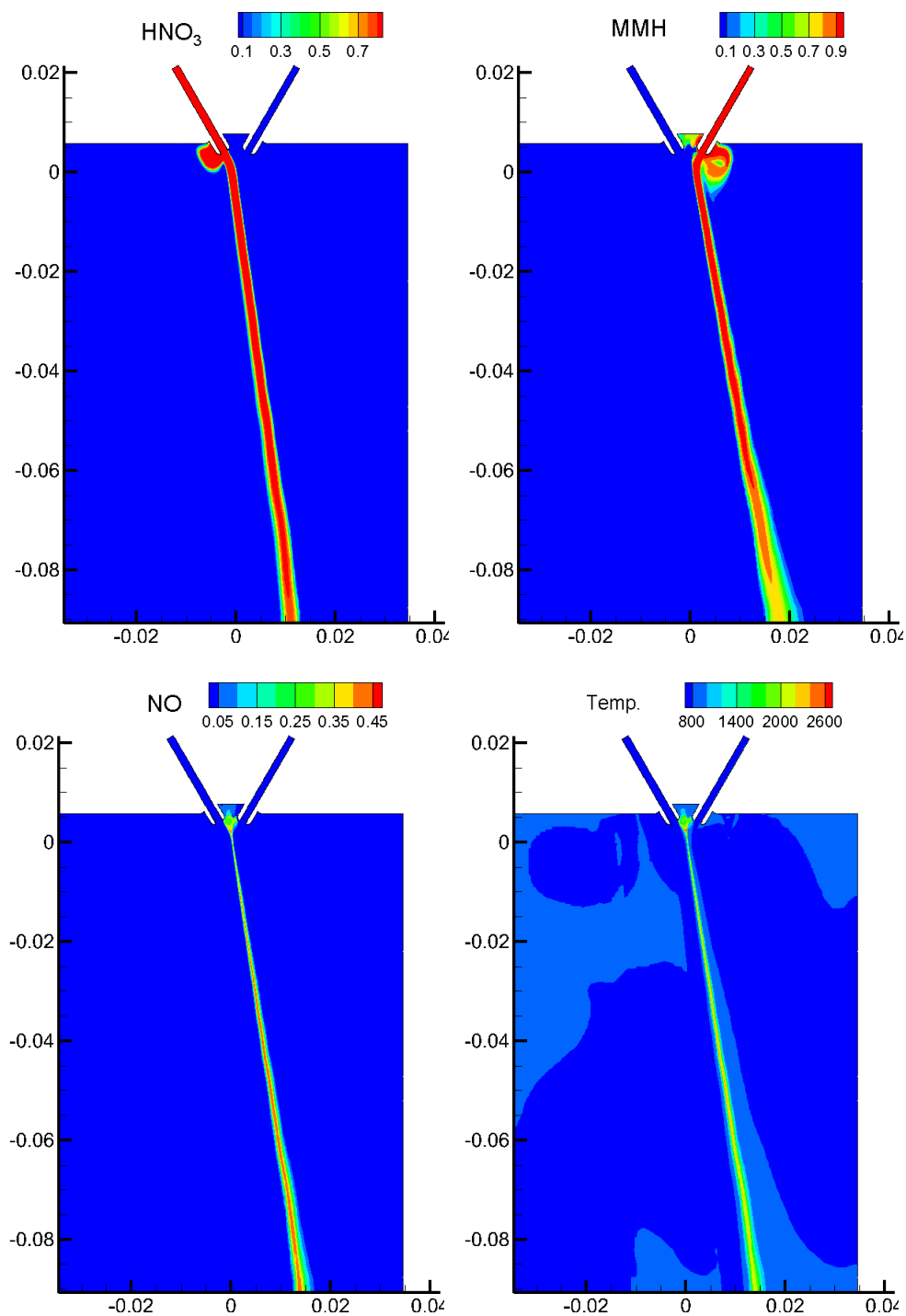


Figure 4.24. Mass fraction contours of MMH, HNO₃ and NO along with temperature for helium at $t=40ms$, $10132500Pa$.

approximately half-way through the domain whereas for helium both propellants extend through the domain and exit the bottom outlet. The peak temperatures in the argon environment are, however, lower than those in the helium environment. The production of NO, a predominant product of combustion, is also very different. In the argon environment the NO is widely dispersed and extends over a large fraction of the width resulting in a wider combustion zone downstream. In the helium environment NO remains in a narrow band. The temperature profiles are similarly identical until the argon environment leads to a wider brush of above ambient temperature gas while the helium environment results in a narrow band. This is seen more clearly when we compare the time-averaged temperature profiles at $y = -0.02m$ and $y = -0.08m$ in Fig. 4.27 (Refer to Fig. 4.5 for location reference). The temperature profile for argon is shown in black while that for helium is shown in red. The peak temperature near the orifice ($y=-0.02m$) is higher for the argon ambient than for the helium environment. At the downstream location ($y=-0.08m$) the helium profile still shows peak temperature while the argon does not exhibit a peak and has clearly diffused over a much larger region.

In Fig. 4.28 and Fig. 4.29 the mass fraction of the reactants, dominant products and intermediate species are shown at the same two locations $y = -0.02$ and $-0.08m$. At the location closer to the orifice the reactants and products for both helium and argon are confined to a narrow region. In helium environment the MMH and HNO₃ mass fractions are higher than those of argon environment showing a larger amount of propellant has reacted in argon an observation that is consistent with the higher temperature noted earlier. The mass fraction of the intermediate species, CH₄N₂ and HONO are higher than in helium environment. The higher CH₄N₂ which is formed from pyrolysis of MMH indicates lower temperatures which is a result of NO₂ reacting with MMH. This explain the higher temperature at this location in Fig. 4.27. The NO, N₂ and H₂O mass fractions are about the same in both whereas the CO mass fraction is higher in the helium environment while the CO₂ curve is higher in argon.

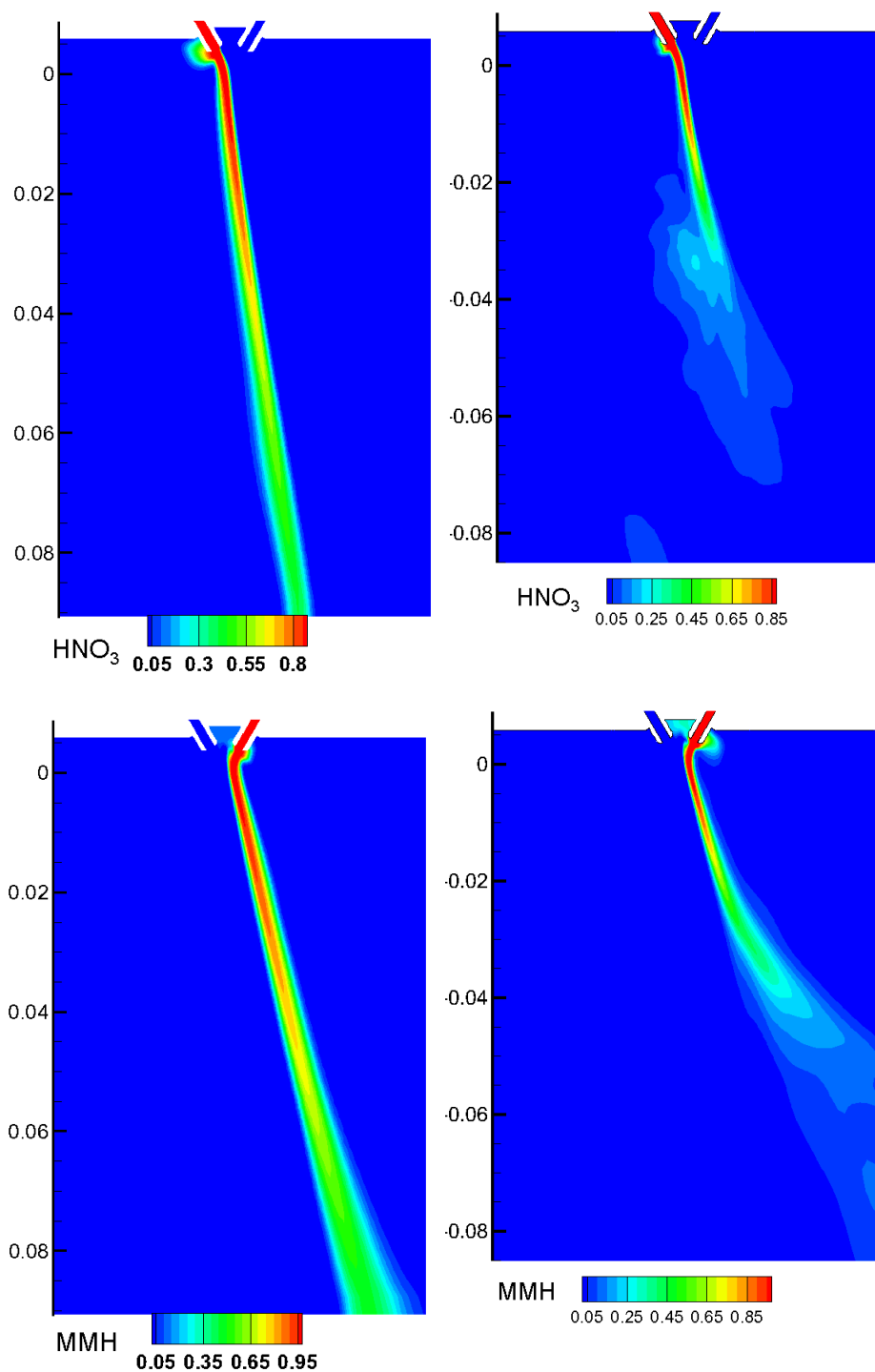


Figure 4.25. Time-averaged mass fraction contours of HNO_3 and MMH for argon (right) and helium (left) environment at $p=101325\text{ Pa}$.

At the downstream location, $y=-0.08m$, Fig. 4.29, all the species mass fractions in argon have diffused across the domain due to enhanced mixing for the argon case while those for helium are still confined to a narrow band in much the same fashion as for temperature. The HNO_3 mass fraction is spread across the domain and the MMH and CH_4N_2 are nearly gone although a small amount resides on the fuel side. In helium considerable portion of the species still remain. This same pattern is observed for all other remaining species. Clearly, the oxidation of MMH has proceeded further in the case of argon than helium as was also reflected in the temperature plots in Fig. 4.27.

Corresponding results at 100atm are given in Figs. 4.30 - 4.34 and similar patterns are seen. Figures 4.30 and Fig. 4.31 show the time average contour plots of MMH, HNO_3 , NO and temperature for $p = 10132500\text{Pa}$ is shown for helium and ambient environments respectively. At the high pressure condition the argon propellant mass fraction becomes depleted as we move away from the orifices while that in helium continues downstream and exits at the boundary in a manner similar to the 1atm results. The shear layer does not develop instabilities and remains intact for the entire domain. The effect of higher pressure appears to disperse the reactants/products more rapidly in argon while keeping them more closely combined in helium.

Figure 4.32 compares the line plots of temperature at two locations $y= -0.02m$ and $y=-0.08m$ for the helium and argon cases. The argon environment shows considerably lower temperatures compared to the helium environment which shows temperature as high as 2300K . The higher temperature also shows the reactions going to completion close to the orifice. The temperature drops as we go to the downstream location for helium. The combustion zone is restricted to a small fraction of the domain cross-section in helium. The peak temperature for the argon case does not drop but the temperature profile is much wider at the downstream location again due to unsteadiness. The width of the combustion zone for argon at high pressures is smaller compared to low pressures.

In Fig. 4.33 and Fig. 4.34 the species mass fractions of reactants, prominent products and intermediate species of reactions are compared at locations $-0.02m$ and $-0.08m$ respectively. At both the locations the species mass is redistributed across the cross section for argon ambient conditions while that of helium is confined to a narrow region. The species concentration peaks are higher for helium than argon particularly for the products showing that helium ambient is promoting combustion at higher pressures. The higher NO mass fraction peak at both locations for helium confirms this fact. The intermediate reaction species mass fractions are much lower in the case of argon compared to helium. Both CH_4N_2 and HONO mass fractions are lower in the shear layer due to the lower temperatures for argon ambient. Thus, though argon promotes mixing of the fuel and oxidizer streams due to instability of the shear layer the heat generated from the initial step of oxidation of MMH by NO_2 dissipated due to mixing. This inhibits further reaction from occurring and combustion is stalled.

4.5 Unsteady Three-Dimensional Analysis

The previous section using the planar assumption highlighted that the given chemical kinetics mechanism resulted in combustion behavior which is dependent on the background gas. In the present section the planar assumption is relaxed and the impinging jet geometry identical to planar case is analyzed in three-dimensions. The approach used in the previous section is applied in setting up the solution for the problem. The reactive flow equations consisting of 26 species conservation equations are solved according to the methodology described in CHAPTER 2. The finite rate Arrhenius model for determining the species source term is employed which assumes perfect mixing at the sub-grid level.

The focus of the three-dimensional analysis will be to again understand combustion behavior using the newly proposed chemical kinetic mechanism. In particular attention will be given to initiation, flame propagation, holding and sustenance. Again,

variations in background gas properties are considered. Similar to the planar case solution at two pressures is presented, one at 1 *atm* and the other at 100 *atm* with the MMH/RFNA propagating into helium and argon as background gas. In the next section the three-dimensional computational grid along with the boundary conditions is described, following which results from the analysis are presented.

4.5.1 Problem Definition

The fuel and oxidizer passages adopted for 3-D computations is similar in dimensions to planar case except that the two passages are now axisymmetric. An ambient domain where the fuel/oxidizer combination, impinge, propagate downstream and react is provided. The cavity enclosed between the two orifices has an additional degree of freedom for the gases trapped in between the orifices. It was seen in the planar case that the reactive gases formed at the interface escape into the cavity and result in a second ignition in the cavity. In 3-D, however, the reactive gases may not occupy the cavity to result in second ignition.

Due to the exorbitant cost of performing 3-D computations (with 32 equations to be solved at each cell center) it is beneficial to explore ways by which the grid number can be reduced. The impinging jet geometry has a plane of symmetry passing through both the orifices which can be readily exploited to reduce the problem into half. The result is that the mean properties will be considered symmetric which is correct in the time-averaged sense but will also result in the turbulence being considered planar symmetric. The planar symmetric assumption for turbulence goes against the 3-D nature of turbulence but owing to the large computational time for 3-D problem the planar symmetric assumption is employed in the present situation.

The computational domain for the computations performed in this section is shown in Fig. 4.35 in an isometric view. The plane of symmetry is as marked and can be seen passing through the centers of both the passages. The boundary conditions are as marked in the figure. The plane of symmetry is treated as a symmetric

boundary while the face opposite to it is given outlet boundary conditions whose back pressure corresponds to the ambient domain. The three walls opposite to the orifices are treated as outlet boundaries as well. The boundary in between the two orifices is treated as a viscous wall with two ambient inlets extending from either side of the wall. The passage walls, both inner and outer, are treated as viscous walls. The boundary layer resolution employed for this grid at the walls is similar to the axisymmetric case. The extent of the ambient domain is smaller by about 20 *mm* compared to the planar case but sufficient to capture the flow of interest. In Fig. 4.36 and Fig. 4.37 the domain as seen from different direction is shown along with a representative grid. Also marked are the extents of the domain in *mm*. The flame in the 3-D configuration will spread in the *z*-direction as a result the exterior domain is seen to extend by about 11 *mm* in the *z*-direction. The details of grid in the RFNA and MMH passages is shown for the plane of symmetry in Fig. 4.38.

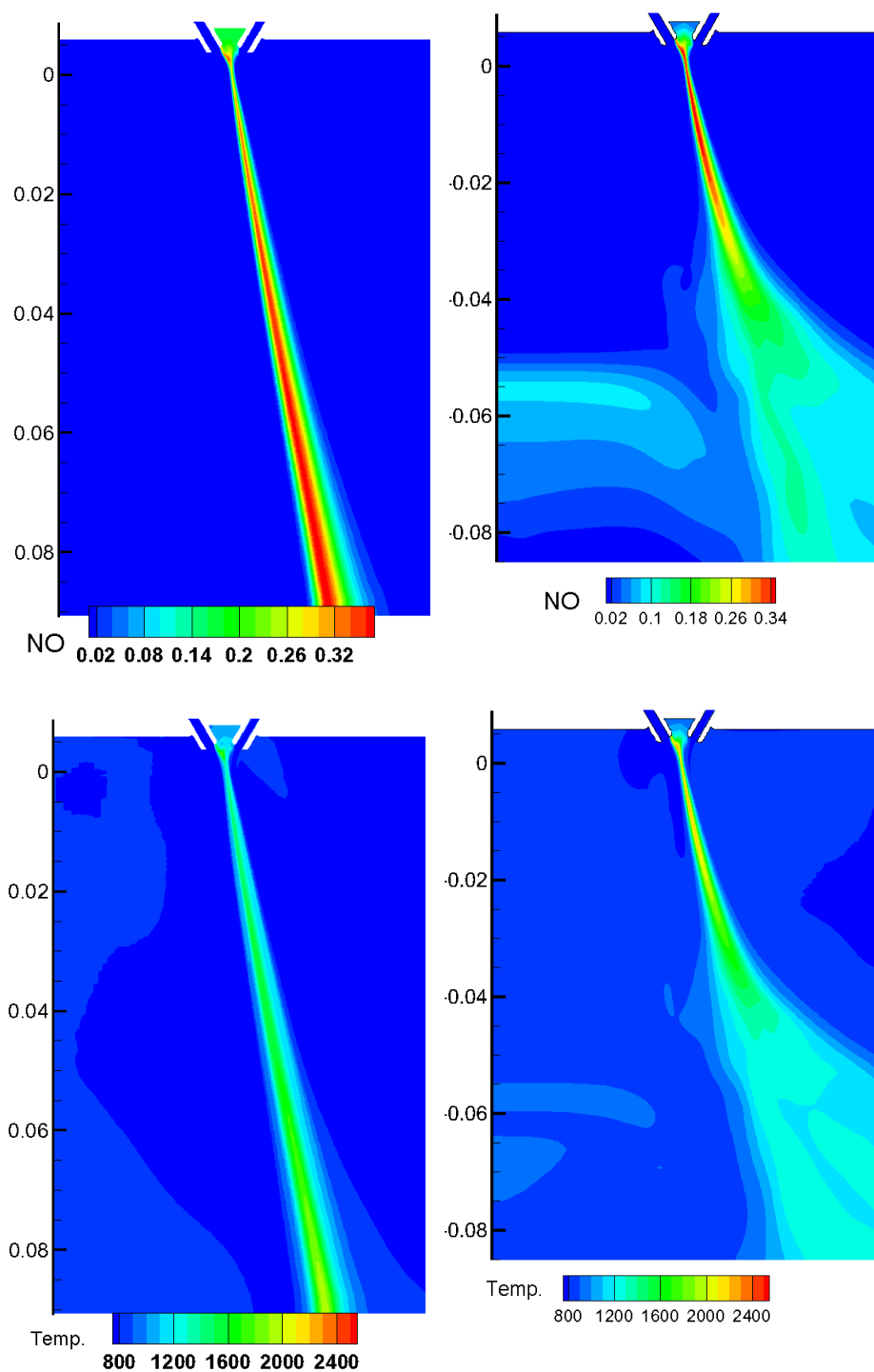


Figure 4.26. Time-averaged contours of mass fraction of NO and temperature for argon (right) and helium (left) environment at $p=101325 Pa$.

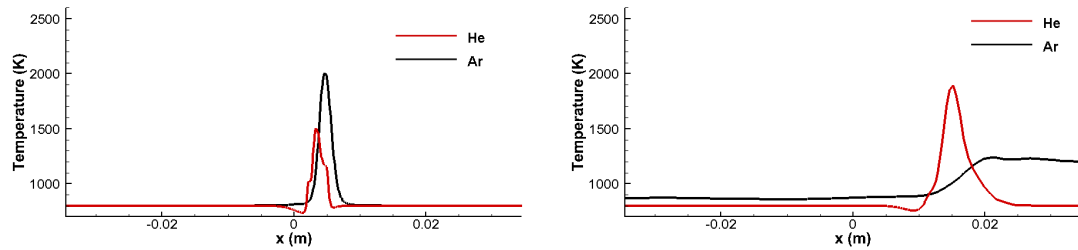


Figure 4.27. Time averaged temperature at $y = -0.02m$ (left) and $y = -0.08m$ for argon (black) and helium (red) ambient environment at $p = 101325Pa$.

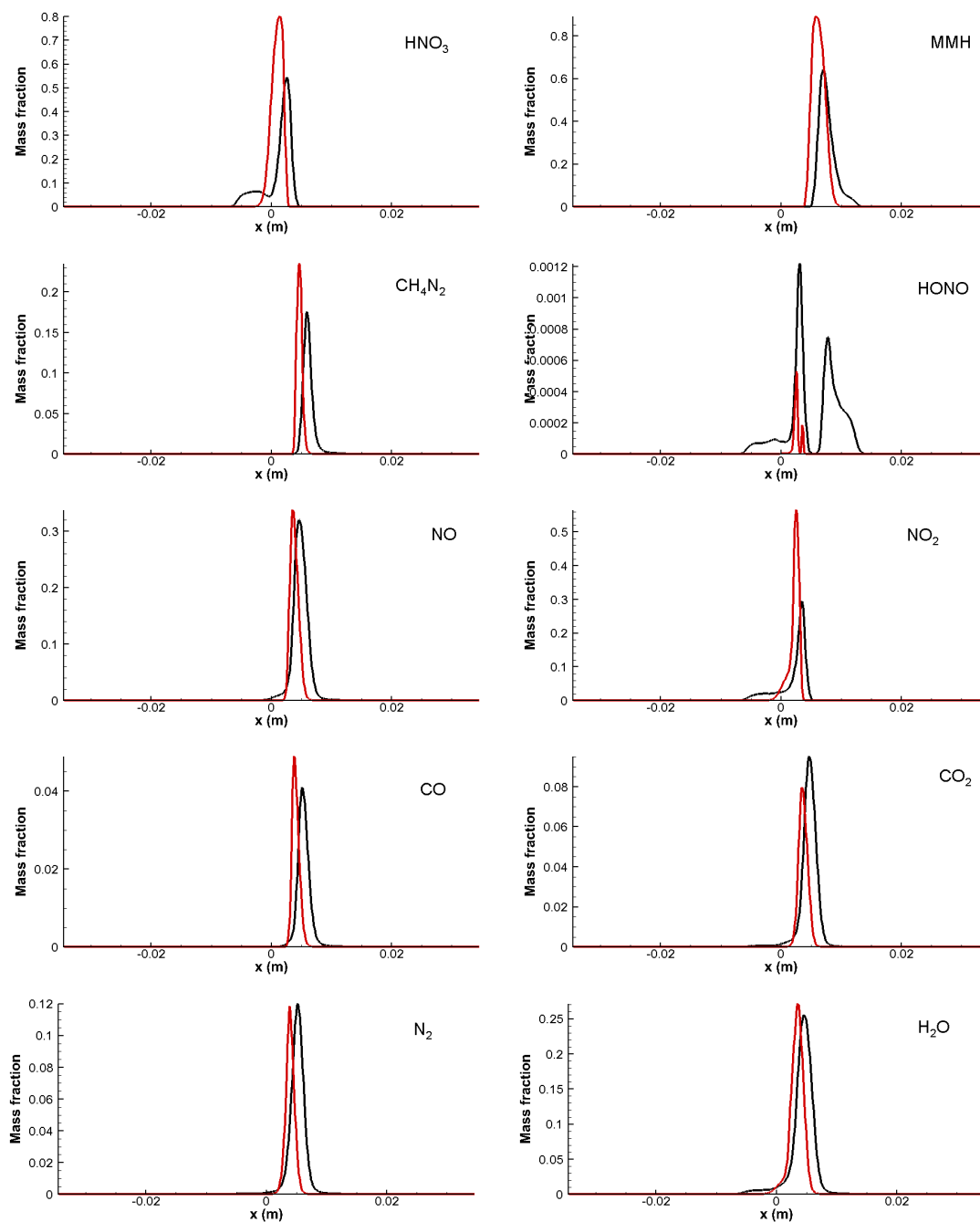


Figure 4.28. Time averaged species mass fraction at $y = -0.02\text{m}$ for argon (black) and helium (red) ambient environment at $p = 101325 \text{ Pa}$.

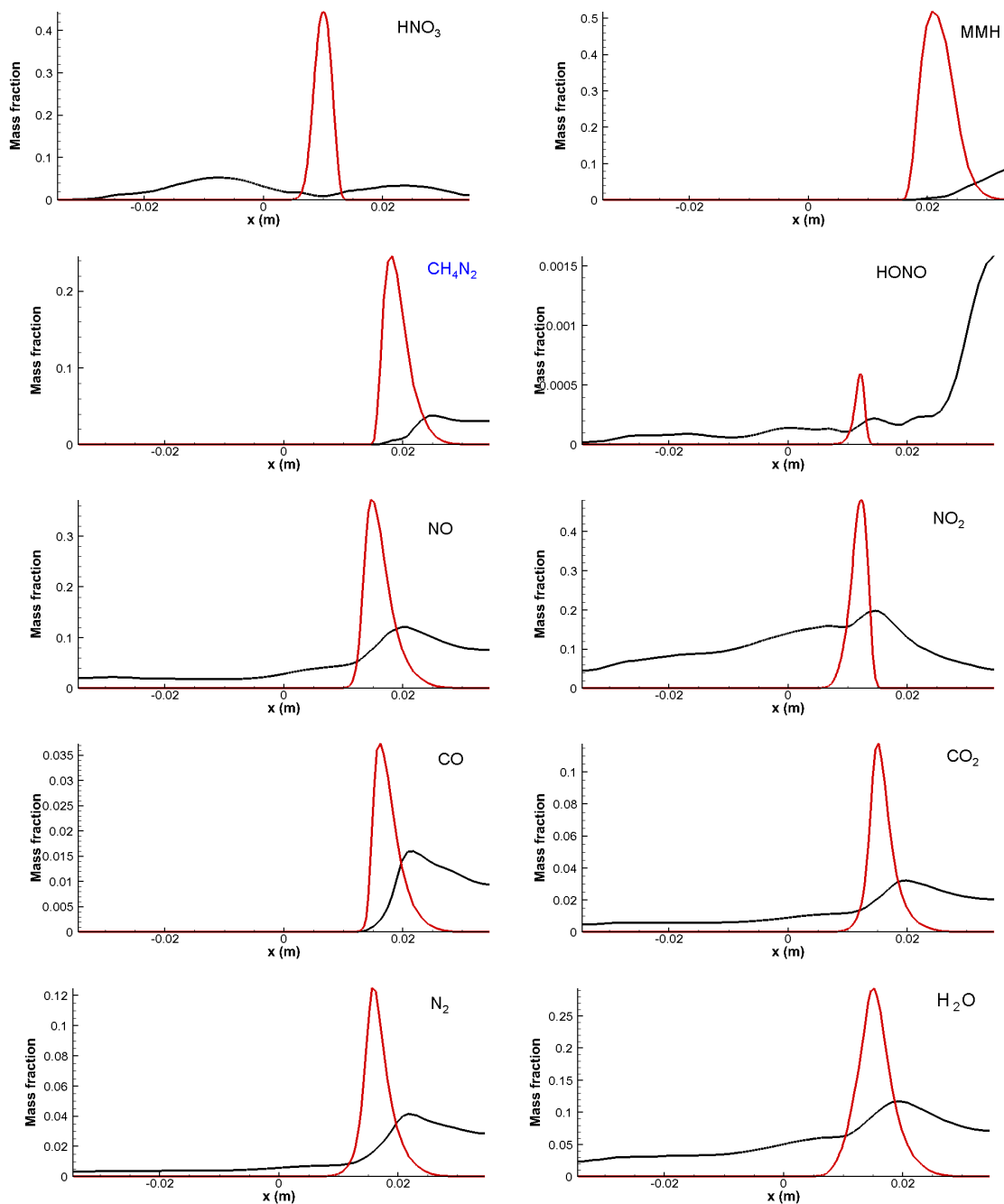


Figure 4.29. Time averaged species mass fraction at $y = -0.08m$ for argon (black) and helium (red) ambient environment at $p = 101325 Pa$.

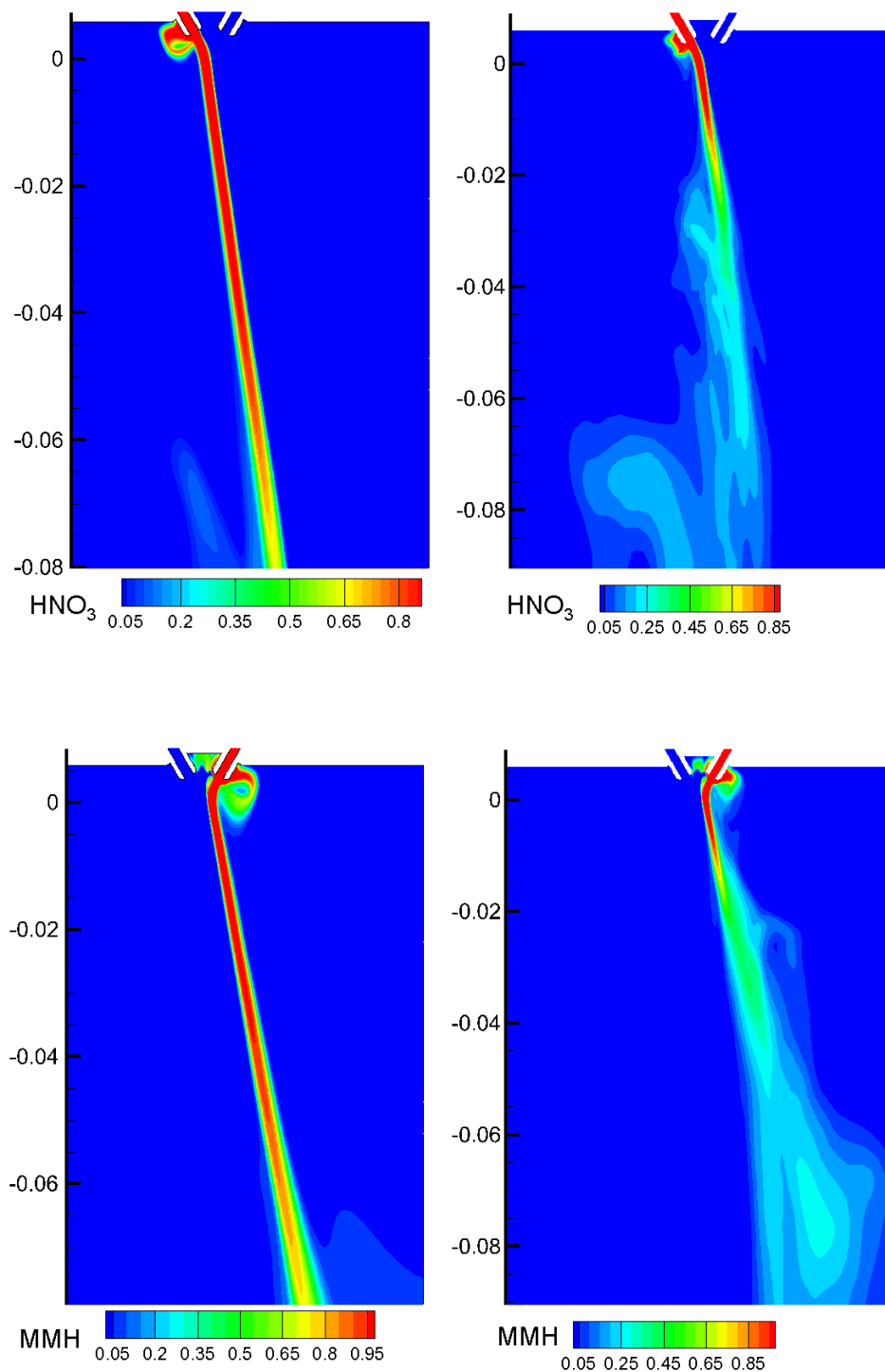


Figure 4.30. Time-averaged mass fraction contours of HNO₃ and MMH for helium (left) and argon (right) environment at $p=10132500 Pa$.

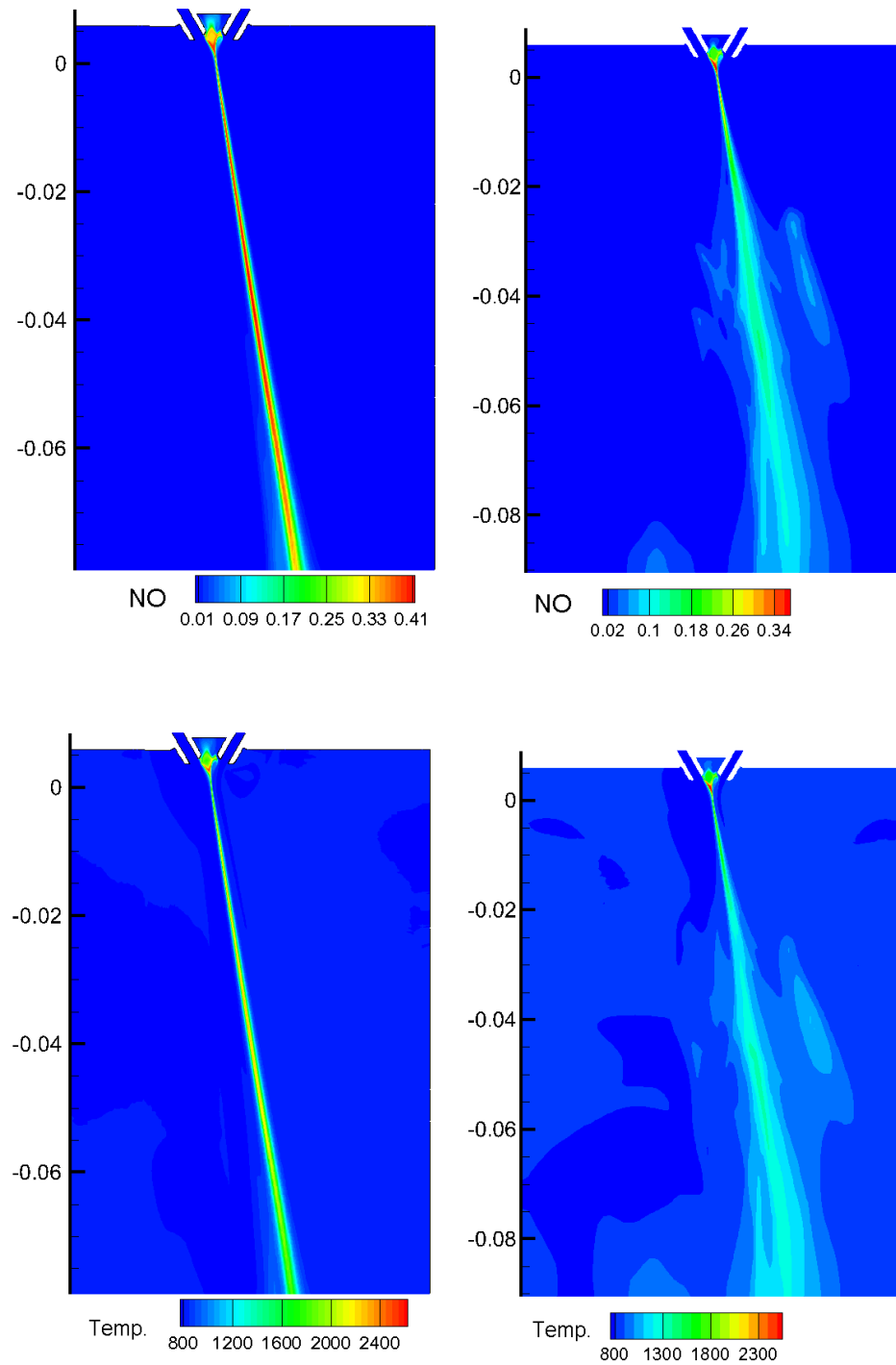


Figure 4.31. Time-averaged mass fraction contour of NO along with temperature contour for helium (left) and argon (right) environment at $p=10132500Pa$.

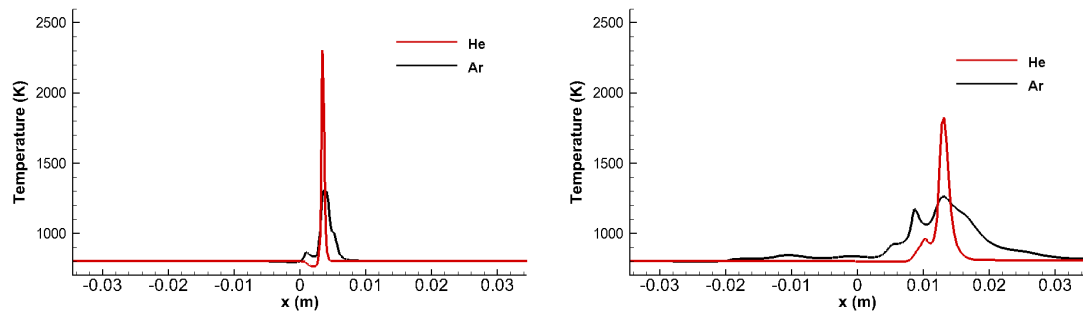


Figure 4.32. Time averaged temperature at $y = -0.02m$ (left) and $y = -0.08m$ for argon (black) and helium (red) ambient environment at $p = 10132500Pa$.

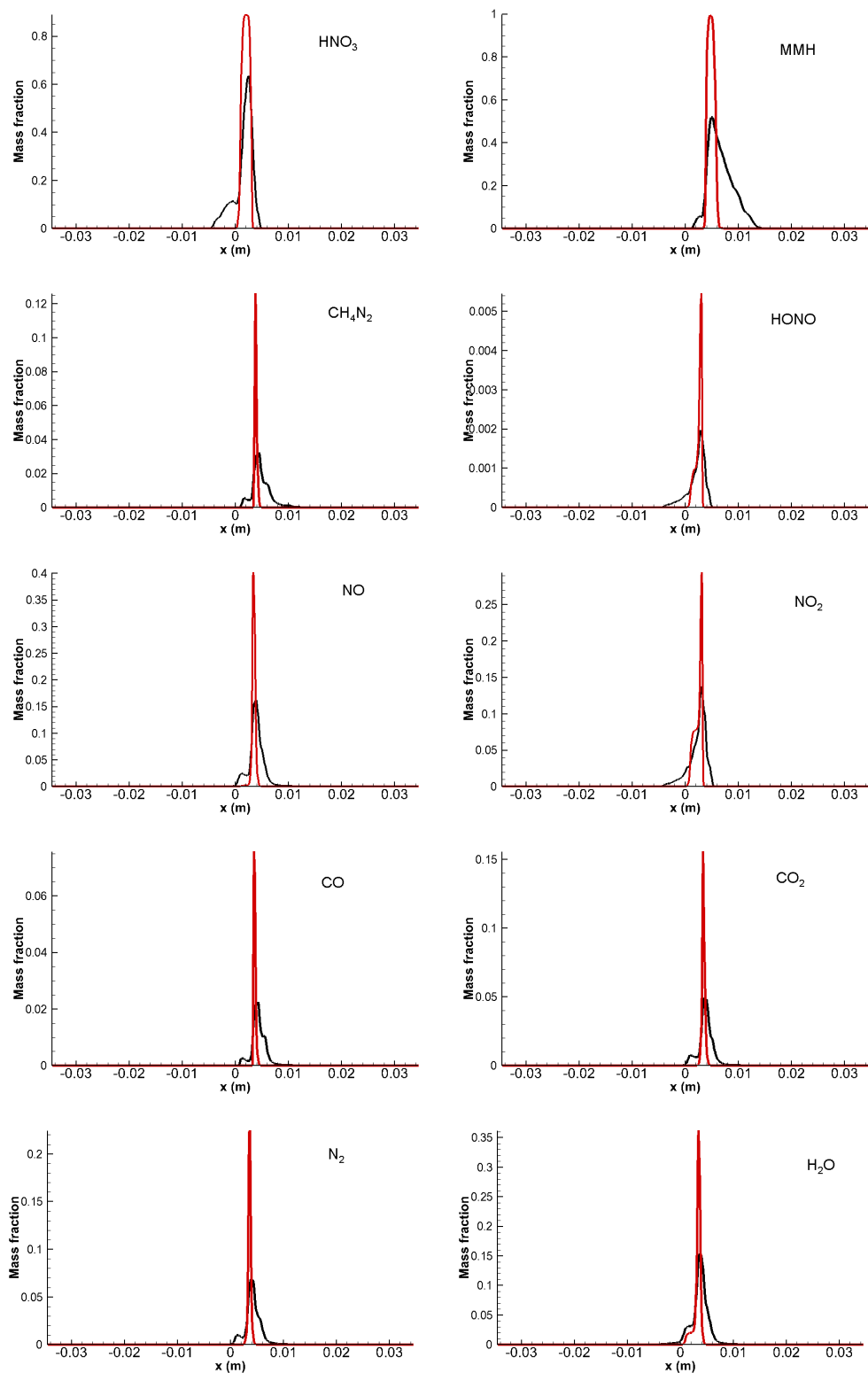


Figure 4.33. Time averaged species mass fraction at $y = -0.02m$ for argon (black) and helium (red) ambient environment at $p = 10132500 \text{ Pa}$.

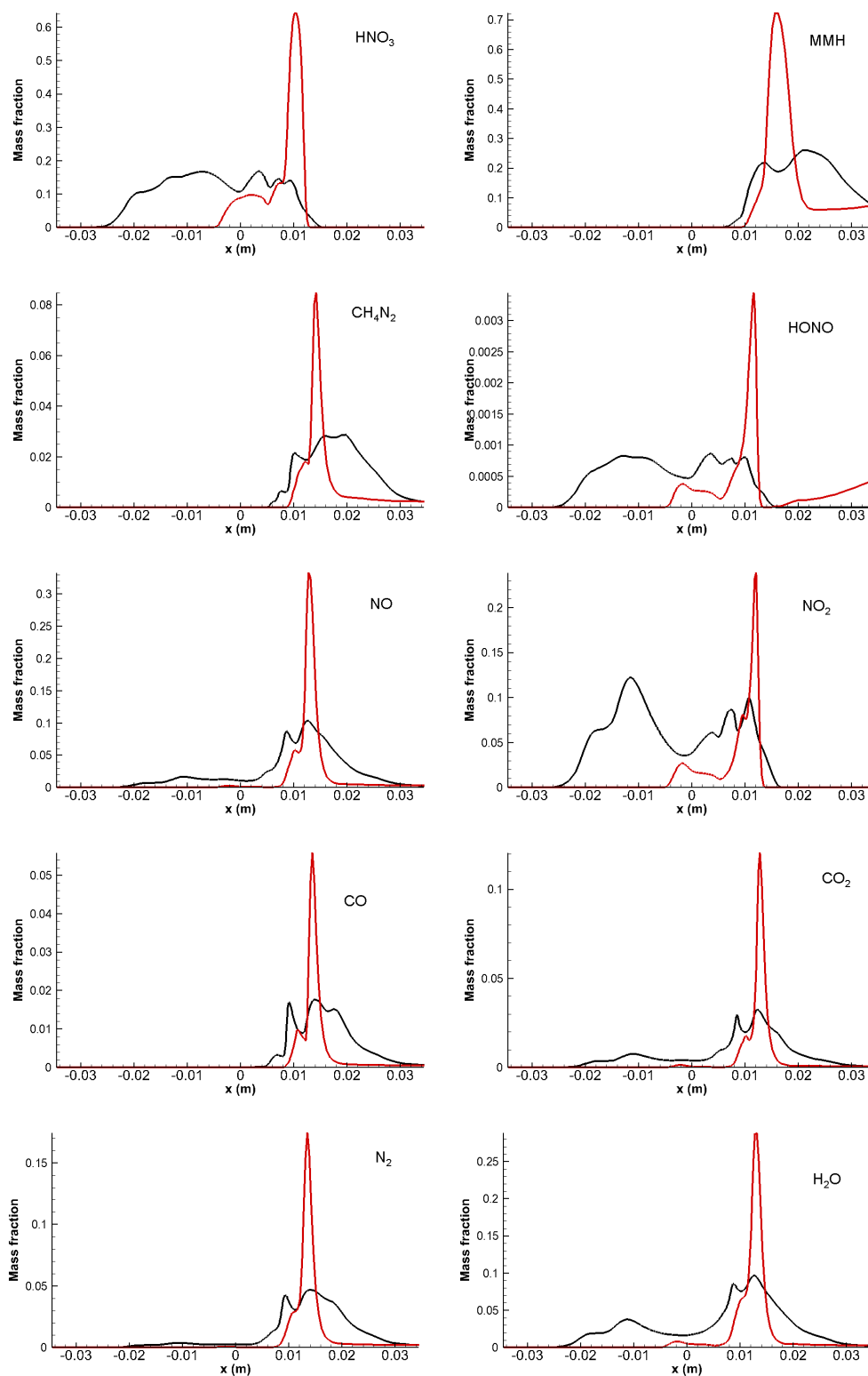


Figure 4.34. Time averaged species mass fraction at $y = -0.08m$ for argon (black) and helium (red) ambient environment at $p = 10132500Pa$.

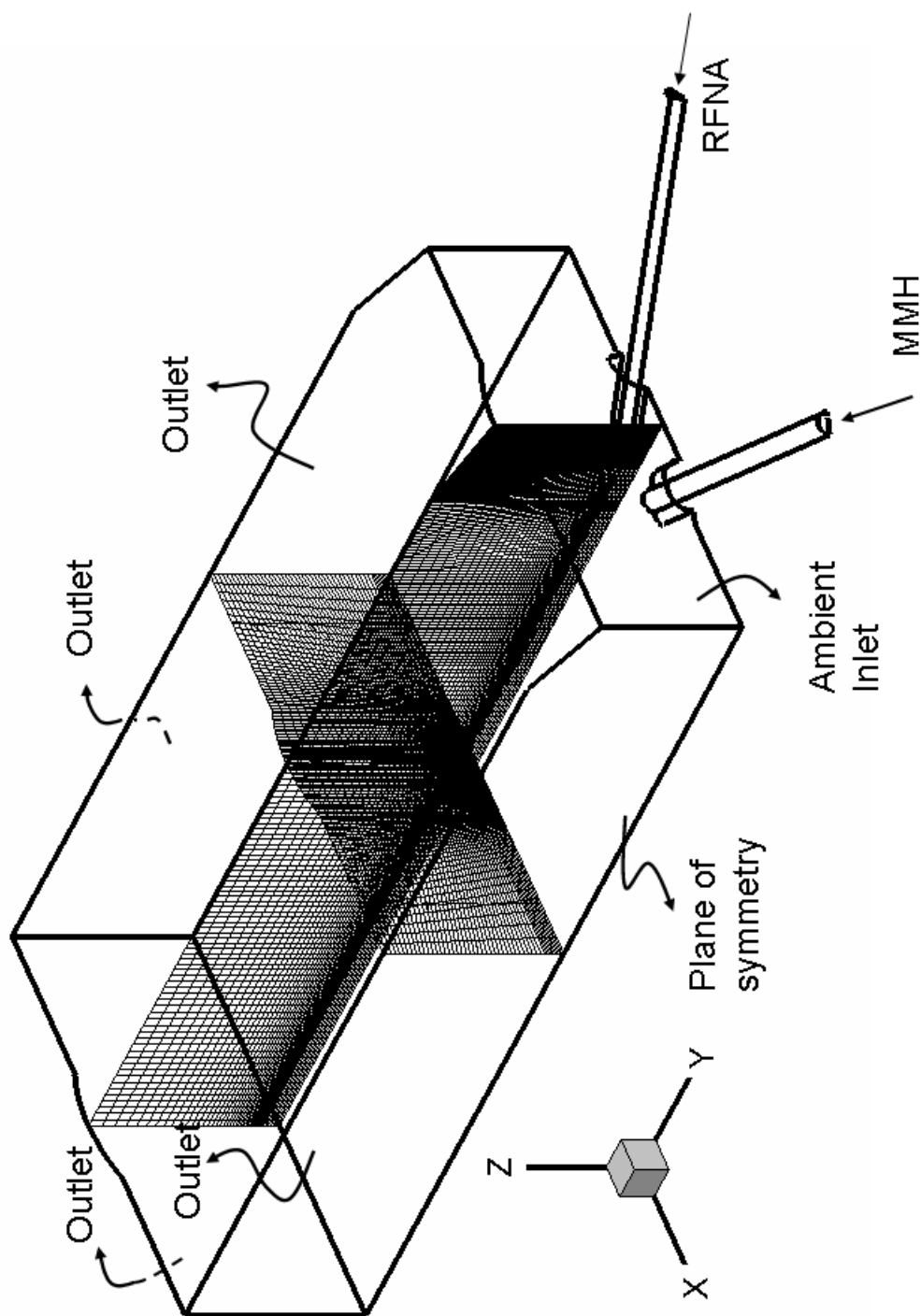


Figure 4.35. Isometric view of the computational domain with plane of symmetry marked along with grids at two planes perpendicular to each other. The boundary conditions are as marked.

4.6 Three-Dimensional Combustion Behavior

Similar to the planar case the effect of background gas pressure, mass and thermal properties are of interest in the present simulations. For this the two initial pressures of the propellants as well as the ambient gas are studied: 1 *atm* and 100 *atm* at an initial temperature of 800K. The temperature is again based on the results of constant volume combustion problem. To study the effect of background gas again helium and argon were considered. The section begins by discussing the results at the lower pressure of 1 *atm* followed by the 100 *atm* case.

4.6.1 Combustion at 800K and 101325Pa

The inlet boundary conditions at the MMH and RFNA inlets are given in Table 4.5. The inlet mass flow rate is specified such that exit velocity at the fuel and oxidizer passages is close to that observed in the planar case. This will allow for the three-dimensional computations to be contrasted with the axisymmetric case. At the initial transient the two flows traverse through the orifices, impinge at a downstream location and propagate through the domain. This is similar to the planar case. Recall that in the planar case combustion is initiated at a downstream location followed by a second ignition in the cavity. The two flame fronts, one from the cavity and the downstream flame, merge and span the entire domain. The time for the first ignition event to occur was about 4ms in both argon and helium gases. In the case of three-dimensional computations, however, no combustion is initiated either in argon or helium background gas at low pressures. The unsteady computations were performed till the two gases reach the outlet. In Fig. 4.39 the contour plots of MMH, RFNA and temperature are shown for at 10 ms in the plane of symmetry. The MMH and RFNA streams reach the domain exit and remain in contact with each other. The temperature is seen to rise only by a fraction at the interface indicating that the interfacial reactions are not proceeding as was seen in planar case. The planar case showed continuously increasing temperature at the interface due to reactions at the

Table 4.5 Computations detail for $T=800K$, $p=10132500Pa$.

Flow property	Fuel Stream	Oxidizer stream
Gas composition	MMH	RFNA
Temperature(K)	800	800
Mass flow rate(kg/s)	6×10^{-6}	10.0×10^{-6}
Density (kg/m^3)	0.722	0.975
Velocity (m/s)	23	22
Thermal conductivity ($W/m - K$)	0.0826	0.0545

interface of the two streams. It is unclear as to why there is no combustion initiation in the three-dimensional computations using the same chemical mechanism as in the planar case.

4.6.2 Combustion at 800K and 10132500Pa

The background pressure gas pressure is raised to 100 *atm* to study combustion. The inlet boundary conditions at the RFNA and MMH passages is shown in Table 4.6 and is used for both argon and helium as background gas. The mass flow rates are 200 times that of the case at 1 *atm*. In this case again the two streams impinge at a downstream location as soon as they come into contact, similar to what was observed in the planar case. The combustion is initiated at a downstream location at time $t = 1.2 ms$ almost twice as fast as the planar case. In Fig. 4.40 the instantaneous contour plots at time $t = 10 ms$ is shown for MMH, HNO_3 and temperature in helium environment. This time instant corresponds to a later time instant when the flow has almost reached steady state. In the three-dimensional case the combustion initiates at a location close to the orifice but remains anchored at that position without propagating upstream into the cavity region as seen from the figure. In the planar case it was shown that the flame propagates in between the two streams till it reaches

Table 4.6 Computations detail for $T=800K$, $p=10132500Pa$.

Flow property	Fuel Stream	Oxidizer stream
Gas composition	MMH	RFNA
Temperature(K)	800	800
Mass flow rate(kg/s)	12×10^{-4}	20.0×10^{-4}
Density (kg/m^3)	72.2	97.5
Velocity (m/s)	30	27
Thermal conductivity ($W/m - K$)	0.0826	0.0545

the cavity and establishes itself along the two streams. Thus, the three-dimensional combustion behavior is seen to differ from the planar case.

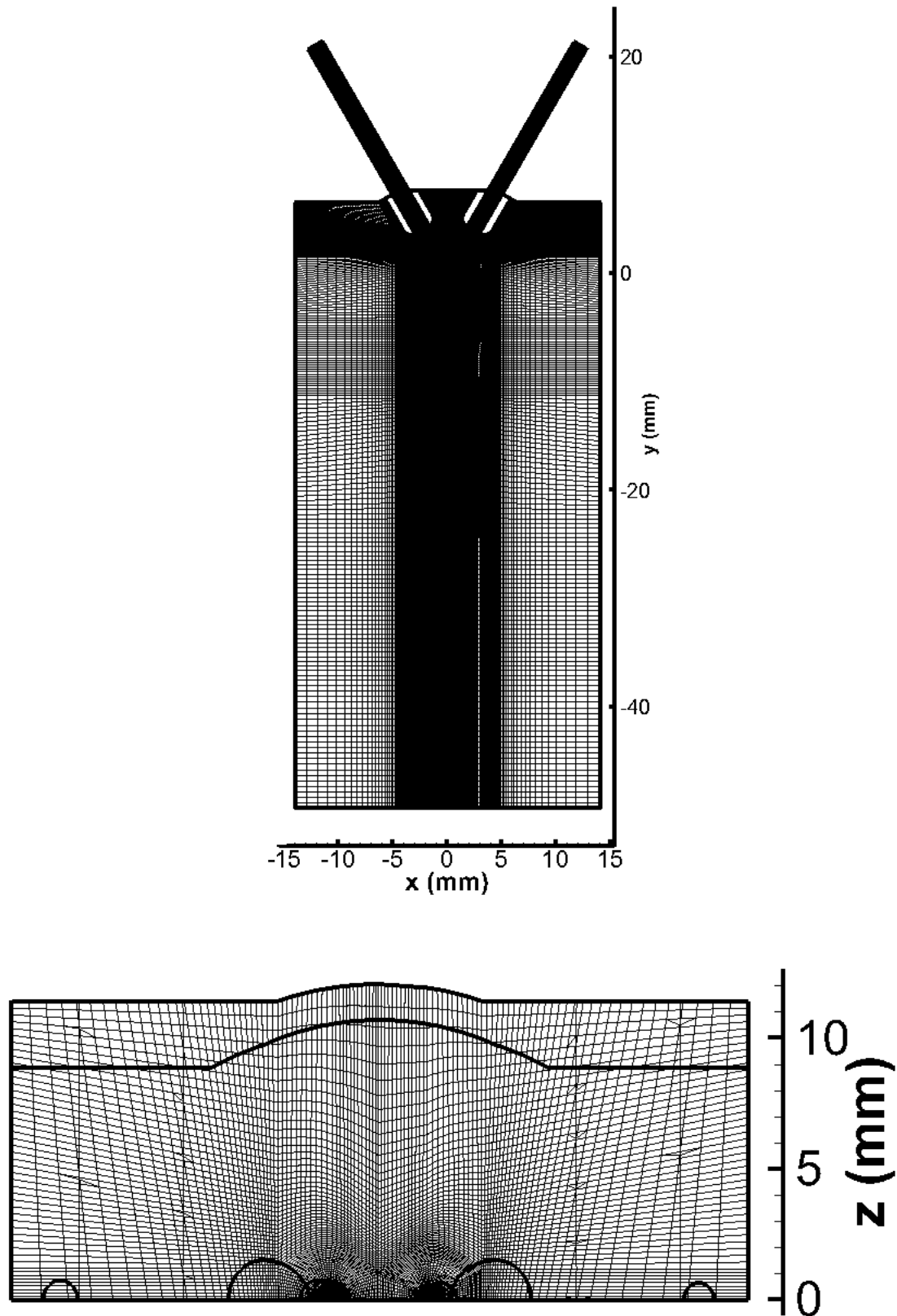


Figure 4.36. View of the domain from the top (top) and in the upstream direction (bottom). Also shown is the detail of grid at the plane of symmetry (top) and at a location midway between orifices and outlet.

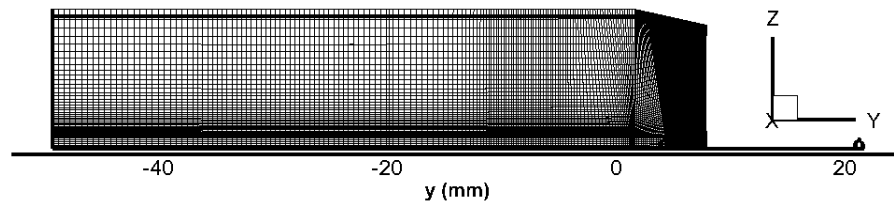


Figure 4.37. View of the domain seen perpendicular to flow direction along with the grid at a plane.

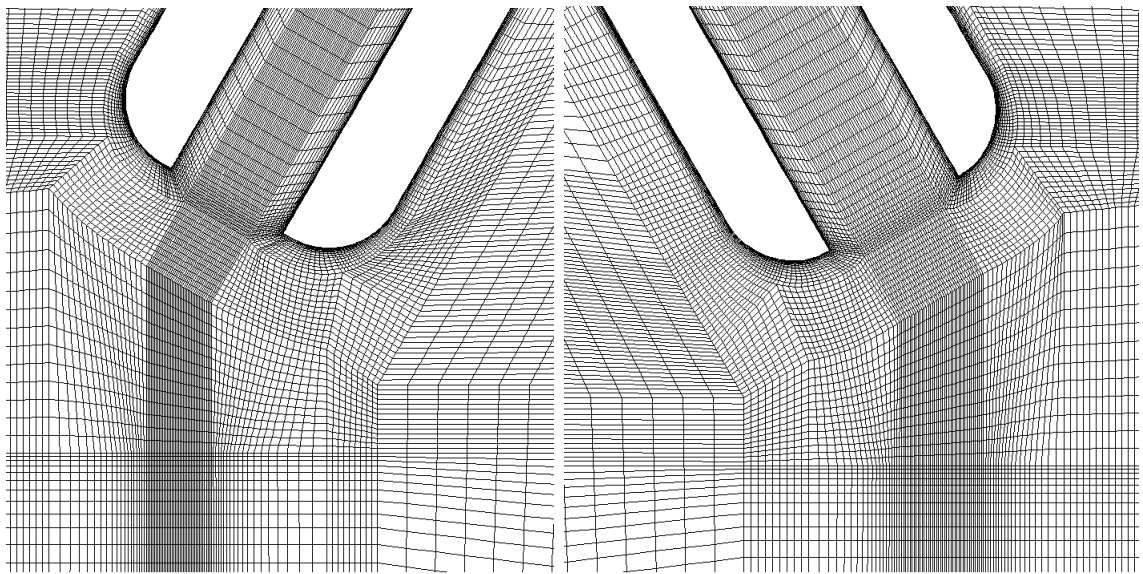


Figure 4.38. Detail of grid in the plane of symmetry close to the RFNA orifice (left) and MMH orifice (right)

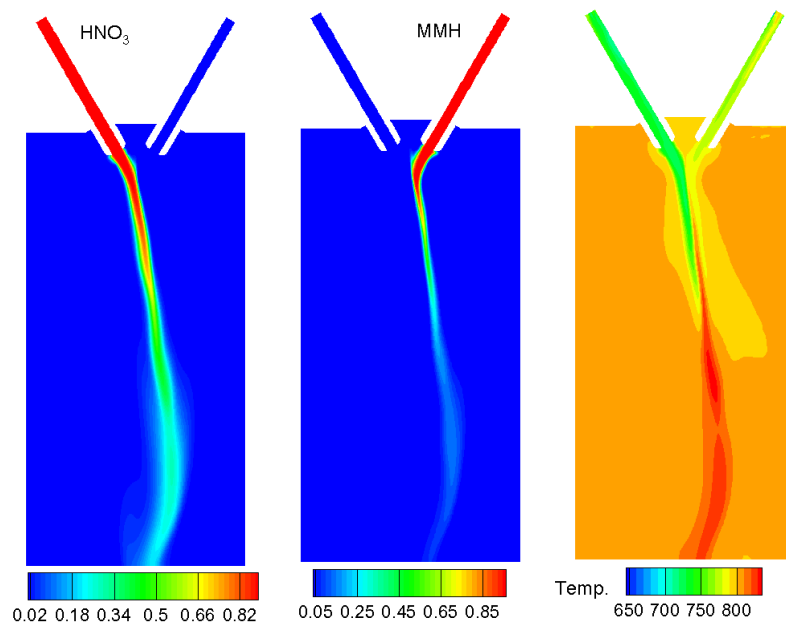


Figure 4.39. Contour plot of HNO₃ (left), MMH (center) and temperature (right) at a pressure of 1 *atm* in argon environment.

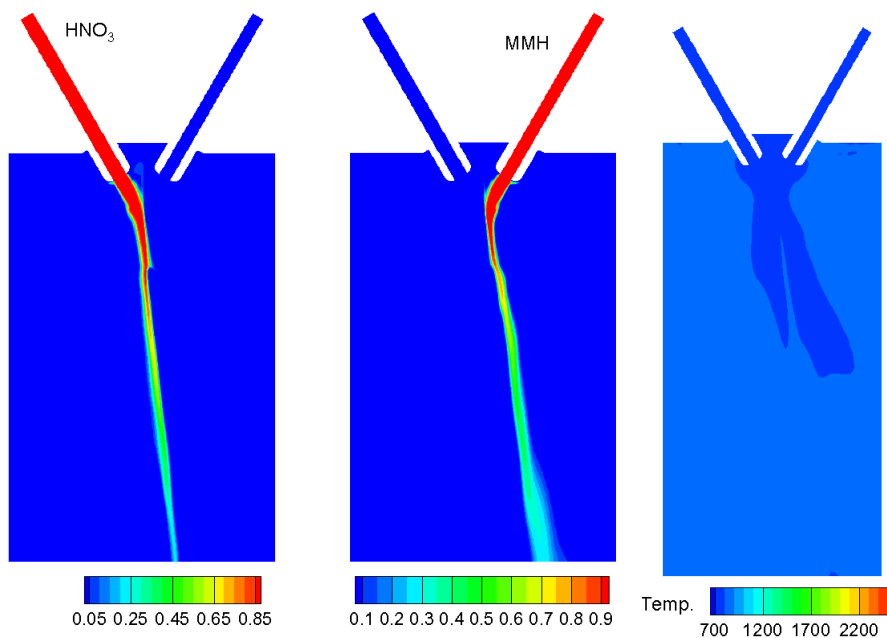


Figure 4.40. Contour plot of HNO₃ (left), MMH (center) and temperature (right) at a pressure of 100 *atm* in helium environment.

CHAPTER 5. SUMMARY AND CONCLUSIONS

The computational analyses of two fluid mechanics problems, one a non-reacting flow of a shrouded plug nozzle concept and the other a reacting jet impingement have been addressed. The solution for both problems employed a preconditioned dual-time step algorithm based finite volume solver. The turbulence closure is based upon the filtered averaged equations and is achieved through the $k - \omega$ turbulence model coupled with a DES approach for large turbulent scales. Combustion is incorporated by means of a finite rate Arrhenius model that takes into account multi-species and multi-step kinetics and evaluates species source terms from the filtered averaged quantities at the cell center.

The shrouded plug nozzle corresponds to a concept that has been proposed for a commercial aircraft. The geometry of this concept is unique from traditional plug nozzles because of the extended shroud and the NPR operation range giving characteristics that resemble those of converging diverging sections while also retaining characteristics of plug nozzle flowfield. Results from an experimental sub-scale model by Tapee [40] and Cummings [41] are used to provide validation for the computations. Simultaneously the computations serve as an aid in interpreting the experimental results and in interpolating between measured variables. The test model used a host of instrumentation and imaging capabilities: static pressure probes on the plug and shroud wall, Kulite transducers to measure pressure oscillation frequency coupled with shadowgraph and schlieren systems that provided a picture of the flowfield. This sub-scale model formed the basis for computational simulations of CHAPTER 3.

Analyses of the nozzle included both axisymmetric and three-dimensional configurations both of which were done as steady and unsteady problems. The results highlighted the complexity of the internal flowfield, primarily the interaction of the

shock in the diverging section with the adjacent boundary layer on the shroud and plug wall. The steady computations showed that the shock progressed from a normal shock to a lambda pattern at NPR's below 2.0. At moderate NPR's (2.25-3.1) the shock structure goes from Mach reflection to a regular reflection. This is followed by an oblique shock impinging on the plug wall at high NPR's until nearly perfect expansion to ambient conditions is achieved at design NPR. As the shock structure varied with NPR, the separation region behind the shock went from a fully separated FSS (Free Shock Separation) mode at NPR's below 2.0 to a reattached RSS (Restricted Shock Separation) mode above 2.25.

Overall axisymmetric steady computations compared well with experiments. Comparisons of computational schlieren pictures with experimental schlieren and shadowgraph gave a visual confirmation of the multitude of shock structures predicted by computations with varying NPR's. A direct comparison of static pressure distributions on the plug and shroud wall with data starting from NPR of 1.26 to design ascertained the accuracy of computations. The approach of using experimental data in conjunction with experiments was useful in reinterpreting what was considered to be an incorrectly functioning pressure tap. In actuality they were a result of flow features that were understood by computations and which were not discernible in experiments. Thus, computations helped to ascertain integrity and correctness of the experimental procedure.

The understanding of the flow characteristics from the steady computations and unsteady axisymmetric computations were successful in explaining the shifts in the experimentally measured peak frequency of pressure oscillations as a function of NPR. In experiments at the lowest NPR of 1.26, a preferred frequency of 170Hz was obtained. This then shifted to a constant frequency of 200Hz for NPR's below 2.0. At NPR's starting at 2.0 the experimentally observed frequency increased monotonically with NPR till 2.23. Finally, past this NPR the spectral characteristics was characterized by an absence of preferred frequencies. The axisymmetric unsteady results showed that the frequency of 170Hz at lowest NPR was as a result of the nozzle throat

choking and unchoking. The constant frequency region occurred below NPR of 2.0 because the nozzle was in the FSS regime, a regime whose extent was established by using both computations and experiments. The monotonically increasing frequency region corresponded to the transition between RSS and FSS (the only region which was observed to exhibit azimuthal asymmetry by static pressure measurements in the experiments). The reason for the disappearance of the peak frequency was that the shock and the associated separated region has moved downstream of the probe. The location of the shock and the associated separation region with respect to dynamic pressure transducers were established by the steady computations validated with data. The region of azimuthal asymmetry occurring during transition from FSS to RSS was studied with steady 3-D computations but they predicted axisymmetric flow.

Unsteady 3-D computations performed at two NPR's, 1.26 and 1.59 showed two distinct behaviors. At NPR of 1.26 the shock system and the ensuing recirculation region exhibited relatively strong oscillations and again as in the unsteady axisymmetric case demonstrated periodic choking and unchoking of the throat. The dynamic flowfield predicted by the 3-D unsteady computations, however, remained axisymmetric throughout this fluctuations. Both the axisymmetric and unsteady 3-D computations predicted a pressure oscillation frequency of 120Hz but much below the measured frequency of 170Hz . Time-averaged unsteady results from axisymmetric and 3-D computations matched closely with the data. In contrast to NPR of 1.26, the 3-D unsteady results at NPR of 1.59 showed that the dynamic flowfield was azimuthally asymmetric. The time-averaged flow field obtained from the 3-D unsteady computations at both NPR's was found to be axisymmetric similar to what is seen from the 3-D steady computations as well as the static pressure probes. Time-averaged pressure distributions from 3-D unsteady computations at NPR of 1.59 were closer to the data than that predicted by axisymmetric unsteady computations. In comparison to 70Hz frequency predicted by axisymmetric unsteady computations at NPR of 1.59,

the predicted frequency by 3-D unsteady computations of 150Hz was much closer to the measured frequency of 200Hz .

The analysis of impinging jets consisted the reaction between MMH and RFNA. At the outset of the study, there were no mechanisms available to describe reaction between MMH and RFNA, and as a consequence a primary goal of the present simulations were to understand the characteristic behavior of a newly developed reduced mechanism. This reduced mechanism consisted of 25 species and 98 reactions. The characteristic chemical time scales of the mechanism were first evaluated using a simple homogeneous constant volume combustion problem with time to ignite as a metric. The combustion kinetics are strongly dependent on initial temperature and pressure of the propellant mixture. The reduced kinetics showed that a temperature of 800K was needed to initiate combustion in a millisecond time frame while lower temperatures take 100's of milliseconds to ignite. Similar conclusions were also obtained from other chemical kinetics studies performed in literature. With the propellant mixture initially at a temperature of 800K combustion was observed at both one and 100atm although the higher pressure gave considerably faster combustion response.

Following the understanding of the chemical time scales gained in the above analysis an impinging jet configuration similar to that used in practical applications of propellant combustion was studied. The configuration is studied as a planar unsteady problem primarily to evaluate chemical kinetic mechanism before 3-D analysis can be taken up. The reaction between the impinging jets involves convection and diffusion processes that play a dominant role in real combustion processes. Based upon recent experiments that showed that the background gases into which impinging jets are injected has a strong effect on ignition and combustion, the computations in a similar fashion investigate the same two gases, argon and helium. Also, to understand effect on combustion two pressures were considered, one at experimental conditions (1atm) and the other similar to practical applications (100atm). First the planar 2-D problem was studied to provide a quick first step in understanding combustion. In agreement with experiments, the two background gases with different thermal and mass diffu-

sive properties resulted in considerably different flowfields and combustion processes. Similarly the two different pressures had a considerable effect on the combustion.

The computations at low pressures, where lab-scale experimental data are available, indicates that the initial mixing layer first ignites at a downstream location. Following this, the cavity region between the two orifices ignites and a flame front from the cavity region propagates downstream and merges with the initial flame to give a flame front that extends from the RFNA orifice to the domain outlet. This description of the ignition process is analogous to that observed in the experiments. The timing of these events differed in argon and helium with argon showing longer times. Argon mixtures due to their higher densities induced stabilities in the reacting shear layer that were not seen in helium.

The combustion occurred much faster at higher pressures of 100 atm . In the case of high pressures, however, the flame is seen to propagate in the opposite direction to the flow in between the two propellant streams and there was no difference between the argon and helium mixtures.

Limited three-dimensional computations of the impinging jet combustion showed a considerable difference from the 2-D results. At low pressure, combustion initiation was not observed but did occur at high pressures. Even the combustion behavior was different than at the planar case. The flame front remained anchored at the downstream location in 3-D at the high pressure.

Future Work

The literature for predicting accurate shock physics considers simple configurations like compression corners to understand flowfield unsteadiness. However, it appears that there is limited understanding about pressure oscillation prediction and its source even in these simple configurations. It may be beneficial to see explore other models proposed in the literature to see if improved predictions can be obtained. Though no pressure oscillation data is available from the experiments in the RSS regime literature indicates that the shock system is associated with a high frequency pressure oscillation even in this regime. As a further step to understand

pressure oscillation throughout the entire NPR range for the nozzle an unsteady analysis can be conducted at one particular NPR in the RSS regime.

In the case of the reaction problem of MMH and RFNA basis was laid for computational analysis in 3-D. The three-dimensional analysis can be completed with similar approach adopted in planar computations. The chemical mechanism was observed to promote combustion behavior analogous to the experiments for similar conditions. Since, combustion is dependent on the geometry of fuel and oxidizer passages (length to diameter ratio) and injection velocity, it will be instructive to understand the effect of these parameters on combustion behavior.

LIST OF REFERENCES

LIST OF REFERENCES

- [1] P.E.O Buelow, S. Venkateswaran, and C.L. Merkle. The effect of grid aspect ratio on convergence. *AIAA Journal*, 32(12):2401–2408, 1994.
- [2] C. Lian, G. Xia, and C.L. Merkle. Impact of source terms on reliability of cfd algorithms. Number AIAA-2009-4142, 2009.
- [3] R. Cowart and T. Grindle. An overview of the gulfstream / nasa quiet spike flight test program. Number AIAA 2008-0123, 2008.
- [4] T.R. Conners, D.C. Howe, J.R. Whurr, and C.F. Smith. Conceptual design, integration, and development plan for an efficient low sonic boom propulsion system employing advanced supersonic engine cycles. Technical Report Final Report Public Distribution, Contract NNC04CA29C, NASA, 2005.
- [5] R. Wolz. A summary of recent supersonic vehicle studies at gulfstream aerospace. Number AIAA 2003-0558, 2003.
- [6] T.R. Conners and D.C. Howe. Supersonic inlet shaping for dramatic reductions in drag and sonic boom strength. Number AIAA-2006-0030.
- [7] T.R. Conners, J.M. Merret, D.C. Howe, K.M. Tacina, and S.M. Hirt. Wind tunnel testing of an axisymmetric isentropic relaxed external compression inlet at mach 1.97 design speed. Number AIAA-2007-5066, 2007.
- [8] L. E Stitt. Exhaust nozzles for propulsion systems with special emphasis on supersonic cruise aircraft. Technical Report NASA RP-1235, NASA, 1991.
- [9] G.V.R Rao. Recent developments in rocket nozzle configurations. *ARS Journal*, 31(11), 1961.
- [10] H. G. Krull and W.T. Beal. Effect of outer shell design on performance characteristics of convergent plug exhaust nozzles. Technical Report NACA RM-E54K22, NACA, 1955.
- [11] G. Angelino. Approximate method for plug nozzle design. *AIAA Journal*, 2, 1964.
- [12] Berman K. Performance of plug type rocket exhaust nozzles. *ARS Journal*, 31(1), 1961.
- [13] T. Rommel, G. Hagemann, C.-A. Schley, G. Krulle, and D. Manski. Plug nozzle flowfield analysis. *AIAA Journal*, 13:629–634.
- [14] M. Onofri. Plug nozzles: Summary of flow features and engine performance. Number AIAA 2002-0584.

- [15] P. Henne. The case for small supersonic civil aircraft. Number AIAA 2003-2555, 2003.
- [16] T. Hsieh, T.J. Bogar, and T.J. Coakley. Numerical simulation and comparison with experiment for self-excited oscillations in a diffuser flow. *AIAA Journal*, 25(7), 1987.
- [17] M.-S. Liou and T.J. Coakley. Numerical simulations of unsteady transonic flow in diffusers. *AIAA Journal*, 22(8), 1984.
- [18] T. Hsieh, A. B. JR. Wardlaw, P. Collins, and T. Coakley. Numerical investigation of unsteady inlet flowfields. *AIAA Journal*, 25(1), 1987.
- [19] F.E.C. Culick and T. Rogers. The response of normal shocks in diffusers. *AIAA Journal*, 21:1382–1390, 1983.
- [20] V. Yang and F. E. C. Culick. Analysis of unsteady diffuser flow with a shock wave. *AIAA J. of Propulsion and Power*, 1:222–228, 1985.
- [21] T.J. Bogar, M. Sajben, and J.C. Kroutil. Characteristic frequencies of transonic diffuser flow oscillations. *AIAA Journal*, 9:1232–1240.
- [22] M. Sajben and J.C. Kroutil. Effect of initial boundary layer thickness on transonic diffuser flow. *AIAA Journal*, 19:1386–1393, 1983.
- [23] M. Sajben, J.C. Kroutil, and C.P. Chen. Unsteady transonic flow in a two-dimensional diffuser. Technical Report CP 227, AGARD, 1977.
- [24] M. Sajben, T.J. Bogar, and J.C. Kroutil. 1984.
- [25] T. Handa, Y. Miyazato, M. Masuda, and K. Matsuo K. Formation of multiple shocklets in a transonic diffuser flow. *Shock Waves*, 11:423–430, 2002.
- [26] A. Johnson and D. Papamoschou. Shock motion and flow instabilities in supersonic flow separation. Number AIAA 2008-3846, 2008.
- [27] K.C. Muck, J.-P. Dussauge, and S.M. Bogdonoff. Structure of the wall pressure fluctuations in a shock-induced separated turbulent flow. Number AIAA 1985-0179, 1985.
- [28] D. Papamoschou and A. Johnson. Unsteady phenomenon in supersonic nozzle flow separation. Number AIAA 2006-3300.
- [29] J.M. Delery. Experimental investigation of turbulence properties in transonic shock/turbulent boundary layer interaction. *AIAA Journal*, 21, 1983.
- [30] K.J. Plotkin. Shock wave oscillation driven by turbulent-boundary layer fluctuations. *AIAA Journal*, 13:1036–1040.
- [31] G. Hagemann, M. Frey, and W. Koschel. Appearance of restricted shock separation in rocket nozzles. *Journal of Propulsion and Power*, 18(3), 2002.
- [32] A. Gross and Weiland C. Numerical simulation of separated cold gas nozzle flows. *Journal of Propulsion and Power*, 20(3), 2004.

- [33] T. Alziary de Roquefort. Unsteadiness and side-loads in over-expanded nozzles. Proc. of 4th European Symposium on Aerothermodynamics for Space Applications, 2001.
- [34] S. Deck and A. T. Nguyen. Unsteady side loads in a thrust-optimized contour nozzle at hysteresis regime. *AIAA Journal*, 42(9), 2004.
- [35] S.B. Verma. Performance characteristics of an annular conical aerospike nozzle with freestream effect. Number AIAA 2008-5290, 2008.
- [36] C-C. Fan, X. Xiao, and Hassan H. A. Baurle R. A. Edwards, J. R. Hybrid large-eddy/reynolds-averaged navier-stokes simulations of shock-separated flows. *AIAA Journal of Spacecraft and Rockets*, 41(6):897–906, 2004.
- [37] S. Priebe, M. Wu, and M.P. Martn. Direct numerical simulation of a reflected shockwave and turbulent boundary layer interaction. *AIAA Journal*, 47(5), 2009.
- [38] A.A. Zheltovodov. Some advances in research on shock wave turbulent boundary layer interactions. Number AIAA 2006-496, 2006.
- [39] D. Knight, H. Yan, A.G. Panaras, and A. Zheltovodov. Advances in cfd prediction of shock wave turbulent boundary layer interaction. *Progress in Aerospace Sciences*, 39, 2003.
- [40] J. Tapee. *Experimental Analysis of a Plug Nozzle*. Master's thesis, Purdue University, May 2009.
- [41] C. Cummings. *Bi-Annular Nozzle Rig (BANR) Facility Checkout and Plug Nozzle Performance Test Data*. Master's thesis, Aeronautical and Astronautical Engineering, Purdue University, August 2010.
- [42] M. J. Nusca, N. P. Mathias, and Michaels R. S. Reacting flow cfd model of the throttling in the army's impinging stream vortex engine. Number AIAA 2008-4836.
- [43] K. Ohminami, H. Ogawa, and K. T. Uesugi. Numerical bipropellant thruster simulation with hydrazine and nto reduced kinetic model. Number AIAA 2009-452.
- [44] W. R. Anderson, McQuaid M. J., M. J. Nusca, and A. J. Kotlar. A detailed finite rate chemistry mechanism for monomethylhydrazine- red fuming nitric acid. Technical Report ARL TR 5088, ARL, 2010.
- [45] P. Westmoreland and Nicole L. Reation kinetics studies, muri. Technical report, Private Communication, 2010.
- [46] T. L. Pourpoint and W. E. Anderson. Hypergolic reaction mechanisms of catalytically promoted fuels with rocket grade hydrogen peroxide. *Combustion Science and Technology*, 179:2107–2133, 2007.
- [47] P. Timothy and W. E. Anderson. Environmental effects on hypergolic ignition. Number AIAA 2005-3581.
- [48] M. James, T. Kubal, S. Son, W. Anderson, , and T.L. Pourpoint. Calibration of an impinging jet injector suitable for liquid and gelled hypergolic propellants. Number AIAA-2009-4882, 2009.

- [49] T. Kubal, E. Dambach, S. Son, W. Anderson, and T.L. Pourpoint. Aspects of monomethylhydrazine and red fuming nitric acid ignition. Number AIAA-2010-6902, 2010.
- [50] B. R. Lawver and B. P. Breen. Hypergolic stream impingement phenomenon-nitrogen tetroxide/hydrazine. Number NASA N68-37831.
- [51] W. A. Wood and W. L. Kleb. 2-d/axisymmetric formulation of multi-dimensional upwind schemes. Number AIAA 2001-2630, 2001.
- [52] D.C. Wilcox. Formulation of the $k - \omega$ turbulence model revisited. Reno, NV, January 2007. 45th AIAA Aerospace Sciences Meeting and Exhibit.
- [53] P. R. Spalart, W. H. Jou, M. Strelets, and S. R. Allmaras. Comments on the feasibility of les for wings and on a hybrid rans/les approach. Proceedings of the 1st U.S. Air Force Office of Scientific Research Office Conference on DNS/LES, pages 137–147, 1997.
- [54] M. Strelets. Detached eddy simulation of massively separated flows. Number AIAA 2001-0879, 2001.
- [55] Spalding D. B. Development of the eddy break up model of turbulent combustion. 16th symposium on combustion, pages 1657–1663, 1976.
- [56] K.K. Kuo. *Principles of Combustion*. John Wiley and Sons, New York, 1986.
- [57] N. Peters. *Turbulent Combustion*. Cambridge University Press, 2000.
- [58] Peters N. The turbulent burning velocity of large scale and small-scale turbulence. *Journal of Fluid Mechanics*, 384:107–132, 1999.
- [59] K.N.C Bray, P. A. Libby, G. Masuya, and J. B. Moss. Turbulence production in premixed turbulence flames. *Combustion Science and Technology*, 25:127–140, 1981.
- [60] K.N.C Bray, P. A. Libby, and J. B. Moss. Flamelet crossing frequencies and mean reaction rates in premixed turbulent combustion. *Combustion Science and Technology*, 41:143–172, 1984.
- [61] S. B. Pope. Pdf methods for turbulent reacting flows. *Progress in Energy and Combustion Science*, 19:119–192, 1985.
- [62] S. B. Pope. Computations of turbulent combustion: progress and challenges. *23rd symposium on combustion, The Combustion Institute*, pages 591–612, 1990.
- [63] C. Dopazo. *Turbulent Reacting Flows*. Academic, London, 1994.
- [64] S. B. Pope. Computationally efficient implementation of combustion chemistry using in situ adaptive tabulation. *Combustion Theory and Modeling*, 1:41–63, 1997.
- [65] W. Tsang and J. T. Herron. Chemical kinetic database for propellant combustion i. reactions involving no, no₂, hno, hno₂, hcn and n₂o. *J. Phys. Chem. Ref. Data*, 20:609–663, 1991.

- [66] W. Sutherland. The viscosity of gases and molecular force. *Philosophical Magazine*, 5(36):507–531, 193.
- [67] T. Poinsot and D. Veynante. *Theoretical and Numerical Combustion*. R.T. Edwards, Inc, Flourtown, second edition, 2005.
- [68] RC Reid, JM Prausnitz, and TK Sherwood. *The Properties of gases and liquids*. Mc-Graw-Hill, New York, 1977.
- [69] B.J. McBride, M.J. Zehe, and S. Gordon. Nasa glenn coefficients for calculating thermodynamic properties of individual species. Technical Report TP-2002-211556, NASA, 2002.
- [70] V. Sankaran and C.L. Merkle. Dual time stepping and preconditioning for unsteady computations. *AIAA*, (95-0078), 1995.
- [71] P.L. Roe. Approximate reimann solvers, parameter vectors, and difference schemes. *Journal of Computational Physics*, 43:357–372, 1981.
- [72] S. Venketeswaran and C.L. Merkle. Analysis of preconditioning methods for the euler and the navier-stokes equations. Technical Report VKI LS 1999-03., von Karman Institute for Fluid Dynamics., 1993.
- [73] and Hyman M. J. Harten, A. Self adjusting grid methods for one-dimensional hyperbolic conservation laws. *Journal of Computational Physics*, 2:235–269, 193.
- [74] C. R. Mitchell. Improved reconstruction schemes for the navier-stokes equations on unstructured meshes. Number AIAA 1994-0642, 1994.
- [75] T.J. Barth and D.C. Jespersen. The design and application of upwind schemes on unstructured meshes. Number AIAA 1989-0366, 1989.
- [76] M. Berger, M. J. Aftosmis, and S. M. Murman. Analysis of slope limiters on irregular grids. Number AIAA 2005-490, 2005.
- [77] V. Venkatakrisnan. Convergence to steady state solutions of the euler equations on unstructured grids with limiters. *Journal of Computational Physics*, 11(1):120–130, 1995.
- [78] X. Zeng. *Convergence and Robustness Issues in Computational Fluids*. PhD thesis, The University of Tennessee, Knoxville, December 2004.
- [79] A. Trebs. *Bi-Annular Nozzle Rig Facility Development*. Master's thesis, Aeronautical and Astronautical Engineering, Purdue University, May 2008.
- [80] A. Sandroni. *Plume and Performance measurements on a plug nozzle supersonic business jet applications*. Master's thesis, Purdue University, May 2009.
- [81] A. Chpoun, D. Passerel, H. Li, and G. Ben-Dor. Reconsideration of oblique shock wave reflections in steady flows. part 1. experimental investigation. *Journal of Fluid Mechanics*, 301:19–35, 1995.
- [82] J.-P. Dussauge, P. P. Dupont, and J.-F. Debieve. Unsteadiness in shock-wave boundary layer interactions with separation. *Aerospace Science and Technology*, 10:85–91, 2006.

- [83] M. Frey and G. Hagemann. Status of flow separation prediction in rocket nozzles. Number AIAA 1998-3619, 1998.
- [84] E. Dambach, K. Cho, T.L. Pourpoint, and S. Hiester. Ignition of advanced hypergolic propellants. Number AIAA 2010-6984, 2010.
- [85] Hampton C., K. Ramesh, and J. Smith. Importance of chemical delay time in understanding hypergolic ignition behaviors. Number AIAA 2003-1359, 2003.

APPENDIX

APPENDIX: REDUCED MECHANISM FOR MMH/RFNA

ELEMENTS CONSIDERED	ATOMIC WEIGHT
1. H	1.00797
2. C	12.0112
3. O	15.9994
4. N	14.0067

SPECIES CONSIDERED	S E	G E	MOLECULAR WEIGHT	TEMPERATURE		ELEMENT COUNT			
				LOW	HIGH	H	C	O	N
1. CH ₃ NHNH ₂	G	0	46.07237	298	6000	6	1	0	2
2. CH ₃ NNH ₂	G	0	45.06440	200	6000	5	1	0	2
3. CH ₃ NNH	G	0	44.05643	200	6000	4	1	0	2
4. CH ₃ NN	G	0	43.04846	200	6000	3	1	0	2
5. H	G	0	1.00797	300	5000	1	0	0	0
6. H ₂	G	0	2.01594	300	5000	2	0	0	0
7. O ₂	G	0	31.99880	300	5000	0	0	2	0
8. H ₂ O	G	0	18.01534	300	5000	2	0	1	0

9. CO2	G	0	44.00995	300	5000	0	1	2	0
10. CO	G	0	28.01055	300	5000	0	1	1	0
11. N2	G	0	28.01340	300	5000	0	0	0	2
12. NO2	G	0	46.00550	300	5000	0	0	2	1
13. NO	G	0	30.00610	300	5000	0	0	1	1
14. HONO	G	0	47.01347	300	5000	1	0	2	1
15. OH	G	0	17.00737	300	5000	1	0	1	0
16. O	G	0	15.99940	300	5000	0	0	1	0
17. HO2	G	0	33.00677	300	5000	1	0	2	0
18. CH3O	G	0	31.03446	300	3000	3	1	1	0
19. CH3	G	0	15.03506	300	5000	3	1	0	0
20. CH2O	G	0	30.02649	300	5000	2	1	1	0
21. CH3OH	G	0	32.04243	300	5000	4	1	1	0
22. HCO	G	0	29.01852	300	5000	1	1	1	0
23. HNO	G	0	31.01407	300	5000	1	0	1	1
24. HNO3	G	0	63.01287	300	5000	1	0	3	1
25. N2O4	G	0	92.01100	300	5000	0	0	4	2

NOTE: A units mole-cm-sec-K, E units cal/mole

$$(k = A T^{**b} \exp(-E/RT))$$

REACTIONS CONSIDERED	A	b	E
1. NO2(+M)=NO+O(+M)	7.60E+18	-1.3	73290.0
Low pressure limit:	0.24700E+29	-0.33700E+01	0.74800E+05
H2O	Enhanced by	4.400E+00	
N2	Enhanced by	1.000E+00	
CO2	Enhanced by	2.300E+00	

2.	$H+NO(+M)=HNO(+M)$	1.52E+15	-0.4	0.0
	Low pressure limit:	0.40000E+21	-0.17500E+01	0.00000E+00
	H2O	Enhanced by	5.000E+00	
	N2	Enhanced by	1.000E+00	
	CO2	Enhanced by	1.300E+00	
3.	$NO+OH(+M)=HONO(+M)$	1.99E+12	-0.1	-721.0
	Low pressure limit:	0.50800E+24	-0.25100E+01	-0.67600E+02
	H2O	Enhanced by	8.300E+00	
	N2	Enhanced by	1.000E+00	
	CO2	Enhanced by	1.500E+00	
4.	$NO2+NO2=NO+NO+O2$	4.51E+12	0.0	27600.0
5.	$HNO+O2=H2O+NO$	1.00E+13	0.0	25000.0
6.	$HNO+NO2=HONO+NO$	4.42E+04	2.6	4042.0
7.	$HONO+O=OH+NO2$	1.20E+13	0.0	5961.0
8.	$HONO+OH=H2O+NO2$	1.27E+10	1.0	135.0
9.	$HNO+O=OH+NO$	3.61E+13	0.0	0.0
10.	$HCO+OH=H2O+CO$	1.00E+14	0.0	0.0
11.	$HCO+M=H+CO+M$	2.50E+14	0.0	16802.0
	CO	Enhanced by	1.900E+00	
	H2	Enhanced by	1.900E+00	
	CO2	Enhanced by	3.000E+00	
	H2O	Enhanced by	5.000E+00	
12.	$HCO+H=CO+H2$	1.19E+13	0.2	0.0
13.	$HCO+O=CO+OH$	3.00E+13	0.0	0.0
14.	$HCO+O=CO2+H$	3.00E+13	0.0	0.0
15.	$HCO+O2=H2O+CO$	3.30E+13	-0.4	0.0
16.	$CO+O(+M)=CO2(+M)$	1.80E+10	0.0	2380.0
	Low pressure limit:	0.13500E+25	-0.27900E+01	0.41900E+04
	H2O	Enhanced by	1.200E+01	

H2	Enhanced by	2.500E+00		
CO	Enhanced by	1.900E+00		
CO2	Enhanced by	3.800E+00		
17. CO+OH=CO2+H		1.51E+07	1.3	-758.0
18. CO+O2=CO2+O		2.53E+12	0.0	47688.0
19. H02+CO=CO2+OH		5.80E+13	0.0	22934.0
20. OH+H2=H2O+H		2.16E+08	1.5	3430.0
21. O2+H=O+OH		3.52E+16	-0.7	17070.0
22. O+H2=OH+H		5.06E+04	2.7	6290.0
23. H+O2+M=H02+M		3.61E+17	-0.7	0.0
H2O	Enhanced by	1.860E+01		
CO2	Enhanced by	4.200E+00		
H2	Enhanced by	2.900E+00		
CO	Enhanced by	2.100E+00		
N2	Enhanced by	1.300E+00		
24. OH+H02=H2O+O2		7.50E+12	0.0	0.0
25. H+H02=2OH		1.69E+14	0.0	874.0
26. H+H02=H2+O2		4.28E+13	0.0	1411.0
27. H+H02=O+H2O		3.01E+13	0.0	1721.0
28. O+H02=O2+OH		1.40E+13	0.0	1073.0
29. OH+OH=H2O+O		3.57E+04	2.4	2112.0
30. 2H+M=H2+M		1.00E+18	-1.0	0.0
H2	Enhanced by	0.000E+00		
H2O	Enhanced by	0.000E+00		
CO2	Enhanced by	0.000E+00		
31. 2H+H2=2H2		9.20E+16	-0.6	0.0
32. 2H+H2O=H2+H2O		6.00E+19	-1.2	0.0
33. 2H+CO2=H2+CO2		5.49E+20	-2.0	0.0
34. H+OH+M=H2O+M		1.60E+22	-2.0	0.0

H2O	Enhanced by	5.000E+00			
35. H+O+M=OH+M		6.20E+16	-0.6	0.0	
H2O	Enhanced by	5.000E+00			
36. O+O+M=O2+M		1.89E+13	0.0	-1788.0	
37. NO+HO2=NO2+OH		2.11E+12	0.0	-479.0	
38. NO2+H=NO+OH		1.30E+14	0.0	361.0	
39. NO2+O=NO+O2		3.90E+12	0.0	-238.0	
40. HNO+OH=NO+H2O		1.30E+07	1.9	-958.0	
41. H+HNO=H2+NO		4.46E+11	0.7	655.0	
42. CO+NO2=NO+CO2		9.04E+13	0.0	33780.0	
43. H2+NO2=HONO+H		1.30E+04	2.8	29770.0	
44. HONO+H=HNO+OH		5.63E+10	0.9	4969.0	
45. HONO+H=H2O+NO		8.13E+06	1.9	3847.0	
46. 2HONO=NO+NO2+H2O		3.49E-01	3.6	12140.0	
47. HCO+NO=HNO+CO		7.23E+12	0.0	0.0	
48. O+CH3<=>H+CH2O		5.06E+13	0.0	0.0	
49. O+CH2O<=>OH+HCO		3.90E+13	0.0	3540.0	
50. O+CH3O<=>OH+CH2O		1.00E+13	0.0	0.0	
51. O2+CH2O<=>HO2+HCO		1.00E+14	0.0	40000.0	
52. H+HCO(+M)<=>CH2O(+M)		1.09E+12	0.5	-260.0	
Low pressure limit:		0.24700E+25	-0.25700E+01	0.42500E+03	
TR0E centering:		0.78240E+00	0.27100E+03	0.27550E+04	0.65700E+04
H2	Enhanced by	2.000E+00			
H2O	Enhanced by	6.000E+00			
CO	Enhanced by	1.500E+00			
CO2	Enhanced by	2.000E+00			
53. H+CH2O<=>HCO+H2		5.74E+07	1.9	2742.0	
54. H+CH3O(+M)<=>CH3OH(+M)		2.43E+12	0.5	50.0	
Low pressure limit:		0.46600E+42	-0.74400E+01	0.14080E+05	

TR0E centering:	0.70000E+00	0.10000E+03	0.90000E+05	0.10000E+05
H2	Enhanced by	2.000E+00		
H2O	Enhanced by	6.000E+00		
CO	Enhanced by	1.500E+00		
CO2	Enhanced by	2.000E+00		
55. H+CH3O<=>H2+CH2O		2.00E+13	0.0	0.0
56. H+CH3O<=>OH+CH3		1.50E+12	0.5	-110.0
57. H+CH3OH<=>CH3O+H2		4.20E+06	2.1	4870.0
58. H2+CO(+M)<=>CH2O(+M)		4.30E+07	1.5	79600.0
Low pressure limit:	0.50700E+28	-0.34000E+01	0.84350E+05	
TR0E centering:	0.93200E+00	0.19700E+03	0.15400E+04	0.10300E+05
H2	Enhanced by	2.000E+00		
H2O	Enhanced by	6.000E+00		
CO	Enhanced by	1.500E+00		
CO2	Enhanced by	2.000E+00		
59. OH+CH3(+M)<=>CH3OH(+M)		2.79E+18	-1.4	1330.0
Low pressure limit:	0.40000E+37	-0.59200E+01	0.31400E+04	
TR0E centering:	0.41200E+00	0.19500E+03	0.59000E+04	0.63940E+04
H2	Enhanced by	2.000E+00		
H2O	Enhanced by	6.000E+00		
CO	Enhanced by	1.500E+00		
CO2	Enhanced by	2.000E+00		
60. OH+CH2O<=>HCO+H2O		3.43E+09	1.2	-447.0
61. OH+CH3O<=>H2O+CH2O		5.00E+12	0.0	0.0
62. OH+CH3OH<=>CH3O+H2O		6.30E+06	2.0	1500.0
63. HO2+CH3<=>OH+CH3O		2.00E+13	0.0	0.0
64. CH3+O2<=>O+CH3O		3.56E+13	0.0	30480.0
65. CH3+O2<=>OH+CH2O		2.31E+12	0.0	20315.0
66. CH3O+O2<=>HO2+CH2O		4.28E-13	7.6	-3530.0

67.	$\text{OH}+\text{NO}_2(+\text{M})=\text{HNO}_3(+\text{M})$	2.41E+13	0.0	0.0
	Low pressure limit:	0.64200E+33	-0.54900E+01	0.23500E+04
	H2O	Enhanced by	9.000E+00	
	N2	Enhanced by	1.000E+00	
	HNO3	Enhanced by	5.000E+00	
68.	$\text{HNO}_3+\text{H}=\text{NO}_2+\text{H}_2\text{O}$	6.00E+13	0.0	9800.0
69.	$\text{HNO}_3+\text{H}=\text{HONO}+\text{OH}$	2.00E+13	0.0	8000.0
70.	$\text{HNO}_3+\text{NO}=\text{HONO}+\text{NO}_2$	8.00E+06	2.0	11000.0
71.	$\text{NO}_2+\text{HO}_2=\text{HONO}+\text{O}_2$	1.00E+12	0.0	5000.0
72.	$\text{HCO}+\text{HNO}=\text{CH}_2\text{O}+\text{NO}$	6.00E+11	0.0	2000.0
73.	$\text{CH}_2\text{O}+\text{NO}_2=\text{HCO}+\text{HONO}$	8.02E+02	2.8	13730.0
74.	$\text{HCO}+\text{NO}_2=\text{CO}+\text{HONO}$	1.24E+23	-3.3	2355.0
75.	$\text{HCO}+\text{NO}_2=\text{H}+\text{CO}_2+\text{NO}$	8.39E+15	-0.8	1930.0
76.	$\text{HCO}+\text{HCO}=\text{CH}_2\text{O}+\text{CO}$	3.00E+13	0.0	0.0
77.	$\text{HCO}+\text{HCO}=\text{H}_2+\text{CO}+\text{CO}$	5.20E+12	0.0	0.0
78.	$\text{CH}_3+\text{NO}_2=\text{CH}_3\text{O}+\text{NO}$	1.40E+13	0.0	0.0
79.	$\text{CH}_3\text{NHNH}_2+\text{H}=\text{CH}_3\text{NNH}_2+\text{H}_2$	1.30E+13	0.0	2500.0
80.	$\text{CH}_3\text{NNH}_2+\text{M}=\text{CH}_3\text{NNH}+\text{H}+\text{M}$	1.00E+17	0.0	35770.0
81.	$\text{CH}_3\text{NN}=\text{CH}_3+\text{N}_2$	3.00E+06	0.0	0.0
82.	$\text{CH}_3\text{NHNH}_2=\text{CH}_3\text{NNH}+\text{H}_2$	3.16E+13	0.0	57000.0
83.	$\text{CH}_3\text{NNH}_2+\text{HO}_2=\text{CH}_3\text{NHNH}_2+\text{O}_2$	1.00E+06	2.0	0.0
84.	$\text{CH}_3\text{NN}+\text{HO}_2=\text{CH}_3\text{NNH}+\text{O}_2$	1.00E+06	2.0	0.0
85.	$\text{CH}_3\text{NHNH}_2+\text{O}=\text{CH}_3\text{NNH}+\text{H}_2\text{O}$	9.60E+12	0.0	0.0
86.	$\text{CH}_3\text{NNH}_2+\text{OH}=\text{CH}_3\text{NNH}+\text{H}_2\text{O}$	1.00E+08	2.0	0.0
87.	$\text{CH}_3\text{NNH}_2+\text{O}=\text{CH}_3\text{NNH}+\text{OH}$	1.00E+08	2.0	0.0
88.	$\text{CH}_3\text{NNH}_2+\text{O}_2=\text{CH}_3\text{NNH}+\text{HO}_2$	4.00E+12	0.0	0.0
89.	$\text{CH}_3\text{NHNH}_2+\text{OH}=\text{CH}_3\text{NNH}_2+\text{H}_2\text{O}$	3.92E+13	0.0	0.0
90.	$\text{CH}_3\text{NNH}+\text{OH}=\text{CH}_3\text{NN}+\text{H}_2\text{O}$	3.92E+13	0.0	0.0
91.	$\text{CH}_3\text{NHNH}_2+\text{O}=\text{CH}_3\text{NNH}_2+\text{OH}$	9.60E+12	0.0	0.0

92.	$\text{CH}_3\text{NNH}+\text{O}=\text{CH}_3\text{NN}+\text{OH}$	9.60E+12	0.0	0.0
93.	$\text{CH}_3\text{NHNH}_2+\text{NO}_2=\text{CH}_3\text{NNH}_2+\text{HONO}$	2.20E+11	0.0	5900.0
94.	$\text{CH}_3\text{NNH}+\text{NO}_2=\text{CH}_3\text{NN}+\text{HONO}$	2.20E+11	0.0	5900.0
95.	$\text{CH}_3\text{NNH}_2+\text{NO}_2=\text{CH}_3\text{NNH}+\text{HONO}$	1.00E+08	2.0	0.0
96.	$\text{N}_2\text{O}_4(+\text{M})=\text{NO}_2+\text{NO}_2(+\text{M})$	4.05E+18	-1.1	12840.0
Low pressure limit: 0.19600E+29 -0.38000E+01 0.12800E+05				
97.	$\text{CH}_3\text{O}+\text{NO}=\text{CH}_2\text{O}+\text{HNO}$	1.30E+14	-0.7	0.0
98.	$\text{CH}_3\text{O}+\text{NO}_2=\text{CH}_2\text{O}+\text{HONO}$	6.00E+12	0.0	2285.0

VITA

VITA

Sravan Kumar Dheeraj Kapilavai was born on the 25th of December 1984 in what was then a sleepy city of Hyderabad in peninsular India. His initial interest in mathematics, physics and chemistry was established thanks to his schooling in the competitive yet friendly academic environment of Hyderabad. He obtained a Bachelor of Technology degree majoring in Aerospace engineering in 2006 from the Indian Institute of Technology in Chennai, India. Following this, he started graduate school at Purdue University where he obtained a M.S. degree in Aeronautics and Astronautics in 2008 and finishing school with a Doctor of Philosophy in Mechanical engineering in 2011. He was awarded the best technical paper award by the Air Breathing Propulsion Systems Integration (ABPSI) Technical Committee in 2010 for a paper presented on Shrouded Plug Nozzles at the 2009 Joint Propulsion Conference.